Faculty of Engineering and Physical Sciences

School of Engineering

Institute of Sound and Vibration Research (ISVR)

Combining Transient and Steady-state Methods for Acoustic Leak Detection

by

Ndubuisi Uchendu

ORCID ID https://orcid.org/0000-0002-4199-5839

Thesis for the degree of Doctor of Philosophy

January 2024

University of Southampton

ABSTRACT

Faculty of Engineering and Physical Sciences

School of Engineering

Institute of Sound and Vibration Research (ISVR)

Doctor of Philosophy

Combining Transient and Steady-state Methods for Acoustic Leak Detection

by

Ndubuisi Uchendu

This thesis is concerned with the improvement of acoustic leak detection methods. While acoustic methods have been successfully used for detecting and locating leaks in metallic water pipes, they are generally less effective in plastic pipes due to the higher attenuation of acoustic waves in plastic pipes. Another motivation for the research is the need to fully utilise data acquired by monitoring devices installed in water distribution networks, for which existing acoustic methods are inadequate. Three specific problems associated with the application of existing acoustic methods are addressed in this thesis: long time required for identification of leaks, inaccurate leak localisation due to uncertainties in wave speed values, and non-robust time delay estimation (TDE). To deal with the first two issues, new transient and steady-state methods are developed by considering the acoustic leak detection problem from alternative perspectives, including transient/signal detection, multipath identification, and system identification. Transient methods are based on detecting and processing acoustic transients, while steady-state methods analyse signals generated by an ongoing leak. To facilitate transient analysis, a procedure for detecting, locating, and assessing the nature of acoustic transients is developed based on a change metric known as non-stationarity measure (NSM). An approach that combines multiple acoustic transient and steady-state methods is also developed. Alternative methodologies based on wavelet transforms, data-adaptive decompositions, and cepstral analysis are proposed for estimating time delays in leak signals. Also, new approaches for assessing accuracy of the time delay estimate are developed by exploiting the statistical properties of the cross-correlation function (CCF).

The alternative methods developed in this work offer practical benefits over existing methods. Application of transient/signal detection principles reduces the time required to detect the presence of a leak. The methods based on the multipath identification and system identification viewpoints do not require a priori knowledge of pipe material properties or wave speed to locate the leak. The synergy of methods in the combined approach ensures more reliable acoustic leak detection in a ‘self-contained’ manner, as essential leak detection tasks can be executed directly from measured leak signals without need for ‘third-party’ data or additional measurements. Unlike the commonly used generalised cross-correlation (GCC) methods, the alternative TDE methods proposed in this work do not require signals to be first filtered prior to estimating the time delay. Moreover, the new quality assessment metrics developed in this work provide a simple means to infer the accuracy of the time delay estimate as well as to select best parameters required for accurate TDE results. These new methods allow for fuller utilisation of data than is possible with currently employed acoustic methods. This is especially relevant considering the current drive towards massive deployment of transient loggers by water companies. A laboratory leakage test rig was designed and built specifically for the experimental investigation of the proposed methods.

TABLE OF CONTENTS

ABSTRACT i

TABLE OF CONTENTS i

LIST OF TABLES vi

LIST OF FIGURES vii

DECLARATION OF AUTHORSHIP xi

ACKNOWLEDGEMENTS xii

LIST OF ABBREVIATIONS xiii

LIST OF SYMBOLS xvi

CHAPTER 1 INTRODUCTION 1

1.1 Overview of water leak detection methods 1

1.2 Roles and limitations of acoustic methods in water leak detection 5

1.2.1 Acoustic wave attenuation 6

1.2.2 Wave speed estimation/measurement 6

1.2.3 Time delay estimation 8

1.2.4 Long leak identification time and unsuitability for leak size estimation 10

1.3 Alternative perspectives and strategies for acoustic leak detection 10

1.4 Objectives of the thesis 13

1.5 Original contributions 14

1.6 Thesis outline 15

CHAPTER 2 DESCRIPTION AND CHARACTERISATION OF THE LEAKAGE TEST RIG AND EXPERIMENTAL PROCEDURES 17

2.1 Description of the leakage test rig 17

2.2 Instrumentation and data acquisition 17

2.3 Experimental characterisation of the leakage test rig 19

2.3.1 Determination of pipe material properties 19

2.3.2 Wave speed measurement 21

2.3.3 Characterisation of noise sources 22
2.3.4 Determination of system transfer function 24
2.4 Experimental procedures and data analysis 26
2.5 Limitations of the leakage test rig 27
2.6 Summary and conclusion 28

CHAPTER 3 ACOUSTIC LEAK DETECTION AS A TRANSIENT AND SIGNAL DETECTION PROBLEM 30

3.1 Recasting leak detection as a transient and signal detection problem 30
3.2 Acoustic leak detection by transient analysis 33
3.2.1 Acoustic transient detection using the non-stationarity measure 33
3.2.1.1 Description of the Non-Stationarity Measure 34
3.2.1.2 Selection of transient detection threshold 36
3.2.1.3 Evaluation of the performance of the non-stationarity measure transient detector 38
3.2.2 Acoustic transient leak confirmation 43
3.3 Acoustic leak detection by steady-state analysis 46
3.3.1 Description of the passive steady-state leak detection method 47
3.3.2 Important considerations in the passive steady-state leak detection method 48
3.4 Experimental results and discussion 50
3.4.1 Experimental investigation of the passive transient leak detection method 50
3.4.2 Experimental investigation of the passive steady-state leak detection method 56
3.5 Advantages and limitations of acoustic transient and steady-state leak detection methods 60
3.6 Summary and conclusion 63

CHAPTER 4 ACOUSTIC LEAK DETECTION AS A MULTIPATH IDENTIFICATION PROBLEM 64

4.1 Recasting leak localisation as a multipath identification problem 64
4.2 Active transient acoustic leak detection by multipath identification 65
4.3 Steady-state multipath identification leak localisation method 68
4.4 Multipath identification methods 70
4.4.1 Autocorrelation multipath identification method 71
4.4.2 Cepstral multipath identification method 72
4.4.3 Comparison of autocorrelation and cepstral multipath identification techniques 73

4.4.4 Identification of the primary reflection among multiple reflections 75
4.5 Simulation results 76
4.5.1 Description of the simulation process and signals 76
4.5.2 Simulation results for the active transient leak localisation method 77
4.5.3 Simulation results for the steady-state leak localisation method 81
4.5.3.1 Comparison of multipath identification techniques 83
4.5.3.2 Effects of pipe properties on multipath identification 84
4.6 Application of multipath identification leak detection methods to experimental data 86
4.6.1 Experimental results for the active transient leak localisation method 86
4.6.2 Experimental results for the steady-state leak localisation method 91
4.7 Limitations of multipath identification leak detection methods 94
4.8 Summary and conclusion 95
CHAPTER 5 ACOUSTIC LEAK DETECTION AS A SYSTEM IDENTIFICATION PROBLEM ...96
5.1 Recasting leak localisation as a system identification problem 96
5.2 Normalised multichannel frequency least-mean squares blind channel identification 97
5.3 Estimation of channel length and propagation times of the leak noise in the pipe channels 100
5.3.1 Spectrally constrained blind channel identification method 101
5.3.2 Estimation of channel length 103
5.3.3 Estimation of propagation times of the leak noise in the acoustic leak pipe channels .104
5.4 Acoustic leak localisation procedures using blind channel identification 106
5.5 Results and discussion 108
5.5.1 Simulation results for the blind channel identification leak localisation method 108
5.5.2 Application to experimental leak signals 111
5.6 Limitations of the system identification leak localisation method 114
5.7 Summary and conclusion 115
CHAPTER 6 CORRELATION QUALITY ASSESSEMENT 117
6.1 Quantitative assessment of the impact of time delay estimation error on leak localisation .117
6.2 Existing time delay quality assessment metrics 118
6.3 Alternative approaches for assessing accuracy of the time delay estimate 121
6.3.1 Information criterion approach 122

6.3.1.1 Distribution of the cross-correlation function peak value 122
6.3.1.2 Description of information criteria 124
6.3.1.3 Steps in the information criterion approach 126
6.3.2 Processing gain approach 127
6.3.2.1 Peak-to-side lobe ratio 128
6.3.2.2 Peak-to-mean ratio 130
6.3.3 Statistical approach 131
6.4 Evaluation of quality assessment metrics using experimental leak signals 133
6.4.1 Comparative study of quality assessment metrics in leak signals 133
6.4.2 Selection of time delay estimation parameters using quality assessment metrics 137
6.5 Limitations of the correlation quality assessment metrics 141
6.6 Summary and conclusion 142
CHAPTER 7 ALTERNATIVE TIME DELAY ESTIMATION METHODS 143
7.1 Time delay estimators with inherent filtering property 143
7.1.1 Variance of the time delay estimate 144
7.1.2 Factors affecting the variance of the time delay estimate 145
7.2 Wavelet transform-based time delay estimator 146
7.2.1 Selection of wavelet function and decomposition level 148
7.2.2 Simulation results for the wavelet transform-based time delay estimator 150
7.3 Data-adaptive time delay estimator 151
7.4 Cepstral time delay estimator 155
7.4.1 Variance of the cepstral time delay estimate 156
7.4.2 Comparison of cepstral and inherent bandpass time delay estimators 157
7.5 Experimental results 158
7.6 Benefits and limitations of the time delay estimators 163
7.7 Summary and conclusion 164
CHAPTER 8 COMBINING TRANSIENT AND STEADY-STATE METHODS FOR ACOUSTIC LEAK DETECTION 165
8.1 Comparison of acoustic leak detection methods 165
8.2 Combined acoustic leak detection approach 169
8.2.1 Selection of leak detection methods and sensors in the combined approach 169

8.2.2 Description of combined leak detection approach 171
8.3 Experimental results 173
8.4 Benefits and limitations of the combined leak detection approach 176
8.5 Summary and conclusion 177
CHAPTER 9 CONCLUSIONS AND RECOMMENDATIONS FOR FUTURE WORK 178
9.1 Conclusions 178
9.2 Recommendations for future work 180
APPENDICES 183
Appendix A. Formulae for time-domain and spectral features 183
Appendix B. Deriving the distribution of the non-stationarity measure 185
Appendix C. Power cepstrum of leak signals 187
Appendix D. Deriving the performance metrics of the autocorrelation and cepstral multipath identification methods 189
Appendix D1. Time delay resolution 189
Appendix D2. Detection signal-to-noise ratio 189
Appendix E. Deriving the spectrally constrained normalised multichannel frequency least-mean squares (NMCFLMS) blind channel identification algorithm 192
Appendix E1. Deriving the blind channel identification update equation 192
Appendix E2. Deriving the update equation for the spectrally constrained NMCFLMS 193
Appendix F. Deriving the expressions for the peak-to-side lobe ratio 196
Appendix G. Deriving the variance of the time delay estimate 197
Appendix G1. Inherent bandpass filtering time delay estimate 197
Appendix G2: Cepstral time delay estimate 200
REFERENCES 202

LIST OF TABLES

Table 1.1. Weighting functions in the GCC methods. 8

Table 2.1: Metrological characteristics of the B200 hydrophone and 352C22 accelerometer. 19

Table 2.2: Young's modulus, loss factor, and ring frequency values corresponding to the circumferential modes of the MDPE pipe in the leakage test rig. 21

Table 3.1: Time- and frequency-domain features for noise-only (before leak simulation) and leak signal (after leak simulation) portions of an acceleration signal measured at X1 31

Table 3.2: Parameters and results of Brown-Forsythe test applied to the steady-state portions—before and after the transients—of the experimental signals with leak and active transients. 52

Table 3.3: Cross-section of experimental results for passive transient leak detection. 53

Table 3.4: Description of datasets of steady-state leak signals acquired on the leakage test rig. 56

Table 3.5: Time and frequency-domain features for noise-only and leak measurements measured at X1 and X3 on the leakage test rig. 57

Table 3.6: LDM values obtained for the noise and leak signals in the datasets in Table 3.4. 58

Table 4.1: Expressions for the performance metrics. 73

Table 4.2: Optimal combination of TDOAs P_{opt} in the simulation example. 80

Table 4.3: Optimal combination of TDOAs P_{opt} for the experimental signal acquired at X3 on the leakage test rig. 88

Table 4.4: Leak location and wave speed estimates obtained for the datasets. 89

Table 5.1: Cross-section of BCI wave speed estimates and BCI and GCC leak location estimates obtained for experimental leak signals in the datasets described in Table 3.4. 114

Table 6.1: Scales for the interpretation of the BF. 126

Table 6.2: TDE quality assessment results for experimental leak signals. 135

Table 6.3: Summary of TDE quality assessment results for experimental leak signals measured on the leakage test rig at X1, X2, and X3. 136

Table 8.1: Summary of steady-state and transient methods. 166

Table 8.2: Leak location estimates using the combined approach. 174

LIST OF FIGURES

Figure 1.1: Schematic of a pipe with a leak bracketed by two sensors. 3

Figure 1.2: Typical leak detection procedure in the water industry. 5

Figure 1.3: Typical CCF of a bandpass signal with centre frequency ω_c and bandwidth $\Delta\omega$. 9

Figure 2.1: Schematic of the leakage test rig. 18

Figure 2.2: Parts of the leakage test rig: (a) Inlet section. (b) Setup for leak simulation. (c) Access points for installation of acoustic/vibration sensors. 18

Figure 2.3: Determining the material properties of the MDPE pipe. (a) Mounting accelerometer on a freely suspended thin ring cut from the MDPE pipe to measure its radial acceleration response to a point excitation. (b) Point accelerance $A_c(f)$ of the ring. 20

Figure 2.4: Estimating the time delay in X1 and X2 accelerometer signals for wave speed calculation. (a) Normalised CPS modulus and MSC. (b) Unwrapped cross-spectral phase and linear fit. 22

Figure 2.5: Background noise and leak accelerometer signals acquired at X3 with the L1 valve open halfway: (a) Time histories. (b) PSDs. 23

Figure 2.6: Spectrum of the input excitation signal measured with an accelerometer on Pipe 1 at a location 1 metre from the elbow. 25

Figure 2.7: Theoretical and experimental FRFs of the MDPE pipe determined from acceleration signals measured on Pipe 1 in the leakage test rig. (a) Magnitude. (b) Unwrapped phase. 26

Figure 3.1: Acceleration leak signal measured at X1 on the leakage test rig with a leak simulated by opening the L1 valve halfway. (a) Time history. (b) Spectrogram in dB. 30

Figure 3.2: Acoustic leak detection algorithm based on transient/signal detection. 32

Figure 3.3: Probability distribution of the NSM output. (a) Theoretical PDF (Equation (3.5)), empirical PDF, and normal fitted PDF obtained for a simulated white Gaussian noise signal. (b) Theoretical SDF (Equation (3.6)) computed for L_g = 11, 101, 1001 and ξ = 0.001. 38

Figure 3.4: Computing the NSM of the generated time series. (a) Signal with leak transient. (b) Signal with active transient. 40

Figure 3.5. Detection rate of NSM and GLD transient detectors vs (a) 'SNR'. (b) AFPR. 41

Figure 3.6: Comparison of transient onset detection accuracy. (a) NSM and the GLD onsets. (b) GLD output. 42

Figure 3.7: Spectrogram of an acceleration signal containing an active transient. Unit is dB. 44

Figure 3.8: Computing the NSM of experimental signals: (i) Time histories of the measured signals. (ii) NSM outputs of whole signals. (iii) NSM outputs of steady-state segments. 51

Figure 3.9: Cases for which the passive transient leak detection method fails. (a) Unsuccessful transient detection. (b) Unsuccessful leak confirmation. (i) Time history. (ii) NSM output. 55

Figure 3.10: Time histories and PSDs in successful and unsuccessful leak detection cases. 59

Figure 3.11: PSD of the signal whose time history is shown in Figure 3.9(b). 60

Figure 4.1: Illustration of the phenomenon of acoustic wave reflection at a discontinuity. 64

Figure 4.2: Schematic of simulated pipe. 77

Figure 4.3: Matching method applied to the simulated leak signals. 78

Figure 4.4: The RMSE of the leak location and wave speed estimates obtained using the matching method for simulated transient signals with 'SNRs' between -6 and 3 dB. 81

Figure 4.5: Correlation functions and power cepstra of simulated steady-state leak signals. 82

Figure 4.6: RMSE of autocorrelation and cepstral leak location and wave speed estimates obtained using the steady-state multipath identification leak localisation method for simulated leak signals. 84

Figure 4.7: Comparison of the ACF and power cepstrum of simulated S1 leak signal with SNR of -6 dB. (a) ACF. (b) Power cepstrum. 84

Figure 4.8: Multipath identification in the simulated S2 leak signal in an MDPE pipe with a loss factor of 0.2. (a) ACF. (b) Power cepstrum. 85

Figure 4.9: RMSE of leak location and wave speed estimates obtained in pipes of different attenuation factors using the cepstral technique. 85

Figure 4.10: Applying the matching method to the experimental signal measured at X3 when a transient is induced via impact at the endcap close to X3. 87

Figure 4.11: Applying the matching method to X1 and X3 signals in Dataset 5. 90

Figure 4.12: Applying the steady-state multipath identification methods to experimental leak signals measured at X1 and X2. 92

Figure 4.13: Summary of results for the experimental steady-state leak signals: (a) leak localisation error. (b) wave speed. 93

Figure 4.14: Power cepstrum of the X1 signal in an unsuccessful leak localisation case. 93

Figure 5.1. Representations of a SITO system with a leading delay. (a) Inherent delay in the transfer functions. (b) Delayed input. 100

Figure 5.2: Determining optimal channel length and common delay in the simulated channels. 109

Figure 5.3: Comparison of the simulated pipe channels and the BCI channel estimates. 110

Figure 5.4: Average wave speed and leak location estimates obtained using the BCI and GCC for simulated leak signals. 111

Figure 5.5: Determining the optimal channel length and common delay in the pipe channels from the X1 and X2 hydrophone leak signals in Dataset 1 in Table 3.4. 112

Figure 5.6: IRFs and FRFs blindly estimated from X1 and X2 hydrophone leak signals in Dataset 1 in Table 3.4. (a) Estimated IRFs of the pipe channels. (b) Magnitude and unwrapped phase of the estimated channel FRFs. 113

Figure 6.1: Leak localisation error due to TDE error for different relative leak locations in a cross-section measurement setup with c = 354 m/s and d = 100 metres 118

Figure 6.2: Comparison of the GEV and normal distributions for describing the PDF of the CCF peak in the case of: (a) uncorrelated noise. (b) correlated signals. 124

Figure 6.3: Comparison of the PSR for uncorrelated noise and correlated leak signals. The PSR is calculated for N_c = 1001, 2001, and 3001. 129

Figure 6.4: Comparison of the ICS and PiCE for uncorrelated noise and leak signals. 132

Figure 6.5: Examples CCFs obtained from accelerometer signals measured on the leakage rig in the presence of a leak at L1. (a) High-quality CCF of the X1 and X2 signals. (b) Low-quality CCF of the X1 and X3 signals. 134

Figure 6.6: Summary of correlation quality assessment metrics for experimental signals acquired on the leakage test rig at X1, X2, and X3. The leak signals are from the datasets described in Table 3.4. 136

Figure 6.7. Schematic of the Ottawa leakage test facility and spectral properties of the experimental hydrophone signals acquired at the facility 138

Figure 6.8: Quality assessment of CCFs of raw and filtered hydrophone leak signals acquired at the Ottawa facility. (a) Raw signals. (b)-(e) Filtered signals. (f) Quality assessment metrics. 139

Figure 6.9: Weighted CCFs of raw hydrophone signals. 140

Figure 7.1: Comparison of the low-SNR and high-SNR approximations of the variance. 146

Figure 7.2: Frequency responses of haar, db4, sym14, fk18 wavelets at different decomposition levels. (a) Level 1. (b) Level 2. (c) Level 3. (d) Level 5. 148

Figure 7.3: Simulation results for the WTCC. (a) Variance of the time delay estimate. (b) RWE and PSR for the db4 wavelet. 150

Figure 7.4: RMSE of the WTCC and GCC time delay estimates for different wavelets: (a) haar. (b) db4. (c) sym14. (d) fk18. 151

Figure 7.5: EMD of simulated leak signals. (a) Auto-power spectra of the IMFs. (b) Binary logarithm of the number of zero crossings. 153

Figure 7.6: Simulation results for the EMD-CC. (a) RMSE of time delay estimate. (b) RIE and PSR. 154

Figure 7.7: RMSE of the CEPS-TDE time delay estimate for simulated leak signals. 158

Figure 7.8: Spectral properties and CCF of the X1 and X2 experimental leak signals. 159

Figure 7.9: Selection of best decomposition levels for X1 and X2 experimental leak signals. (a) RWE and PSR. (b) RIE and PSR. 160

Figure 7.10: Time delay estimates for unfiltered leak signals. (a) WTCC and DD-CC. (b) Residual power cepstrum. 161

Figure 7.11: CCFs obtained from the EMD IMFs for the X1 and X2 signals: (a) IMF 3 only. (b) Sum of IMFs 2 and 3 161

Figure 7.12: Estimating time delay in the Ottawa hydrophone signals. (a) RWE and PSR. (b) RIE and PSR. (c) Residual cepstrum. (d) Time delay estimates for raw and filtered signals. 162

Figure 8.1: Combined acoustic leak detection approach. 172

DECLARATION OF AUTHORSHIP

I, Ndubuisi Uchendu, declare that this thesis titled 'Combining Transient and Steady-state Methods for Acoustic Leak Detection', and the work presented in it are my own and has been generated by me as the result of my own original research.

I confirm that:

1. This work was done wholly or mainly while in candidature for a research degree at this University;
2. Where any part of this thesis has previously been submitted for a degree or any other qualification at this University or any other institution, this has been clearly stated;
3. Where I have consulted the published work of others, this is always clearly attributed;
4. Where I have quoted from the work of others, the source is always given. With the exception of such quotations, this thesis is entirely my own work;
5. I have acknowledged all main sources of help;
6. Where the thesis is based on work done by myself jointly with others, I have made clear exactly what was done by others and what I have contributed myself;
7. Parts of this work have been published as:

   Uchendu, N., Muggleton, J., Rustighi, E., and White, P. (2020). Comparative study of time delay estimators for steady-state and transient acoustic leak signals. *Proceedings of the 29th International Conference on Noise and Vibration Engineering (ISMA2020) and the 8th International Conference on Uncertainty in Structural Dynamics (USD2020)*, 2801-2815. https://past.isma-isaac.be/downloads/isma2020/proceedings/Proceedings_ISMA-USD2020.pdf

Signature:..... Date: 22 January 2024

ACKNOWLEDGEMENTS

I would like to express my deepest appreciation to all the people and organisations that contributed to the success of this PhD research project. I am sincerely grateful to my supervisors Dr Jennifer Muggleton, Prof Paul White, and Dr Emiliano Rustighi for their valuable guidance, support, and patience throughout the duration of the project. Their assistance and encouragement were instrumental to the completion of the project. I would also like to thank Prof David Simpson and Dr Neil Ferguson for their encouragement and suggestions during the two progression reviews.

I acknowledge with great appreciation the financial support provided by the Nigerian Petroleum Development Trust Fund (PTDF), the United Kingdom Water Industry Research (UKWIR), and University of Southampton Centre for Doctoral Training (CDT), without which this PhD programme would not have been possible. In particular, I would like to thank Mr Dennis Dellow, whose feedback during review sessions with UKWIR was very helpful and insightful. I also recognise with gratitude the important roles played by my research colleagues Joshua Hooper and Adila Nalisa Mohd Roslan during the execution of vital experimental work. Also, I express my sincere thanks to Dr Fabricio Almeida from São Paulo State University and Dr Paul Linford from SYRINIX for providing experimental data used in validating the results of this work.

Lastly, I am especially grateful to my family for their love, support, and encouragement throughout the course of this project. I owe the success of my PhD programme to the help and support of the people and organisations mentioned above.

LIST OF ABBREVIATIONS

ACF	Autocorrelation function
AFPR	Allowable false positive rate
AIC	Akaike information criterion
AICc	AIC with a correction for small sample size
BCC	Basic cross-correlation
BCFR	Bandwidth-to-centre-frequency ratio
BCI	Blind channel identification
BF	Bayes factor
BIC	Bayesian information criterion
BSIE	Blind system identification and equalisation
CCF	Cross-correlation function
CDF	Cumulative distribution function
CEPS-TDE	Cepstral time delay estimation method
CPS	Cross-power spectrum
CQI	Cross-correlation function quality index
CR	Cross-relation
CUSUM	Cumulative sum
CWT	Continuous wavelet transform
DAS	Data acquisition system
DD-CC	Data-adaptive decomposition cross-correlation
DFT	Discrete Fourier transform
DWT	Discrete wavelet transform
EMD	Empirical mode decomposition
EWT	Empirical wavelet transform
FFT	Fast Fourier transform
FIR	Finite impulse response
FNR	False negative rate
FPR	False positive rate
FRF	Frequency response function
FSI	Fluid-structure interaction
FT	Fourier transform
GCC	Generalised cross-correlation
GCC-ML	Generalised cross-correlation maximum likelihood
GCC-PHAT	Generalised cross-correlation phase transform

GCC-SCOT	Generalised cross-correlation smoothed coherence transform
GCC-WIEN	Generalised cross-correlation Wiener estimator
GEV	Generalised extreme value
GLD	Gaussian likelihood detector
GPS	Global positioning system
GRLT	Generalised likelihood ratio test
IB-TDE	Inherent bandpass filtering time delay estimation method
ICS	Inconsistency score
IEPE	Integrated electronics piezo-electric
IFT	Inverse Fourier transform
IMF	Intrinsic mode function
IRF	Impulse response function
LDM	Leak detection metric
LMS	Least mean squares
LSSE	Least sum of squared equation error
MCDA	Multi-criteria decision analysis
MDPE	Medium density polyethylene
ME-LMS	Multiple-error least mean squares
MINT	Multichannel input/output theory
MODWT	Maximal overlap discrete wavelet transform
MSC	Magnitude-squared coherence
NMCFLMS	Normalised multichannel frequency least mean squares
NSM	Non-stationarity measure
PDF	Probability distribution function
PG	Processing gain
PiCE	Proportion of inconsistent estimates
PMR	Peak-to-mean ratio
PSD	Power spectral density
PSR	Peak-to-side lobe ratio
PVC	Polyvinyl chloride
RIE	Relative IMF energy
RL	Relative likelihood
RMS	Root-mean square
RMSE	Root-mean square error
ROC	Receiver operating characteristic
RWE	Relative wavelet energy
SDF	Survival distribution function

SDR	Standard dimension ratio
SITO	Single-input two-output
SNR	Signal-to-noise ratio
STFT	Short-time Fourier transform
TDE	Time delay estimation
TDOA	Time difference of arrival
TNR	True negative rate
TPR	True positive rate
VMD	Variational mode decomposition
WT	Wavelet transform
WTCC	Wavelet transform cross-correlation

LIST OF SYMBOLS

$\sim$	Has the probability distribution of
$\rightarrow$	Tends towards
$(\bullet)^*$	Complex conjugate
$(\bullet)^\dagger$	Pseudoinverse
$(\bullet)^H$	Hermitian transpose
$(\bullet)^T$	Transpose
$\lvert\bullet\rvert$	Absolute value
$\lVert\bullet\rVert_2$	ℓ^2 norm
$\lceil\bullet\rceil$	Ceiling function
$\lfloor\bullet\rfloor$	Floor function
$(\hat{\bullet})$	Estimate
$(\underline{\bullet})$	A frequency domain quantity
$\otimes$	Linear convolution
$\odot$	Element-wise multiplication
∇J_{e}, ∇J_{ph}, ∇J_{ls}, ∇J_{rb}	Stacked column vectors of the respective gradients in the two channels
$\nabla J_{\text{e},i}$, $\nabla J_{\text{ls},i}$, $\nabla J_{\text{ph},i}$, $\nabla J_{\text{rb},i}$	Gradient of the original, log-spectrum, phase, ℓ^p norm penalty terms in the spectrally constrained NMCFLMS algorithm
$\mathbf{0}_{K\times P}$	A null matrix of size $K \times P$
$\mathbf{1}_K$	K-column vector of ones
$a(\omega)$, $A(\omega)$	Quantities defined in Equations (4.12) and (7.14)
a_p	Pipe radius
$\arg\{\bullet\}$	Argument of complex number
$A_c(\omega)$	Point accelerance
AIC_M, $\text{AIC}_{\min}$	AIC of model M, minimum AIC value obtained for candidate models
b	Wavelet translation parameter
$B(\omega)$	Quantity defined in Equation (7.14)
$B_{l_1}^2$, $B_{l_2}^2$	Effective bandwidth of $l_1(t)$ and $l_2(t)$
B_0	One-sided bandwidth of the noise signals $n_1(t)$ and $n_2(t)$
B_d	Statistical bandwidth of the direct-path signal
B_f	Fluid bulk modulus of elasticity

BF_{M_1,M_2}	Bayes factor of models M_1 and M_2
BIC_M	BIC of model M
c, $\hat{c}$	Pipe acoustic wave speed, its estimate
c_f	Fluid wave speed
$\hat{c}_1$, $\hat{c}_2$	Wave speed estimate obtained from the first, second signal in the passive steady-state leak localisation method
$c_{\min}$, $c_{\max}$	Minimum, maximum possible value of the wave speed
coif N	Coiflet wavelet with N vanishing moments
$\mathrm{cov}\{\bullet,\bullet\}$	Covariance
$\tilde{c}$, c_{opt}	Wave speed value in the matching method, its optimal value
$C(P_l,\tilde{c})$	Cost function in the matching method
C_s	Inconsistency score
d	Inter-sensor distance
d_{PR}	Distance travelled by the primary reflection
d_{PW}	Distance travelled by the direct-path wave
d_Σ	$d_{PW}+d_{PR}$
d_1, d_2	Distance between the leak and the first, second measurement points
db N	Daubechies wavelet with N vanishing moments
$\mathrm{diag}\{\bullet\}$	A diagonal matrix created with a given vector
D, $D_{\max}$, D_{opt}, $\bar{D}_{opt}$	Leading delay in the first acoustic channel, its maximum possible value, its optimal value, average of its estimates
$\underline{\mathcal{D}}_i(m)$	A diagonal matrix created with the DFT of stacked vectors of the $(m-1)$th and m th time blocks
$D_{\mathrm{KL}}(P\|Q)$	Kullback-Liebler divergence of Q from P
D_p	Pipe diameter
$D_{\mathrm{snr,ACF}}$	Autocorrelation detection signal-to-noise ratio
$D_{\mathrm{snr,CEPS}}$	Cepstral detection signal-to-noise ratio
$\mathbf{e}$	Time-domain cross-relation error
$\underline{\mathbf{e}}$, $\underline{\mathbf{e}}^{01}$	Frequency-domain cross-relation error, its zero-padded version
$\mathrm{env}\{\bullet\}$	Envelope
e_1, e_2	Deconvolution error for the first, second channel estimate
$\mathrm{E}\{\bullet\}$	Mathematical expectation or averaging
E_p	Young's modulus of the pipe material
E_{1,IMF_k}, $E_{2,\mathrm{IMF}_{\tilde{k}}}$	Energy in the selected k th IMFs
$\mathrm{E}_1(\bullet)$	First-order exponential function
$E_{1,k}$, $E_{2,k}$	Energy in the k th decomposition level of the WT
$E_{1,\mathrm{tot}}$, $E_{2,\mathrm{tot}}$	Total energy in the first, second signal

$\mathrm{Ei}(\bullet)$	The exponential integral
$\mathrm{F}\{\bullet\}$	Fourier transform
$\mathrm{F}^{-1}\{\bullet\}$	Inverse Fourier transform
fk N	Fejer-Korovkin wavelet with N vanishing moments
f_n, $f_{n-1/2}$, $f_{n+1/2}$	n th resonance frequency in the accelerance plot, lower and upper half-power frequencies of this peak
f_{ring}	Ring frequency of the pipe
$f_X(\bullet)$,	Probability distribution function of random variable X
$F_{1-\alpha,\,\nu_1,\,\nu_2}$	Upper critical value of the F distribution with ν_1 and ν_2 degrees of freedom at a significance level of α.
$\mathbf{F}_K$	$K \times K$ discrete Fourier transform matrix
$\mathbf{F}_K^{-1}$	$K \times K$ inverse discrete Fourier transform matrix
F_s	Sampling frequency
$F_X(\bullet)$, $F_X^{-1}(\bullet)$	CDF of random variable X, inverse of the CDF
g_{nsm}	NSM observation window
$\hat{g}_1$, $\hat{g}_2$	Multichannel inverse filters of the estimated channels
$g_m(q)$, $g_{1,m}(q)$, $g_{2,m}(q)$, $g_{12,m}$	Quantities defined in Equations (4.12) and (7.14)
$G_d(\omega)$	Spectral density of the direct-path signal
G_m	Shear modulus of medium surrounding the pipe
$G_{x_1x_2}(\omega)$	Cross-power spectrum of signals x_1 and x_2
$G_{xx}(\omega)$	Auto-power spectrum of signal x
$\mathrm{GEV}_1(\mu, s)$	Type I GEV (Gumbel) distribution with location parameter μ and scale parameter s
h_{nsm}	NSM sliding window
$\hat{\underline{\mathbf{h}}}_i$, $\hat{\underline{\mathbf{h}}}_i^{10}$	Frequency spectrum of the i th channel estimate, its zero-padded version
$\hat{\underline{h}}_{i,k}^{10}$	The k th element of $\hat{\underline{\mathbf{h}}}_i^{10}$
h_{dir}	Direct-path IRF
$\hat{\mathbf{h}}$	Stacked vector of the channel estimates $\hat{\underline{\mathbf{h}}}_1$ and $\hat{\underline{\mathbf{h}}}_2$
h_i, $\mathbf{h}_i$, $\hat{\mathbf{h}}_i$, $\hat{\mathbf{h}}_i^{10}$	IRF between signals at the leak position and the i th measurement point, its representation in FIR filter form, its estimate, zero-padded estimate
$h_{k,ref}$	Portion of the IRF that accounts for the k th reflection
h_p	Pipe wall thickness
$H(\omega, u)$	FRF between the signal generated at the leak location and the measurement at distance u from the leak

$H_0(z)$	Common factor shared by the transfer functions $H_1(z)$ and $H_2(z)$
$H_1(z)$, $H_2(z)$	z-transform of the first, second pipe channel IRFs
$H_{d1}(z)$, $H_{d2}(z)$	Distinct factors in the transfer functions $H_1(z)$ and $H_2(z)$
$H_{dir}(\omega, d_{PW})$	FRF between the signal at the leak location and the direct-path wave
$H_{ref}(\omega, d_{PR})$	FRF between the signal at the leak location and the reflected wave
$\hat{H}_1(z,L)$, $\hat{H}_2(z,L)$	z-transforms of channel estimates obtained with an overestimated channel length L
i	Dummy variable
I_i	Interval to search for peaks in the ACF and power cepstrum
$\mathbf{I}_K$	$K \times K$ Identity matrix
$\mathrm{Im}\{\bullet\}$	Imaginary part
IMF_k	k th IMF in data-adaptive decompositions
$\mathrm{IMF}_{k,1}$, $\mathrm{IMF}_{k,2}$	IMFs of signals x_1 and x_2
$\mathrm{IMF}_{\tilde{k},2}$	IMF $\mathrm{IMF}_{k,2}$ whose centre frequency is closest to that of $\mathrm{IMF}_{k,1}$
j	Imaginary unit $\sqrt{-1}$
$\tilde{J}$	Cost function of the spectrally constrained NMCFLMS algorithm
$\mathrm{JD}(P,Q)$	Jeffrey's divergence between probability distributions P and Q
J_{e}	Cost function of the NMCFLMS algorithm
J_{ls}, J_{ph}, J_{rb}; $J_{\mathrm{ls},i}$, $J_{\mathrm{ph},i}$, $J_{\mathrm{rb},i}$	Log-spectrum, phase, ℓ^p-norm penalty terms in the cost function of the spectrally constrained NMCFLMS algorithm; their components for the i th channel
$\mathbf{J}_K$	$K \times K$ Matrix of ones
J_{LSSE}	Least-squares sum error cost function
J_{sp}	Cost function in Spiesberger's algorithm
J_β	Attenuation factor-based cost function
J_ε	Deconvolution error cost function
k	Counter variable. Decomposition level.
k_1	Wavenumber of the s = 1 wave
k_b, k_{co}, k_{ph}, k_{pk}, k_{sh}	Bandwidth index, coherence index, phase index, peak index, and shape index in the CQI
k_B	Number of groups in the Brown-Forsythe test
k_M	Number of parameters estimated by the model M
K, $\bar{K}$	Arbitrary point, stationary point in $\mathbf{R}^{L_g}$
$l(t)$	Signal generated at the leak location
$\hat{l}$	An estimate of the input signal $l(t)$
$l_1(t)$, $l_2(t)$	Noise-free component of leak signals $x_1(t)$ and $x_2(t)$

$\log\{\bullet\}$, $\log_a\{\bullet\}$	Natural logarithm, logarithm in base a
L, $L_{\min}$, $L_{\max}$, L_{opt}	FIR filter length in the BCI algorithm, its minimum and maximum values, its optimal value
L_g, L_h	Lengths of the NSM observation and sliding windows
L_M	Maximised value of the likelihood function of a model (distribution)
LSSE	Least-squares sum error
$\max\{\bullet\}$	Maximum value
$m_r(n)$, $\hat{m}_r(n)$	r th moment, its estimate
M_{12}	Number of peaks in the CCF
$M_k(\omega)$	Quantity defined in Equation (7.14)
$n(t)$	Additive background noise
$n_1(t)$, $n_2(t)$	Additive noise at the first and second measurement points
$\mathcal{N}(\mu,\sigma^2)$	Normal distribution with expected value μ and variance σ^2
N_0	Power spectral densities of the noise signals n_1 and n_2
N_1, N_2	Number of multipaths in x_1 and x_2
N_{B1}, N_{B2}, N_B	Number of samples in the steady-state segments before and after the transient in the Brown-Forsythe test, their sum
N_c	CCF size
N_d	Number of known discontinuities in the matching method
N_{imf}	The number of extracted IMFs
N_{ref}	Number of detectable reflections in the leak signal
N_R	Number of CCF realisations in the information criterion and statistical approaches
N_s	Number of simulation runs
N_{zcross}	Number of zero-crossings in the IMF
p	Order of the ℓ^p-norm or NSM order
p_v	p-value in the Brown-Forsythe test
P_1, P_2	Number of positively lagged peaks in the ACFs
P_D	Transient detection rate
P_{emp}, P_{th}, P_{normal}, P_{GEV_1}	Empirical PDF, theoretical PDF, normal fitted PDF, type I GEV fitted PDF
P_l, P_{opt}	Combinations of the estimated locations of the discontinuities in the matching method, the optimal combination
P_{noise}, P_{signal}	Noise power, signal power
$\Pr\{\bullet\}$	Probability
q	Quefrency of the cepstrum
$Q_k(q)$	Quantity defined in Equation (7.14)

$R(q)$, $R_1(q)$, $R_2(q)$	Quantities defined in Equations (4.12) and (7.14)
$\mathbf{R}^{L_g}$	L_g -dimensional NSM vector space
$R_{\max}$	Maximum value of the CCF
$R_N(\tau)$	Sum of the noise components in the CCF
$R_{xx}(\tau)$	Autocorrelation function of signal x
$R_{x_1x_2}(\tau)$	CCF of signals x_1 and x_2
$R_{x_1x_2}\left(\tau\vert_{\text{second peak}}\right)$	Second highest peak in the CCF
$R'_{x_1x_2}(\tau)$, $R''_{x_1x_2}(\tau)$	First, second partial derivative of $R_{x_1x_2}(\tau)$ with respect to τ
$R^{DD}_{x_1x_2}(\tau,k)$	CCF of the k th IMFs of data-adaptive decomposition 'DD'
$\mathrm{Re}\{\bullet\}$	Real part of a complex number
RIE_k	Relative energy of the selected k th IMFs
RL_M	Relative likelihood of model M
$\mathrm{RMSE}(\theta)$	RMSE of the estimates of a quantity θ
RWE_k	Relative wavelet energy for decomposition level k
$R^{\psi}_{x_1x_2}(\tau,k)$	CCF of the k th decomposition level MODWTs of x_1 and x_2 with respect to wavelet ψ
s	Wavelet scale parameter
$s_{\Upsilon}(N)$	Scale parameter of the type I GEV (Gumbel) distribution describing the maximum value of N independent and identically distributed normal variables with CDF Υ
S_0	Power spectral density of the signal generated at the leak location
SNR_1, SNR_2	Signal to noise ratio of signals x_1 and x_2
SNR_{in}, SNR_{out}	SNR of the input, output of a signal processor
$\mathrm{sym}\,N$	Symlet wavelet with N vanishing moments
t_1, t_2	Propagation time of the leak noise from the leak location to the first and second measurement points
T	Signal duration in seconds
$T_i[m]$	Time of arrival of the m th wave arriving at the i th sensor
T_{onset}	Transient onset
T_{peak}	Time delay between the signals in samples
u	Dummy variable
$\mathrm{unwrap}\{\bullet\}$	Phase unwrapping operation
U_1, U_2	Possible selections of the TDOAs in each signal in Spiesberger's algorithm
$v_1(t)$	$n_1(t)+n_2(t)$
$v_2(t)$	$n_1(t)-n_2(t)$

$\mathrm{var}\{\bullet\}$	Variance
$w(t)$	Function constructed from an appropriate transform in the IB-TDE method
$w_1,\ w_2,\ w_3,\ w_4$	Weights assigned to the spectral descriptors in the LDM
W_B	Brown-Forsythe test statistic
$W_g,\ W_h$	Positive integers (half lengths of NSM windows)
$W(\omega)$	Weighting function in the IB-TDE method
$W_\psi x$	Wavelet transform of signal x with respect to wavelet function ψ
$x(n)$	Discrete or sampled signal
$\breve{x}(q)$	Power cepstrum of signal x
$x_1(t),\ x_2(t)$	Leak signals acquired at the first and second measurement points
$\mathbf{x}_i(m)$	m th time blocks of L samples of signal x_i
$\tilde{x}_1(t),\ \tilde{x}_2(t)$	Transformed signals
$\hat{y}(k)$	Non-stationarity measure output for the signal segment centred at time point k
$\hat{y}_r$	Second-order non-stationarity measure output for the r th moment
Y_r	Quadratic form of a multivariate normal variable for computing the PDF of the NSM output
$\tilde{Y}_{i\cdot}$	Measure of spread in the Brown-Forsythe test
$z(q)$	Residual cepstrum ($\breve{z}_1(q)-\breve{z}_2(q)$)
$z_1(t)$	$x_1(t)+x_2(t)$
$z_2(t)$	$x_1(t)-x_2(t)$
$\mathrm{Z}\{\bullet\}$	Z-transform
$\mathbb{Z}$	Set of integers
α	Significance level in Brown-Forsythe test
β	Pipe attenuation factor
$\hat{\beta}_1,\ \hat{\beta}_2$	Estimates of the attenuation factor obtained from the magnitude of the first, second estimated channel frfs
Γ	Reflection coefficient
γ	Euler-Mascheroni constant
$\gamma^2_{x_1x_2}(\omega)$	Magnitude-squared coherence between signals x_1 and x_2
$\delta(\bullet)$	Dirac delta function
δ_{bci}	Regularisation parameter
Δc	Error in wave speed value ($\hat{c}-c$)
Δd	d_2-d_1 or $d_{\mathrm{PR}}-d_{\mathrm{PW}}$
$\Delta d_1,\ \Delta d_2$	Error in the estimated distance between the leak and the sensors
$\Delta l_{\mathrm{in},1},\ \Delta l_{\mathrm{in},2}$	Distance between an in-bracket discontinuity and the first, second measurement points

Δl_k , $\Delta \hat{l}_k$	Known distance between the k th discontinuity and the measurement location in the matching method, its estimated value
$\Delta l_{\text{out},1}$, $\Delta l_{\text{out},2}$	Distance between the out-of-bracket discontinuity and the first, second measurement points
$\Delta_p\left(K, \bar{K}\right)$	P-norm distance between points K and $\bar{K}$ in $\mathbf{R}^{L_g}$
$\Delta_{\text{ph}}\left(\omega\right)$	Ratio of the experimental unwrapped cross-spectral phase to its least squares fit
ΔT_{onset}	Difference between transient onsets
$\Delta \tau_{\text{peak}}$	Error in the time delay estimate ($\hat{\tau}_{\text{peak}} - \tau_{\text{peak}}$)
$\Delta \omega$	Leak signal bandwidth ($\omega_2 - \omega_1$)
$\varepsilon\left(\omega\right)$	Random fluctuations in the auto-power spectral estimate
$\varepsilon_i\left(\omega\right)$	Random fluctuations in the auto-power spectral estimates of $z_i\left(t\right)$
ζ_1 , ζ_2	Ratio of the ACFs of the first, second noise-free signals and the background noise
$\zeta_d\left(\omega\right)$	Ratio of the spectral densities of the direct-path signal and background noise
η_{ls} , η_{ph} , η_{rb}	Step sizes for log-spectrum, phase, and p-norm constraints in the spectrally constrained NMCFLMS algorithm
η_p	Loss factor of the pipe material
ϑ	Ratio of the heights of the adjacent and main peaks in the CCF envelope
θ	Statistical parameter
$\boldsymbol{\theta}$, θ_k	Vector of values of θ , its k th element
$\hat{\theta}_i$	Estimate from the *i*th simulation run
$\bar{\theta}$	Coordinates of the stationary point $\bar{K}$ in $\mathbf{R}^{L_g}$
$\kappa\left(\tau\right)$	CCF normalised by the mean of its absolute values
λ_{GLD}	GLD transient detection threshold
λ_{ICS}	ICS threshold
λ_{NSM}	NSM transient detection threshold
λ_{PMR}	PMR threshold
λ_{PSR}	PSR threshold
Λ_{norm}	LDM normalisation factor
μ_{bci}	Step-size parameter for the NMCFLMS algorithm
$\mu_{R_{\max}}$	Mean of $R_{\max}$
$\mu_{\Upsilon}\left(N\right)$	Location parameter of the type I GEV (Gumbel) distribution describing the maximum value of N independent and identically distributed normal variables with CDF Υ
$\nu_1\left(\omega\right)$, $\nu_2\left(\omega\right)$	Quantities defined in Equation (7.14)
ξ	AFPR

ϖ_{flat}, ϖ_{flux}, ϖ_{kurt}, ϖ_{skew}	Spectral flatness, spectral flux, spectral kurtosis, spectral skewness
ρ_p	Pipe material density
$\rho_{x_1x_2}(\tau)$	Normalised CCF
$\sigma_{l_1}^2$, $\sigma_{l_2}^2$	Variace of noise-free components of the first, second leak signals
σ_u^2	Variance of u
$\sigma_{\hat{\tau}_{\text{peak,CEPS}}}^2$, $\sigma_{\hat{\tau}_{\text{peak,CEPS}}}^2\Big\vert_{\text{high}}$, $\sigma_{\hat{\tau}_{\text{peak,CEPS}}}^2\Big\vert_{\text{low}}$	Variance of the time delay estimate in the CEPS-TDE method, its high-SNR and low-SNR approximations
$\sigma_{\hat{\tau}_{\text{peak}},\text{IB}}^2$, $\sigma_{\hat{\tau}_{\text{peak}},\text{IB}}^2\Big\vert_{\text{high}}$, $\sigma_{\hat{\tau}_{\text{peak}},\text{IB}}^2\Big\vert_{\text{low}}$	Variance of the time delay estimate in the IB-TDE method, its high-SNR and low-SNR approximations
τ	Time lag
τ_{far}	Set of time lags *far* from the CCF peak
$\tau_{ik}[m,n]$	Difference between the travel times of the m th wave arriving at the i th sensor and the n th wave arriving at the k th sensor
τ_k	TDOA of k th reflected wave relative to the direct-path wave in the matching method
τ_{peak}, $\hat{\tau}_{\text{peak}}$	Time delay between leak signals in seconds, its estimate
$\tilde{\tau}_{\text{peak}}$, $\hat{\tau}_{\text{peak},i}$	Assumed true delay (statistical mode of time delay estimates), time delay estimate from the i th CCF realisation in the statistical approach
τ_{PR}	TDOA of the primary reflection relative to the direct-path wave
$\tau_{\text{res,ACF}}$	Autocorrelation time delay resolution
$\tau_{\text{res,CEPS}}$	Cepstral time delay resolution
$\Phi(\bullet)$, $\Phi^{-1}(\bullet)$	CDF of the standard normal distribution, its inverse
$\chi(\omega)$	Quantity defined in Equations (4.12) and (7.14)
ψ	Wavelet function
$\underline{\psi}(\omega)$	FT of $\psi(t)$
$\underline{\psi}_k(\omega)$	Squared magnitude of the FT of wavelet ψ at k th decomposition level
$\psi_{s,b}(t)$	Wavelet function $\psi(t)$ scaled by s and translated by b in time
$\boldsymbol{\Psi}_i$, $\Psi_{i,k}$	Log-spectrum vector of the i th channel estimates, its k th element
ω	Radial frequency
ω_1, ω_2	Lower and upper cut-off frequencies
ω_c	Centre frequency
$\boldsymbol{\Omega}_i$, $\Omega_{i,k}$	Unwrapped phase vector of the FRF of the i th channel estimate, its k th element

CHAPTER 1
INTRODUCTION

Water distribution networks are essential infrastructure used to transport water, a vital resource, to consumers. Due to ageing and other factors, they are susceptible to leakages, which represent a substantial portion of non-revenue water lost by water companies. By definition, any water that escapes from a water distribution network by means other than a controlled action is considered leakages (Ofwat, 2023). This includes losses from pipe damage and faulty joints. Currently, about 22% of the water produced in the UK is lost through leakages, with daily losses in England and Wales estimated to be about 2.9 billion litres of water (Ofwat, 2022).

Water leakages have serious social, economic, and ecological consequences (Cramer et al., 2015). Flooding from burst pipes can damage infrastructure such as roads, airports, farmlands, and buildings, thereby adversely impacting people's lives. Lost revenue from leakages and cost of repair works place increased financial burden on water companies and may result in higher prices for the consumers. Water leakages also constitute a serious sustainability issue, especially considering the dwindling freshwater supply and the rising water demand driven by increasing world population (Rogers, 2014). The global urban population facing water scarcity is projected to increase from 930 million in 2016 to 1.7–2.4 billion people in 2050 (UNESCO, 2023). The treatment and pumping of water for urban and industrial purposes accounts for about 4% of global energy consumption (IEA, 2017). With approximately 30-50% of water lost globally due to water leakages (Liemberger and Wyatt, 2018), the wasted energy consumption accounts for about 1-2% of the global carbon footprint.

Due to these possibly disastrous consequences of water leakages, their timely detection and repair are of primal importance. To achieve this, different methods have been proposed for use in the water industry. The methods are briefly outlined in the next section with particular emphasis on acoustic and transient methods, two methods which are of interest in this thesis.

1.1 Overview of water leak detection methods

The main methods commonly used for leak detection in the water industry are the acoustic methods and fluid transient methods. In acoustic leak detection methods, acoustic/vibration sensors, typically hydrophones and accelerometers, installed in the fluid or on the pipe measure acoustic waves generated by a leak in the pipe. The measured signals are analysed to detect and locate the leak. The simplest acoustic leak detection technique is the use of listening devices or ground microphones to 'listen' for sounds produced by leaks on hydrants, valves, and other conveniently located fittings, or above the ground along the pipeline. Traditionally, a listening device consists of a metal rod with a wooden block at the end for mechanically amplifying the leak sound heard by the operator, but some

modern listening devices are electroacoustic with a digital amplifier instead of a wooden block (Hamilton and Charalambous, 2020). The sound produced by a leak is generally louder at points close to the leak, so points of high sound intensity can be used to detect and possibly locate leaks. This acoustic method is mostly used during routine survey and for confirming the location of leaks before excavating the soil for pipe repair. Its effectiveness depends on the experience and skill of the operator. Other commonly used acoustic leak detection techniques are acoustic noise logging and cross-correlation (Brennan et al., 2017).

In acoustic noise logging, leak noise loggers that consist of integrated acoustic/vibration sensing and data logging units are used to measure signals on the pipe or fluid at pre-programmed periods, usually during the night (El-Zahab and Zayed, 2019). The presence of a leak in the water distribution network is inferred when the recorded signal is consistently higher than the 'normal' or baseline level over several nights, allowing further investigation to be carried out to determine the leak location. Leak noise loggers may be permanently installed, or operated on a temporary basis using a 'lift and shift' scheme (Bykerk and Valls Miro, 2022). In the 'lift and shift' scheme, the devices are placed in a different location of the network each night or two, where they record signals at the pre-programmed times. Acoustic noise logging allows a large area of the pipe network to be surveyed automatically. It is generally a suitable option for detecting leaks in noisy and busy areas where manual surveys using listening devices might be difficult to carry out (Hunaidi, 2012).

The cross-correlation technique is the most commonly used leak localisation method in water distribution networks. In this method, the leak is located by analysing acoustic/vibration signals measured on either side of the suspected leak (Brennan et al., 2017). Figure 1.1 shows the practical setup for the cross-correlation method. The measurement points are usually hydrants, valves, and other pipe fixtures on which acoustic/vibration sensors can be attached. The measured signals $x_1(t)$ and $x_2(t)$ are transmitted to a leak noise correlator, a device that estimates leak location from the algebraic formula

$$d_1 = \frac{d - c \cdot \tau_{\text{peak}}}{2} \tag{1.1}$$

where d_1 is the distance between the leak and the first measurement point, c is the speed of propagation of acoustic waves in the pipe, d is the total distance between the sensors, and τ_{peak} is the time delay between $x_1(t)$ and $x_2(t)$. The effectiveness of leak localisation using this technique depends on the accuracies of the wave speed value and time delay estimate. The roles, advantages, and limitations of acoustic methods will be discussed further in the next section.

Hydraulic or fluid transient methods include all methods that detect and locate leaks by analysing rapid unsteady variations in the pressure or flow rate in the pipe system, caused by pipe

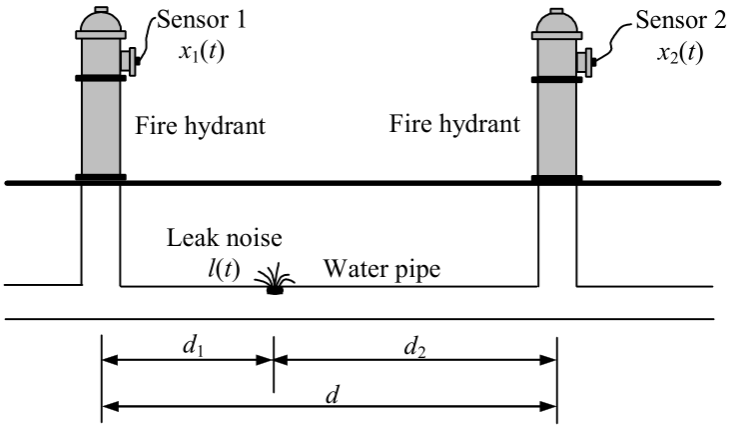

Figure 1.1: Schematic of a pipe with a leak bracketed by two sensors.

burst, start-up and shutdown of pumps, and fast manoeuvre of valves, or any other event that abruptly changes the transmission conditions in the pipe system. Such rapid variations are known as fluid (hydraulic) transients or more commonly as *water hammer* (Rathnayaka et al., 2015). Fluid transient methods can be model-based or data-driven. In model-based methods, the values of hydraulic quantities (pressure, flow rate) measured in the pipe system are compared with those predicted by a mathematical model that represents the state of the pipe based on physical principles, viz., conservation of mass, conservation of momentum, and equations of state (Turkowski et al., 2007). A large discrepancy between the predicted and measured values is considered indicative of the presence of a leak. Examples of model-based fluid transient methods are inverse transient analysis (Liggett and Chen, 1994), transient damping (Wang et al., 2002), frequency response (Mpesha et al., 2002), and impulse response analysis methods (Lee, 2005). Inverse transient analysis method solves the least-squares minimisation inverse problem of determining unknown parameters, such as leak location, leak size, and pipe roughness, from pressure and/or flow rate measured at strategic locations in the pipe system. In the frequency response and impulse response analysis methods, the presence and location of a leak are inferred from the frequency response function (FRF) or impulse response function (IRF) of the pipe extracted from a measured transient pressure trace. A deviation of the extracted FRF or IRF from that of an intact pipe may be indicative of a leak. Transient damping method detects and locates a leak by comparing the damping rate caused by the pipe-wall friction and other loss elements in the pipe system obtained with and without leaks. An important advantage of model-based fluid transient methods is the ability to estimate leak size (Geiger, 2008). However, their application in real systems is limited by uncertainties in the hydraulic model, high computational complexity, and high cost of implementation (Puust et al., 2010).

Data-driven fluid transient methods are based on statistical analysis of pressure and/or flow data. Examples of such methods are leak reflectometry (Brunone and Ferrante, 2001; Ghazali et al., 2012), pressure-based (Lin and Zhang, 2006), cumulative sum (CUSUM) (Misiunas et al., 2005), and prediction-classification methods (Romano et al., 2014). Leak reflectometry methods detect and locate leaks by identifying the waves that are reflected when a hydraulic transient encounters a leak in the

pipe. The CUSUM method is used to detect a pipe burst by observing changes induced in a measured signal by hydraulic transients accompanying the burst event. Pressure-based methods such as the pressure point analysis (bin Md Akib et al., 2011), negative pressure (Delgado and Begovich Mendoza, 2017), and gradient methods (Geiger et al., 2003) detect leak by observing a change in the time-history of a pressure signal measured at a single point on the pipeline or its deviation from a statistical trend. Prediction-classification methods use machine learning methods and statistical chart tools to detect the presence of anomalies, such as leaks, in the long-term measurements of fluid transients. Since data-driven methods do not require a mathematical model of the pipe system, they are computationally less expensive and less sensitive to structural and operational complexities of the network than model-based methods (Wu and Liu, 2017). This makes them suitable for different pipeline configurations. Other advantages of these methods include reduced leak detection time and cost effectiveness (some data-driven methods require measurement from just one or several positions to detect and locate the leak). Their main disadvantages are susceptibility to measurement noise and need for extensive tuning of the pipe system under different operating conditions in the absence of a leak (Zhang and Di Mauro, 1998).

Apart from acoustic and fluid transient methods, other methods used for detecting leaks in water distribution networks include use of ground-penetrating radar, thermography, tracer gas method, and fibre optic methods. Thermography and use of ground-penetrating radar rely on detecting changes in the properties of the soil in the vicinity of a leak, for example, reduction in the soil temperature and radar propagation velocity (Demirci et al., 2012). These techniques are generally not effective for finding leaks in pipes buried in a depth greater than 3 metres (Bimpas et al., 2010). Furthermore, leak localisation accuracy of these techniques may not be high since the leaking water can move far from the actual leak location. In the tracer gas method, a non-toxic, volatile, and non-combustible gas, typically a mixture of hydrogen and nitrogen, is introduced into the pipe section with the suspected leak (Hunaidi et al., 2000). As the gas diffuses to the surface via the leak, it can be detected with a highly sensitive gas leak detector. This method is labour-intensive and causes service interruption, as the pipes to be inspected have to be taken out of service and drained first. Moreover, leaks at the bottom of the pipe cannot be detected using this method. Fibre optic method detects leaks by monitoring the variation of the physical and chemical properties of fibre optic cables installed along the exterior of the pipeline (Mishra et al., 2017). This method is suitable for continuous pipeline monitoring, accurate leak localisation, and detecting small leaks. However, its serious shortcomings include high cost, difficulty of retrofitting fibre cables to existing pipelines, and short lifespan due to instability of the fibre chemical coating over time (Murvay and Silea, 2012). Adegboye et al. (2019) has carried out a comprehensive review of these and other leak detection methods, including their main advantages, disadvantages, and applications.

1.2 Roles and limitations of acoustic methods in water leak detection

The important roles played by acoustic methods can be highlighted by considering the typical leak detection process in the water industry depicted in Figure 1.2. The presence of leaks within a water distribution network is usually inferred via minimum night flow analysis (Fantozzi and Lambert, 2012), pressure monitoring (Rathnayaka et al., 2015), or acoustic noise logging. Leaks can also be discovered through routine manual surveys or when consumers report a visible water leak. When the presence of a leak is discovered, information from leak noise loggers or transient pressure loggers installed in the network is analysed further to identify the network section where the leak is located. Then, leak noise correlators are deployed to localise the leak. Following a successful cross-correlation, the exact location of the leak is pinpointed using a listening device or ground microphone which is moved along the ground directly over the pipe at the correlated position. After pinpointing the leak, the ground is excavated, and the pipe damage is repaired. Based on these typical leak detection procedures, it can be observed that acoustic methods are currently the primary means of detecting and locating water leakages. They are employed for major leak detection tasks, including *leak awareness* (acoustic noise logging), leak localisation (cross-correlation), and leak pinpointing (use of listening devices and ground microphones). The term 'leak awareness' or 'leak identification' is used in this work to denote the discovery of a leak within the pipe system. Widespread use of acoustic methods can be attributed to their ease of deployment and relatively low cost (Liu et al., 2012). Moreover, they are non-intrusive, and hence, do not disrupt the operations of the water distribution network during leak detection. Also, safety concerns associated with the deliberate introduction of external transients (as in fluid transient methods) or substances (as in tracer gas method) are avoided.

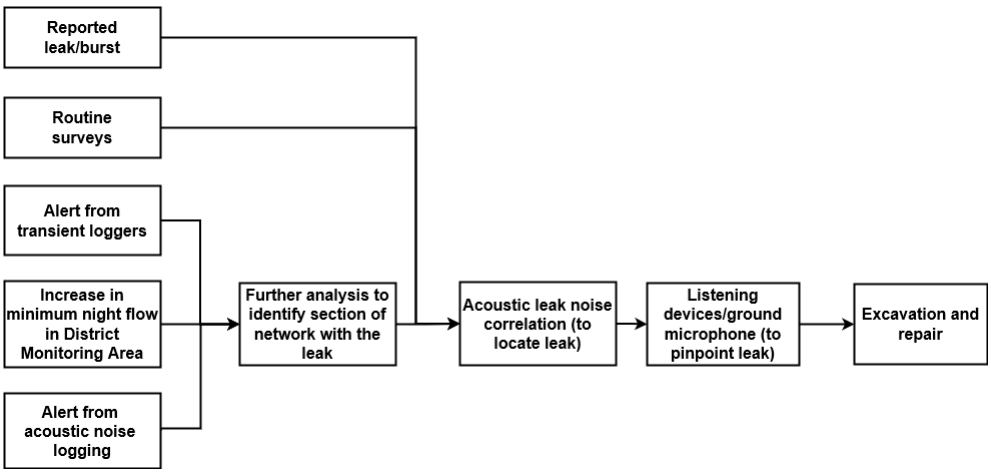

Figure 1.2: Typical leak detection procedure in the water industry.

While acoustic methods are the methods of choice for various leak detection tasks in the water industry, there are certain factors that limit their effectiveness, including acoustic wave attenuation, uncertainties in wave speed values, issues with time delay estimation (TDE), relatively long leak identification time, and unsuitability for leak size estimation. These issues are highlighted in this section.

1.2.1 Acoustic wave attenuation

Acoustic wave propagation in a fluid-filled pipe is complex. The vibro-acoustic behaviour of the pipe is related to two-dimensional patterns, which are composed of circumferential modes (denoted as n) and associated waves (denoted as s) related to each mode (Muggleton et al., 2004). Each circumferential mode has a characteristic shape and frequency content and can only propagate above a certain frequency known as its cut-off frequency. There are theoretically infinite number of waves s related to each circumferential mode n. However, at frequencies well below the so-called ring frequency of the pipe (see Equation (2.3) in Chapter 2), two non-dispersive plane waves are responsible for most of the acoustic energy transfer in a pipe: the predominantly fluid-borne wave (termed $s = 1$) and the predominantly pipe-borne wave (termed $s = 2$) (Fuller and Fahy, 1982; Pinnington and Briscoe, 1994). Both waves correspond to the axisymmetric fundamental mode $n = 0$. Experimental results indicate that the $s = 1$ wave is the predominant wave responsible for transmitting leak noise energy in plastic pipes (Muggleton et al., 2002; Gao and Liu, 2017). As acoustic waves propagate in the pipe, they lose part of their energy to the pipe wall. A measure of the loss within the pipe wall is the attenuation factor β, which at low frequencies below the ring frequency can be calculated as (Muggleton et al., 2002)

$$\beta = -\frac{\mathrm{Im}\{k\}}{\omega} = \frac{1}{c_f}\frac{\eta_p B_f D_p}{2E_p h_p}\left(1+\frac{B_f D_p}{E_p h_p}\right)^{-1/2} \tag{1.2}$$

where $\mathrm{Im}\{k_1\}$ denotes the imaginary part of the complex wavenumber k_1 of the $s = 1$ wave; D_p, h_p are the pipe diameter and pipe-wall thickness, respectively; E_p is the Young's modulus of the pipe material; B_f is the fluid bulk modulus of elasticity; η_p is the loss factor of the pipe material; c_f is the fluid wave speed; and ω is the radial frequency. Other factors that contribute to acoustic wave attenuation include radiation into the surrounding soil and losses at discontinuities (Muggleton and Yan, 2013). Since acoustic methods depend on the ability to detect the leak noise, they are prone to failure when the acoustic waves are severely attenuated, for example, when the measurement points are far from the leak. This is particularly a problem in plastic pipes, which generally have higher attenuation than metallic pipes of a similar size (Muggleton et al., 2002). As a result, acoustic waves do not propagate as far in plastic pipes as they do in metallic pipes. Since recent research has shown that many new polyethylene pipe networks are responsible for a significant proportion of water leakages (Farrow et al., 2017), this issue represents a serious practical concern.

1.2.2 Wave speed estimation/measurement

A prerequisite in the cross-correlation technique is a priori knowledge of the wave speed. In most leak noise correlators, the wave speed is either obtained from tabulated values or calculated using a

formula. If fluid inertial effects are neglected, the acoustic wave speed c can be calculated from the real part of the complex wavenumber of the fluid-borne $s = 1$ wave as (Muggleton and Yan, 2013)

$$c = c_f \left(1 + \frac{2B_f}{E_p h_p / a_p - \omega^2 \rho_p a_p h_p + 2G_m} \right)^{-1/2} \tag{1.3}$$

where ρ_p is the density of the pipe material, $a_p = D_p/2$ is the pipe radius, and G_m is the shear modulus of the surrounding medium. At low frequencies below the ring frequency of the pipe (see Equation (2.3) in Chapter 2), the ω^2 term can be neglected. Using this wave speed formula is problematic for two main reasons. Firstly, the properties of the pipe may differ drastically from their original or typical values due to ageing and deterioration. Also, the properties of the surrounding soil may not be known, and the values of G_m can vary in a large range even for soils of the same type (Kavazanjian et al., 1997; Seed et al., 1986). This is not taken into consideration in most leak noise correlators, and G_m is usually set to zero when calculating the wave speed (Becker, 2015). However, this may lead to inaccurate leak localisation results, since the type of surrounding medium can have substantial effects on the wave speed in the pipe, as can be observed in the results reported by Scussel et al. (2018) for pipes in the United Kingdom (sandy soil) and Brazil (clay soil). Secondly, the experimental results from a number of studies suggest that the wave speed is affected by seasonal variations and temperature, which are not accounted for in the formula. For instance, the wave speed in a buried polyvinyl chloride (PVC) pipe has been observed to vary from 484 m/s in the summer to 515 m/s in the winter (Hunaidi and Chu, 1999). In a series of experiments conducted by Almeida (2013) on a bespoke test rig, the wave speed in a buried medium density polyethylene (MDPE) pipe ranged from 350 m/s to 420 m/s over a couple of months. It was also observed that measured wave speeds differed significantly (about 25%) between pipe sections in the test rig. Several in-situ methods have been proposed for measuring the wave speed on-site at the same time when the leak signals are acquired, but the application of these methods is not always feasible due to certain practical constraints. For example, the correlation envelope method (Almeida et al., 2015), in which the wave speed is calculated from the responses of the pipe to white noise excitation at the measurement positions, requires a shaker to be attached to the measurement points. This makes the method cumbersome to apply in practice. Also, the accuracy of the wave speed estimate is strongly affected by the properties of the excitation signals employed in this method. In the hydrant simulation method (Hunaidi et al., 2000), the wave speed is estimated from signals measured at known locations on the pipe when water is deliberately released from a hydrant. This method introduces safety issues due to the possibly damaging effects of the resulting transients on pipe components. Also, unavailability of conveniently located access points can limit its applicability. It can be concluded that even with availability of in-situ methods, uncertainties in the wave speed remain a challenge in current acoustic leak detection practice.

1.2.3 Time delay estimation

Locating the leak using acoustic cross-correlation involves the estimation of the time delay between the measured leak signals $x_1(t)$ and $x_2(t)$. The most commonly used method for estimating time delays between stationary signals is the generalised cross-correlation (GCC) method, in which the time delay is given by the time lag that maximises the cross-correlation function (CCF) $R_{x_1x_2}(\tau)$ of $x_1(t)$ and $x_2(t)$ (Gao et al., 2006). The CCF is computed as the inverse Fourier Transform (IFT) of suitably weighted cross-power spectrum (CPS) $G_{x_1x_2}(\omega)$ of the signals (Knapp and Carter, 1976). Table 1.1 outlines the weighting functions in some existing GCC methods, including the basic cross-correlation (BCC), phase transform (GCC-PHAT), smoothed coherence transform (GCC-SCOT), maximum likelihood (GCC-ML), and Wiener estimator (GCC-WIEN). The symbol $\gamma^2_{x_1x_2}(\omega)$ denotes the magnitude-squared coherence (MSC) of the signals.

Table 1.1. Weighting functions in the GCC methods.

GCC Method	BCC	GCC-PHAT	GCC-SCOT	GCC-ML	GCC-WIEN
Weighting function	1	$\frac{1}{\lvert G_{x_1x_2}(\omega)\rvert}$	$\frac{1}{\sqrt{G_{x_1x_1}(\omega)\cdot G_{x_2x_2}(\omega)}}$	$\frac{1}{\lvert G_{x_1x_2}(\omega)\rvert}\cdot\frac{\lvert\gamma_{x_1x_2}(\omega)\rvert^2}{1-\lvert\gamma_{x_1x_2}(\omega)\rvert^2}$	$\gamma^2_{x_1x_2}(\omega)$

The GCC-PHAT is known to perform well in the presence of reverberation and low noise in signals (Gao et al., 2009) but poorly in the presence of tonal components and resonances (Almeida, 2013). Such tonal components are suppressed by the GCC-SCOT (Carter et al., 1973). By weighting the CPS according to the coherence, both the GCC-ML and GCC-WIEN attenuate the signals in frequency bands with low signal to noise ratio (SNR) while emphasising spectral regions with high coherence. The GCC-ML is asymptotically efficient for uncorrelated Gaussian signals and long observation intervals (Hannan and Thomson, 1973) but has the effect of overemphasising and underemphasising the signals at certain frequencies compared to the GCC-WIEN (Hero and Schwartz, 1985). As can be inferred from this discussion, each weighting function can only perform well under certain conditions. Since the conditions of the signals and measurement environment cannot always be determined a priori, the selection of appropriate GCC method may prove difficult in practice. While results of multiple studies have shown that the other GCC methods generally outperform the BCC (Gao et al., 2006; Uchendu et al., 2020; Almeida, 2013), their practical application in current acoustic leak detection practice is still very limited. Most leak noise correlators calculate the time delay using the BCC (Dray et al., 2012). This is mostly because there is currently no straightforward or simple way to select the best GCC method suitable for given leak signals.

As stated above, acoustic wave propagation is modal in nature, and the pipe effectively acts as a lowpass filter due to the damping in the pipe wall as shown by Equation (1.2). As a result, acoustic

leak detection in most plastic pipes is only successful with low-frequency leak signals resulting from a non-dispersive propagating wave. Hence, in practice, prior to cross-correlating the measured leak signals, they are passed through a bandpass filter in order to attenuate the signals outside the frequency range where the leak noise propagates. These include the low-frequency region dominated by background noise and the high-frequency region where the leak noise is severely attenuated by the pipe (Gao et al., 2006). As shown by Gao et al. (2005), the cut-off frequencies of the applied filter have substantial effects on the accuracy of the time delay estimate. Bandpass filtering operation modulates the shape of the CCF, resulting in oscillatory behaviour of the CCF. This is illustrated in Figure 1.3, where the typical CCF response for a bandpass signal with centre frequency ω_c and bandwidth $\Delta\omega$ is shown. The CCF oscillates at the centre frequency ω_c with modulation controlled by the bandwidth $\Delta\omega$. If the centre frequency is large, adjacent peaks spaced at $1/\omega_c$ intervals in the CCF will have very nearly equal height, and thus difficulty may arise in unambiguously identifying the correct time delay. Also, a small signal bandwidth leads to a large width of the main CCF peak, resulting in poor resolution of the time delay estimate. The peaks in the nearby of the main peak associated with the effects of the bandwidth and centre frequency are suppressed in the CCF envelope, i.e., the magnitude of its analytic representation defined using the Hilbert transform (Oppenheim and Schafer, 2010; Marple, 1999).

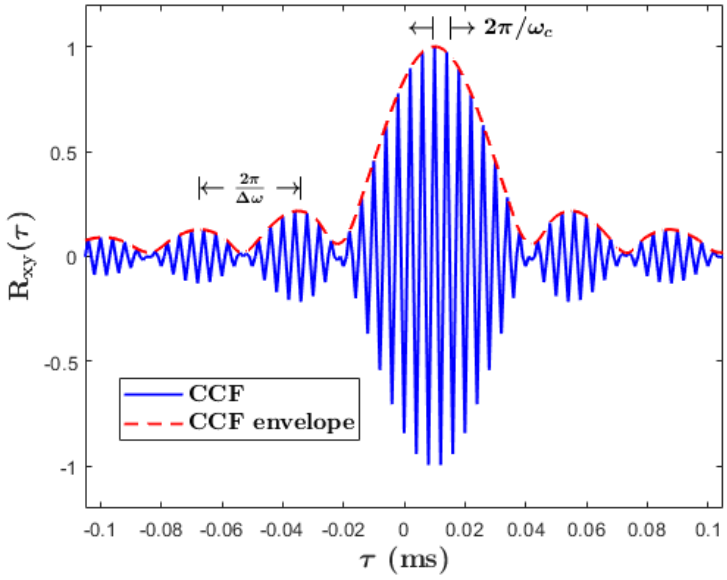

Figure 1.3: Typical CCF of a bandpass signal with centre frequency ω_c and bandwidth $\Delta\omega$. (Reproduced from Weinstein and Weiss (1984)).

The right selection of the cut-off frequencies of the filter is therefore important for accurate TDE in leak signals. Arbitrary selection of these frequencies without considering the properties of the pipe and leak signals can lead to inaccurate time delay estimates, as has been observed in a survey of commercial leak noise correlators (Dray et al., 2012). Several criteria have been proposed for use in selecting the cut-off frequencies of the filter, including one based on the coherence of the signals

(Muggleton et al., 2011) and another based on the CPS magnitude (Almeida, 2013). However, the former has been found to provide incorrect estimates in some commonly encountered situations, for example, when resonances are present in the signals (Almeida et al., 2015), while the latter fails in cases where the maximum of the CPS modulus occurs at the resonant frequencies. Hence, in practice, selection of suitable filters can be challenging and adds an extra layer of complexity to the acoustic leak localisation process.

1.2.4 Long leak identification time and unsuitability for leak size estimation

Since leak noise loggers usually operate intermittently at pre-programmed times, acoustic noise logging may take several days to confirm the presence of a leak in the network, and even longer to locate the section of the network with the leak. Hence, it is not suitable for real-time leak awareness, especially when implemented using a 'lift and shift' scheme. Another challenge with acoustic methods is the inability to estimate leak size since there is currently no available relationship between leak size and the acoustic/vibration signals measured on the pipe. Leak size estimation is an important leak detection task as it serves as a basis for subsequent leakage control actions and prioritisation of repairs. Methods proposed in the literature for inferring leak size from acoustic/vibration measurements are generally based on the application of machine learning tools (Butterfield, 2018). However, such methods are usually specific to a particular pipe system, thereby making generalisation difficult. Furthermore, their implementation requires a large amount of historical data, which may not be readily available. Long leak identification time and inability to estimate leak size using existing acoustic methods may lead to increased water losses from leakages prior to their discovery and repair.

In order to improve the effectiveness of detecting and locating leaks through acoustic means, the practical limitations highlighted in this section have to be addressed. This can be achieved by adopting alternative acoustic leak detection methodologies. Possible strategies for achieving this are considered in the next section.

1.3 Alternative perspectives and strategies for acoustic leak detection

One possible strategy to deal with some of the issues identified in the preceding section is to consider acoustic leak detection problem from new perspectives. It must be noted that only issues which can be addressed through signal processing means (specifically, long leak identification time, wave speed measurement, and TDE) are considered in this work. Inherent limitations associated with acoustic wave attenuation and inability to estimate leak size are not considered. In existing acoustic leak detection methods, the problem of detecting and locating a leak is considered primarily as a pattern recognition problem and a TDE problem, respectively. The basic idea employed for leak awareness using acoustic noise logging is that the occurrence of a new leak generally results in a *sustained* increase in the level of acoustic signals measured in the pipe. Leak localisation using the cross-

correlation technique boils down to the problem of estimating the time delay between measured acoustic/vibration signals. These points of view make implicit assumptions that limit the extent to which leaks can be effectively located using existing acoustic methods. For instance, the cross-correlation technique assumes a priori 'third-party' knowledge of the acoustic propagation wave speed in the pipe, while acoustic noise logging assumes that the presence of a leak must necessarily result in increased level of the measured signals. Alternative perspectives for considering the acoustic leak detection problem can be adopted from other leak detection methods, fluid transient methodologies in particular.

A motivation for considering the possible application of fluid transient principles to acoustic leak detection is the close relationship between fluid transients and acoustic transients. In this work, *acoustic transients* refer to rapid variations in the *acoustic pressure* or structural pipe motion which can be sensed with acoustic/vibration sensors. Like fluid transients, they can be caused by pipe rupture, pipe impacts, or any other event that results in abrupt change in the condition of the fluid or the pipe. These two signal types are interconnected due to the presence of fluid-structure interaction (FSI) in a fluid-filled pipe. FSI is the two-way interaction or transfer of energy which takes place between the fluid and the pipe; changes in fluid flow or pressure results in structural excitation of the pipe and vice versa (Tijsseling, 1996). Due to FSI, the hydraulic and structural responses of the pipe and fluid to transient excitations (rapid valve closure, impacts, pipe burst, etc.) generally occur simultaneously through various coupling mechanisms (Moody and Winterbone, 1991; Li, 2011; Pinnington and Briscoe, 1994). This observation has been exploited for the non-intrusive detection and quantification of water hammer effects using acoustic measurements (Digulescu et al., 2015). Fluid and acoustic transients are both governed by the same principles of wave propagation in an acoustic medium, and like all known waves, they undergo the phenomenon of reflection when they encounter the boundary between two media of different physical properties, referred to as a *discontinuity* (Chien, 1967). Another motivation for considering fluid transient methodologies is the recent initiative for mass installation of transient pressure loggers by water companies in their distribution networks driven by recognition of the ubiquitous presence and adverse impact of hydraulic transients on pipe network assets (Hossein et al., 2022). This has made it possible to capture a large amount of data using commercially available transient loggers than was previously possible. However, it is notable that most of the available transient loggers are targeted towards survey applications, with their software offering only basic data viewing and limited capability for in-depth analysis (Hoskins, 2015). As a result, the data acquired by the loggers are not being fully utilised for network assessment and leak detection. Since hydraulic and vibroacoustic phenomena generally accompany each other due to the presence of FSI effects, data acquired with transient loggers may contain acoustic/vibration signals, extraction of which can provide additional information about the presence and location of leaks. The simultaneous occurrence of these two types of transients, similarity in their interaction with discontinuities in the pipe, and possibility of extracting acoustic/vibration signals from fluid transient

measurements suggest that principles of fluid transient methods may be applicable to the analysis of acoustic transients.

The occurrence of a leak in a fluid-filled pipe generates two types of acoustic waves: an initial impulsive signal (referred to as *leak transients* in this thesis) and a subsequent continuous signal (referred to as *steady-state signal* in this thesis) (Fuchs and Riehle, 1991; API, 1996). Existing acoustic leak detection methods are based on the analysis of the latter only. Both types of waves are transmitted along the pipe wall and the fluid in the pipe, leading to variations in the fluid acoustic pressure and vibration of the pipe wall that can be detected using acoustic/vibration sensors. This allows acoustic leak detection to be considered from a transient methodology viewpoint—as a transient detection problem, the aim of which is to detect the initial acoustic transients generated by a new leak. Since the subsequent generation of continuous steady-state signals by the leak results in a change in the properties of the measured signals (relative to the background noise), the problem of detecting a leak reduces to that of observing unique signatures in the signals, i.e., a signal detection problem. These viewpoints, transient and signal detection, emphasise the decision aspect of leak detection and consider leak detection problem as a statistical detection or anomaly detection problem which can be solved using statistical tools (as in the data-driven fluid transient methods). One possible benefit of implementing leak detection using these viewpoints is reducing the time required for leak awareness, as leaks can be detected as they occur or from short-term measurements.

As already stated above, like fluid transients, all acoustic waves propagating in the pipe system interact with features in the system. For instance, when an acoustic wave encounters a discontinuity, such as a leak or joint, it may be partially or completely reflected. This similarity with fluid transients allows the possibility of applying reflectometry principles (as in transient leak reflectometry methods) to acoustic leak detection. Based on this, leak detection can be considered a multipath identification problem, the aim of which is to detect acoustic transients or leak noise reflected by pipe defects in the measured signals. One possible benefit of considering leak detection from this angle is that leak can be detected and located using readily available data without need for 'third-party' information about the wave speed or pipe material properties.

In frequency response and impulse response fluid transient methodology, leak detection mainly requires knowledge of the behaviour of a pipeline in the absence and presence of a leak. The behaviour of the pipeline is described fully by its FRF or IRF, which indicates how the pipe modifies a signal propagating through it in the frequency and time domain, respectively. Since the FRF or IRF encapsulates all the information about wave propagation in the pipe and is independent of the type of signal propagating in the pipe, it is possible to consider acoustic leak detection as the problem of extracting the pipe FRF or IRF (a system identification problem). Conventional system identification requires the measurement of the response of a system to a known input signal (Ljung, 1999). However, the input signal, the leak noise generated at the leak location, is not available in acoustic

leak detection practice, so the system identification procedures used in fluid transient methods cannot be employed. Instead, a technique known as blind channel identification (BCI) (Haque and Hasan, 2008) must be used to extract the pipe FRF or IRF from the measured leak signals exclusively. The feasibility of using the BCI technique for acoustic leak detection may make it possible to locate leaks without a priori knowledge of the wave speed since this information is already available in the pipe FRF or IRF.

To deal with issues associated with estimating time delays in leak signals, it is worthwhile to view the TDE process in acoustic leak detection as consisting of two aspects: computing the time delay value and assessing the accuracy of this value. The second aspect can provide an effective means of resolving the challenges related to incorrect selection of TDE parameters, namely bandpass filters and GCC weighting function. Most research works dealing with the problem of filter design for TDE in acoustic leak detection generally focus on developing adequate or robust criteria to facilitate the selection of cut-off frequencies (see Almeida (2013) and Muggleton et al. (2011)). A more interesting and perhaps better approach is to consider alternative TDE methodologies where the choice of these parameters is not crucial to performance. Such alternative strategies may possibly be provided by transforms with inherent filtering capabilities. Developing approaches for achieving this is considered an important objective in this work.

The alternative points of view identified above for acoustic leak detection and TDE form the basis for the objectives of this thesis, which are outlined in the next section.

1.4 Objectives of the thesis

The main aim of this research work is the improvement of acoustic leak detection in water pipes. In particular, this thesis focuses on development of techniques for addressing some of the issues identified in Section 1.2, including non-robust TDE, uncertainty in wave speed value, and long leak identification time. The objectives of this thesis can be stated as follows:

1. To develop procedures for discovering leaks using signal and transient detection principles, i.e., by analysing temporal and spectral properties of acoustic transient and steady-state signals acquired in the pipe system.

2. To develop alternative acoustic methods for detecting and locating leaks using multipath identification principles, i.e., by identifying reflections of acoustic transients or the leak noise in the measured acoustic/vibration signals.

3. To develop an alternative acoustic method for locating leaks directly from the measured acoustic/vibration signals by extracting the pipe FRF or IRF.

4. To develop alternative methods for estimating time delays in leak signals, performance of which is not limited by the choice of weighting function or selection of a bandpass filter. Also, to develop approaches or metrics for quantifying the quality of the time delay estimate.

5. To compare different acoustic leak detection methodologies and develop an approach for combining them for more robust leak detection.

6. To validate the proposed methods using numerical and experimental data.

To limit the scope of the research, any method proposed in this thesis must fulfil certain requirements, including capability of being realised with existing acoustic measurement setup and sensors, ease and convenience for practical application, and utilisation of only readily available data.

1.5 Original contributions

The main contributions from this research are:

i. A procedure for detecting and locating acoustic transients in signals based on a change metric known as the non-stationarity measure (NSM) has been developed. The distribution and statistical properties of this transient detector have been derived.

ii. The NSM-based transient detector has been used to implement a method for detecting leaks by identifying the initial acoustic transients generated when a leak occurs in the pipe.

iii. A new acoustic method that detects leaks by analysing the spectral properties of the measured steady-state signals has been proposed.

iv. Two alternative acoustic leak localisation methods based on identifying the reflections of acoustic transients and leak noise in measured acoustic/vibration signals have been proposed.

v. A method for estimating the pipe FRFs and IRFs exclusively from leak signals has been developed for the purpose of locating leaks under the cross-correlation setup without knowledge of the wave speed or pipe material properties.

vi. Two alternative methodologies for estimating time delays between leak signals without need to select a weighting function or first apply a bandpass filter have been proposed.

vii. Three approaches for assessing the quality of the time delay estimate have been developed for use in acoustic leak detection.

viii. A method that combines multiple acoustic leak detection methodologies has been developed.

1.6 Thesis outline

The main body of this thesis consists of 9 chapters. This chapter (**Chapter 1**) presents a brief overview of water leakages and their consequences. Various leak detection methods employed in the water industry are briefly described, with particular attention on acoustic and fluid transient methods, the former being the main focus of this research. An overview of the roles and limitations of existing acoustic leak detection methods is presented. Based on the review of fluid transient methods, possible alternative strategies and perspectives for dealing with some of these limitations are identified. The objectives of the research project are formulated, and the original contributions are outlined.

Chapter 2 concerns the description of the laboratory pipe leakage test rig used extensively to validate the results in this research. Its characteristics, layout, and instrumentation, as well as the procedures adopted in carrying out leak simulation experiments, are described. Lastly, the limitations of the leakage test rig in comparison with real pipe systems are discussed.

Based on the first strategy identified in Chapter 1, the possibility of treating acoustic leak detection as a transient/signal detection problem is explored in **Chapter 3**. Two approaches, one based on transient analysis and the other based on analysis of steady-state signals, are proposed for leak awareness. The signal processing techniques for implementing these approaches are developed, including a new transient detection method. The proposed leak awareness approaches are experimentally investigated using data acquired on the leakage test rig. Finally, their benefits and limitations are highlighted.

Chapter 4 concerns the implementation of the second strategy identified in Chapter 1. Acoustic leak detection and localisation is recast as a multipath identification problem, and two reflection-based methods (transient and steady-state) are developed for detecting and locating leaks in water pipes. To implement these methods, two multipath identification techniques—the autocorrelation and the cepstrum—are derived, analysed, and compared for leak signals. The proposed leak detection methods are investigated using numerical simulation and experimental data, and their limitations are identified.

The possibility of performing acoustic leak detection using system identification (the third strategy identified in Chapter 1) is explored in **Chapter 5**. A blind channel identification (BCI) technique for extracting the pipe impulse response function (IRF) between the leak location and the measurement points is introduced. An algorithm for locating leaks directly from the measured signals without knowledge of the wave speed or pipe properties under the cross-correlation measurement setup is implemented using the BCI technique. Measures for dealing with possible challenges limiting the applicability of this technique to acoustic leak detection are developed. Numerical simulations and experimental data are then used to investigate the viability of the technique and compare its performance to the conventional cross-correlation method. Finally, the benefits and limitations of the technique are highlighted.

Chapter 6 presents three approaches (metrics) for assessing the accuracy or quality of the time delay estimate based on the statistical properties of the cross-correlation function (CCF) of uncorrelated noise and correlated leak signals. The basic principles of the approaches are described and statistically analysed. In order to evaluate the effectiveness of the proposed metrics, they are employed to assess the quality of the time delay estimates of experimental leak signals. Lastly, the limitations of the metrics are discussed.

Two alternative time delay estimation (TDE) methodologies are developed in **Chapter 7**. The first is implemented using transforms with inherent filtering, namely, the wavelet transform (WT) and data-adaptive decompositions, while the second is based on the cepstrum. The variance of the time delay estimate in the two methods is derived. The performances of the proposed methods for leak signals are compared with the conventional GCC methods numerically and experimentally. Finally, their advantages and disadvantages are outlined.

Chapter 8 discusses an approach for combining the transient and steady-state methods proposed in this thesis. Various acoustic leak detection methods are compared in terms of criteria, such as cost, applicability, and ease of data analysis. The benefits of combining different leak detection methodologies are discussed. An algorithm implementing the combined leak detection approach is described, and its effectiveness is demonstrated using experimental data.

In the final chapter (**Chapter 9**), the major conclusions of the thesis are summarised, and recommendations for future work are given.

CHAPTER 2
DESCRIPTION AND CHARACTERISATION OF THE LEAKAGE TEST RIG AND EXPERIMENTAL PROCEDURES

Data acquired on an in-vacuo leakage test rig have been extensively used for validating the results reported in this thesis. The aim of this chapter is to give a brief description of the rig and to outline the procedures used in acquiring the experimental data.

2.1 Description of the leakage test rig

Figure 2.1 shows the schematic plan of the leakage test rig. The L-shaped layout of the rig was determined by the available space in the laboratory where it was installed. It consists of two 6-metre MDPE pipes joined with a 90° elbow. Each pipe has outer diameter of 63 mm and thickness of 6.2 mm. The inlet of the rig is connected to a tap through a 25-m long, 19-mm diameter PVC hose as shown in Figure 2.2(a). A ball valve installed at the inlet is used to control the water infeed into the rig. The water pressure is slightly over 4 bar at the tap outlet but reduces to 3.7 bar at the rig inlet. The ends of the rig are terminated with MDPE end caps. For the purpose of simulating leaks, 6-mm holes were drilled on the side of Pipe 2 at the two points marked L1 and L2 in the schematic. In order to control the size of the leak, a valve is connected to a pipe clamp fitted over the leak hole, as shown in Figure 2.2(b). Hydrophones and accelerometers are installed/mounted at the access points labelled X1, X2, and X3 in the schematic. Each access point consists of a 9 mm hole over which a pipe clamp is fitted. As shown in Figure 2.2(c), the hydrophones are fitted with sleeved cable grommets and secured in the pipe clamps with cable glands, while the accelerometers are mounted directly on the pipe clamps using beeswax.

2.2 Instrumentation and data acquisition

The rig is fitted with B200 hydrophones (https://www.neptune-sonar.co.uk/products/hydrophones/b200) and 352C22 accelerometers (https://www.pcb.com/it/products-it-it?model=352c22), the metrological characteristics of which are summarised in Table 2.1. Two data acquisition systems (DASs), a USB-powered Quattro data analyser (https://www.dataphysics.com) and a mains-powered Prosig P8004 (https://prosig.com/), connected to a laptop are used for data acquisition and storage. Each DAS has four independent analogue inputs for direct voltage signals (hydrophones) or integrated electronics piezo-electric (IEPE) signals (accelerometers). They also have a built-in anti-aliasing filter,

the cut-off frequency of which is automatically adjusted by the DAS based on the sampling rate set by the user.

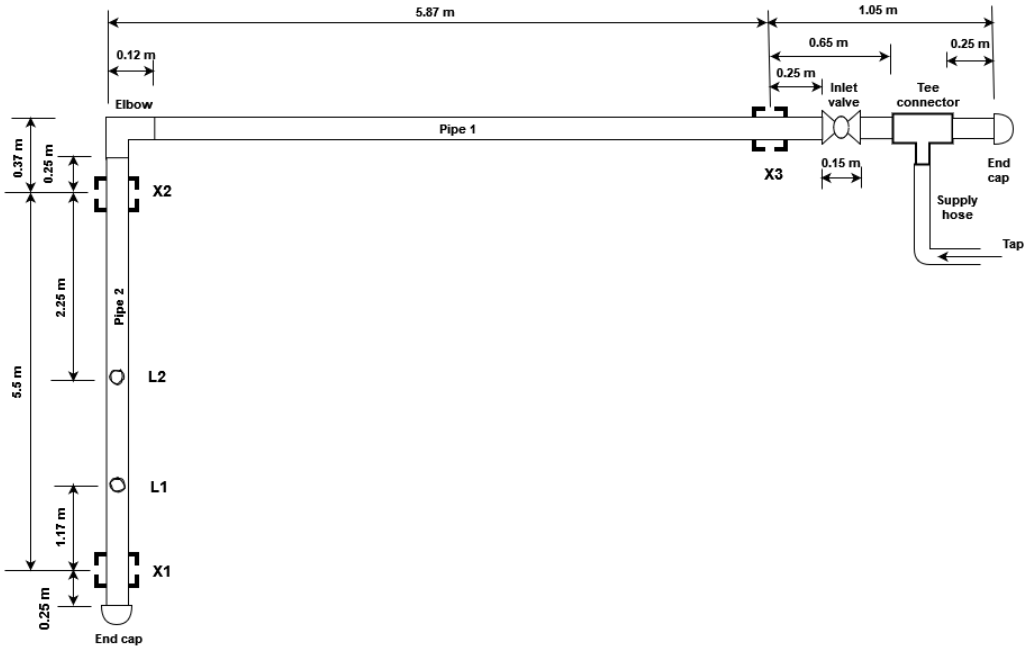

Figure 2.1: Schematic of the leakage test rig.

Figure 2.2: Parts of the leakage test rig: (a) Inlet section. (b) Setup for leak simulation. (c) Access points for installation of acoustic/vibration sensors.

Table 2.1: Metrological characteristics of the B200 hydrophone and 352C22 accelerometer.

	B200 hydrophone	**352C22 accelerometer**
Sensitivity	-212 dB re 1 V/mPa (2.8×10^{-5} mV/mPa)	1.0 mV/ms^{-2}
Useful frequency range	10 Hz to 180 kHz	0.3 Hz to 20 kHz
Resonant frequency	170 kHz	≥ 50 kHz
Measurement range	Not available	± 4900 ms^{-2} peak
Operating temperature	-5 to +40 °C	-54 to +121 °C

2.3 Experimental characterisation of the leakage test rig

Prior to the use of leakage test rig for experiments, tests were carried out to evaluate its physical characteristics with the aim of obtaining benchmarks for comparing results of leak detection experiments. The results of the characterisation tests are presented in this section.

2.3.1 Determination of pipe material properties

To measure the material properties of the MDPE pipes, the impact excitation method described by Lord and Morrell (2006) was employed. Using this method, the Young's modulus, loss factor, and ring frequency of the pipe were calculated from the point accelerance of a thin ring cut from the pipe. The length and mass of the ring are 97.4 mm and 10.2 g, respectively, and its material density is 942.1 kg/m^3. The point accelerance $A_c(\omega)$ of a structure is the ratio of the acceleration response measured at a point on the structure to the excitation force applied at a given point. The peaks in the point accelerance correspond to the natural frequencies of the structure. To obtain the point accelerance of the MDPE pipe, the ring was freely suspended and tapped radially with an instrumented hammer in line with the direction of a 352C22 accelerometer mounted on the side of the ring as depicted in Figure 2.3(a). The accelerometer was oriented in a way to measure the radial acceleration of the ring in order to observe a range of its circumferential modes. The resulting response was recorded in the range 0-6.5 kHz using Quattro data analyser unit, which automatically filters out frequencies above this range to avoid aliasing. Figure 2.3(b) shows the point accelerance (with a reference of 1 ms^{-2}/N) obtained from data averaged over five impacts. The resonance frequencies associated with circumferential modes are each marked with a red dot.

The relationship between the resonance frequency f_n in the accelerance plot and the pipe material properties is given by (Blevins and Plunkett, 1980)

$$f_n = \frac{n\left(n^2-1\right)\cdot h_p}{2\pi a_p^2\left(n^2-1\right)^{1/2}}\cdot\sqrt{\frac{E_p}{12\cdot\rho_p}} \tag{2.1}$$

where $n = 2,3,4,\ldots$ is the circumferential modal number. The modal loss factor η_p of the pipe material can be calculated from the half-power frequencies of the resonance peaks $f_{n+1/2}$ and $f_{n-1/2}$ using (Ewins and Saunders, 1986)

$$\eta_p = \frac{f_{n+1/2} - f_{n-1/2}}{f_n}. \tag{2.2}$$

The half-power frequencies $f_{n+1/2}$ and $f_{n-1/2}$ associated with the resonance peak f_n are the frequencies at which the point accelerance has dropped by 3 dB from its value at f_n, i.e., to half of the resonance peak amplitude value.

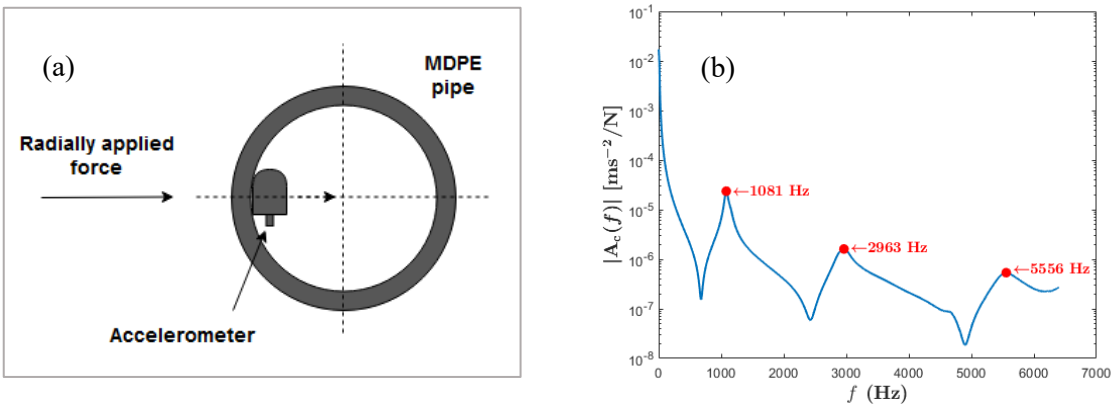

Figure 2.3: Determining the material properties of the MDPE pipe. (a) Mounting accelerometer on a freely suspended thin ring cut from the MDPE pipe to measure its radial acceleration response to a point excitation. (b) Point accelerance $A_c(f)$ of the ring. The frequency f is shown in Hertz.

The ring frequency f_{ring} is the frequency at which the wavelength of a longitudinal wave in the shell material of the pipe equals its circumference (Moore, 2016). It is given by

$$f_{\text{ring}} = \frac{1}{2\pi a_p}\sqrt{\frac{E_p}{\rho_p}}. \tag{2.3}$$

The ring frequency is an important quantity in describing the dynamics or wave behaviour of cylindrical shells. It divides the shell behaviour into two regions (Cremer et al., 2010). At frequencies above the ring frequency, the wavelengths of circumferential modes are much shorter than the circumference, and the shell behaves as an infinite flat plate. The vibroacoustic behaviour and energy transmission in the pipe at frequencies well below the ring frequency are dominated by plane waves corresponding to the axisymmetric circumferential modes $n = 0$ and $n = 1$, where the pipe's cross section remains circular (Moore, 2016).

The Young's modulus and the loss factor calculated using Equations (2.1) and (2.2) are presented in Table 2.2. Since Equation (2.1) is only valid for thin rings and low frequencies (Blevins and Plunkett, 1980), the value of the pipe Young's modulus is taken as the value 1.2 GPa evaluated for the resonance peak attributed to the $n = 2$ mode. This value is higher than the typical value of 0.8 GPa reported for MDPE pipes (Matweb, 2023).The loss factor is also taken as the value 0.015 corresponding to the $n = 2$ mode. Using Equation (2.3), the ring frequency of the MDPE pipes is obtained as 6.3 kHz. The low-frequency leak noise propagation model (Muggleton et al., 2002) can be assumed to be valid for the MDPE pipe at frequencies below this value.

Table 2.2: Young's modulus, loss factor, and ring frequency values corresponding to the circumferential modes of the MDPE pipe in the leakage test rig.

Property	**Circumferential modal number**		
	$n = 2$	$n = 3$	$n = 4$
Young's modulus E_p, GPa	1.2	1.1	0.9
Loss factor η_p	0.015	0.021	0.019
Ring frequency f_{ring}, kHz	6.3	6.1	6.0

2.3.2 Wave speed measurement

The acoustic wave speed in the pipe was determined experimentally from the time delay $\hat{\tau}_{\text{peak}}$ between hydrophone or accelerometer signals measured at access points X1 and X2 when the pipe was excited with a white noise signal using a shaker at a known *out-of-bracket* location (in this case the elbow). The term *out-of-bracket* is used in this work to indicate that a feature is located outside the range enclosed by the two access points being considered. The value of the wave speed in the pipe is given by the expression $c = d/\hat{\tau}_{\text{peak}}$, where d = 5.5 metres is the distance between X1 and X2. The time delay $\hat{\tau}_{\text{peak}}$ was estimated as the gradient of the unwrapped cross-spectral phase, calculated over the effective bandwidth (EB), i.e., the frequency range in which reliable time delay information is located (Almeida, 2013). This frequency region is characterised by high values of the CPS modulus and MSC. Figure 2.4(a) shows the CPS modulus (normalised by its maximum value) and the MSC of the X1 and X2 accelerometer signals. Based on the criterion given by Almeida (2013), the EB is taken as the frequency region where the normalised CPS modulus exceeds a threshold of 0.1. In this case, the EB encompasses frequencies between 400 and 650 Hz, indicated by the vertical dashed lines. It can be observed that the cross-spectral phase is approximately linear in this frequency range as illustrated in Figure 2.4(b). For this particular example, the time delay is obtained as $\hat{\tau}_{\text{peak}}$ = 15.4 ms, giving the wave speed as 357 m/s. Using the same procedures, the wave speed was estimated from 10 hydrophone and accelerometer measurements. The average wave speed value for the hydrophone and

accelerometer signals was 352 m/s and 361 m/s, respectively. The wave speed estimates are close, even though they are obtained over different EBs. The value of 354 m/s given by the average of all the hydrophone and accelerometer wave speed estimates will be taken as the true wave speed in the analysis in this work.

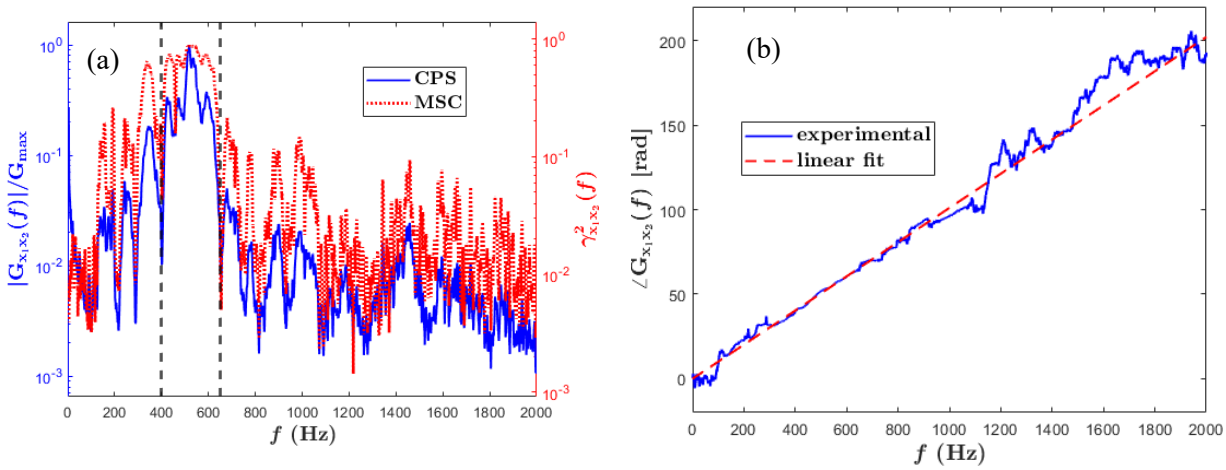

Figure 2.4: Estimating the time delay in X1 and X2 accelerometer signals for wave speed calculation. (a) Normalised CPS modulus and MSC. (b) Unwrapped cross-spectral phase and linear fit. $G_{\max}$ is the maximum value of the CPS modulus. The vertical dashed lines denote the limits of the EB.

Substituting the typical values of B_f = 2.2 GPa and c_f = 1500 m/s for water and the experimentally determined value of E_p = 1.2 GPa in the wave speed formula (Equation (1.3)) gives the theoretical wave speed in the MDPE pipe as 339 m/s, which differs by 4% from the experimentally determined value. The close agreement between these values can be attributed to the fact that the material properties of the pipe have been explicitly determined. If instead, the typical value of E_p = 0.8 GPa for an MDPE pipe is used in the calculation, then the theoretical wave speed is obtained as 279 m/s, which differs by 21% from the experimentally determined wave speed. This illustrates the danger of using calculated wave speed value when the pipe material cannot be determined reliably, thus emphasising the need for in-situ measurement of the wave speed or its direct estimation from measured signals.

2.3.3 Characterisation of noise sources

The signals captured by acoustic/vibration sensors during leak detection experiments on the leakage test rig may contain signals generated by the leak, acoustic transients introduced by operation of rig components and pipe impacts, and background noise. Only the first two are useful for acoustic leak detection and localisation. High background noise level can lead to poor coherence between measured leak signals (Papastefanou, 2011), thereby resulting in inaccurate time delay estimate and leak

detection results (Gao et al., 2004). The leakage test rig can only be useful for leak detection experiments if the leak noise generated by the simulated leak is not completely 'drowned out' (masked) by the background noise, or completely attenuated by the pipe. Possible sources of background noise include noise from the water supply source (the tap), ground vibration, electrical interference, etc. The aim of this section is to determine the suitability of the test rig for experiments by assessing the contributions of the background noise sources. To achieve this, leak signals acquired at an access point furthest from the leak are compared with the background noise.

Figure 2.5 shows the time histories and power spectral densities (PSDs) of the background noise and leak measurements captured at X3 when a leak was simulated by opening the L1 valve halfway (the minimum valve opening used in the experiments in this work). The SNR of the leak signal was evaluated to be 4 dB. In this work, the SNR of leak signals is calculated as the ratio of the average signal power (P_{signal}) and the average noise power (P_{noise}):

$$\text{SNR} = \frac{P_{\text{signal}}}{P_{\text{noise}}} = 10 \cdot \log_{10}\left\{\frac{P_{\text{signal}}}{P_{\text{noise}}}\right\} \quad [\text{dB}] \tag{2.4}$$

where P_{signal} and P_{noise} are given by the area under the signal and noise PSDs (in $\left(\text{ms}^{-2}\right)^2/\text{Hz}$ or Pa^2/Hz, not in dB), respectively, within a selected frequency range; and $\log_{10}\{\bullet\}$ denotes the logarithm in base 10. Unless otherwise specified, the SNR is evaluated over the whole signal bandwidth (this is equivalent to computing the mean square of the time-domain samples).

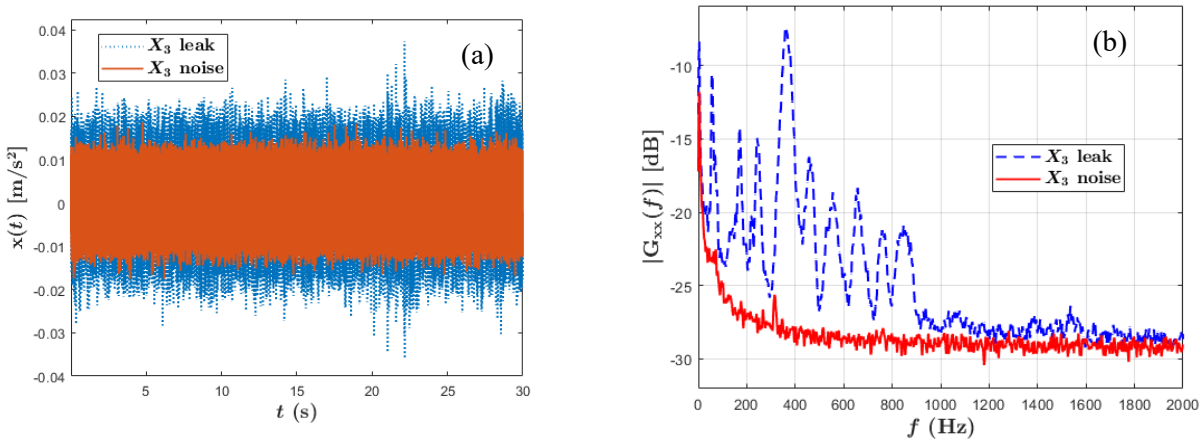

Figure 2.5: Background noise and leak accelerometer signals acquired at X3 with the L1 valve open halfway: (a) Time histories. (b) PSDs.

As can be observed from the plots, the presence of a leak results in higher signal energy as well as noticeable increase in the low-frequency content (up to 900 Hz in this case), indicating that the leak noise is detectable even at the access point furthest from the leak simulation location. Nonetheless, some measures were deployed to reduce the contributions of background noise sources, including mounting the pipes on pipe clips (to limit the effects of ground vibration) and using a long supply hose (to reduce the contributions of tap noise). Furthermore, the leak detection experiments were carried out

only when the laboratory was relatively quiet to ensure low background noise levels. Peaks in the leak signal PSD in Figure 2.5(b) indicate the presence of reflections and resonances in the leakage test rig (see Gao et al. (2009) and Almeida (2013)).

2.3.4 Determination of system transfer function

At frequencies below the pipe ring frequency, the FRF relating the leak noise (signal generated by the leak) and the signal measured at a distance u from the leak in an infinite pipe without discontinuities is given by (Gao et al., 2006)

$$H(\omega,u)=e^{-|\omega|\beta u}e^{-j|\omega|u/c} \tag{2.5}$$

where $j=\sqrt{-1}$. The attenuation factor β and the wave speed c are given by Equations (1.2) and (1.3), respectively. Note that the acoustic pressure at the leak location is related to the pipe velocity and acceleration in the frequency domain by a factor of $\frac{j\omega a_p^2}{E_p h_p}$ and $-\frac{a_p^2\omega^2}{E_p h_p}$, respectively. These expressions are derived from the linear relationship $W_r=\frac{P_{\text{int}}a_p^2}{E_p h_p}$ between the internal pressure amplitude P_{int} and the radial wall displacement amplitude W_r at low frequencies (Pinnington and Briscoe, 1994).

Two properties of the FRF in Equation (2.5) which are of interest in this work because of their relevance to some proposed leak detection methods are the linearity of the phase and exponential decay of the magnitude. The validity of these properties for the MDPE pipe was verified by experimentally determining the FRF of the pipe using system identification methodology (Ljung, 1999). In the system identification methodology, the FRF of a system is determined from the response of the system to a known excitation signal. Specifically, the FRF $H(f)$ of the system is estimated as the ratio of the CPS of the input excitation signal $x(t)$ and the measured output signal $y(t)$ to the auto-power spectrum of the input, i.e.,

$$H(f)=\frac{G_{yx}(f)}{G_{xx}(f)} \tag{2.6}$$

where $f=\omega/2\pi$ is frequency in Hertz. The FRF obtained using this equation is referred to as the H_1 estimate in contrast with the H_2 estimate given by $G_{yy}(f)/G_{xy}(f)$. The H_1 estimate assumes that the background noise is not correlated with the input, while the H_2 estimate assumes that the noise is not correlated with the output (Bendat and Piersol, 2010). When the noise is not correlated with either the input or the output signal, the two estimates are very similar. It is important to note that since Equation (2.5) assumes an infinitely long pipe with no discontinuities, it does not take into account the

presence of reflections in the input and output signals. A possible approach to reduce the effects of reflections on the FRF estimate is to set the measurement duration to less than the time required for the arrival of the reflections from the nearest discontinuity at the response measurement location. However, this approach is difficult to apply in the leakage test rig, as extremely short measurement duration will be required due to the short distances between the measurement points and discontinuities in the rig. For example, measuring the response of the pipe at X2 to an excitation signal at L1 will require the measurement duration to be set to 14 milliseconds, which is less than the minimum measurement duration allowed by the DASs. As a result, the FRF was determined without excluding the reflections in the signals.

To determine the FRF of the pipe, the pipe was excited at one location (1 metre from the elbow on Pipe 1) with a white noise signal with bandwidth up to 20 kHz using a shaker, and the resulting response was measured at a different known location (2 metres from X3 on Pipe 1) for 30 seconds at a sampling rate of 40 kHz. Figure 2.6 shows the spectrum of the excitation signal measured with an accelerometer. This excitation signal does not have a flat spectrum over its whole bandwidth, but only the results from the frequency range below the ring frequency where the spectrum is nearly flat are considered to be accurate (up to 5 kHz).

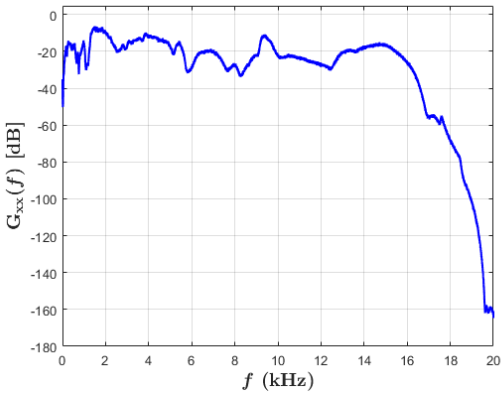

Figure 2.6: Spectrum of the input excitation signal measured with an accelerometer on Pipe 1 at a location 1 metre from the elbow.

The magnitude and unwrapped phase of the H_1 estimate of the FRF (Equation (2.6)) are shown in Figure 2.7. The auto-power spectrum $G_{xx}(f)$ and the CPS $G_{yx}(f)$ were computed using the Welch segment averaging method employing a 40000-sample Hanning window with 50% overlap between segments. Also shown in Figure 2.7 are the magnitude and unwrapped phase of the theoretical FRF obtained by substituting the wave speed value c = 354 m/s and the pipe attenuation factor β = 2.1×10^{-5} s/m in Equation (2.5). The pipe attenuation was computed using η_p = 0.015 in Equation (1.3). It can be observed that the experimentally determined unwrapped phase is approximately linear within the frequency range up to 1 kHz in good agreement with the prediction from the FRF model. The magnitude of the FRF, on the other hand, agrees with the model to a smaller extent. However, the

low-pass nature of the pipe is evident from Figure 2.7(a) in the frequency regions below the ring frequency of the pipe (6.3 kHz). One factor that might account for the lesser agreement between the experimental and theoretical FRF magnitude is the presence of discontinuities in the pipe that give rise to reflections in the signals measured on the leakage test rig, as indicated by the PSD in Figure 2.5(b) above. As Gao et al. (2009) have shown, the effects of reflections are generally more severe on the magnitude than on the phase of the FRF. Based on the linearity of the phase and low-pass nature of the FRF, the leakage test rig can be considered adequate for validating leak detection methods involving the use of the theoretical FRF model in Equation (2.5).

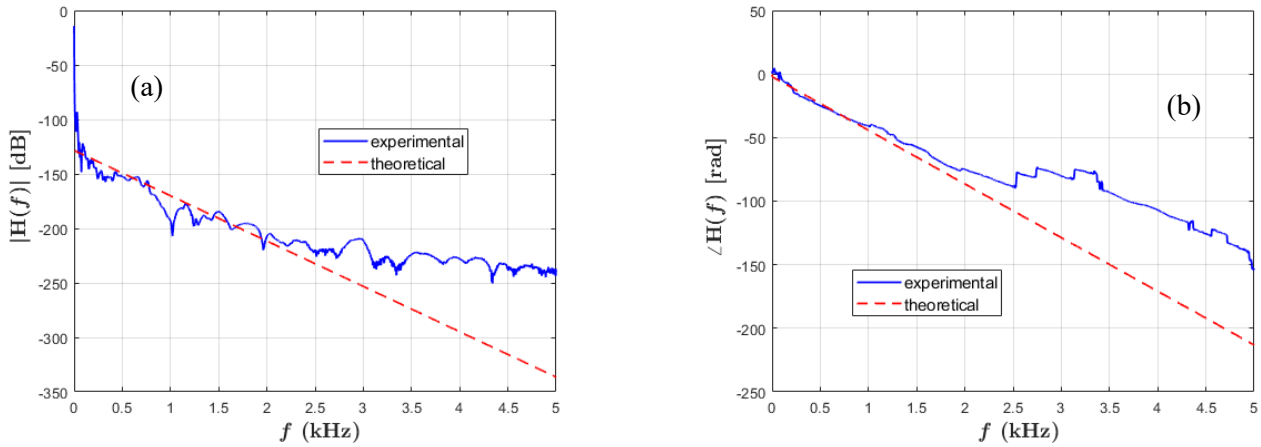

Figure 2.7: Theoretical and experimental FRFs of the MDPE pipe determined from acceleration signals measured on Pipe 1 in the leakage test rig. (a) Magnitude. (b) Unwrapped phase.

2.4 Experimental procedures and data analysis

The experimental procedures for the leak detection experiments carried out on the leakage test rig can be summarised as follows:

1. Set up the DAS and connect the sensors.
2. Close the leak simulation valves and open the inlet valve.
3. Open the tap and fill up the rig with water. Check for and repair any leaking component.
4. Start the DAS.
5. Measure the background noise for at least 30 seconds. A long measurement duration is desirable for accurate spectral analysis (see Bendat and Piersol (2010)), so the minimum measurement time in the experiments is set to 30 seconds.
6. Open the leak simulation valve L1 or L2 to the required leak size.
7. Measure the leak signals for at least 30 seconds. If required, simulate acoustic transients by hitting the pipe with a metallic rod (impact excitation) or operating the infeed valve.
8. Stop the DAS.
9. Close the leak simulation valve.
10. Turn off the tap.

Depending on the requirements of the experiments, steps 8 and 9 can be interchanged, for instance, when there is necessity to capture the end of a leak. Water from the leak disposed into the air and could be collected with a bucket in order to determine the volumetric flow rate of the leak if required. It is important to ensure that the DAS was always put into operational mode before leak simulation to enable acquisition of the initial transients associated with leak occurrence. Also, the tap and the in-feed valve should remain open throughout the duration of the experiment.

The length of the pipes in the leakage test rig is limited by the available space in the laboratory where it was installed. Due to the relatively short length of the test rig, the time delay between measured signals will be relatively small (in samples), which may make further analysis difficult. For example, at a sampling rate of 1 kHz, the true time delay between signals measured at X1 and X2 with the leak simulated at L1 is only 9 samples. Therefore, the sampling rate in all leak detection experiments carried out on the leakage rig was set to at least 2.5 kHz, with 40 kHz being the most commonly used. Note that the use of a high sampling rate is merely for the ease of computing time delays. The signals can be downsampled prior to the analysis when necessary.

Analysis of the measured signals was carried out using MATLAB, a proprietary numeric computing environment developed by MathWorks (https://uk.mathworks.com/). The measured signals were first converted into MAT files (the native MATLAB format), and pre-processing operations, such as notch filtering to remove 50 Hz mains harmonics, were applied where necessary to improve the quality of the data before analysis. Unless otherwise stated, the method employed for spectral analysis in this work is Welch segment averaging method using a Hanning window with 50% overlap. length of the window was set to the sampling frequency in most of the spectral analysis. The default TDE methods used were the BCC, GCC-ML, and GCC-PHAT.

2.5 Limitations of the leakage test rig

It is important to highlight a number of differences between the rig and real pipe systems that must be taken into consideration when interpreting or generalising the experimental results presented in this thesis. The first difference is associated with the short length of the rig compared to real water pipes. This has a number of implications that naturally affect the interpretation of results. Firstly, acoustic/vibration signals obtained on the test rig contain relatively higher frequencies, whereas values reported in the literature for leaks occurring in larger and longer plastic water distribution pipes are typically below 200 Hz (Hunaidi and Chu, 1999, Pal et al., 2010; Gao et al., 2005). The length of the rig is approximately 13 metres, whereas the inter-sensor distance in the United Kingdom is typically in the range 90–180 metres (HMFSI, 1998). This implies that signals measured on real pipe systems undergo higher levels of attenuation before reaching the sensors. This factor is important to consider when generalising the experimental results reported for the proposed methods where such higher level of signal attenuation can impact effectiveness in real pipes. A second consequence of the short pipe

length is the presence of higher reflection levels than what might be obtained in a real pipe system. Due to the short distances between the features in the leakage test rig, transients and reflections can be easily captured by the sensors, unlike in real systems, where greater distances of travel imply lower detectability for reflections. For example, the endcap located a short distance from X1 leads to substantial reflections in any signal measured at X1. This also affects the selection of suitable methods for signal processing. As an example, without appropriate pre-processing, the GCC-PHAT fails for estimating time delays in some leak signals acquired on the leakage test rig.

The second difference is that the leakage test rig is in-vacuo in contrast with majority of real water pipes, which are buried. It is known that environmental conditions may play an important role in leak detection practice. As previously mentioned in Chapter 1, the type of surrounding medium has substantial effects on acoustic wave propagation in plastic pipes, with the stiffness effects of the surrounding soil increasing the wave speed and attenuation in buried pipes compared to in-vacuo pipes (Muggleton et al., 2004; Muggleton and Yan, 2013). The third difference is the higher accessibility of the leakage rig compared to buried pipes. This makes it easier to induce transients via pipe impact, an excitation method which is very difficult to apply in real buried pipes. Hence, some of the findings obtained using this method of excitation may be difficult to extend to real systems.

Despite these differences, the good agreement between theoretical predictions and the results in the characterisation experiments, namely, wave speed measurement and FRF estimation, shows that the leakage test rig can be used for rudimentary validation of applicable leak detection methods. This also provides some reasonable basis for generalising the conclusions of this research project and extending them to real water pipes.

2.6 Summary and conclusion

This chapter has described the physical layout and instrumentation of the MDPE leakage test rig used extensively to validate results in the research project. To provide benchmarks for comparing experimental results, a number of characterisation tests were carried out to determine the pipe material properties. The Young's modulus, loss factor, and ring frequency of the pipe were determined from the point accelerance of a thin ring cut from the pipe, while the wave speed was calculated from the time delay between two signals measured at two access points in the rig when the pipe was excited at a known location. This experimentally determined wave speed differs from the wave speed calculated using the explicitly measured pipe material properties by only 4%. The phase and magnitude (to a smaller extent) of the frequency response function (FRF) of the pipe agree with theoretical predictions, showing that the rig is appropriate for validating methods where the theoretical FRF is used. The experimental procedures and signal processing methods employed in analysing the data were outlined. Lastly, the differences between the leakage test rig and real pipe systems were highlighted. Based on

the results of the characterisation tests, it was concluded that the leakage test rig is suitable for the experimental investigation of leak detection methods relevant to the thesis.

CHAPTER 3
ACOUSTIC LEAK DETECTION AS A TRANSIENT AND SIGNAL DETECTION PROBLEM

One of the alternative perspectives identified in Chapter 1 for viewing leak detection problem is as a transient/signal detection problem. In this chapter, the possibility of employing transient and signal detection principles in acoustic leak detection will be explored.

3.1 Recasting leak detection as a transient and signal detection problem

Figure 3.1 shows the time history and 256-sample spectrogram of an acceleration signal measured at X1 on the leakage test rig described in Chapter 2 when a 3-mm diameter leak is simulated by suddenly opening the valve at L1 halfway. As can be observed from the time history and spectrogram around the 8-second mark, leak occurrence is accompanied by the generation of acoustic transients, which can be detected using acoustic/vibration sensors. Examination of the spectrogram reveals a change in the frequency content of the signal after the occurrence of the leak. Both the background noise and leak-related vibrations are characterised by stationary signals with most of the signal energy in certain frequency bands. In contrast with the background noise and leak signals, acoustic transients feature high vibration levels over nearly the entire spectrum or are characterised by variable frequency content. From the spectrogram in Figure 3.1(b) and the PSDs in Figure 2.5(b), it can be observed that the shape and distribution of energy in the signal spectrum differ for leak and background noise signals. When a leak is present, certain frequency bands have higher energy in the signal spectrum compared to the noise spectrum. Thus, the spectrum of a signal in a leaking condition will display characteristic frequency content clearly distinguishable from the background noise.

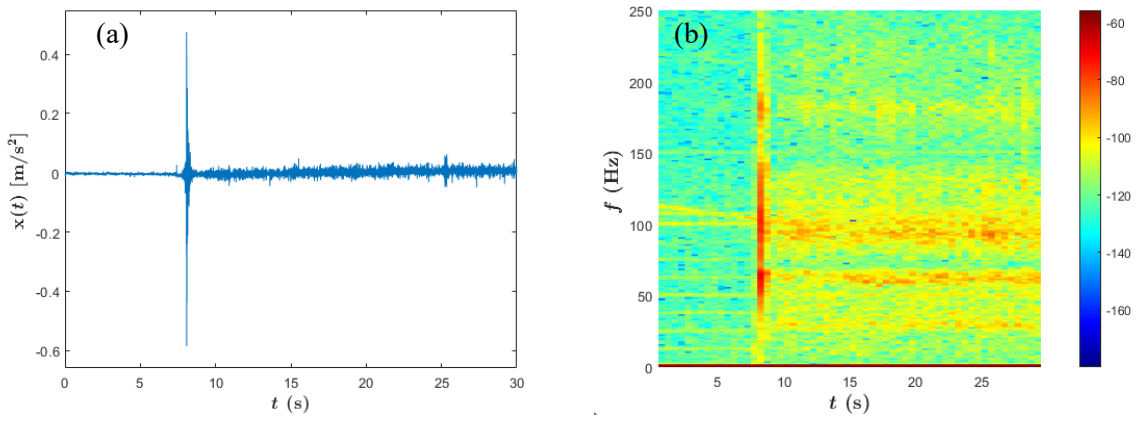

Figure 3.1: Acceleration leak signal measured at X1 on the leakage test rig with a leak simulated by opening the L1 valve halfway. (a) Time history. (b) Spectrogram in dB.

Apart from modifying the signal spectrum, the presence of a leak can also result in changes in the time-domain properties of the signal. This is illustrated in Table 3.1, where the values of different time-domain and frequency-domain properties are compared for the noise-only portion (before leak simulation) and leak signal portion (after leak simulation) of the signal. These include features that characterise signal energy (root-mean square (RMS), standard deviation), signal shape (crest factor, shape factor, kurtosis, skewness), spectrum shape (spectral centroid, spectral kurtosis, spectral skewness), and spectral variation (spectral flatness, spectral flux). The mathematical formulae for the time-domain and frequency-domain features are listed in Table A.1 in Appendix A. A review of the frequency-domain features, formally known as *spectral descriptors* in audio signal processing, can be found in the report by Peeters (2004). Note that due to similarity of calculation methodology, some signal features are highly correlated with each other, for example, RMS and standard deviation. In this thesis, very small and large numbers in tables are presented in scientific (exponential) notation, for example, 2.89E+05 denotes the value 2.89×10^{5}.

Table 3.1: Time- and frequency-domain features for noise-only (before leak simulation) and leak signal (after leak simulation) portions of an acceleration signal measured at X1.

Background noise portion				**Leak signal portion**			
Feature	**Value**	**Feature**	**Value**	**Feature**	**Value**	**Feature**	**Value**
RMS (ms^{-2})	0.10	Skewness	-0.013	RMS (ms^{-2})	0.83	Skewness	-0.027
Standard deviation (ms^{-2})	0.10	Kurtosis	3.05	Standard deviation (ms^{-2})	0.83	Kurtosis	3.16
Clearance factor	79.79	Shape factor	0.13	Clearance factor	9.45	Shape factor	1.04
Crest factor	50.53	Entropy	-4735	Crest factor	5.97	Entropy	30063
Spectral centroid (Hz)	7927	Spectral spread (Hz)	4955	Spectral centroid (Hz)	785	Spectral spread (Hz)	1153
Spectral flatness	0.23	Spectral skewness	0.062	Spectral flatness	0.0095	Spectral skewness	9.98
Spectral flux	0.0005	Spectral kurtosis	1.73	Spectral flux	0.18	Spectral kurtosis	114.65
Spectral crest	26.97	Spectral roll-off	15592	Spectral crest	128.22	Spectral roll-off	958.88
Spectral decrease	-0.01	Spectral entropy	0.88	Spectral decrease	0.036	Spectral entropy	0.44
Spectral slope	-2.44E-07			Spectral slope	-2.69E-06		

It can be observed that the presence of a leak leads to noticeable changes in some signal features, with the most substantial changes (on average) occurring in the quantities related to signal energy and spectral variation. In contrast, features that describe the shape of the time-domain signal,

such as the kurtosis and skewness, appear to be less sensitive to the presence of the leak. This agrees with experimental results reported by Martini et al. (2015). The values of these features can be interpreted in some way. For instance, a high spectral flatness (approaching 1.0 for white noise signals) indicates that the spectrum has a similar amount of energy in all spectral bands, while a low spectral flatness indicates that spectral power is concentrated in a relatively small number of bands.

Since the presence of acoustic transients in a measured signal or changes in its temporal and spectral properties may be indicative of a leak, the problem of detecting a leak in the pipe can be viewed as a transient and signal detection problem. Figure 3.2 displays an algorithm implementing acoustic leak detection methods based on this viewpoint. The rest of this chapter concerns the description and experimental investigation of this algorithm.

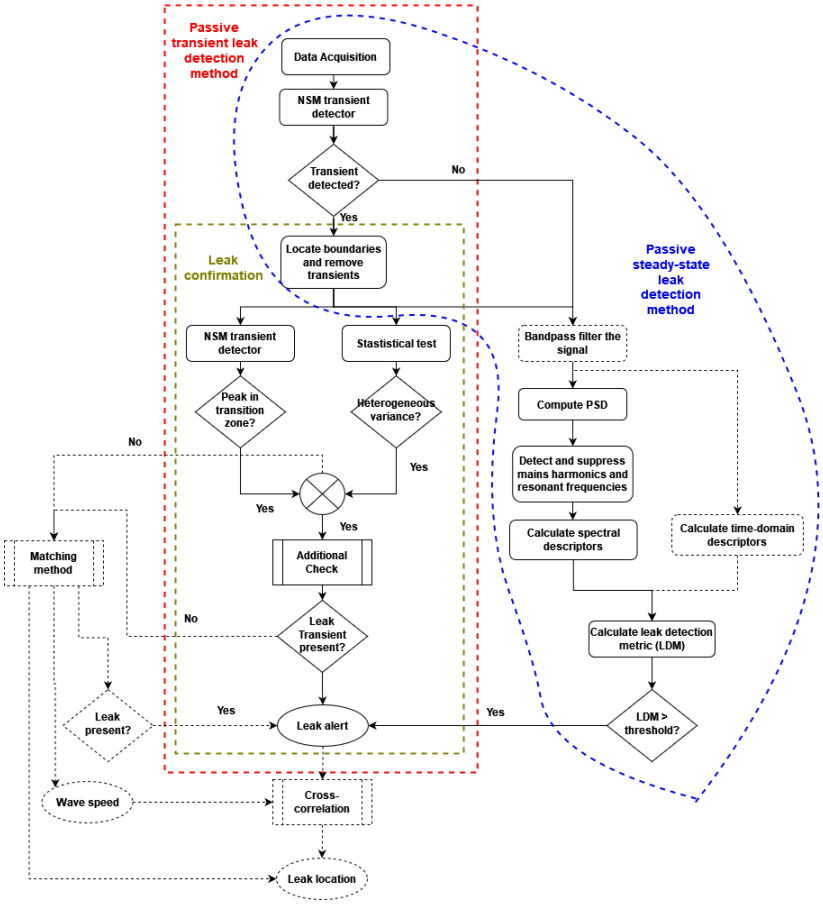

Figure 3.2: Acoustic leak detection algorithm based on transient/signal detection. Optional steps are indicated with dashed elements in the flowchart.

Remark. In this thesis, any acoustic method that involves the analysis of acoustic transients will be referred to as *transient*, while other methods (including existing acoustic methods) will be termed *steady-state*. Furthermore, each leak detection method is classified as *passive* if it is based on analysing signals generated by the leak, or *active* otherwise. All steady-state methods are passive. For convenience, acoustic transients will be classified based on their source as either *leak transients* (generated by leak occurrence or pipe burst) or *active transients* (induced by non-leak events, for example, operation of valves and pipe impacts).

3.2 Acoustic leak detection by transient analysis

As shown by the illustration in Figure 3.1 above, leak transients represent a demarcation between noise-only and leak measurements, so their identification provides a straightforward way to detect the occurrence of a new leak. This leak detection approach referred to in this work as *passive transient leak detection method* involves two steps: acoustic transient detection and leak confirmation (see Figure 3.2). The necessity of the second step is to distinguish leak transients from active transients, which might incorrectly trigger an alert for leaks. The details of the implementation of the two steps are described in the following subsections.

3.2.1 Acoustic transient detection using the non-stationarity measure

Detecting the presence of acoustic transients in a signal is essentially a binary hypothesis testing problem with a null hypothesis that the signal contains only background noise and an alternative hypothesis that it contains acoustic transients embedded in background noise. A signal containing an acoustic transient can be considered a succession of homogeneous or stationary segments ('steady states') separated by non-stationary or transitory segments (transients) that are of very short duration compared to the observation time. Homogeneity can be defined with respect to any property of the signal (mean, variance, spectral density, etc.). By considering the signal this way, transient detection becomes the problem of deciding in each time interval whether a transition exists or not, i.e., whether the signal is stationary or non-stationary. For the purpose of leak detection, it is necessary not only to detect the presence of a transient but also to determine its *time boundaries* (onset and end) in the signal. To achieve this, a procedure based on a changepoint detection metric known as non-stationarity measure (NSM) is proposed for detecting acoustic transients in this work. The NSM is a metric which can detect and locate the presence of a transition or *break* in an otherwise stationary signal (Liu et al., 1995). Originally proposed by Liu (1994), the NSM has found application in edge detection and segmentation of ultrasound images (Xu, 2013).

As will become evident in later sections, this novel application of the NSM for transient detection is based on the following considerations: simplicity and ease of implementation, robustness to noise, precise determination of transient boundaries, flexibility, and inherent indication of relative 'strength' of transients. The terms 'strong' and 'weak' are used to denote how detectable a transient relative to the background noise—the more easily detectable it is, the 'stronger' it is said to be. In contrast with transient detection approaches based on the generalised likelihood ratio test (GRLT), such as Gaussian likelihood detector (GLD) (White, 1996) and auto-regressive segmentation algorithm (Chen, 1984), the NSM-based method does not assume any model or probability distribution for the background noise or transient. Hence, it is suitable for detecting acoustic transients, properties of which are generally unpredictable and vary depending on the operating conditions in the pipe.

It should be noted that all transient detection methods including the NSM-based method employed in this work operate on the same principle of comparing an appropriate test statistic against a given threshold. The presence of a transient is inferred if the test statistic exceeds the threshold. The difference between transient detection methods boils down to the test statistic used. In the following subsections, the basic principles, implementation, and statistics of the NSM are described.

3.2.1.1 Description of the Non-Stationarity Measure

The NSM quantifies changes in a signal by measuring its degree of *local non-stationarity*. A signal $x(n)$ is considered to be locally stationary (or 'steady-state') within a given observation window g_{nsm} of length $L_g = 2W_g + 1$ (W_g is a positive integer), with respect to a statistical parameter θ if θ remains invariant in some sense (for example, constant or slowly varying) within that window. The estimates $\hat{\theta}$ of θ at time points within the observation window define an L_g-dimensional vector space denoted as $\mathbf{R}^{L_g}$, each point of which corresponds to an L_g-sample segment of the signal in the time domain. If the coordinates $\left[\hat{\theta}_1 = \hat{\theta}(k - W_g), \hat{\theta}_2 = \hat{\theta}(k - W_g + 1), \cdots, \hat{\theta}_{L_g} = \hat{\theta}(k + W_g)\right]$ of a point K in $\mathbf{R}^{L_g}$ are all equal, i.e., $\hat{\theta}_1 = \hat{\theta}_2 = \cdots = \hat{\theta}_{L_g}$, then K is referred to as a stationary point, and the corresponding signal segment $\left[x(k - W_g), \cdots, x(k), \cdots, x(k + W_g)\right]$ is considered to be locally stationary regarding θ. In contrast, points in $\mathbf{R}^{L_g}$ whose coordinates are not all equal correspond to locally non-stationary signal segments. The distance between the point K and the nearest stationary point $\mathbf{R}^{L_g}$ is mapped into the time domain, and this defines the NSM $\hat{y}(k)$ of the central time point k of the signal segment corresponding to the point K. In principle, any distance metric can be used to define the NSM as long as the metric can appropriately quantify the distance between points in the vector space. Following the definition of the p-norm, the distance $\Delta_p(K, \bar{K})$ between the point $K \in \mathbf{R}^{L_g}$ with coordinates $\left[\hat{\theta}_1, \hat{\theta}_2, \cdots, \hat{\theta}_{L_g}\right]$ and the nearest stationary point $\bar{K} \in \mathbf{R}^{L_g}$ whose coordinates are all equal to $\bar{\theta}$ can be expressed as (Xu, 2013)

$$\Delta_p(K, \bar{K}) = \left(\sum_{i=1}^{L_g} g_{\text{nsm}}(i) \cdot \left| \hat{\theta}_i - \bar{\theta} \right|^p \right)^{\frac{1}{p}} \tag{3.1}$$

where $g_{\text{nsm}}(i)$ is determined by the observation window function g_{nsm}. The coordinate $\bar{\theta}$ of $\bar{K}$ can be estimated by setting $\partial \Delta_p(K, \bar{K}) / \partial \bar{\theta}$ (i.e., the partial derivative of $\Delta_p(K, \bar{K})$ with respect to $\bar{\theta}$) to zero. By raising the distance in Equation (3.1) to power p to counteract the p th root, the NSM $\hat{y}(k)$ is obtained as

$$\hat{y}(k) = \sum_{i=1}^{L_g} g_{\text{nsm}}(i) \cdot \left| \hat{\theta}_i - \bar{\theta}_i \right|^p \quad . \tag{3.2}$$

The parameter $p > 0$ will be referred to as the order of the NSM. By definition of local stationarity, the NSM $\hat{y}(k)$ will be very small if the signal segment centred at time point k within the observation window is locally stationary regarding θ. On the other hand, its value will be large for segments that are locally non-stationary. Large values in the NSM of a signal can thus reveal presence of abrupt changes in the signal (with respect to θ), while their amplitude indicate the magnitude of the changes. Since segments that contain transients in a signal are generally characterised by abrupt changes in some statistical properties of the signal within a short period of time, the NSM output defined in Equation (3.2) can be regarded essentially as a test statistic that implements a transient detection method. By observing the NSM output of a signal at each time point, the presence and location of transients can thus be easily inferred. This will be demonstrated in Section 3.2.1.3. It should be noted that the concept of local stationarity in the NSM is different from the strict-sense stationarity (SSS) and the wide-sense stationarity (WSS) in stochastic process. Both SSS and WSS define a stationary random process by requiring multiple statistical parameters to be independent of time (Bendat and Piersol, 2010). However, in some applications, it is desirable to know the stationarity or non-stationarity of the signal regarding only a particular statistical parameter; for instance, it may be desirable to know if a signal contains a change in its mean but no change in its variance (i.e., to know if its variance is independent of time, but its mean is not). With the concept of local stationarity, the signal can be said to be stationary regarding its variance and non-stationary regarding its mean, while it is simply considered non-stationary according to the WSS or the SSS.

There are three important parameters to define when implementing the NSM transient detector: the choice of θ, observation window, and the transient detection threshold. The first two are discussed in this subsection, while the third will be discussed in the next subsection. The statistical parameter θ in the formulation of the NSM can be mean, variance, higher-order moments, even more complex statistics that can describe the signal at each time instant. Among these, only the raw moment will be considered in this work, mostly for computational ease. Specifically, for $p = 2$ (this is the only case considered in the rest of this work), the NSM $\hat{y}_r(k)$ at time point k of the signal $x(n)$ regarding its r th moment is given by (Xu, 2013)

$$\hat{y}_r(k) = \sum_{i=k-W_g}^{k+W_g} g_{\text{nsm}}(i) \cdot \left[\hat{m}_r(i) \right]^2 - \left[\sum_{i=k-W_g}^{k+W_g} g_{\text{nsm}}(i) \cdot \hat{m}_r(i) \right]^2 \tag{3.3}$$

where $\hat{m}_r(n) = \sum_{i=n-W_h}^{n+W_h} h_{\text{nsm}}(i-n) \cdot x^r(i) = \frac{1}{L_h} \sum_{i=n-W_h}^{n+W_h} x^r(i)$ is an estimate of the r th moment of $x(n)$ calculated over a sliding window h_{nsm} of length $L_h = 2W_h + 1$ (W_h is a positive integer). Because the signal to be processed is usually obtained in a single acquisition, it is assumed that the signal is

ergodic, so that the ensemble averages of θ at each time point can be replaced with the moving time averages calculated over the sliding window h_{nsm}. A computationally efficient choice for the NSM observation window g_{nsm} is a normalised rectangular window. For this choice of observation window, the NSM in Equation (3.3) is essentially the sample variance of the r th moment. It should be noted that a concave window produces a higher NSM output than a rectangular window (Xu, 2013), but it takes longer to compute and is more difficult to analyse. It is suggested to select the observation window length L_g as the duration of the transient expected to be detected. A large value of L_g makes the NSM operator less sensitive to noise, but at the cost of increased detection time and lower resolution of the peak. On the other hand, use of short windows results in inaccurate estimates of the statistical parameter and high variability of the NSM output. When the sliding and observation window lengths are equal, the height of the NSM peak depends on the amplitude of the change in the signal only and not on the actual values of L_g and L_h (Liu et al., 1995). Hence, the sliding window length L_h is set to be equal to L_g in this work.

3.2.1.2 Selection of transient detection threshold

As in all transient detection methods, the presence of a transient in a signal is inferred if the test statistic (in this case, the NSM output $\hat{y}_r$) exceeds some transient detection threshold (denoted as λ_{NSM} for the NSM transient detector) at any time point. The threshold λ_{NSM} is a major factor that determines the sensitivity of a transient detector. A robust approach proposed in this work is to set λ_{NSM} based on the concept of significance in hypothesis testing as the value such that

$$\xi = \Pr\left\{\hat{y}_r > \lambda_{\text{NSM}}\right\} \tag{3.4}$$

where $\Pr\left\{\hat{y}_r > \lambda_{\text{NSM}}\right\}$ is the survival distribution function (SDF) of the NSM output under the null hypothesis, and ξ is the probability that $\hat{y}_r$ exceeds λ_{NSM} in a locally stationary segment (i.e., in the absence of a transient in the signal). The parameter ξ will be referred to as the allowable false positive rate (AFPR). Setting the threshold based on the SDF in Equation (3.4) requires knowledge of the probability distribution of the NSM output, which to the author's best knowledge, has not been derived previously in the literature.

As shown in Appendix B, the probability distribution function (PDF) $f_{\hat{y}_r}$ of the NSM output $\hat{y}_r$ in Equation (3.3) calculated with a rectangular observation window can be obtained via a simple transformation from the distribution of the quadratic form $Y_r = \boldsymbol{\theta}^T \mathbf{M} \boldsymbol{\theta}$, where $\boldsymbol{\theta} = \left[\hat{\theta}_1, \hat{\theta}_2, \cdots, \hat{\theta}_{L_g}\right]^T$,

$\hat{\theta}_i = \hat{m}_r(i)$, $\mathbf{M} = \mathbf{I}_{L_g} - \frac{1}{L_g}\mathbf{J}_{L_g}$, $\mathbf{I}_{L_g}$ denotes $L_g \times L_g$ identity matrix, $\mathbf{J}_{L_g}$ denotes $L_g \times L_g$ matrix of ones, and the superscript ^{T} denotes the transpose operation. Specifically, the PDF of $\hat{y}_r$ is given by

$$f_{\hat{y}_r}(u) = L_g \cdot f_{Y_r}(L_g u) \tag{3.5}$$

while its SDF is given by

$$\Pr\{\hat{y}_r > u\} = 1 - \Pr\{Y_r \le L_g u\} \ . \tag{3.6}$$

A review of methods available for computing the distribution of Y_r has been carried out by Bodenham and Adams (2015). Among these methods, the saddlepoint approximation (Kuonen, 1999) is used in this work for computational efficiency. Figure 3.3(a) compares the theoretical PDF given in Equation (3.5) with the empirical PDF of the NSM output of a simulated unit-variance, zero-mean Gaussian white noise signal, taken as an example of a locally stationary signal (with respect to the second moment). The 8192-sample signal was generated using the Gaussian white noise generator function 'wgn' in MATLAB, and its NSM output was computed using normalised rectangular sliding and observation windows of length L_g = 101. The empirical PDF of the NSM output of the white noise signal was estimated using the MATLAB function 'ksdensity', which returns a probability density estimate for the input data, calculated based on a normal kernel function and evaluated at either specified input points or at equally-spaced points that cover the range of the input data. The agreement between these PDFs can be objectively assessed using distribution similarity measures, such as Jeffrey's divergence (JD), which for two probability distributions P and Q defined in the same sample space $\mathcal{X}$ is given by (Jeffreys, 1998)

$$\mathrm{JD}(P,Q) = \sum_{u \in \mathcal{X}} \left(P(u) - Q(u)\right) \cdot \log\left\{\frac{P(u)}{Q(u)}\right\} \tag{3.7}$$

where $\log\{\bullet\}$ denotes the natural logarithm. The JD is the symmetrised form of the well-known Kullback-Liebler divergence (KLD) (also called relative entropy) (Kullback and Leibler, 1951). It evaluates the variation or difference in information between two probability distributions; in other words, $\mathrm{JD}(P,Q)$ can be interpreted as some sort of loss due to using the wrong distribution Q as a model when the actual distribution is P, and vice versa. A small value of the JD implies high similarity between the distributions, while a high JD indicates that the distributions are very different. As shown in the annotation in Figure 3.3(a), the JD $JD(P_{\mathrm{th}}, P_{\mathrm{emp}})$ between the empirical distribution P_{emp} and the theoretical distribution P_{th} of the NSM output is 0.11. It is difficult to interpret this value without any baseline. Hence, for comparison, a normal distribution P_{normal} is empirically fitted on the NSM output of the simulated signal using the MATLAB function 'fitdist', which fits the specified distribution to the input data. The expected value and standard deviation of P_{normal} are given by the

mean and standard deviation of the NSM output of the simulated signal. The JD $JD\left(P_{\text{th}}, P_{\text{normal}}\right)$ between the theoretical distribution and this normal fit is evaluated as 0.92, which is almost 9 times higher than $JD\left(P_{\text{th}}, P_{\text{emp}}\right)$. These values imply that P_{emp} has a better fit with P_{th} than P_{normal}, an observation that can be confirmed via a visual inspection of Figure 3.3(a). Based on these results, it can be concluded that the derived distribution in Equation (3.5) adequately describes the NSM output under the null hypothesis, i.e., for locally stationary signals. Evaluating the value of λ_{NSM} based on the SDF given in Equation (3.6) can be computationally expensive or infeasible for a large value of L_g. Since the sample variance is inversely proportional to the sample size, λ_{NSM} can be obtained by scaling the threshold value calculated for a much smaller window size and the given AFPR. This approach is illustrated in Figure 3.3(b), which compares the NSM thresholds calculated for three different window lengths (L_g = 11, 101, and 1001) and an AFPR of ξ = 0.001. It can be observed that the value of λ_{NSM} (indicated with vertical dashed lines) indeed varies proportionately as the observation window size. However, it is important to note that in practice, the calculated threshold λ_{NSM} may have to be adjusted appropriately to account for other factors, especially level of typical operational transients. In the next section, the effectiveness of the NSM-based transient detector is investigated using numerical simulations.

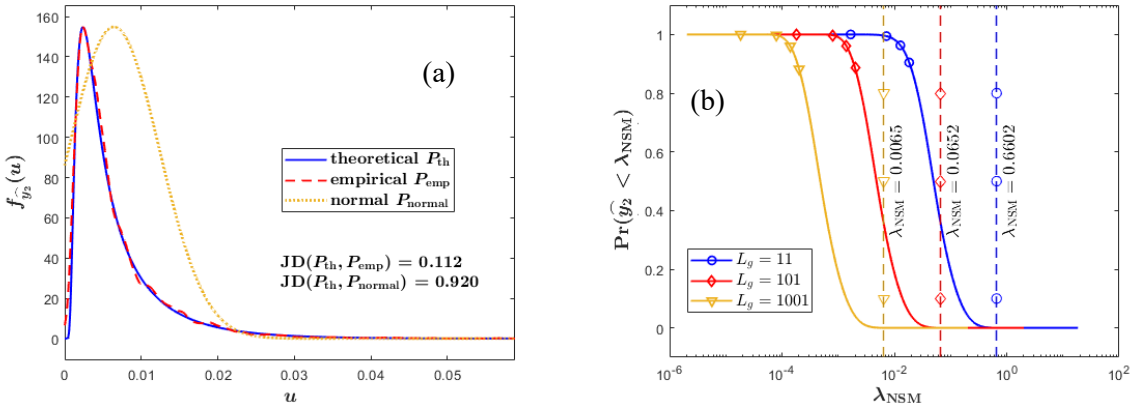

Figure 3.3: Probability distribution of the NSM output. (a) Theoretical PDF (Equation (3.5)), empirical PDF, and normal fitted PDF obtained for a simulated white Gaussian noise signal. (b) Theoretical SDF (Equation (3.6)) computed for L_g = 11, 101, 1001 and ξ = 0.001.

3.2.1.3 Evaluation of the performance of the non-stationarity measure transient detector

To evaluate the performance of the NSM operator as a transient detector, trials were conducted using datasets consisting of simulated white Gaussian noise signals in which measured acoustic transients have been inserted at a known time point. The objective was to create time series with controllable 'SNRs' by adding the background noise and transient together at variable levels. In order to allow for interpretation and comparison of results in these trials, the 'SNR' of the signal will be defined as the

ratio of the mean square value of the inserted transient to the variance of the simulated noise. This provides a simple means to characterise the *strength* of the transient relative to the noise, with a higher 'SNR' implying a 'stronger' transient that is easier to detect.

Figures 3.4(a.i) and 3.4(b.i) show the time histories of signals measured on the leakage test rig during leak simulation and when the pipe is hit with a metallic rod, respectively. The vertical dashed lines indicate the onset and end of the leak and active transients determined by visual inspection. Note that the presence of noise tends to obscure the exact onset and end of the transient in the original signal, thus making it difficult to extract only the transient portions. Figures 3.4(a.ii) and 3.4(b.ii) show the time histories of the 30-second-long noise signals to which the extracted transients have been added at the 12-second mark. The 'SNR' of the resulting signals is -3 dB. Although the presence of the transients is completely masked by noise in the time histories, they are successfully detected by the NSM operator as indicated by the peaks in the NSM outputs $\widehat{y}_2$ shown in Figures 3.4(a.iii) and 3.4(b.iii). Examination of these NSM outputs reveals some interesting observations. Firstly, the NSM peak actually consists of two close but separate peaks (marked with black diamond markers in Figures 3.4(a.iii) and 3.4(b.iii)). These peaks are associated with the transition of the signal from a stationary state to a transitory state, and vice versa. The location of the first peak coincides with the onset of the transient in the signal, while the second peak denotes the end of the transient as the signal transitions back to a steady state. Note the NSM output peak will be unimodal in the case of very short transients. Secondly, the width of the NSM peaks is dependent on the selected window length. The two peaks are one observation window length apart. A large mismatch between the duration of the transient and the window length results in wider peaks, and this may decrease the accuracy of estimating the transient boundaries. This effect becomes more substantial if the selected window length is significantly longer than the transient duration. Thirdly, the heights of the NSM peaks give a rough indication of strength of the transient relative to the background noise. As already stated, since the lengths of the observation and sliding windows are equal, the amplitude of the NSM output is determined solely by the change in the statistical parameter (in this case, the second moment). This provides a way to quantify the strength of a detected transient (relative to the background noise) by simply observing the prominence of the NSM output peak. For two transients measured in the same background noise, the NSM peaks corresponding to the stronger transient will be higher. Based on these observations, it can be seen that the NSM not only detects the presence of a transient, but also provides an indication of both its location and magnitude. This feature can be exploited for the leak confirmation step in the algorithm.

To examine the performance of the NSM transient detector in terms of detection power (detection rate) P_D and AFPR ξ, two tests were conducted using the generated datasets. In the first test, the transient detection rate P_D was calculated for 'SNR' values between -10 and 6 dB with ξ fixed at 0.001. In the second test, P_D was calculated at a fixed 'SNR' value of -4 dB while varying ξ.

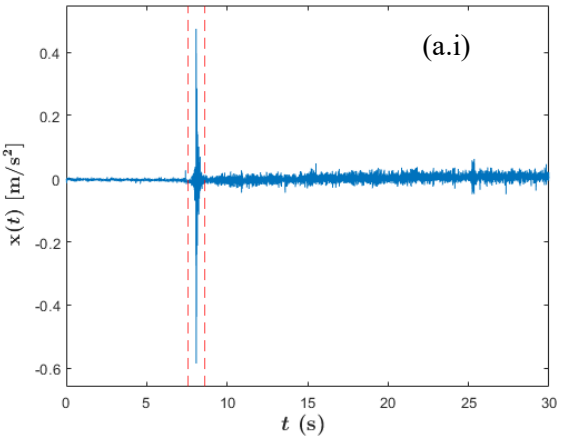

(a.i) Time history of signal with leak transient measured on the leakage test rig.

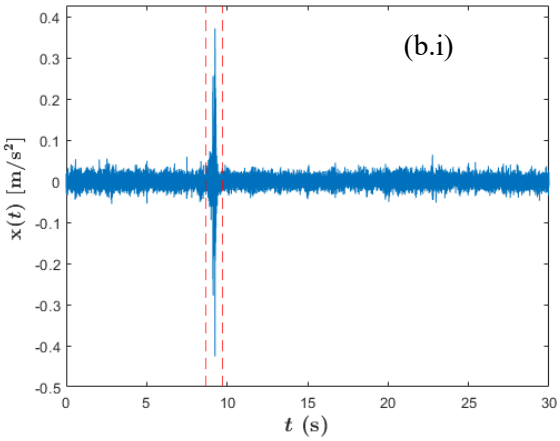

(b.i) Time history of signal with active transient measured on the leakage test rig.

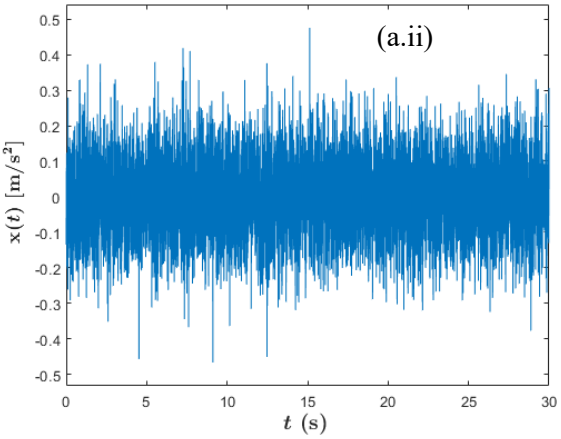

(a.ii) Time history of simulated white noise signal with transient from (a.i) inserted.

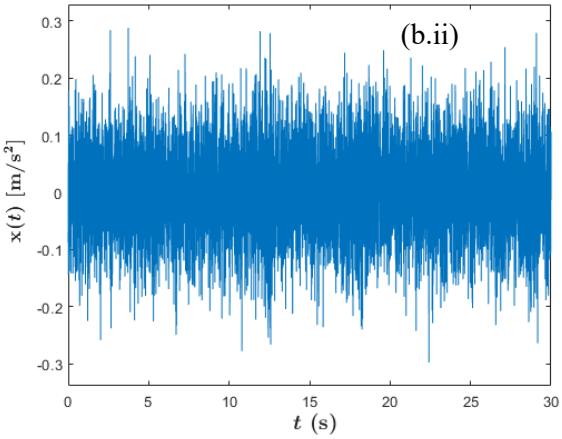

(b.ii) Time history of simulated white noise signal with transient from (b.i) inserted.

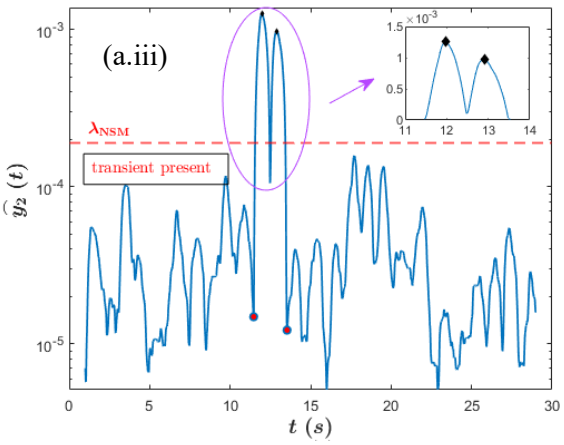

(a.iii) NSM output of signal in (a.ii).

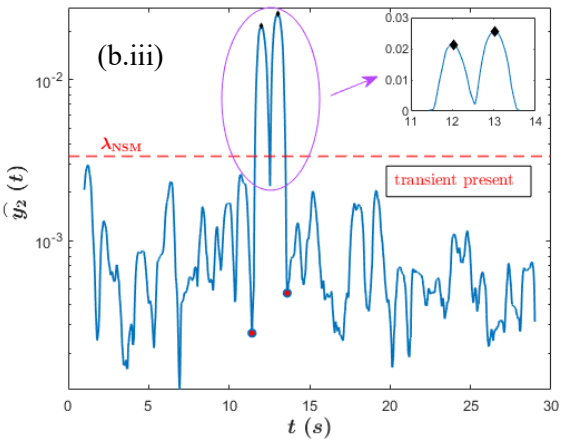

(b.iii) NSM output of signal in (b.ii).

Figure 3.4: Computing the NSM of the generated time series. (a) Signal with leak transient. (b) Signal with active transient. The red horizontal dashed lines indicate the transient detection thresholds λ_{NSM} calculated using an AFPR of 0.001. The black diamond markers indicate the NSM peaks, while the red dots mark the 'feet' of the NSM, i.e., the points at which it starts to rise towards or falls off from the peak.

For comparison, the results obtained using the GLD are also presented. The GLD detection threshold λ_{GLD} was calculated based on a normal approximation of the chi-squared distributed test statistic of the GLD (for details, see White (1996)). A typical GLD test statistic is shown below in Figure 3.6(b). The lengths of the NSM windows and the GLD test window were both set to the duration of the extracted transient, while the GLD reference window was twice as long. Note that unlike the GLD threshold λ_{GLD}, the NSM detection threshold λ_{NSM} varies depending on the level of background noise since it relates to the properties of the stationary portions of the signal. The results obtained in the first test over 100 trials at each 'SNR' are shown in Figure 3.5(a), while the results from the second test are summarised in the form of the receiver operating characteristic (ROC) curve in Figure 3.5(b). The robustness of the transient detection methods is indicated by the 'SNR' detection threshold, which is defined as the lowest 'SNR' at which a 100% detection rate is achieved. The NSM achieves an 'SNR' detection threshold of -3 dB compared to -1 dB for the GLD. Both 'SNR' detection thresholds are negative, indicating that the detectors work at levels below the background noise level. They achieve similar performance above -1 dB possibly because they are both based on estimation of the same statistical parameter (the second moment). Below this 'SNR' value, the NSM outperforms the GLD, as shown by the ROC curve.

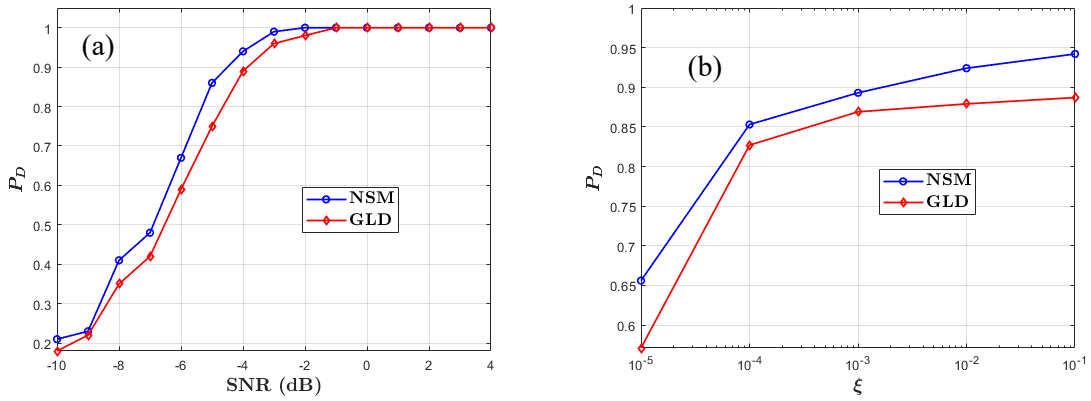

Figure 3.5. Detection rate of NSM and GLD transient detectors vs (a) 'SNR'. (b) AFPR.

Figure 3.6(a) compares the root-mean square error (RMSE) of transient onset values T_{onset} estimated from the NSM and GLD test statistics. Analogously to its definition for the NSM, the transient onset is taken as the time corresponding to the maximum of the GLD test statistic (marked with red dot in the GLD output in Figure 3.6(b)). Only values from cases where the transient was successfully detected have been included in the calculation. The RMSE $\text{RMSE}(\theta)$ of the estimates of a quantity θ obtained over N_s simulation runs is defined as

$$\text{RMSE}(\theta) = \sqrt{\frac{1}{N_s}\sum_{i=1}^{N_s}\left(\hat{\theta}_i - \theta_{\text{true}}\right)^2} \tag{3.8}$$

where $\hat{\theta}_i$ is the estimate from the *i*th run, and θ_{true} is the true value. It denotes the variability in the estimates around the true value. The transient onset detected by the NSM operator is closer to the true value of 12 seconds at all 'SNR' values than the GLD onset estimates. In fact, the T_{onset} values estimated from the NSM outputs are practically exact for 'SNR' values greater than -4 dB. On the other hand, the GLD estimates exhibit higher variability even at high 'SNR' values. Due to its ability to track local value of the statistical parameter, the NSM can precisely locate the point at which a drastic change or transition occurs in a signal. This can be confirmed by comparing the resolution of the peaks in the NSM and GLD outputs in Figures 3.5(b.iii) and 3.6(b). While the extremum of the NSM output is sharp, the peak of the GLD output is more spread out, making it difficult to unambiguously locate its exact position. High transient onset detection accuracy is one of the advantages that make the NSM suitable for implementing the passive transient leak detection method. In fact, this property makes the NSM-based transient detector a particularly attractive option in applications where accurately determining the start and end of a transient is important. A particularly relevant and useful example of such application is the analysis of pressure transients in transient pressure loggers (Hossein et al., 2022).

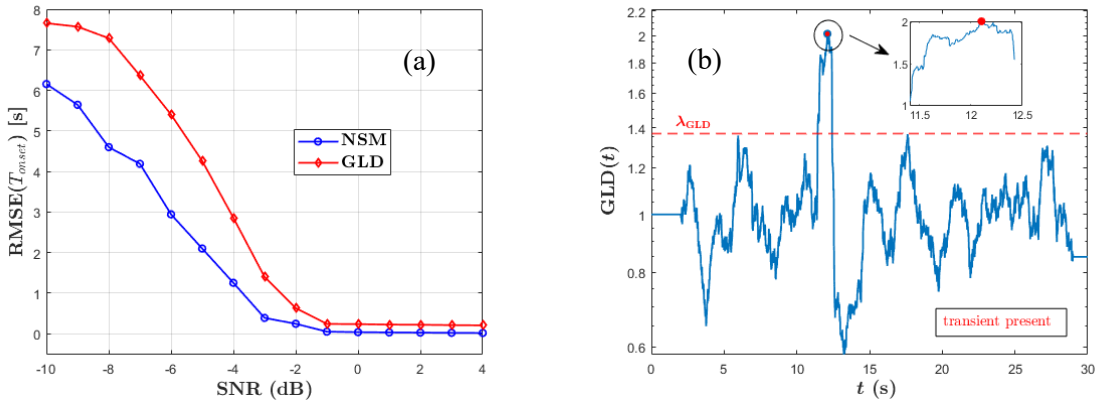

Figure 3.6: Comparison of transient onset detection accuracy. (a) NSM and the GLD onsets. (b) GLD output. λ_{GLD} is the GLD transient detection threshold.

It is important to note some limitations that must be considered when interpreting or generalising the results of the study above. The results have been obtained under the idealised condition in which the background noise is assumed to be white and Gaussian. However, this may not be a realistic assumption for some measurement environments, in which case, the transient detectors will be less effective than suggested by these results. Like other transient detectors based on a GLRT, the performance of the GLD is strongly dependent on the assumed distribution of the signals being satisfied. Since the GLD assumes a Gaussian distribution for the background noise under the null hypothesis, its performance is likely to degrade in the case of non-Gaussian noise. On the other hand, the distribution of the signals is not relevant to the formulation of the NSM, and this can offer practical benefits in situations where the background noise is non-Gaussian but locally stationary regarding a

given statistical property. Another factor to consider when generalising the reported results is that the term 'transients' is used to denote a wide range of acoustic events (White, 1996), which may not necessarily conform to the concept of transients used in the simulation. As such, the transient test signals used in the simulation studies may not be representative of *all* types of acoustic transients obtainable in water distribution networks. The performance of the transient detectors may vary for different classes of transients, and largely depends on the selection of parameters, for example, statistical feature and window lengths. Improvement in their performance for particular classes of transients may be possible by varying the selected parameters. Good choice of parameters can either be derived from a careful study of background noise characteristics or by executing a multi-parametric process and selecting the combination with the best results for noise and leak measurements. Further validation on signals acquired in different real water distribution networks is, therefore, recommended. Nonetheless, the ability of the NSM to achieve a better performance than an 'optimal' detector, albeit in an idealised situation, demonstrates its viability and effectiveness for transient detection. The NSM will be employed to detect acoustic transients in experimental signals in Section 3.4.

3.2.2 Acoustic transient leak confirmation

After detecting and locating acoustic transients in the measured signals, the next step in the passive transient leak detection method is to confirm whether the detected transients are due to a leak occurrence, i.e., whether they are leak or active transients. To illustrate the difference between these two types of transients, a signal containing an active acoustic transient is examined using the same approach as in Section 3.1. Figure 3.7 shows the spectrogram of the signal whose time history is shown in Figure 3.4(b.i) above. It is difficult to distinguish the type of transients present in a signal from the time histories only. On the other hand, the spectrograms give a clear indication of the differences between the two transients (compare Figure 3.7 and Figure 3.1(b)). As shown in Figure 3.7, the changes in the signal spectrum induced by an active transient are momentary, lasting only as long as the transient event. Based on the similarity of the spectrum before and after the transient, it can be inferred that that the signal returns to its previous *steady state* after the transient has subsided. In contrast, the spectrogram in Figure 3.1(b) indicates that a leak transient induces *sustained* changes in properties of the signal, thereby resulting in a new steady state. Thus, the changes induced in the measured signals by an acoustic transient are either *sustained* or momentary, depending on the nature of the transient. This observation provides a straightforward way to distinguish between leak and active transients, to infer the presence of a leak. Specifically, *statistically significant* difference between the steady states before and after a transient segment indicates the presence of a new signal source, which may be a leak.

Based on this discussion, the leak confirmation step can therefore be considered the problem of determining whether the steady states before and after the transitory segment in the signal are *homogeneous* as defined in the NSM formulation, i.e., the segments correspond to the same value of

the statistical parameter. It can be implemented in three different ways: using the NSM, as a statistical test, and using the steady-state method proposed in Section 3.3. The procedures for the first two approaches are described as follows. In the NSM-based implementation, the transient portion corresponding to the signal segment between the 'feet' of the NSM peaks (marked with red dots in Figures 3.4(a.iii) and 3.4(b.iii) above) are removed, leaving only the stationary segments before and after the transient event. Then the NSM of the modified signal is calculated. If the steady states before and after the transient event are *inhomogeneous*, a distinct peak will be observed in this NSM output at the transition point between the previous and new steady states. Due to the finite duration of the transitory state (if it exists), the peak in the new NSM output may not occur exactly at the transition point but within its neighbourhood. Hence, new peaks should be searched for within a region, half an NSM window length on either side of the transition point. This region will be referred to as the *transition zone*. The presence of a distinct and prominent peak in the transition zone indicates the detected transient in the signal is potentially due to a leak event.

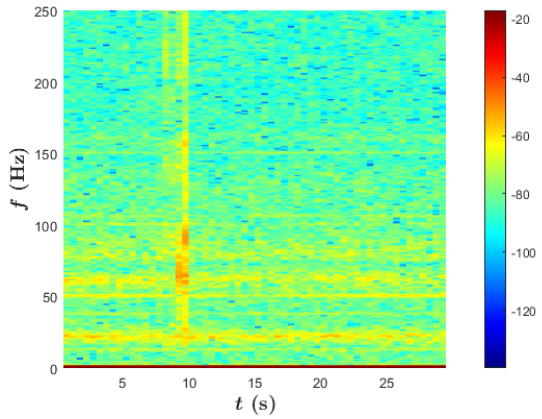

Figure 3.7: Spectrogram of an acceleration signal containing an active transient. Unit is dB.

The alternative approach for implementing the leak confirmation step is to design a statistical test on the signal segments preceding and succeeding the transient event. The purpose of the test is to infer whether there is a *statistically significant* difference in the properties of the measured signals before and after the occurrence of the acoustic transient. Examples of such tests include F-test of equality of variances (Snedecor and Cochran, 1989), Bartlett's test (Bartlett, 1937), Levene's test for homogeneity of variance (Levene, 1961), and Brown-Forsythe test (Brown and Forsythe, 1974). These tests are used to check if multiple data samples have equal variances, against the alternative that at least two of the data samples do not have equal variances. Levene's and Brown-Forsythe tests are less sensitive to departures from normality than the F-test and Bartlett's test (NIST, 2012). The test statistic W_B in these two tests is calculated as (Brown and Forsythe, 1974)

$$W_B = \frac{(N_B - k_B)}{(k_B - 1)} \cdot \frac{\sum_{i=1}^{k_B} N_{Bi} (Z_{i\cdot} - Z_{\cdot\cdot})^2}{\sum_{i=1}^{k_B} \sum_{k=1}^{N_{Bi}} N_{Bi} (Z_{ik} - Z_{k\cdot})^2} \tag{3.9}$$

where $k_B = 2$ is the number of signal segments being considered; $N_{\mathrm{B}i}$, $i = 1, 2$, is the number of samples in the i th segment; N_B is the total number of samples in all segments; $Z_{ik} = \left| Y_{ik} - \tilde{Y}_{i\cdot} \right|$, Y_{ik} is the value of the k th sample from the i th segment, $\tilde{Y}_{i\cdot}$ is a measure of the spread within the i th segment (for example, the mean or median of the segment); $Z_{i\cdot} = \frac{1}{N_{\mathrm{B}i}} \sum_{k=1}^{N_{\mathrm{B}i}} Z_{ik}$ is the mean of the Z_{ik} for the i th segment; and $Z_{\cdot\cdot} = \frac{1}{N_B} \sum_{i=1}^{k_B} \sum_{k=1}^{N_{\mathrm{B}i}} Z_{ik}$ is the mean of all Z_{ik}. The test statistic W_B is approximately F-distributed with $k_B - 1$ and $N_B - k_B$ degrees of freedom. If the resulting p-value p_v is less than the selected significance level α (set to a default value of 0.01 in this work), the null hypothesis is rejected. In other words, it is concluded that the two steady states are *inhomogeneous* or significantly different with respect to the variance or second moment if

$$W_B > F_{1-\alpha,\, 1,\, N_B - 2} \tag{3.10}$$

where $F_{1-\alpha,\, 1,\, N_B - 2}$ is the upper critical value of the F distribution with 1 and $N_B - 2$ degrees of freedom at a significance level of α. In this case, the presence of a leak transient is inferred. Conversely, if p_v is greater than α (i.e., $W_B \leq F_{1-\alpha,\, 1,\, N_B - 2}$), the two states are considered to be *not* significantly different, and the detected transient is considered an active transient. The only difference between Levene's and Brown-Forsythe tests is the choice of $\tilde{Y}_{i\cdot}$ in the calculation of the test statistic in Equation (3.9): Levene's test uses the mean whereas Brown-Forsythe test uses the median. Although the optimal choice of $\tilde{Y}_{i\cdot}$ depends on the distribution of the underlying data, the definition based on the median is recommended as the choice that provides good robustness against many types of non-normal data while retaining good statistical power (Derrick et al., 2018). Based on its comparatively higher stability against deviation of the underlying data from normality, the Brown-Forsythe test is selected for use in the leak confirmation step in this work. The Brown-Forsythe test as well as the other tests listed above are available in the MATLAB function 'vartestn', which returns the value of the test statistic, the number of degrees of freedom, and the p-value. These tests are only suitable for assessing the homogeneity of the signal segments with respect to the variance or second moment. If the NSM transient detection step is implemented using a different statistical property, then it is necessary to consider alternative more appropriate tests.

In order to reduce incidents of false alarm, a leak alert is issued in the passive transient leak detection algorithm only if at least two of the three approaches (NSM-based approach, statistical test, and steady-state method) give positive inferences. It is important to note that the presence of a new persistent background noise source can also lead to a sustained change in the steady states of the measured signal. An additional check may therefore be necessary to account for such non-leak signal

sources that could change the signal state temporarily but long enough not to be rejected by the leak confirmation process described above. This additional check can be carried out some set period after the potential leak alert is triggered. If within this period, the steady-state value of the statistical parameter becomes equal to the previous steady-state value, the leak trigger event is classified as a false alarm. The time before the additional check has to be configured to apply to the particular pipe system under consideration. After the presence of a leak is confirmed, its location can be obtained using any applicable leak localisation method, including the methods proposed in Chapters 4 and 5. The proposed passive transient leak detection method will be demonstrated using experimental signals in Section 3.4.

3.3 Acoustic leak detection by steady-state analysis

As demonstrated in Section 3.1, leak and background noise signals exhibit differing properties, so by examining features in the measured signals, inference can be made about the presence of a leak. Existing leak detection methods based on this principle include acoustic noise logging, RMS-based method (Kampelopoulos et al., 2021), and standard-deviation-based method (Martini et al., 2015). In these methods, the presence of a leak is inferred when some property of the measured signal, for example, amplitude, RMS, or standard deviation, exceeds a given threshold. With such methods, a leak event is considered an outlier that can eventually be detected via time-domain analysis of long-term measurements. Some disadvantages of these methods can be highlighted. They require either multiple measurements made over several nights (acoustic noise logging and standard-deviation-based method) or continuous measurements over a long period of time (RMS-based method). Hence, their applicability may be limited in situations where practical constraints preclude capability for long-term measurements. Moreover, leak-free reference measurements acquired before the occurrence of the leak may not always be available. Furthermore, in the presence of significant noise levels, the presence of a leak may not be obvious from time-domain features. This is one of the reasons why acoustic noise logging is generally ineffective during the day.

Based on the results in Section 3.1, the spectrum of leak signals generally displays characteristic frequency content and spectral shape clearly distinguishable from the background noise, thus allowing leak detection in the frequency domain. Therefore, an alternative method based on spectral features is considered for acoustic leak detection in this section. Such a steady-state method has the potential to deal with the shortcomings of the existing time-domain methods mentioned above. The basic principles of the method, referred to as *passive steady-state leak detection method* in this thesis, are described in the next subsection.

3.3.1 Description of the passive steady-state leak detection method

The general algorithm of the passive steady-state leak detection method that incorporate spectral features is shown in Figure 3.2. In this method, acoustic leak detection is viewed as a signal detection problem, the main objective of which is to distinguish a potential leak event from normal operating noise by characterising the shape and variation of the spectrum of acoustic/vibration signals via the use of appropriate spectral descriptors. The method involves the following main steps:

1. The measured signals are pre-processed to remove any transient perturbations present. This excludes events that may cause momentary changes in the signals, ensuring that only stationary (steady-state) parts are taken into account while analysing the signals for a leak. Removal of transient perturbations can be achieved using the first step in the NSM leak confirmation step described in the preceding section.

2. Appropriate filters may be applied to ensure only frequency regions where the leak noise is likely to be dominant over the background noise are included in calculating spectral descriptors. If at least two sensors are present, then the cut-off frequencies of the filter can be selected using either the coherence or the CPS criterion mentioned in Section 1.2.3. The latter is recommended as it appears to be more robust, especially when resonances are present in the signals. If only one sensor is available, then the cut-off frequencies may be set based on historical data or measurements on similar pipes (if available). This step is optional.

3. Selected spectral descriptors are calculated from the PSDs. Prior to calculating the spectral descriptors, frequency-domain artefacts not related to the leak, such as mains harmonics and resonances, should be removed from the PSDs using notch filters. Selection of spectral descriptors should be based on the relative difference in their values for background noise and leak signals. The spectral descriptors that exhibit the highest relative difference in their values for background noise and leak signals are likely to be the best indicators of a leak, so they should be selected for implementing the passive steady-state leak detection method.

4. The presence or absence of a leak is then inferred based on the value of a leak detection metric (LDM) computed by combining weighted values of the descriptors. Definition of the LDM depends on the selected descriptors and their expected values. If the LDM exceeds a given threshold, then the presence of a leak is inferred. An example for defining this metric and its threshold is included in the next subsection. As indicated in Figure 3.2, time-domain features can also be considered when defining the LDM in order to improve the robustness and reliability of the passive steady-state leak detection method.

As already mentioned in Section 3.2.2, this steady-state method can be used to confirm the presence of a leak after the acoustic transient detection step in the passive transient leak detection method. The steady-state method can be adapted for continuous or real-time monitoring by calculating

the spectral descriptors and LDM over a sliding window. This ensures the capability to detect leaks as they occur. It should be noted that this method is not intended for leak localisation. Once a leak is detected, it may be located using the cross-correlation technique. Factors that must be taken into account when implementing the proposed method, including selection of spectral descriptors, sensor placement, and leak detection inference, are briefly discussed in the next subsection.

3.3.2 Important considerations in the passive steady-state leak detection method

As already stated in Section 3.1, a variety of signal features can be used to characterise the measured signals in the time and frequency domains. The selection of spectral descriptors can be based on the following considerations. The background noise will tend to be dominated by low frequencies and 'flatten' out at higher frequencies. This assertion is supported by experimental evidence in this thesis and other studies (see Martini et al. (2015)). In the ideal situation where the background noise is a white noise process, the noise PSD will be flat, having almost the same energy in all frequency bands. On the other hand, leak signals propagating in the pipe is modified by the pipe FRF, and its PSD will have a characteristic shape due to the filtering nature of the pipe (Gao et al., 2004). Therefore, spectral descriptors that characterise the shape or variation of the signal spectrum can be employed to distinguish the presence of a leak, for example, spectral flatness, spectral flux, spectral kurtosis, and spectral skewness. One important factor to consider is the choice of frequency bands to include in the computation of the spectral descriptors. Since background noise generally dominates at low frequencies and the high frequencies are severely attenuated by the pipe, the very low and high frequencies should be excluded from the calculation. In fact, it is recommended that only frequency bands that fall within the passband of the applied filter (if any) should be included in the calculation. It is also important to exclude frequencies above the cut-off frequency of the anti-aliasing filter of the DAS, as these frequencies are naturally suppressed prior to sampling by the DAS. When possible, appropriate spectral descriptors should be selected based on a preliminary study of noise spectra obtained in the measurement environment. If included in the implementation of the algorithm, time-domain features can be selected based on their sensitivity to the presence of leak signals (possibly based on preliminary studies or historical data). For example, the shape factor appears to be very sensitive to the presence of leaks on the leakage test rig and can therefore be considered for inclusion in the steady-state method. In contrast with spectral descriptors, appropriate time-domain features are more likely to differ for different measurement environments.

An important aspect of the leak detection method is the placement of the acoustic/vibration sensors. The spectral signature of signals from a leak may be obvious or more subtle at different sensor locations due to different local geometries and spectral response of pipe-sensor system. Signals acquired closer to the leak are more likely to exhibit more distinguishable spectral variations indicative of the leak. Conversely, if the sensor is too far away from the leak, the sensor may be unable to detect that specific leak. The spacing between sensors should, therefore, not be too large (less than 100

metres) to allow for the effective detection of leaks along the whole pipeline. This distance represents the effective leak detection range of acoustic methods in plastic pipes (Covas et al., 2006). In practice, however, in addition to economic constraints, sensor placement may be limited by the unavailability of access points.

Leak detection inference in the proposed steady-state method is simply based on the value of the LDM; in other words, the presence of a leak is inferred if the LDM exceeds an appropriate threshold. A suggested approach is to define the LDM in such a way that its value is close to unity for background noise measurements but *substantially* greater than unity in the presence of a leak. What denotes a substantial difference from unity is somewhat *subjective* and may have to be defined separately for each pipeline and measurement environment. An example is provided in this subsection to illustrate the suggested approach for defining the LDM. Based on the results obtained for measurements on the leakage test rig (see Tables 3.1 and 3.5), the spectral features that exhibit the highest relative difference (on average) between noise and leak signals are spectral flatness ϖ_{flat}, spectral flux ϖ_{flux}, spectral kurtosis ϖ_{kurt}, and spectral skewness ϖ_{skew}. In the presence of a leak, the spectral flatness of the measured signal decreases, whereas the other three descriptors increase. This suggests the following definition for the LDM:

$$\mathrm{LDM} = \frac{1}{\Lambda_{norm}} \cdot \frac{\left[\varpi_{flux}\right]^{w_1} \cdot \left[\varpi_{skew}\right]^{w_2} \cdot \left[\varpi_{kurt}\right]^{w_3}}{\left[\varpi_{flat}\right]^{w_4}} \tag{3.11}$$

where w_1, w_2, w_3, w_4 are weights assigned to the spectral descriptors, and Λ_{norm} is a normalisation factor that ensures that the LDM has a value close to unity for noise-only measurements. The weights are selected such that they sum to unity, and the normalisation factor is defined based on the average values of the spectral descriptors for background noise signals. An advantage of the LDM form in Equation (3.11) is that it provides the possibility of controlling the relative importance given to each spectral descriptor. Spectral descriptors that are more sensitive to the presence of a leak in a given system can be assigned a higher weight. Determining appropriate values of the weights and normalisation factor can be based on a preliminary study of leak signals and background noise acquired in the same or similar measurement environment. If noise-only measurements are not available, then the normalisation factor may be set to 1; however, this may reduce the reliability of leak detection. It should be noted that in principle a different definition of the LDM can be employed as long as it properly quantifies the difference between leak and noise-only measurements as well as ensures that LDM achieves a value close to unity for the latter and a substantially high value for the former. The LDM can also be used to indicate the efficiency of leak detection and leak detectability—the larger the LDM, the more detectable the leak and the more efficient the leak detection algorithm. As already stated, in order to improve the reliability of leak detection results, it may be beneficial to either include some time-domain features in defining the LDM or define an additional LDM involving

only time-domain features. For example, in the leakage test rig, the RMS, shape factor, crest factor, and clearance factor appear to be quite sensitive to the presence of a leak (see Tables 3.1 and 3.5). Another important factor to consider is the LDM threshold. While the LDM has been defined in such a way that its value is close to unity for noise measurements and greater than unity for leak signals, it is still important to set the threshold greater than unity to reduce the incidents of false alarms. The availability of leak-free noise signals can help in improving the reliability and objectivity of the method. Such reference noise signals can be used to study the noise spectral characteristics in order to set a more robust threshold for the LDM. In the absence of such measurements, it is still possible to detect the presence of a leak, as values of the selected descriptors in leak signals are likely to differ substantially from those *expected* for noise-only signals. Further refinement in this regard is likely to make the method more robust for practical application. The effectiveness of the proposed leak detection methods will be evaluated using experimental signals in the next section.

3.4 Experimental results and discussion

The two acoustic leak detection methods proposed in this chapter were employed to detect leaks in the leakage test rig described in Chapter 2. Datasets consisting of signals acquired simultaneously using hydrophones and accelerometers on the leakage test rig were analysed to evaluate the effectiveness of the methods. The signals were measured at X1, X2, X3, and sometimes one additional point located 2 metres from X3 (which will be denoted as X4). The datasets are divided into four different categories based on the type of signals they contain. The first dataset category includes only background noise signals, while the second dataset category consists of signals containing leak transients generated by opening the leak valve at L1. On the other hand, the signals in the third dataset category contain active transients induced by hitting the pipe with a metallic rod in the presence of an ongoing leak at L1 or L2. The fourth dataset category consists of steady-state leak signals acquired with leaks simulated at L1 or L2. There are 10 datasets in each category, and each signal was acquired at a sampling rate of 40 kHz using the procedures outlined in Section 2.4. The measurement duration ranged from 30 to 60 seconds.

3.4.1 Experimental investigation of the passive transient leak detection method

The passive transient leak detection method was applied to the datasets described above. One representative result for each of the four dataset categories is first presented, then the results for all available datasets are summarised at the end of the subsection. Figure 3.8 shows the time histories and 1-second NSM outputs of accelerometer signals from each dataset category acquired at two different locations. It can be observed that the NSM successfully detects and locates the acoustic transients in the signals from the second and third dataset categories, while correctly inferring the absence of transients in the noise-only and steady-state leak signals. Also, transients acquired at locations closer

(a) Background noise signals measured at X1 and X3.

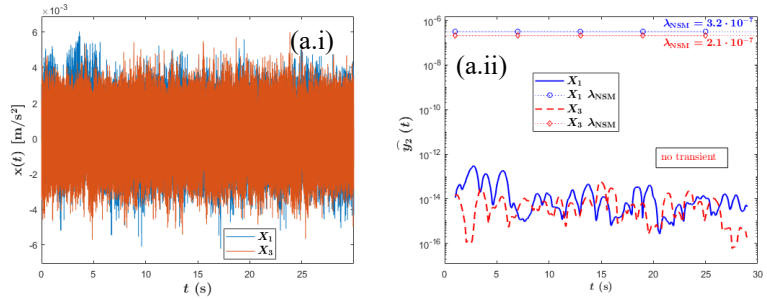

(b) Signals with leak transients induced by opening valve at L1. Measured at X1 and X2

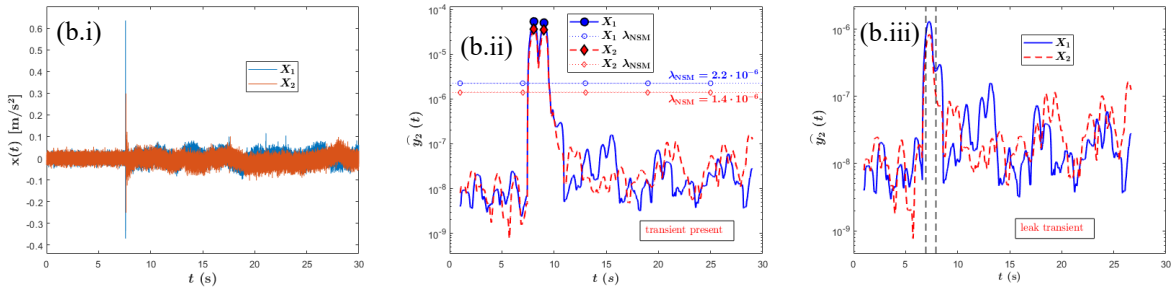

(c) Signals with active transients induced by hitting the endcap close to X3 in the presence of a leak at L2. Measured at X1 and X3

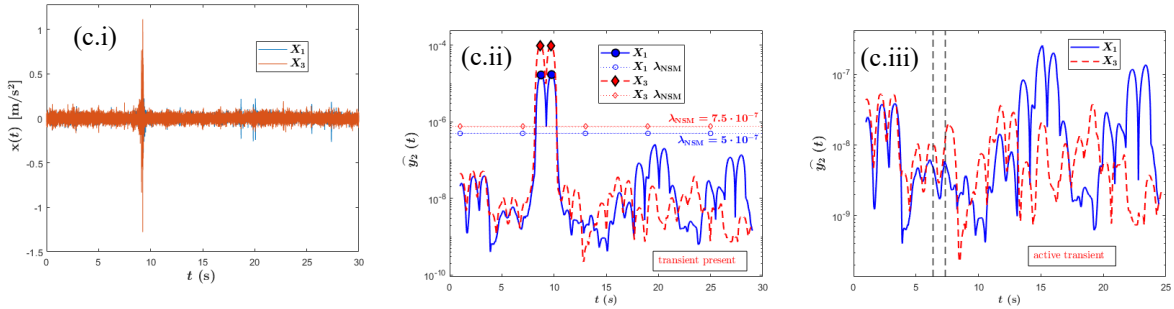

(d) Steady-state leak signals measured at X1 and X3 in the presence of a leak at L1.

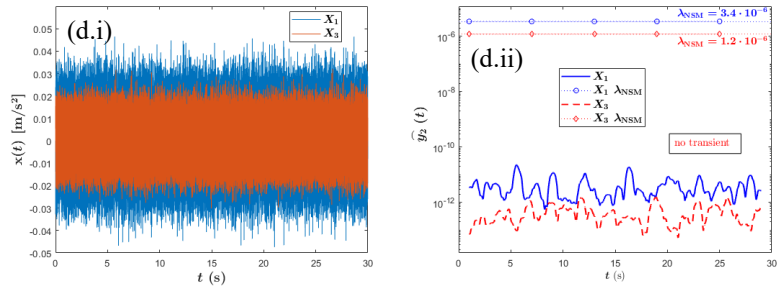

Figure 3.8: Computing the NSM of experimental signals: (i) Time histories of the measured signals. (ii) NSM outputs of whole signals. (iii) NSM outputs of steady-state segments. The dashed horizontal lines denote the NSM transient detection thresholds corresponding to an AFPR of 0.001, while the filled dot and diamond markers denote the NSM peaks. The vertical dashed lines in (b.iii) and (c.iii) indicate the transition zones.

to the transient source correspond to NSM peaks with higher magnitude. Figures 3.8(b.iii) and 3.8(c.iii) show the NSM outputs of the signals in the second and third dataset categories (i.e., signals with leak transients and signals with active transients) after the transient sections have been removed. The transition zones for the signals are indicated with vertical dashed lines in the NSM outputs. Based on the presence of a distinct peak in the transition zone in Figure 3.8(b.iii), the presence of a leak transient in the signals from the second dataset category can be inferred. On the other hand, the absence of a peak in the transition zone in Figure 3.8(c.iii) shows that the transients in the signals from the third dataset category are not due to a leak. Table 3.2 displays the results of the Brown-Forsythe test applied to signal segments before and after the transients in the signals from the second and third dataset categories. For the signals with leak transients, the test statistic exceeds the critical value $F_{1-\alpha,\,1,\,N_B-2}$ = 6.63, whereas it is less than this value in the case of the signals with active transients. These results thus affirm the conclusions from the NSM outputs.

Table 3.2: Parameters and results of Brown-Forsythe test applied to the steady-state portions—before and after the transients—of the experimental signals with leak and active transients.

Signal	**Measurement point**	N_B	p_v	W_B	$F_{1-\alpha,\,1,\,N_B-2}$	**Inference**
Signal with leak transients	X1	1065093	5.60E-43	191.13	6.63	Reject null hypothesis
	X2	1066718	8.51E-05	15.45	6.63	Reject null hypothesis
Signal with active transients	X1	1099687	0.029	4.80	6.63	Do not reject null hypothesis
	X3	1079843	0.285	1.14	6.63	Do not reject null hypothesis

After the presence of a leak has been confirmed in the signals from the second dataset category, the leak was located via the cross-correlation technique using the time delay ΔT_{onset} = 9.8 ms given by the difference between transient onsets in the NSM outputs of the signals. Since the distance between the two sensors is d = 5.5 metres and acoustic propagation speed in the pipe is c = 354 m/s (experimentally determined in Section 2.3.2), Equation (1.1) yields the leak location as $\hat{d}_1$ = 1.02 metres from X1. This value represents an absolute error of 0.15 metres in the leak location estimate. Alternatively, since the signal segments after the leak transients are steady-state signals from the leak, the leak location can be calculated via the conventional cross-correlation technique. In this case, the time delay estimate obtained by cross-correlating the steady-state signal segments after the transients is $\hat{\tau}_{\text{peak}}$ = 9.4 ms, resulting in a more accurate leak location estimate of $\hat{d}_1$ = 1.10 metres.

A cross-section of the successful and unsuccessful detection results for all the dataset categories are shown in Table 3.3. Only one entry is presented for the first and fourth dataset categories (i.e., the background noise and steady-state leak measurements) because the NSM transient detector yields

Table 3.3: Cross-section of experimental results for passive transient leak detection. In the 'Sensor' column, 'hyd' and 'acc' indicate hydrophone and accelerometer, respectively. $\hat{d}_1$ indicates the estimated distance of the leak from X1 calculated using ΔT_{onset}.

Dataset category	**Transient source**	**Sensor**	**Measurement location**	**Transient visibility in time history**	**Transient detection**	**Leak confirmation**	$\hat{d}_1$ **(m)**
1 and 4 (noise and steady-state signals)	-	hyd / acc	X1	low	No	-	-
			X2	low	No	-	
			X3	low	No	-	
2 (signals with leak transients)	Leak at L1	hyd	X1	high	Yes	Yes	1.02
			X2	high	Yes	Yes	
			X3	low	No	-	
	Leak at L2	acc	X1	high	Yes	Yes	1.10
			X2	high	Yes	Yes	0.98
			X3	low	Yes	No	0.89
			X4	high	Yes	Yes	
	Leak at L2	acc	X1	high	Yes	Yes	1.10
			X2	high	Yes	Yes	
			X3	low	No	-	
3 (signals with active transients)	Impact at elbow	acc	X1	high	Yes	No	-
			X2	high	Yes	No	
			X3	high	Yes	No	
	Impact endcap close to X1	hyd	X1	high	Yes	No	-
			X2	high	Yes	No	
			X3	low	Yes	No	
	Inlet valve manoeuvre	hyd	X1	low	No	-	-
			X2	low	Yes	No	
			X3	high	Yes	No	

practically the same results for all the signals in these two categories. The strength of the transients present in the signals from the second and third dataset categories are indicated as either 'high' or 'low' based on how visually obvious the transients are in the time history. For example, the transients in Figures 3.8(b.i) and 3.8(c.i) above are classified as 'high', while the transients in Figures 3.9(a) and 3.9(b) below will be considered 'low'. It should be noted that this classification is purely subjective and does not indicate leak size. The purpose for this classification is to demonstrate the capability of the NSM transient detector to detect 'non-obvious' transients, i.e., transients whose presence is not betrayed by the time history. In cases where leak transients have been successfully detected, the leak location estimates obtained from the difference between transient onsets ΔT_{onset} in all the possible pairs of signals in the dataset are also reported in the table. The leak location is computed by substituting ΔT_{onset} as the time delay in the cross-correlation equation. If the leak confirmation step is not applicable due to an unsuccessful transient detection result, this is indicated with '-'. It can be observed that the NSM transient detector was able to detect transients in the cases with 'high' transients and in some cases with 'low' transients. It, however, fails for some cases with 'low'

transients; these are indicated with orange cells in the table. Also, the leak confirmation step succeeds for all the cases where the transients were successfully detected except for the case highlighted in blue on the table. Further information about these unsuccessful cases will be given later in this subsection. Another interesting observation from this cross-section of results is that in all cases where leak transients were successfully detected, the leak location estimate was very close to the true value. The maximum error in the leak location estimates is 28 centimetres, which is better than errors of up to 1 metre obtainable with existing state-of-the-art leak detection systems (Liu et al., 2012). An implication of this result is that the difference between transient onsets ΔT_{onset} is indeed an accurate estimate for the time delay between the signals. This provides an alternative approach for estimating the time delay between signals containing leak transients. Furthermore, if the transient source is known to be out-of-bracket with respect to two sensors, then the difference between the transient onsets can be used to estimate the wave speed in the pipe. This will be demonstrated in Sections 4.5 and 4.6 in Chapter 4.

The summary of the results for all available datasets is now presented. Note that no distinction has been made between hydrophone and accelerometer measurements in these summarised results because there was no noticeable difference in performance between the two signal types. The NSM transient detector correctly infers the absence of transients in all noise and steady-state leak measurements, which indicates that it exhibits a low false alarm rate. Out of the 72 signals available in the second and third dataset categories, the detector successfully detects the presence of transients in 67 signals. This represents a 93% success rate of transient detection. In addition to the three signals indicated with orange cells in Table 3.3 above, the NSM transient detector fails for two accelerometer signals acquired at X1 and X3 in the presence of an active transient (generated by the inlet valve manoeuvre) and leak transient (induced by the simulation of a leak at L1), respectively. Figure 3.9(a) shows the time history and NSM output in one of these cases. In this case, the leak at L1 induces a 'weak' transient (as defined in Section 3.2). The induced transient is not visually noticeable in the time history in Figure 3.9(a.i), indicating that the leak transient may have been severely attenuated before reaching the sensor at X3. A possible reason for the severe attenuation of the transient is the presence of the inline elbow and inlet valve in the leakage test rig. Although the NSM output in Figure 3.9(a.ii) never exceeds the transient detection threshold at any time point, it exhibits a slight peak around the 10.6-second mark. This time is close to the time of leak simulation, which suggests that transient detection may still be possible with a lower threshold. However, this comes with the cost of a higher false alarm for noise-only signals.

Among the 67 cases of successful transient detection, the leak confirmation step correctly identifies the nature of the detected transients (leak or active) in 32 out of 34 signals in the second dataset category (94% success rate) and in 33 out of 33 signals in the third dataset category (100% success rate). One of the cases for which the leak confirmation step fails is shown with blue cells in Table 3.3 above, while the other case corresponds to a hydrophone leak signal measured at X3 when a leak is simulated by opening the L1 valve halfway. Figure 3.9(b) shows the time history and the NSM

outputs of the signal and its steady-state parts in the former case. As can be observed from the NSM output in Figure 3.9(b.ii), the NSM transient detector correctly detects the acoustic transient, the presence of which is not obvious from the time history in Figure 3.9(b.i). As indicated by the absence of peaks in the transition zone (denoted by the vertical dashed lines in Figure 3.9(b.ii)), the NSM-based leak confirmation approach incorrectly classifies the detected transient as an active transient. The Brown-Forsythe test also fails. The test applied to the steady-state segments (N_B = 961039) yields a p-value of p_v = 0.079 and test statistic W_B = 3.08, which is less than the critical value $F_{1-\alpha,\,1,\,N_B-2}$ = 6.63. Based on these results, it can be concluded that while the leak occurrence generates detectable transients, the presence of the leak does not introduce a 'substantial' enough change in the state of the measured signal, thereby causing the NSM-based leak confirmation and Brown-Forsythe test to incorrectly infer the absence of a new leak source.

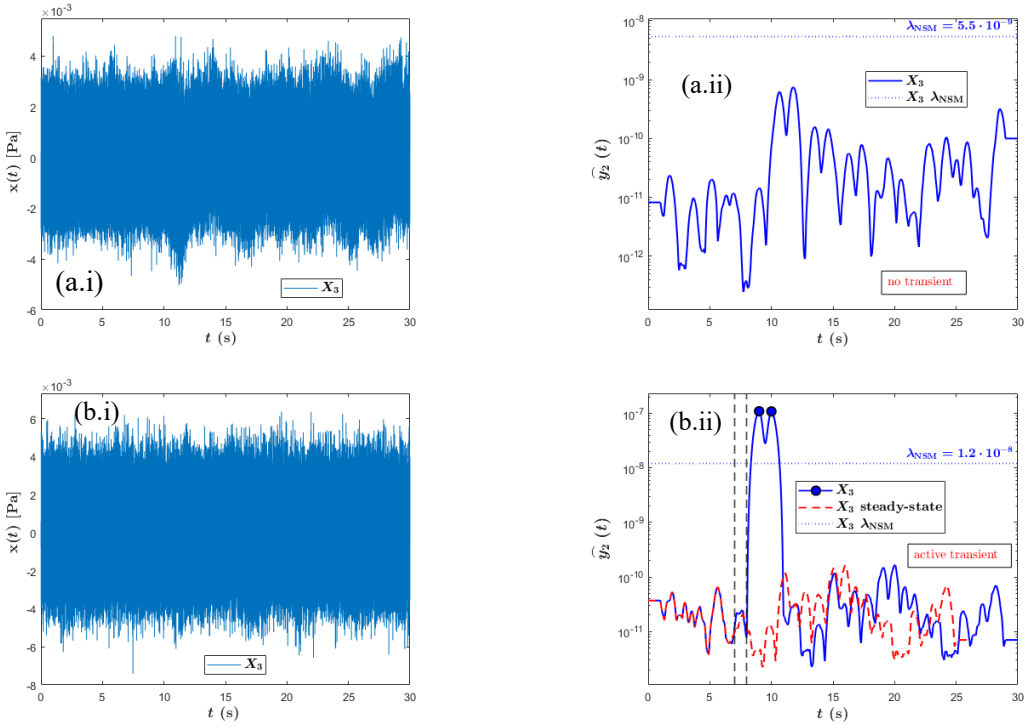

Figure 3.9: Cases for which the passive transient leak detection method fails. (a) Unsuccessful transient detection. (b) Unsuccessful leak confirmation. (i) Time history. (ii) NSM output. The horizontal dashed line denotes the NSM transient detection threshold corresponding to an AFPR of 0.001. The dots and vertical dashed lines in (b.ii) indicate the NSM peaks and the transition zones, respectively.

The two examples of unsuccessful transient detection and leak confirmation highlight one of the shortcomings of the passive transient leak detection method: a leak cannot be detected if it does not produce a sufficiently detectable transient and/or introduce 'substantial' changes in the state of the measured signal. One particularly important practical situation where the effectiveness of the method is likely to reduce is when the sensors are too far from the leak, which may lead to severe attenuation of the leak transient before reaching the sensors. Also, the presence of damping components in the

pipe network may lead to increased dissipation of the leak transients, thereby rendering the method less effective. As already stated, sensor placement is an important aspect which must be considered in the practical application of the method. To ensure the effectiveness of the method over the whole pipeline, sensors should be placed not too far apart (less than 100 metres). It should be noted that it may still be possible to detect the leak in the two failed examples using the passive steady-state leak detection method as will be shown in the next section (see Figure 3.11).

Overall, the leak detection rate of the proposed passive transient leak detection method is 89%. The high success rate in detecting and classifying acoustic transients demonstrates the viability and robustness of the method. Further discussion about its advantages, limitations, and other possible practical applications is included in Section 3.5.

3.4.2 Experimental investigation of the passive steady-state leak detection method

The passive steady-state leak detection algorithm proposed in this chapter was applied to background noise and steady-state leak signals measured on the leakage test rig. Table 3.4 summarises the main information concerning the steady-state leak datasets, including leak valve opening (indicated as either 'halfway' or 'full'), leak location, and the sensor type. It should be noted that the terms 'halfway' and 'full' do not signify the detectability of the leaks, as signals generated by a leak depends on many factors other than the leakage flow rate, including the operating pressure and flow rate, environmental conditions, etc. (Butterfield, 2018). As already mentioned, each dataset consists of signals acquired simultaneously at X1, X2, X3, and sometimes X4 (a point located 2 metres from X3).

Table 3.4: Description of datasets of steady-state leak signals acquired on the leakage test rig.

Dataset	Valve opening	Leak location	Sensor type
1	halfway	L1	Hydrophone
2	full	L1	Hydrophone
3	halfway	L2	Hydrophone
4	full	L2	Hydrophone
5	full	L1	Accelerometer
6	halfway	L1	Accelerometer
7	full	L1	Accelerometer
8	halfway	L2	Accelerometer
9	full	L2	Accelerometer
10	halfway	L2	Accelerometer

A cross-section of cases are reported to highlight the main features of the passive steady-state method. Table 3.5 shows time-domain and spectral descriptors obtained for the raw unfiltered leak signals measured at X1 and X3 in Leak Dataset 1 and Leak Dataset 5. These two cases represent

signals acquired at locations closest and farthest from the L1 leak for halfway and full valve openings. Also shown are the values obtained for noise signals measured at these access points. Note that only the time-domain and spectral features, described in Section 3.1, that exhibit the highest relative difference (on average) between noise and leak signals are reported. Since the standard deviation is identical to the RMS for zero-mean signals, it is not included. It can be observed that these spectral descriptors and time-domain features undergo noticeable changes in their values in the presence of a leak, thus providing a reliable means of detecting the leak. As already discussed in Section 3.3.2, the spectral flatness, spectral flux, spectral kurtosis, and spectral skewness are sensitive to the presence of a leak, and thus, the LDM is defined as in Equation (3.11) with $w_1 = w_2 = w_3 = w_4 = 1/4$ and $\Lambda_{norm} = 0.5$. Equal importance is given to all four spectral descriptors in this case, while the value of the normalisation factor is based on the average values of the LDM obtained for the background noise signals acquired on the leakage test rig (i.e., signals in the first dataset category). For the available signals considered in this work, the current definition of the LDM in Equation (3.11) using only spectral descriptors seems to be sufficient for good results.

Table 3.5: Time and frequency-domain features for noise-only and leak measurements measured at X1 and X3 on the leakage test rig. The leak signals are from Datasets 1 and 5 in Table 3.4.

Measurement location	**X1**			**X3**		
	noise	**Dataset 1**	**Dataset 5**	**noise**	**Dataset 1**	**Dataset 5**
Feature						
RMS	0.093	1.37	2.72	0.093	0.11	1.45
Shape factor	0.12	1.72	3.42	0.12	0.14	1.06
Crest factor	53.66	5.19	1.95	58.00	42.86	14.53
Clearance factor	84.61	8.26	3.10	91.43	67.55	22.18
Spectral flatness	0.24	0.0025	0.0012	0.24	0.018	0.0071
Spectral flux	0.0005	0.11	0.46	0.0005	0.13	0.16
Spectral skewness	0.054	5.58	5.23	0.049	2.58	3.27
Spectral kurtosis	1.75	52.17	54.61	1.73	16.64	39.32

Table 3.6 shows the LDM values and leak detection results for the available steady-state leak signals in the 10 datasets described in Table 3.4. The average SNR for leak signals measured at the given locations is indicated. As noted previously in Section 3.1, high LDM values in the table are presented in scientific (exponential) notation. A positive inference about the presence of a leak is made if the LDM value exceeds a pre-determined threshold of 10. It must be emphasised that this threshold is specific to the leakage test rig. A positive leak detection result is indicated with light blue cells, while orange cells indicate the absence of a leak. The general trend of the LDM values is consistent with the distance of the sensors from the leak. This metric attains a very high value for signals acquired closest to the leak (i.e., at X1 and X2), and relatively lower values for signals measured at X3 and X4, especially for the cases with 'halfway' leak opening. However, even in these cases, the LDM is *much* greater than unity, thus permitting the presence of the leak to be inferred. The observed correlation of the LDM with distance from the leak and signal power demonstrates its viability not

only as a leak detection tool but also as a measure of leak detectability. To gain further insights, the cases of good and relatively poor performance are examined below.

Table 3.6: LDM values obtained for the noise and leak signals in the datasets in Table 3.4.

Measurement location		**X1**	**X2**	**X3**	**X4**
	Noise	0.98	0.91	0.64	0.94
Dataset					
	Average SNR (dB)	**9**	**7**	**1**	**3**
1		2.89E+05	5.29E+04	155	
2		4.82E+05	1.37E+06	2.91E+04	
3		3.65E+05	9.47E+05	3.07E+03	
4		4.50E+06	3.74E+06	1.44E+04	
5		4.88E+05	1.24E+06	1.45E+03	2.95E+04
6		1.29E+03	726	400	622
7		4.79E+05	1.27E+06	3.55E+03	2.92E+04
8		3.88E+05	9.75E+05	3.76E+03	3.32E+03
9		4.50E+06	3.56E+06	3.86E+03	1.54E+04
10		3.82E+05	9.68E+05	51.6	216

Figure 3.10(a) shows the time histories and PSDs of the background noise and leak signal at X1 in Leak Dataset 3, taken as an example of good performance. As predicted, the presence of the leak is indicated by a significant increment of signal level and change in signal spectrum. The selected spectral descriptors change correspondingly (compared to the background noise), thus permitting leak detection using the LDM. More interesting is the analysis of critical signals. A close examination in the time domain of the 3 cases characterised by relatively low values of the LDM reveals low signal levels that make it difficult to distinguish between the background noise and leak signals based on time-domain features only. The low signal levels indicate the severe attenuation of the leak noise before arriving at the sensor. Figure 3.10(b) shows the time history and PSD concerning one of the cases, the X3 signals in Leak Dataset 10. As shown by the time history, the leak signal does not substantially exceed the background noise level. On the other hand, it can be observed that the shape and energy distribution of the signal spectrum are clearly distinguishable from those of the spectrum of the background noise. The spectral variations related to the leak are, however, more subtle compared to the case in Figure 3.10(a.ii). Although the LDM value is lower than for signals measured closer to the leak, it is still *much* greater than unity, allowing the presence of the leak to be inferred. If the spectral descriptors are only calculated in the frequency region where the leak noise is dominant (up to 1 kHz), then the algorithm performs considerably better. The LDM value increases to 1247, thus allowing for a more reliable detection of the leak, though with a lower efficiency compared to the X1 and X2 signals. This result highlights that the application of a properly selected bandpass filter prior to computing the LDM can significantly improve the effectiveness of leak detection using the steady-state method.

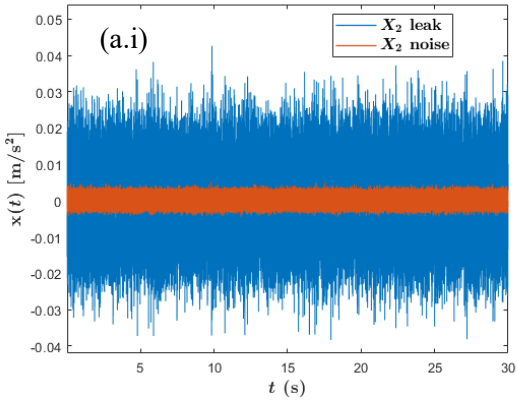

(a.i) Time histories of noise and steady-state leak signals in Dataset 3 measured at X2.

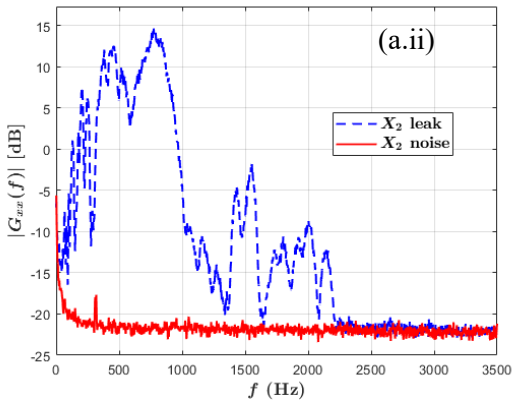

(a.ii) PSDs of the signals in (a.i).

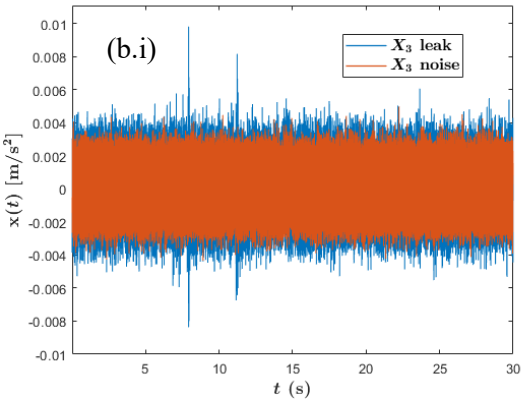

(b.i) Time histories of noise and steady-state leak signals in Dataset 10 measured at X3.

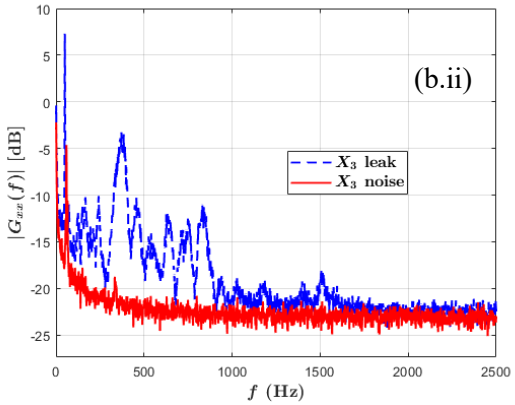

(b.ii) PSDs of the signals in (b.i).

Figure 3.10: Time histories and PSDs in successful and unsuccessful leak detection cases.

As stated in the preceding subsection, it is possible to detect leaks for which the passive transient leak detection method fails. This is illustrated for the signal shown in Figure 3.9(b) for which neither the NSM-based leak confirmation approach nor the Brown-Forsythe test succeeded. The PSD of the signal is shown in Figure 3.11. It can be observed that the shape of the signal spectrum differs from that of the background noise measured at the same location (compare with Figure 3.10(b.ii)). Applying the passive steady-state leak detection method to this signal without filtering yields an LDM value of 34.7, which allows the presence of the leak to be detected. If the signal is first filtered in the frequency interval 250–650 Hz, then the LDM value improves to 524, thereby allowing for a more reliable positive inference about the presence of a leak. This example demonstrates that transient and steady-state methods can complement each other in acoustic leak detection practice. Combination of both types of methods is likely to improve the reliability of leak detection. Such a possibility will be explored in Chapter 8.

The experimental results presented in this section demonstrate that the proposed transient and steady-state methods based on transient/signal detection can successfully distinguish leaks from

background noise. In particular, the methods exhibited no false alarms for signals acquired on the leakage test rig, which indicates their robustness. It is, however, important to consider the limitations of the rig discussed in Section 2.5 when generalising the presented results. Certain properties may make the leakage test rig more favourable for the proposed methods. For example, detectability of leak transients and signals may be relatively lower in real pipe systems, where signals propagate longer distances. Also, leak signals acquired on the test rig have substantially higher frequency contents than those reported for signals measured on real pipe systems. Since signals from real pipe systems may exhibit less spectral variation, this may naturally result in reduced effectiveness of the steady-state method when applied in real water distribution networks. There is, therefore, need for further thorough experimental validation of the methods in real systems. Their advantages and inherent limitations are discussed in the next section.

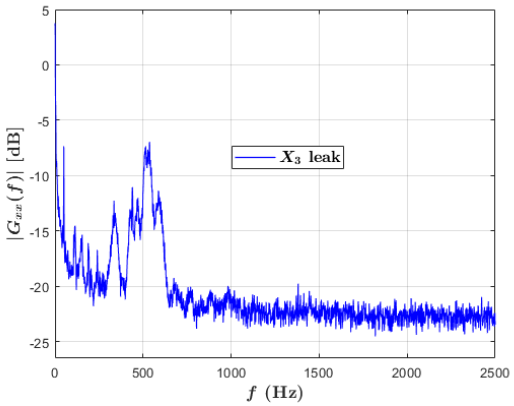

Figure 3.11: PSD of the signal whose time history is shown in Figure 3.9(b).

3.5 Advantages and limitations of acoustic transient and steady-state leak detection methods

The two passive leak detection methods described in this chapter offer some practical benefits. An important advantage that can be highlighted for the transient method is its generality. The NSM transient detector can be employed in any application where detecting transients and their boundaries in signals is required. The distribution of the background noise and transient signals is irrelevant to the performance of this detector, so it is suitable for use in a variety of situations. Examples include detection of acoustic transients in underwater environments, speech processing, etc. While the transient leak detection method has been described in this chapter for acoustic transients, its basic principles can be applied in other areas. One particularly relevant application is inferring pipe condition from transients acquired with transient loggers. As mentioned in Chapter 1, fluid transients can arise from a variety of sources, so one serious issue in fluid transient-based condition monitoring is distinguishing between transients generated by a pipe damage event and those induced by normal pipeline operations. The basic idea of identifying the presence of a new signal source using the concept of local non-stationarity is very general and provides a simple means to resolve this issue.

Classification of fluid transients based on type of sources can be achieved using the NSM transient detection and leak confirmation steps described in this chapter for acoustic transients without much modification.

Advantages of both methods are simplicity and ease of implementation. They can be implemented using simple signal processing tools, and existing acoustic/vibration sensors and measurement setup. The NSM transient detector is not computationally expensive when implemented with rectangular windows, while the descriptors employed in the steady-state method can be calculated in a straightforward manner from the PSD. The use of pre-processing steps, such as removal of non-leak artefacts and bandpass filtering substantially improves the performance of the method with little increase in complexity. Another benefit of the methods is the capability for timely leak detection and even real-time monitoring of the pipe system. Leaks can be detected with these methods without need for measurements over a long period of time or over several nights. The transient method, in particular, is able to detect leaks as they occur. This is practically beneficial as it can help to reduce the amount of water lost from leakages before discovery. In addition, the two methods can be used simultaneously for more robust leak detection performance. The steady-state method can be used to implement the leak confirmation step in the transient method. Also, leaks that trigger weak transients that are difficult to detect using the transient method can potentially be detected using the steady-state method.

The advantages highlighted above make the proposed methods attractive options for acoustic leak detection. However, some limitations can be identified. One big limitation regards the leaks that can be detected. An occurring leak can be discovered using the transient method only if it induces detectable or ‘strong’ acoustic transients, while an ongoing leak must introduce easily distinguishable features in the signal spectrum to be detected using the steady-state method. Therefore, only leaks *not too far* from the installed sensors can be detected successfully. It may, however, not be economically feasible to install sensors at sufficiently close intervals. Also, locations where sensors can be installed are usually limited by unavailability of access points, thereby limiting the extents of the pipeline that can be monitored using the proposed methods.

Since the methods rely on detecting sustained changes induced by a leak, they may give a false positive inference in the presence of signals from persistent non-leak sources. An example is the start-up of a pump which introduces an initial transient and results in a new steady state. One way to reduce the number of false alarms is to run the algorithms outside the timings of such events. As already suggested above, an alternative solution is to re-run the algorithms after a specified period following a positive transient detection inference before a final leak alert is issued. If the dominant frequencies at which the machinery operates are known, then they can be excluded using appropriate notch filters in the pre-processing steps of the algorithm. This permits to distinguish between true leak events and those that generate signals that propagate in the pipe momentarily. It should be noted, however, that

the leak detection algorithm may still issue a false positive result if the non-leak signal source persists after the specified period.

One challenge in the steady-state method is selection of time-domain and spectral descriptors for reliable leak detection performance. Since the properties of leak signals may vary depending on the pipeline properties and operating conditions, each signal feature may achieve vastly different performances in different pipe systems. Selection of appropriate features requires some preliminary studies of the background noise and leak signals measured on the pipe under consideration. However, this may not always be practically possible. Furthermore, the characteristics of the background noise may change over time. One other issue is the validity of the assumptions about the leak and noise spectra. In practice, the spectrum of the background noise may not necessarily exhibit comparatively less spectral variation as assumed, in which case, the steady-state method may post a lot of false positives. An additional challenge is the selection of the LDM threshold, for which a robust methodology based on thorough study of the measurement environment is required. The 'guesswork' approach used in this work is clearly inadequate.

A limitation specific to the transient method is the need for continuous sensor operation. Transients associated with leak occurrence are short-lived, so reliability of detecting leaks as they occur is reduced when sensors operate only intermittently. Continuous operation of the sensors comes with its own set of challenges associated with battery life issues, data storage constraints, communication protocols, etc. Moreover, ability to detect leaks in real time is difficult if the leak transients are masked by background noise. One way to improve applicability of the transient method is to incorporate acoustic/vibration sensors in transient loggers that generally already operate in a continuous mode. In addition, the method can be applied directly to data acquired by transient loggers or acoustic data extracted from these data Technical constraints, such as inaccessibility to appropriate hardware and measurement data, have hindered the investigation of these suggestions in this thesis. However, based on the discussion in Section 1.3, these directions appear to be worth investigating in future steps of the research.

Despite the highlighted issues and limitations of the study, the available experimental results demonstrate that the transient and steady-state methods are potentially viable options for leak detection. Therefore, further investigation and refinement of these methods appears to be worthwhile. To achieve a more robust and effective performance, thorough validation with a more representative database of leak signals acquired in a variety of leak detection environments as well as application of measures to resolve the issues outlined above could be carried in the future steps of the research.

3.6 Summary and conclusion

In this chapter, the possibility of considering acoustic leak detection as a transient and signal detection problem has been established. It has been demonstrated with experimental leak signals that the occurrence of a leak is accompanied by the generation of acoustic transients that can be detected using acoustic/vibration sensors as well as introduction of sustained changes in the temporal and spectral properties of the measured signals. Among these properties, spectral descriptors, i.e., features that characterise the spectral variation of the signal spectrum were found to be the most sensitive to the presence of a leak.

Based on the transient/signal detection principle, two methods—a transient and a steady-state—have been proposed to detect leaks in water pipes. The transient method, which relies on detecting and identifying transients generated by a leak, was implemented using the non-stationarity measure (NSM). The statistics of the NSM were derived, and its effectiveness for acoustic transient detection was demonstrated using numerical simulation and experimental results. The steady-state method is based on examining features in the spectrum of the measured signal. A leak is inferred based on a leak detection metric (LDM) calculated from selected spectral descriptors. An algorithm for implementing the method was described. Important considerations in the practical implementation of the method were outlined, including sensor placement, selection of descriptors, and inference methodology.

Limited experimental results obtained on the leakage test rig demonstrated that the methods are potentially viable and effective means of detecting leaks in water pipes. Their benefits and limitations were highlighted.

CHAPTER 4
ACOUSTIC LEAK DETECTION AS A MULTIPATH IDENTIFICATION PROBLEM

This chapter concerns the implementation of alternative acoustic leak detection methods based on the multipath identification viewpoint identified in Chapter 1. Motivated by fluid transient leak reflectometry methodology, these methods exploit the reflection of acoustic transients or leak noise by discontinuities in the pipe system to detect and locate leaks. This chapter outlines the basic principles of the multipath identification approach and describes its transient and steady-state implementations. Numerical simulation and experimental results are presented to demonstrate the effectiveness of considering acoustic leak detection from this perspective.

4.1 Recasting leak localisation as a multipath identification problem

The reflection of an active acoustic transient at an *in-bracket* discontinuity is illustrated using a spatial-temporal plot in Figure 4.1(a). Examples of discontinuities in a pipe system are dead ends, changes in cross-section, pipe junctions, blockages, and leaks. When the incident acoustic wave arrives at the discontinuity, a reflected wave ensues and propagates towards the first measurement point. Subsequent reflected waves also result from repeated reflection of the propagating and earlier reflected waves off discontinuities. A similar phenomenon occurs when the leak noise encounters discontinuities as illustrated in Figure 4.1(b). The reflected waves from a discontinuity can be captured with an acoustic/vibration sensor installed downstream of the discontinuity.

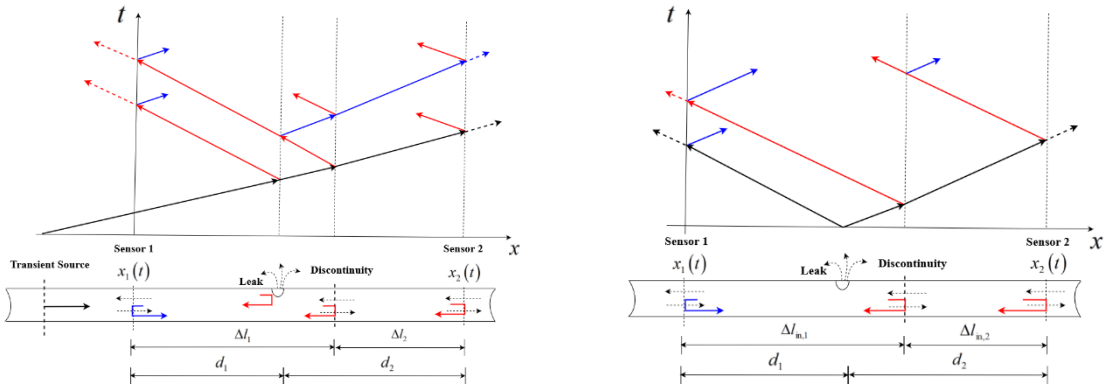

(a) active acoustic transient. (b) leak noise.

Figure 4.1: Illustration of the phenomenon of acoustic wave reflection at a discontinuity. —— direct-path propagating acoustic transient or leak noise; —— reflections propagating towards Sensor 1; —— reflections propagating towards Sensor 2.

Hence, in addition to the *direct-path* waves propagating directly from the signal source (transient source or leak) to the measurement points, the measured signals may also contain waves reflected off discontinuities in the pipe network. Since the reflections in the measured signals arise due to the interaction between the propagating acoustic waves and features in the pipe, it is possible to estimate the leak location and the wave speed by considering the acoustic leak localisation problem from a multipath identification point of view and applying reflectometry principles. The time difference of arrival (TDOA) of a reflected wave with reference to the direct-path wave is related to the distances over which these two waves have travelled before arriving at the sensor locations. If the location of the discontinuity that gives rise to the reflected wave is known, then the wave speed, and consequently, the leak location can be determined from the TDOA. This acoustic leak detection approach can be implemented using transient or steady-state signal analysis, as will be described in the next two sections.

Note that in this work, the following notation is adopted: $\tau_{ik}\left[m,n\right]=T_i\left[m\right]-T_k\left[n\right]$ denotes the TDOA between the m th wave arriving at the i th sensor at time $T_i\left[m\right]$ and the n th wave arriving at the k th sensor at time $T_k\left[n\right]$. For example, $\tau_{21}\left[1,1\right]$ is the time delay between the direct-path waves in the first and second leak signals (termed the *reference time delay*). In this work, the first reflected wave arriving at a sensor is termed *primary reflection*, while subsequent reflected waves are referred to as *secondary reflections*.

4.2 Active transient acoustic leak detection by multipath identification

The transient multipath identification leak detection approach is based on identifying and matching reflected transient waves in the measured acoustic/vibration signals with the discontinuities from which they originate. Any unmatched reflection may be indicative of a leak or pipe defect. This approach will be referred to as the *matching method* in this work, and its main steps include:

1. Detecting and confirming the presence of *active* acoustic transients.
2. Identifying reflections and determining their TDOAs.
3. Matching reflections with the known discontinuities and estimating the leak location.

The first step can be implemented using the NSM just as in the passive transient leak detection method described in Chapter 3. In this case, the presence of active acoustic transients is inferred if the steady states before and after the transient event are *homogeneous*. The aim of the second step is to determine the presence and arrival times of reflections in the signals. Two methods for achieving this will be described in Section 4.3. The result from this step is a list of TDOAs $\tau_k=\tau_{ii}\left[k,1\right]$ of the reflections in the measured signals with respect to the direct-path transient. Each TDOA represents the time for the transient to transverse back and forth the distance between the sensor and the

corresponding discontinuity. Note that it is assumed that the primary reflections from the discontinuities can be unambiguously identified in the signals.

In the third step, the TDOAs τ_k are used to determine the possible locations of unknown discontinuities. This can be achieved using different approaches depending on whether the wave speed and direction of transient propagation are known. If the wave speed c is known, then the estimated distance $\Delta\hat{l}_k$ between the discontinuities and the sensor can be calculated as $\Delta\hat{l}_k = \frac{c \cdot \tau_k}{2}$. This way, reflections in the signals can be matched with the known discontinuities from where they originate. Any unassigned reflection may indicate a leak, other pipe defect, or an unknown discontinuity. If multiple reflections are unmatched, the presence and location of the leak can be confirmed by cross-correlating signals measured at two points on the pipe between the known discontinuities. It should be noted that only known discontinuities located upstream of the sensor are considered in the matching method. In the matching method, the 'upstream' and 'downstream' directions are defined with respect to the direction of propagation of the transient.

When the wave speed and/or direction of propagation of the acoustic transient are unknown (the more likely case in practice), the proposed approach is to define a cost function

$$C\left(P_l, \tilde{c}\right) = \sum_{k=1}^{N_d} \left(\Delta l_k - P_l\left[k\right]\right)^2 \tag{4.1}$$

where Δl_k are the locations of the N_d known discontinuities arranged in ascending order based on their distance from the sensor location (i.e., $\Delta l_1 < \Delta l_2 < \cdots < \Delta l_{N_d}$), $P_l = \left[\Delta\hat{l}_1, \Delta\hat{l}_2, \ldots, \Delta\hat{l}_{N_d}\right]$ denotes N_d-combinations of the estimated locations $\Delta\hat{l}_k = \tilde{c} \cdot \tau_k / 2$ (also arranged in ascending order), and $\tilde{c}$ is the wave speed value. This cost function determines the best match between the TDOAs τ_k and the known discontinuities while adjusting the wave speed. The combination $P_l = P_{\text{opt}}$ and wave speed value $\tilde{c} = c_{\text{opt}}$ that minimise $C\left(P_l, \tilde{c}\right)$ are considered to be the optimal estimates that give the best match. The value of $\tilde{c} = c_{\text{opt}}$ is taken as the propagation wave speed in the pipe. Any location $\Delta\hat{l}_k$ not present in P_{opt} may be the location of a leak. In case of multiple missing locations, cross-correlation can be carried out to determine which is the actual location of the leak. As already stated, only signals from a sensor located downstream of the known discontinuities must be used in the analysis. If only one sensor is available, then the cost function has to be calculated for each of the two possible directions of propagation. The wave speed and discontinuity location estimates from one of the two cases are likely to be 'implausible'. An implausible estimate refers to an estimate that is outside the possible range suggested by the measurement setup and pipe properties. The presence of two sensors may make it easier to determine the direction of propagation by observing the NSM outputs. If the

transient source is known to be located out-of-bracket with respect to the two sensors, then the signal with the earlier transient onset or higher NSM peak height will contain reflections from upstream discontinuities including any leak located between the sensors. This signal can be used to calculate the cost function. Alternatively, for known out-of-bracket transient sources, instead of using the cost function approach, the wave speed can be calculated directly from the inter-sensor distance d and the difference ΔT_{onset} between the transient onsets as $\hat{c} = d/\Delta T_{\text{onset}}$. After the wave speed has been estimated, reflections can be matched with the discontinuities as described above for the case with known wave speed. It should be noted that for the cost function approach to work, there must be at least two known discontinuities upstream of the selected sensor. Otherwise, finding the wave speed via the cost function above is not possible.

It is important to note that onsets may not provide accurate information about the direction of transient propagation if the transient source is located in-bracket with respect to the two sensors. Therefore, if the relative location of the transient source (in-bracket or out-of-bracket) is not known, then it is recommended to consider the following three possible scenarios: one scenario with an out-of-bracket source closer to the first sensor, one scenario with an out-bracket source closer to the second sensor, and one scenario with an in-bracket transient source. Since the location of the transient source must be closer to the sensor with the earlier transient onset, the scenario in which an out-of-bracket transient source is closer to the sensor with the later transient onset, can be disregarded. The cost function is evaluated for the other two feasible scenarios. Then the implausible estimates are disregarded, and the remaining estimates can be verified using cross-correlation.

Unlike fluid transient reflectometry methods, the proposed matching method does not require the introduction of a controlled hydraulic transient at a known location in the pipe. Instead, *ambient* acoustic transients induced by normal pipeline operations or pipe impacts can be analysed. It is, however, implicitly assumed that these ambient acoustic transients are much ‘stronger’ than the background noise and steady-state leak signals. Two important factors that affect the effectiveness of the method are the distance between the sensor and the discontinuities, and the detectability of reflections in the measured signals. Reflections originating from discontinuities at a large distance from the sensor may be severely attenuated and so are not likely be detected. In applying the matching method, it is important to ensure that only discontinuities that are not *too far* from the selected sensor are used in calculating the locations or defining the cost function. Owing to the roundtrip propagation of the transient from the sensor location to the discontinuity, the effective distance over which a leak can be successfully located using reflectometry principles is half that of the conventional cross-correlation technique. The effective leak detection range of acoustic methods in metallic and plastic pipes is 200 and 100 metres, respectively (Covas et al., 2006). Hence, it is recommended that only discontinuities located within a distance of 100 and 50 metres, respectively, from the sensor in metallic and plastic pipes should be considered in the matching method. The matching method will be evaluated using simulated and experimental signals in Sections 4.5 and 4.6, respectively.

4.3 Steady-state multipath identification leak localisation method

The steady-state multipath identification leak localisation approach estimates the leak location and wave speed under the cross-correlation measurement setup without need for the presence of an acoustic transient. Instead, steady-state leak signals are analysed. The general principles of this method are presented in this section. With respect to the direct-path wave, the TDOA of the primary reflection in the i th leak signal can be expressed in a general form as

$$\tau_{ii}[2,1] = \frac{d_{PR} - d_{PW}}{c} \tag{4.2}$$

where $d_{PW} = d_i$ and d_{PR} are the distances covered by the direct-path wave and the primary reflection, respectively. The value of d_{PR}, and hence, the particular form taken by Equation (4.2) depends on the pipe configuration (i.e., the relative locations of the leak, sensors, and discontinuities). Although the distances d_{PW} and d_{PR} are not known a priori, this equation and the cross-correlation equation can be solved simultaneously to determine the leak location and wave speed. There are two aspects to consider in estimating the leak location using this approach: formulating the system of equations based on the pipe configuration and determining the TDOAs of the primary reflections. The first aspect is illustrated in this section, while the methods for estimating the TDOAs are described in Section 4.3.

For the pipe configuration with one in-bracket discontinuity shown in Figure 4.1(b) above, Equation (4.2) takes the form

$$2\Delta l_{\text{in},i} - 2d_i = c_i \cdot \tau_{ii}[2,1] \tag{4.3}$$

where the subscript $i = 1, 2$ in c_i indicates which signal is used in the computation, and $\Delta l_{\text{in},i}$ is the distance between the in-bracket discontinuity and the i th measurement point. Note that it has been assumed that the leak location does not coincide with the location of the discontinuity. In this case, Equation (4.3) and the cross-correlation equation (Equation (1.1)) form a system of two linear equations in two unknowns:

$$\begin{cases} c_i \tau_{ki}[1,1] + 2d_i = d \\ c_i \tau_{ii}[2,1] + 2d_i = 2\Delta l_{\text{in},i} \end{cases}, \quad i,k = 1,2;\ i \neq k\ . \tag{4.4}$$

The solution of these equations gives the estimate of the leak location $\hat{d}_i$ and wave speed $\hat{c}_i$ as

$$\begin{cases} \hat{d}_i = \dfrac{2\Delta l_{\text{in},i} \cdot \tau_{ki}[1,1] - d \cdot \tau_{ii}[2,1]}{2\left(\tau_{ki}[1,1] - \tau_{ii}[2,1]\right)} \\ \hat{c}_i = \dfrac{d - 2\Delta l_{\text{in},i}}{\tau_{ki}[1,1] - \tau_{ii}[2,1]} \end{cases}. \tag{4.5}$$

All the quantities in the right-hand side of the two expressions in Equation (4.5) are either known from the schematic of the pipe system or can be determined from the measured signals, making it possible to calculate both the leak location and wave speed.

There is one important issue that must be resolved: determining which signal to use in formulating Equation (4.3). This choice is based on the relative location of the leak with respect to the discontinuity. If the leak is located downstream of the discontinuity, the first signal $x_1(t)$ should be used; otherwise, $x_2(t)$ must be used. Note that the upstream and downstream directions are defined here in terms of the direction of water flow in the pipe which is assumed to be from the first measurement point to the second measurement point. The more likely of the two possible cases can be determined as follows. Without loss of generality, let $\Delta l_{\text{in},1} < \Delta l_{\text{in},2}$ such that the first sensor is closer to the in-bracket discontinuity. If the reference time delay $\tau_{21}[1,1]$ is negative, then it can be inferred that the leak is upstream of the discontinuity, so Equation (4.5) should be evaluated with $i = 2$. On the other hand, if $\tau_{21}[1,1] > 0$, both the leak and discontinuity are located on the same half of the pipe, and the evidence provided by the ACFs or cepstra of the two signals has to be considered. The presence of a prominent peak in the interval $I_i = \left(0, 2\Delta l_{\text{in},i}/c_{\min}\right]$ in the ACF or cepstrum of the i th signal can be considered evidence supporting the case that the leak is located between the i th sensor and the discontinuity (see Section 4.3). Here, $c_{\min}$ is taken to be the minimum possible value of the wave speed determined by subtracting some tolerance from its historical or calculated value. The upper limit of I_i comes from the inequality $\tau_{ii}[2,1] = 2\left|\Delta l_{\text{in},i} - d_i\right|/c < 2\Delta l_{\text{in},i}/c_{\min}$. In the situation where there is supporting evidence for the two possible cases, it is suggested to calculate the leak location and wave speed for both cases. One of the estimates is likely to be implausible. This will be illustrated in Section4.5. As one of the two possible cases is likely to result in clearly incorrect estimates, the step of determining which signal to use can be skipped. When $\tau_{21}[1,1] = 0$, the leak is exactly at the midpoint of the pipe, and the leak location can be correctly estimated regardless of the value of the wave speed used in the cross-correlation equation.

In a similar fashion, the leak location and wave speed expressions can be derived for a pipe configuration with an out-of-bracket discontinuity located at a distance of $\Delta l_{\text{out},i}$ from the i th sensor as

$$\begin{cases} \hat{d}_i = \dfrac{d \cdot \tau_{ii}[2,1] - 2\Delta l_{\text{out},i} \cdot \tau_{ki}[1,1]}{2\tau_{ii}[2,1]} \\ \hat{c}_i = \dfrac{2\Delta l_{\text{out},i}}{\tau_{ii}[2,1]} \end{cases}. \tag{4.6}$$

For this configuration, the leak location and wave speed must be calculated using the signal from the sensor located closest to the out-of-bracket discontinuity. In the case of pipe configurations with multiple discontinuities (in-bracket and/or out-of-bracket), it is suggested to calculate the leak location and wave speed for each discontinuity using Equation (4.5) or (4.6) depending on whether the discontinuity is in-bracket or out-of-bracket. As already stated, the *incorrect* configurations among these will likely result in implausible estimates. Note that among multiple out-of-bracket discontinuities, it is necessary to consider only the discontinuities closest to each sensor, as they are most likely to be the source of the primary reflection. Thus, using the TDOAs of the primary reflections and information about the locations of the discontinuities in the pipe, the leak location and propagation wave speed can be estimated *passively* from measured leak signals only. The effectiveness of this steady-state passive method will be investigated using simulated and experimental signals in Sections 4.5 and 4.6, respectively.

4.4 Multipath identification methods

An important aspect common to the transient and steady-state methods described in the preceding sections is the estimation of the TDOAs of reflections in the measured signals. Among the multipath identification techniques available in the literature, the autocorrelation and cepstral techniques are selected in this work. The main reason for choosing these techniques is that they do not require a priori knowledge of the direct-path waveform unlike other techniques, such as cross-correlation (Beck et al., 2005) and model-based CUSUM algorithm (Lee et al., 2007). It should be noted that even though the selected multipath identification techniques are derived and analysed only for steady-state leak signals in this section for brevity, the conclusions are also valid for transient signals.

A steady-state leak signal $x(t)$ can be modelled as a multipath (composite) signal consisting of the propagating leak noise $l(t)$ generated at the leak location, and its reflections:

$$x(t) = l(t) \otimes h_{dir} + \sum_{k=1}^{N_{ref}} l(t) \otimes h_{k,ref} + n(t) \tag{4.7}$$

where h_{dir} is the direct-path pipe IRF, $h_{k,ref}$ is the portion of the pipe IRF that accounts for the k th reflection, $n(t)$ is the additive noise at the measurement location, N_{ref} is the number of *detectable* reflections in the signal, and $\otimes$ denotes linear convolution. To simplify the derivation and analysis of multipath identification techniques, only the primary reflection will be considered for now. An approach for dealing with multiple reflections will be described in Section 4.4.4. The Fourier Transform (FT) of the multipath leak signal $X(\omega) = \mathrm{F}\{x(t)\}$ in Equation (4.7) with $N_{ref} = 1$ is given by

$$X(\omega) = L(\omega) H_{dir}(\omega, d_{PW}) + L(\omega) H_{ref}(\omega, d_{PR}) + N(\omega) \tag{4.8}$$

where $L(\omega)=\mathrm{F}\{l(t)\}$, $N(\omega)=\mathrm{F}\{n(t)\}$, $H_{dir}(\omega,d_{PW})=\mathrm{F}\{h_{dir}\}$, and $H_{ref}(\omega,d_{PR})=\mathrm{F}\{h_{1,ref}\}$. Here, $\mathrm{F}\{\bullet\}$ denotes the FT. The direct-path FRF $H_{dir}(\omega,d_{PW})$ is described by the model given in Equation (2.5). Since a reflected wave can be regarded as a shifted and attenuated copy of the direct-path wave, $H_{ref}(\omega,d_{PR})$ has the same form as $H_{dir}(\omega,d_{PW})$ but with additional dependence on the transmission and reflection coefficients of the discontinuities in the pipe. For instance, in the pipe configuration shown in Figure 4.1(b) above, $H_{dir}(\omega,d_{PW})$ and $H_{ref}(\omega,d_{PR})$ for the leak signal at sensor 1 are given by

$$\begin{cases} H_{dir}(\omega,d_{PW})=e^{-|\omega|\beta d_{PW}}e^{-j\omega d_{PW}/c} \\ H_{ref}(\omega,d_{PR})=\Gamma\cdot e^{-|\omega|\beta d_{PR}}e^{-j\omega d_{PR}/c} \end{cases} \tag{4.9}$$

where $d_{PW}=d_1$, $d_{PR}=d_1+2(\Delta l_{\mathrm{in},1}-d_1)$, and Γ is the reflection coefficient of the discontinuity. In this case, the aim of the multipath identification problem is to determine the TDOA of the primary reflection: $\tau_{PR}=\tau_{11}[2,1]=(d_{PR}-d_{PW})/c$.

4.4.1 Autocorrelation multipath identification method

In the autocorrelation method, reflections or echoes in a signal are identified from the peaks in its ACF. Assuming $l(t)$ and $n(t)$ in Equation (4.7) are uncorrelated, the auto-power spectrum $G_{xx}(\omega)$ of the multipath signal $x(t)$ in Equation (4.8) is given by

$$\begin{aligned} G_{xx}(\omega)=G_{ll}(\omega)\left\{\left|H_{dir}(\omega,d_{PW})\right|^2+\left|H_{ref}(\omega,d_{PR})\right|^2\right\}+G_{nn}(\omega) \\ +2G_{ll}(\omega)\,\mathrm{Re}\left\{H_{dir}^{*}(\omega,d_{PW})H_{ref}(\omega,d_{PR})\right\} \end{aligned} \tag{4.10}$$

where the symbol * denotes the complex conjugate. After substituting the values for $H_{dir}(\omega,d_{PW})$ and $H_{ref}(\omega,d_{PR})$ from Equation (4.9), and taking the IFT, the ACF $R_{xx}(\tau)=\mathrm{F}^{-1}\{G_{xx}(\omega)\}$ of the signal is obtained as

$$\begin{aligned} R_{xx}(\tau)=\Gamma\cdot R_{ll}(\tau-\tau_{PR})\otimes\psi_r(\tau)+\Gamma\cdot R_{ll}(\tau+\tau_{PR})\otimes\psi_r(\tau) \\ +R_{ll}(\tau)\otimes\psi_d(\tau)+R_{nn}(\tau) \end{aligned} \tag{4.11}$$

where $R_{ll}(\tau)=\mathrm{F}^{-1}\{G_{ll}(\omega)\}$, $R_{nn}(\tau)=\mathrm{F}^{-1}\{G_{nn}(\omega)\}$, $\psi_r(\tau)=\mathrm{F}^{-1}\{e^{-|\omega|\beta d_{\Sigma}}\}$, $d_{\Sigma}=d_{PW}+d_{PR}$, $\psi_d(\tau)=\mathrm{F}^{-1}\{e^{-2|\omega|\beta d_{PW}}+\Gamma^2e^{-2|\omega|\beta d_{PR}}\}$, and $\mathrm{F}^{-1}\{\bullet\}$ denotes the IFT. The first and second terms in Equation (4.11) have their peaks at $\tau=-\tau_{PR}$ and $\tau=\tau_{PR}$, respectively, while the other terms achieve their peak at $\tau=0$. Thus, an estimate of the TDOA τ_{PR} can be obtained by identifying and locating the peaks at the non-zero lags in the ACF of the multipath signal. Based on Equation (4.11), the

factors that affect the ability to detect reflections and identify their TDOAs from the ACF are signal and pipe properties, propagation distance, and the reflection coefficient. Their effects will be discussed in Section 4.4.3.

4.4.2 Cepstral multipath identification method

The cepstrum first proposed by Bogert et al. (1963) is defined as the IFT of the logarithm of the estimated signal spectrum $\hat{G}_{xx}(\omega)$. There are many variants of the cepstrum, but the most widely used in signal processing applications are the complex cepstrum and the power cepstrum (Hassab and Boucher, 1976). In the power cepstrum, the logarithm is taken from the power spectrum, while the complex cepstrum is calculated as the complex logarithm of the FT. Both the power and complex cepstra are suitable for multipath identification, but the power cepstrum is selected in this work due to its relatively simpler implementation as it does not require phase unwrapping unlike the complex cepstrum (Oppenheim and Schafer, 2010; Akay, 2012). The power cepstrum $\breve{x}(q)$ of the multipath signal $x(t)$ in Equation (4.8) is derived as (Appendix C)

$$\begin{aligned}\breve{x}(q) &= \left|\mathrm{F}^{-1}\left\{\log\left(\hat{G}_{xx}(\omega)\right)\right\}\right| \\ &= R(q)+\sum_{m=1}^{\infty}\frac{(-1)^{m-1}}{m}g_m(q)+\frac{1}{2}\sum_{k=1}^{\infty}(-1)^{k+1}Q_k(q)\otimes\delta(q\pm k\tau_{PR})\end{aligned} \tag{4.12}$$

where $\delta(\bullet)$ denotes the Dirac delta function, $R(q)=\mathrm{F}^{-1}\left\{\log\left\{G_I(\omega)\right\}\right\}$,

$G_I(\omega)=G_d(\omega)\left\{1+\Gamma^2e^{-2|\omega|\beta\Delta d}\right\}+G_{nn}(\omega)=G_{ll}e^{-2|\omega|\beta d_{\mathrm{PW}}}+\Gamma^2G_{ll}e^{-2|\omega|\beta d_{\mathrm{PR}}}+G_{nn}(\omega)$,

$\Delta d=d_{PR}-d_{PW}$, $G_d(\omega)=G_{ll}(\omega)e^{-2|\omega|\beta d_{PW}}$ is the auto-power spectrum of the direct-path signal;

$g_m(q)=\mathrm{F}^{-1}\left\{\left[\frac{\varepsilon(\omega)}{G_{xx}(\omega)}\right]^m\right\}$, $\varepsilon(\omega)=\hat{G}_{xx}(\omega)-G_{xx}(\omega)$ is the random fluctuation in the spectral estimate; $Q_k(q)=\mathrm{F}^{-1}\left\{M_k(\omega)\right\}$, $M_k(\omega)$ are polynomial functions of $A(\omega)=\dfrac{2\Gamma\cdot e^{-|\omega|\beta\Delta d}}{1+\Gamma^2e^{-2|\omega|\beta\Delta d}+G_{nn}(\omega)/G_d(\omega)}$, defined in Appendix C, and the argument q known as the quefrency has unit of time. Note that in deriving the power cepstrum, it has been assumed that the random fluctuations in the spectral estimate are small such that $\left|\frac{\varepsilon(\omega)}{G_{xx}(\omega)}\right|<1$.

It can be observed from the third term in Equation (4.12) that the power cepstrum of a multipath signal has a sequence of spikes with decreasing amplitudes at integer multiples of the time delay τ_{PR}. Hence, the TDOA of the reflection can be determined as the quefrency of the first cepstral peak in the power cepstrum. The TDOA can also be obtained from the complex cepstrum in the same manner.

The term $R(q)$ represents the sum of the cepstra of the direct-path signal, the reflection, and the background noise. Its structure is determined completely by the log modulus of the spectra of these signals. Assuming the spectra of the signals are smooth (lacking in fine structure), $R(q)$ will be confined to low quefrencies (Bolton and Gold, 1984). Hence, to accurately detect the spike corresponding to the TDOA in the power cepstrum, it may be necessary to exclude peaks in the very low quefrencies. Also, the accuracy of multipath identification in steady-state leak signals can be improved by ensemble averaging realisations of the cepstra obtained from either multiple recordings or signal segments. Since the TDOA τ_{PR} remains constant, the portion of the cepstrum corresponding to the reflection will tend to be constant in every realisation while the randomness in $R(q)$ will be suppressed (Bolton and Gold, 1984; Tribolet, 1978). Ability to detect and locate reflections in a signal using the cepstral technique is affected by the same factors as in the autocorrelation technique. In the next section, these two multipath identification techniques are compared.

4.4.3 Comparison of autocorrelation and cepstral multipath identification techniques

The ACF and power cepstrum are closely related; the only difference is that the auto-power spectrum is preconditioned with a logarithmic operation prior to taking the IFT in the power cepstrum. Their performances for leak signals can be compared using two performance metrics: time delay resolution and detection SNR. The time delay resolution, which is the smallest delay that can be observed, is limited by the width of the ACF or cepstral peak. The detection SNR is given by the ratio of the peak to the variance of the background values in the ACF or cepstrum (Van Trees et al., 2013). It defines the prominence of the peak. Note that the detection SNR is similar to a metric known as the peak-to-side lobe ratio (PSR) proposed in Chapter 6 for assessing the quality of time delay estimate between leak signals. Techniques characterised by lower time delay resolution and higher detection SNR are considered more accurate and robust. Table 4.1 shows the expressions for the performance metrics as derived in Appendix D.

Table 4.1: Expressions for the performance metrics.

Method / Performance Metric	**Autocorrelation**	**Power cepstrum**
Time delay resolution	$\tau_{\text{res,ACF}} \approx \dfrac{\pi\beta d_{\Sigma}}{2}$	$\tau_{\text{res,CEPS}} \approx \dfrac{\pi\beta\Delta d}{2}$
Detection SNR	$D_{\text{snr,ACF}} \approx \dfrac{4\Gamma^2 T}{\pi\left(1+1/\zeta_d\right)^2\left(\beta d_{\Sigma}\right)^2}\dfrac{1}{B_d}$	$D_{\text{snr,CEPS}} \approx \dfrac{4\Gamma^2 T}{\pi\left(1+1/\zeta_d\right)^2\left(\beta\Delta d\right)^2}\dfrac{1}{\Delta\omega}$

In Table 4.1, B_d denotes the statistical bandwidth of the direct-path signal, T is the signal duration, and $\zeta_d = \frac{G_d(\omega)}{G_{nn}(\omega)}$ is the ratio of the spectral densities of the direct-path signal and background noise,

which have been assumed to be nearly constant in the analysis frequency region $\omega_1 \le \omega \le \omega_2$, and $\Delta\omega = \omega_2 - \omega_1$. The expressions are valid for small ω_1 and large $\Delta\omega$. It can be observed that the performances of the autocorrelation and cepstral techniques are affected by the same factors: signal and pipe properties, noise, propagation distances, and the reflection coefficient. Low background noise level, small inter-sensor distance, and long measurement time are desirable for better detection of reflections. Both methods achieve better performance in pipes with low attenuation and when the reflection coefficient of the discontinuity is high. It is particularly important to note that the reflection coefficient Γ can be negative, in which case, the reflected signal will be inverted in phase with respect to the direct-path signal. In such a case, which can be observed with an open-ended boundary condition in the pipe (see Peters (2013)), the spikes in the ACF or cepstrum corresponding to the reflection from the discontinuity will have a negative amplitude. Also, as shown in Figure 1.3, the correlation functions of a signal may have a ringing component, which manifests as peaks of lesser magnitude in the neighbourhood of the main peak at intervals spaced at the inverse of the centre frequency. Hence, to correctly identify all reflections, the TDOAs should be extracted from peaks in the envelope of the absolute value of the correlation functions and cepstrum. Taking the absolute values ensures that both peaks associated with in-phase and inverted reflections are identified, while the envelope suppresses the peaks resulting from the effects of the bandwidth and centre frequency of the signal or applied bandpass filter. The extraction of the envelope of a signal can be achieved using the Hilbert transform (see Oppenheim and Schafer (2010); Marple (1999)).

The superiority of cepstrum over the ACF in providing quality estimates can be inferred by comparing the performance metrics. The improvement in time delay resolution provided by power cepstrum over standard ACF is given by

$$\frac{\tau_{\text{res,CEPS}}}{\tau_{\text{res,ACF}}} = \frac{\Delta d}{d_\Sigma} = \frac{d_{PR} - d_{PW}}{d_{PR} + d_{PW}} = \left(\frac{d_{PR}/d_{PW} - 1}{d_{PR}/d_{PW} + 1} \right) < 1 \ . \tag{4.13}$$

It can be seen that a smaller time delay can be detected using the cepstral technique. The ability of cepstrum to improve multipath detection against the background noise is given by

$$\frac{D_{\text{snr,CEPS}}}{D_{\text{snr,ACF}}} \approx \frac{B_d}{\Delta\omega} \cdot \left(\frac{d_{PR} + d_{PW}}{d_{PR} - d_{PW}} \right)^2 \ . \tag{4.14}$$

This expression is greater than 1 as long as the analysis bandwidth is less than the statistical bandwidth of the direct-path signal, i.e., $\Delta\omega < B_d$, a criterion which is satisfied in most practical situations, since the limit ω_2 of the frequency region over which the leak noise propagates is less than B_d. High detection SNR implies that peaks in the power cepstrum are sharper compared to peaks in the ACF. It can be concluded that the power cepstrum yields more accurate TDOA estimates for leak signals than the ACF. The superior performance of the cepstrum is due to the inherent logarithmic conditioning of the auto-power spectrum prior to taking the IFT. Because of this conditioning, the cepstrum is capable

of detecting reflection and producing TDOA estimates in situations where the ACF fails. One such example is when the multipath signal and/or noise spectra contain resonances or tonal components. In this case, the auto-power spectrum of the signal can be represented as

$$\tilde{G}_{xx}(\omega) = G_{xx}(\omega) + \pi \sum_{k=-N_{\text{tonal}}}^{N_{\text{tonal}}} b_k \delta(\omega - \omega_k) \tag{4.15}$$

where N_{tonal} is the number of resonant or tonal components, ω_k and b_k are their angular frequencies and amplitudes, respectively. Taking the IFT of this auto-power spectrum yields the ACF as

$$\tilde{R}_{xx}(\tau) = R_{xx}(\tau) + \sum_{k=1}^{N_{\text{tonal}}} b_k \cos(\omega_k \tau) \ . \tag{4.16}$$

Fluctuations in the ACF contributed by the second term may mask the peak corresponding to the reflection, thereby resulting in false indications of the TDOA. The logarithm operation (through the three terms in Equation (C.3)) inherently suppresses the effects of tonals and resonances in the cepstrum, thus permitting accurate detection of the multipath. Another example where the frequency dependencies (transfer functions) of the direct-path and reflection propagation paths are different are also automatically handled by the cepstrum. Based on this discussion, the power cepstrum is recommended for use in multipath identification problems, including the proposed leak detection methods. The performance of the multipath identification techniques will be compared further in Section 4.5.

4.4.4 Identification of the primary reflection among multiple reflections

The ACF and power cepstrum were derived above for the situation where there is only a single reflection in the leak signal. The presence of multiple reflections results in the appearance of multiple distinguishable peaks in the ACFs and power cepstra. Note that since acoustic waves attenuate with distance, secondary reflections will be harder to detect than primary reflections, so their peaks will be lower. However, in some noisy situations, the primary and secondary reflection peaks may be of comparable heights. To identify the TDOA of the primary reflection in such a case, an algorithm proposed by Spiesberger (1996, 1998) can be employed.

In the algorithm, the TDOAs of the reflections in the signals are identified from the time lags corresponding to the peaks in their ACFs and CCF. The procedures of the algorithm are summarised as follows. Firstly, the number of multipaths (direct path and reflections) N_1 and N_2 in $x_1(t)$ and $x_2(t)$, respectively, are estimated from the number of positively lagged peaks P_1 and P_2 in the ACFs and the number of peaks M_{12} in the CCF. The lags corresponding to the positively lagged peaks in each ACF and the peaks in the CCF are arranged in monotonically increasing order so that $\tau_{ii}[m] < \tau_{ii}[m+1]$, $m = 1, 2, \ldots, P_i$, and $\tau_{21}[k] < \tau_{21}[k+1]$, $k = 1, 2, \ldots, M_{12}$. Then, the TDOAs

$\tau_{11}[N_1,1]$ and $\tau_{22}[N_2,1]$ of the last reflections are identified as the most positively lagged peaks in the ACFs. An exhaustive searching technique is then employed to estimate the TDOAs $\tau_{ii}[m+1,1]$ of the remaining N_i-2 reflections. All $U_i=\begin{pmatrix} P_i-1 \\ N_i-2 \end{pmatrix}$ possible selections of the N_i-2 TDOAs in each signal are considered, and a cost function is defined to select the optimal selection. Each pair of selections, denoted as $\tau_{11}[p_1(m)]$ and $\tau_{22}[p_2(m)]$, one from each signal, yields trial estimates for the TDOAs $\tilde{\tau}_{ii}[m+1,1]=\tau_{ii}[p_i(m)]$. Note that the lags in $\tau_{ii}[p_i(m)]$ have been arranged in increasing order so that $\tau_{ii}[p_i(m)]<\tau_{ii}[p_i(m+1)]$, where $m=1,2,\ldots,N_i-2$ and $p_i(m)\in\{1,2,\ldots,P_i-1\}$. The following four inter-sensor lags are immediately identifiable from $\tau_{11}[p_1(m)]$ and $\tau_{22}[p_2(m)]$: $\tau_{21}[1,N_1]=\tau_{21}[1]$, $\tau_{21}[N_2,1]=\tau_{21}[M_{12}]$, $\tau_{21}[N_2,N_1]=\tau_{21}[1]+\tau_{22}[P_2]$, and the reference time delay $\tau_{21}[1,1]=\tau_{21}[1]+\tau_{11}[P_1]$ $=\tau_{21}[M_{12}]-\tau_{22}[P_2]$. Using the reference time delay as the anchor point, the remaining inter-sensor lags are calculated for the selected pair. Among the U_1U_2 possible pairs of $\tau_{11}[p_1(m)]$ and $\tau_{22}[p_2(m)]$, the optimal pair is determined as the one that minimises the cost function $J_{\text{sp}}=\sum_{p=1}^{M_{12}}\left|\tau_{21}[p]-\tilde{\tau}_{21}[p(n)]\right|$ where $\tilde{\tau}_{21}[p(n)]$ is the lag closest to $\tau_{21}[p]$ in the realisation of the inter-sensor lags. The cost function J_{sp} selects the pair that best fits the measured lags in the CCF. Finally, the required TDOA $\tau_{11}[2,1]$ and/or $\tau_{22}[2,1]$ are obtained from the optimal pair. This algorithm works as long as the CCF has sufficient coherence between multipaths to yield enough peaks to make a definitive identification of multipaths from the respective ACFs. In the algorithm, the ACF estimates can be replaced with those from the cepstra of individual signals. In the next section, the proposed leak detection methodology is investigated using numerical simulations.

4.5 Simulation results

Numerical simulations were used to verify the viability of the proposed leak detection methods and investigate the effects of various factors.

4.5.1 Description of the simulation process and signals

The proposed transient and steady-state methods were employed to detect and locate leaks in a simulated pipe, the schematic of which is shown in Figure 4.2. The simulated pipe has the same

properties as the MDPE pipes in the leakage test rig described in Chapter 2; specifically, wave speed c = 354 m/s and attenuation factor $\beta = 2.1\times10^{-5}$ s/m. The acoustic pressure signals at the measurement points S1 and S2 are a superstition of the propagating leak noise generated at the leak location D1, the propagating transient signal generated at TS, and their reflections off the discontinuities D1-D4 and the measurement points. To simulate the leak signals at the measurement points, a white Gaussian noise signal was filtered with the FRFs between the leak location D1 and the respective measurement points. The same approach was used to generate the transient signals by filtering a short burst of white Gaussian noise and the FRFs between TS and the measurement points. These FRFs were derived using the transmission/reflection coefficient approach, in which the discontinuities are assigned reflection coefficients that denote the proportion of an incident signal that they reflect (Gao, 2006). In the numerical simulations, the reflection coefficients of the discontinuities and measurement points were set to a value of 0.5. Realisations of white Gaussian noise of the same power were added to the two generated signals such that the first signal had an SNR of 3 dB. The sampling rate was set to 1 kHz and the length of the simulated signals was 30 seconds. To mimic the operation of a real data acquisition process, a delay was introduced in the transient signal such that its onset occurred at the 10-second mark in the first signal. It should be noted that the only information available in advance are the locations of the known discontinuities D2-D4 and the measurement points S1 and S2. The relative location of TS, whether it is upstream or downstream of the sensors, is not known in advance and must be determined as part of the leak detection process. The distance between TS and S1 is only assigned a value in Figure 4.2 for the purpose of simulating the transient signal.

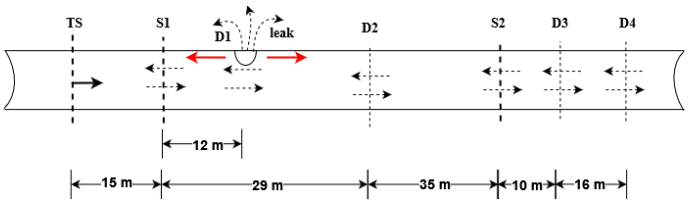

Figure 4.2: Schematic of simulated pipe. TS – transient source; S1, S2 – measurement points; D1–D4 – discontinuities.

4.5.2 Simulation results for the active transient leak localisation method

The time histories and NSM outputs of the simulated signals at S1 and S2 are shown in Figure 4.3. While the presence of a transient is not very obvious from the time histories, it can be easily inferred from the peaks in the NSM outputs of the signals in Figure 4.3(c). The active nature of the detected transient is indicated by the absence of a prominent peak in the transition zone of the NSM outputs of the modified signals in which the transient segments have been removed (Figure 4.3(d)). Also shown are the values of the test statistic W_B and the p-values p_v obtained from the Brown-Forsythe tests applied to the steady-state segments of the S1 and S2 signals. The values of the test statistic W_B = 0.66 (corresponding to p_v = 0.415) and W_B = 4.13 (corresponding to p_v = 0.042) are

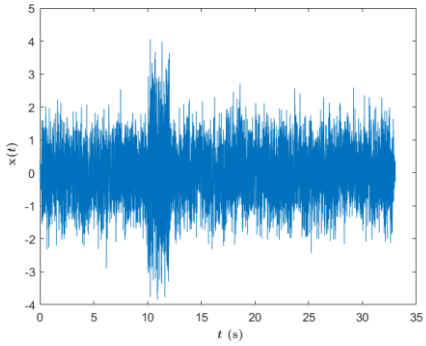

(a) Time history of the simulated S1 signal.

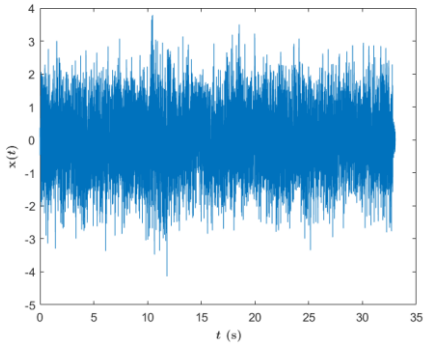

(b) Time history of the simulated S2 signal.

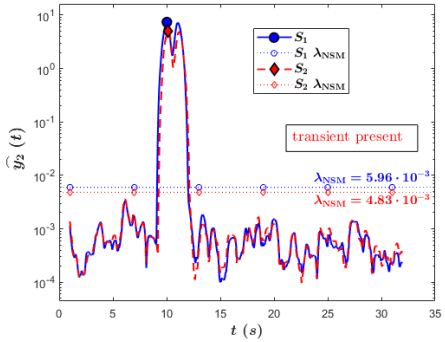

(c) NSM output of S1 and S2 signals.

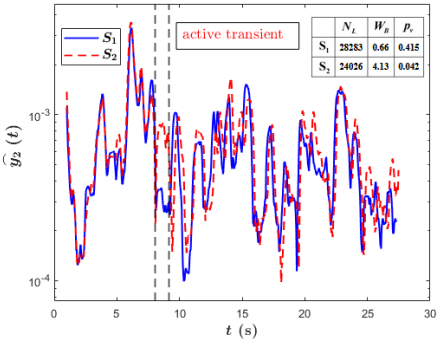

(d) NSM outputs of steady-state parts.

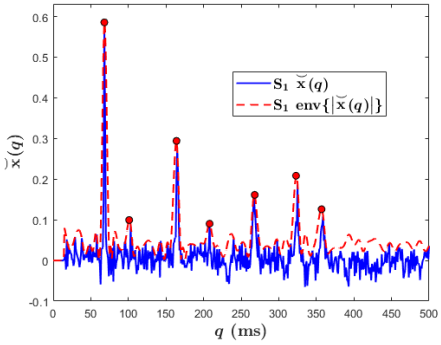

(e) Power cepstrum of the simulated S1 signal.

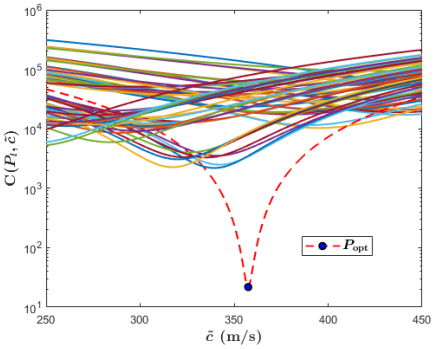

(f) Cost function $C\left(P_l,\tilde{c}\right)$ for S1 signal.

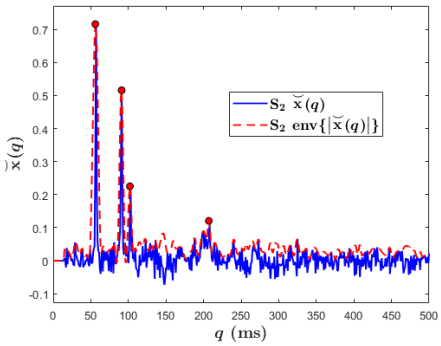

(g) Power cepstrum of the simulated S2 signal.

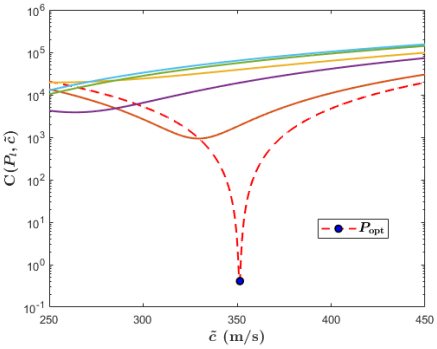

(h) Cost function $C\left(P_l,\tilde{c}\right)$ for S2 signal.

Figure 4.3: Matching method applied to the simulated leak signals. The red dots in the power cepstrum indicate the selected peaks. Each line plot in (f) and (h) denotes the cost function calculated for one of combination of discontinuity locations, whereas the dotted line plot indicates the cost function corresponding to the optimal combination. The blue dot indicates the minimum of the cost function corresponding to the optimal combination.

both less than the critical value $F_{1-\alpha,\,1,\,N_B-2}$ = 6.63. This confirms the inference from the NSM outputs about the detected transients in both signals being active transients.

The first peaks in the NSM outputs of the S1 and S2 signals are located at the 10.031- and 10.16-second marks, respectively. This implies that the transient arrives at S1 129 milliseconds earlier than at S2. Hence, in this simulation example, it can be deduced that only two out of the three theoretically possible scenarios are feasible: one with an out-of-bracket transient source located closer to S1 than S2 and another with an in-bracket transient source located closer to S1. The scenario with an out-of-bracket transient source closer to S2 is not feasible given that the S1 signal has an earlier transient onset. It should be noted that the matching method can only be applied with the S2 signal in the scenario with the in-bracket source because there are no known discontinuities upstream of S1 (relative to the direction of transient propagation in this scenario). The two feasible scenarios are both considered below.

In the scenario with an assumed out-of-bracket transient source, the direction of transient propagation is inferred to be from S1 to S2, so the S1 signal can be used to identify any in-bracket leak present. The TDOAs of reflections from discontinuities downstream of S1 can be identified either from the ACF or cepstrum of the S1 signal, as discussed in Section 4.4. As stated previously, because the reflections can be inverted in phase with respect to the direct-path signal, it is necessary to extract the TDOAs from the envelope or absolute values of the cepstrum. Figure 4.3(e) shows the envelope of the power cepstrum of the transient portion of the S1 signal. In this work, the envelope of signal x will be denoted as $\mathrm{env}\{x\}$. Note that only results obtained with the power cepstrum are reported for the transient method (since they are superior to the autocorrelation results). In order to determine the wave speed and possible leak locations, the cost function $C(P_l, \tilde{c})$ defined in Equation (4.1) was used to search for the wave speed in the interval between 200 and 450 m/s. Since there are 7 TDOAs and 4 known discontinuities within 100 metres downstream of S1 (D2-D4, S2), the total number of realisable combinations P_l is 35. It can be observed from Figure 4.3(f) that the cost function achieves its minimum value at $\tilde{c}$ = 351.5 m/s, which differs from the true wave speed by 0.7%. Alternatively, the wave speed can be determined as $c = d/\Delta T_{\text{onset}}$ = 364 m/s from the distance d = 47 metres between S1 and S2, and the time delay ΔT_{onset} = 129 ms given by the difference between the transient onsets as determined from the NSM outputs. The TDOAs in the combination that minimises the cost function are shown in the upper half of Table 4.2. There are 3 unmatched reflections originating from locations at the indicated distances from S1. To determine which of them is a leak, cross-correlation was applied to the signal segments after the transient. Using the values of the time delay $\hat{\tau}_{\text{peak}}$ = 64.9 ms and wave speed $\tilde{c}$ = 351.5 m/s, the leak location was estimated to be 12.1 metres from S1. Hence, it can be inferred that the discontinuity at 12.1 metres is indeed a leak. Compared to the actual distance

of 12 metres, the error in the estimated leak location is only 0.1 metres. It should be noted that part of the error in the leak location value is due to the limited integer resolution of the TDOA estimates. The other unmatched reflections correspond to secondary reflections (repeated reflections) coming from the discontinuities.

In the second scenario with an assumed in-bracket transient source, only leaks upstream (located after) S2 can be located. It is not possible to locate in-bracket leaks in this case. The TDOAs of reflections from discontinuities upstream of S2 can be estimated from the power cepstrum of the S2 signal shown in Figure 4.3(g). There are 6 ways to assign the 4 TDOAs to the 2 known upstream discontinuities D3 and D4. Figure 4.3(h) shows the cost function $C\left(P_l, \tilde{c}\right)$ evaluated for these 6 possible realisable combinations of the TDOAs. The minimum of the cost function occurs at the value $\tilde{c}$ = 351.5 m/s, which has been used to calculate the locations of the discontinuities shown in the lower half of Table 4.2. The two unmatched reflections indicate unknown discontinuities located at 18.1 and 36.6 metres from X2. These two unmatched reflections actually correspond to secondary reflections (repeated reflections) coming from the discontinuities, but this cannot be inferred without additional information. In a practical situation, another sensor can be deployed upstream of S2 to determine if any of the unknown discontinuities is a leak. Even though it is not possible to reliably infer the presence of a leak in this case, the matching method is still useful, yielding a good estimate of the wave speed that differs by only 0.7% from the true value. Note that even though the transient source is not in-bracket as assumed in this scenario, the direction of propagation was still correct, hence, the reason a plausible estimate of the wave speed was obtained.

Table 4.2: Optimal combination of TDOAs P_{opt} in the simulation example.

S1 signal							
TDOA (ms)	69	103	165	208	267	325	359
Distance from S1 (m)	12.1	18.1	29.0	36.6	46.9	57.1	63.1
Matched discontinuity	**Leak**	-	D2	-	S2	D3	D4
S2 signal							
TDOA (ms)	57	91	103	208			
Distance from S1 (m)	10.0	16.0	18.1	36.6			
Matched discontinuity	D3	D4	-	-			

In order to investigate the robustness of the matching method, the ‘SNR’ (as defined previously in Section 3.4.1 for signals containing transients) of the simulated signals was varied between -6 dB and 3 dB. Figure 4.4 summarises the RMSE (defined in Equation (3.8)) of the leak location and wave speed estimates obtained over 100 runs at each ‘SNR’ value. Different realisations of white Gaussian noise was added to the simulated signals in each run to achieve the given ‘SNR’. Based on these

results, the matching method achieves a good performance for 'SNRs' above -3 dB, especially with regard to the leak location accuracy. The errors in the wave speed estimates are comparatively higher. However, the largest error in the mean wave speed estimate is 14%, which is theoretically better than what is obtainable with in-situ wave speed measurement methods. These simulation results have demonstrated that the proposed matching method is a potentially viable means of detecting and locating leaks as well as estimating the wave speed in the pipe. Ability to estimate the wave speed presents a practical benefit, especially with regard to improving the robustness of leak localisation using the cross-correlation technique. Experimental investigation and further discussion of the method will be carried out in Section 4.6.

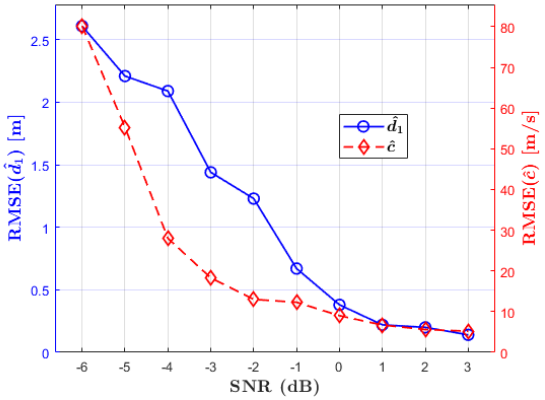

Figure 4.4: The RMSE of the leak location and wave speed estimates obtained using the matching method for simulated transient signals with 'SNRs' between -6 and 3 dB.

4.5.3 Simulation results for the steady-state leak localisation method

The steady-state method was used to locate the leak on the simulated pipe shown in Figure 4.2 above. In this case, only the steady-state portions of the simulated signals were analysed. Figure 4.5 shows the correlation functions and power cepstra of the simulated signals. In this case, white Gaussian noise was added to the signals to achieve an SNR of 3 dB (as defined in Equation (2.4)). Multiple peaks indicated with red dots in the envelopes of the absolute values of the ACFs and power cepstra indicate the presence of reflections in the simulated signals. Peaks in the first 10 milliseconds were disregarded so as to identify only peaks corresponding to reflections. The peak selection thresholds were calculated analogously as the NSM threshold in Section 3.2.1.2 assuming an AFPR of 0.001 and normal distribution for correlation functions and power cepstrum of noise-only signals. The TDOAs of the primary reflections are obvious in the correlation functions and power cepstra and can be determined even without employing Spiesberger's algorithm. Nonetheless, applying Spiesberger's algorithm yields these TDOAs as $\tau_{11}[2,1] = 97$ ms and $\tau_{22}[2,1] = 57$ ms, and the reference time delay as $\tau_{21}[1,1] = 65$ ms. Based on the locations of the known discontinuities, the scenarios with an in-bracket and an out-of-bracket discontinuity are feasible, so they are both considered in the analysis.

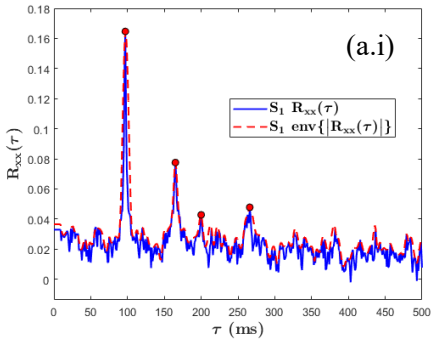

ACF of S1 signal.

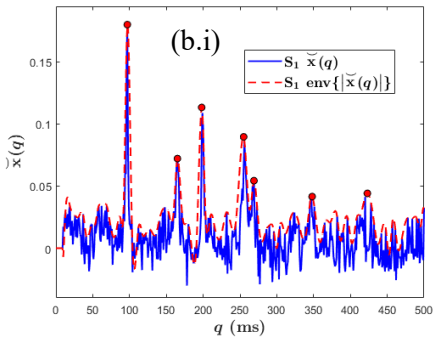

Power cepstrum of S1 signal.

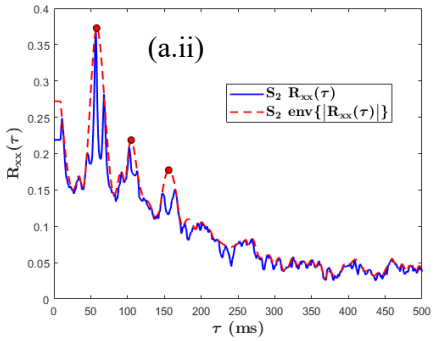

ACF of S2 signal.

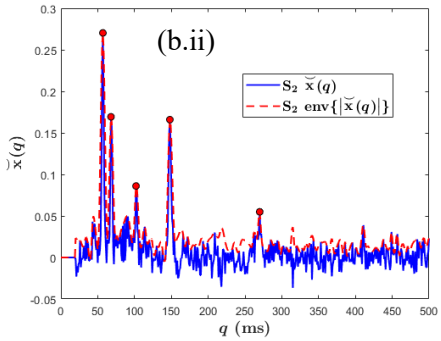

Power cepstrum of S1 signal.

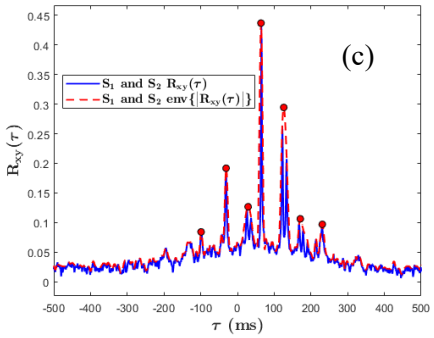

CCF of S1 and S2 signals.

Figure 4.5: Correlation functions and power cepstra of simulated steady-state leak signals. The SNR of the S1 signal is 3 dB.

For the scenario with an in-bracket discontinuity, since the reference time delay $\tau_{21}[1,1]$ is positive, it can be inferred that the leak is located downstream of the known discontinuity D2, so estimates from the S1 signal should be used in locating the leak. Substituting $\tau_{11}[2,1]$, $\tau_{21}[1,1]$, and $\Delta l_{\text{in},1}$ = 29 metres in the expressions for this pipe configuration (Equation (4.5)) gives the leak location as $\hat{d}_1$ = 12.3 metres and wave speed as $\hat{c}_1$ = 344 m/s. These estimates differ by +0.3 metres and 2.8%, respectively, from the true values. As in the matching method, integer resolution of the TDOA limits the accuracy of these estimates. Employing the TDOA estimate $\tau_{22}[2,1]$ from the S2 signal in the leak location and wave speed expressions yields leak location and wave speed values of

$\hat{d}_2$ = 26.4 metres and $\hat{c}_2$ = -90 m/s, respectively. Using the incorrect signal has yielded an implausible wave speed estimate, as stated in Section 4.3. Hence, it is not necessary to explicitly determine the signal to use; the expressions can be evaluated for both signals and the plausible estimates can then be selected.

Since it is known that the primary reflection in the S2 signal does not result from the in-bracket discontinuity (based on the implausible wave speed estimate obtained above), the leak location and wave speed can be estimated from the S2 signal by considering the pipe configuration with one out-of-bracket discontinuity. In this case, the estimates are obtained as $\hat{d}_2$ = 34.9 metres and $\hat{c}_2$ = 351 m/s, respectively, by substituting $\tau_{22}[2,1]$, $\tau_{12}[1,1] = -\tau_{21}[1,1]$, and $\Delta l_{\text{out},2}$ = 10 metres (the closest out-of-bracket discontinuity at D3) in Equation (4.6). The estimates obtained in this case are more accurate because the TDOAs can be identified more clearly from the correlation functions and cepstra due to the shorter distances between S2 and D3.

This simulation example demonstrates the viability of the proposed steady-state leak localisation method. Effects of noise, choice of multipath identification technique, and pipe attenuation on the effectiveness of the method are investigated next.

4.5.3.1 Comparison of multipath identification techniques

To investigate the robustness of the proposed steady-state method and compare multipath identification techniques, the numerical simulation in the example above was repeated for 100 runs at each SNR value between -9 dB and 6 dB, with different realisations of the added white Gaussian noise signal used in each run. The RMSE (defined in Equation (3.8)) of the leak location and wave speed estimates obtained using the autocorrelation and cepstral multipath identification techniques for the out-of-bracket discontinuity scenario are shown in Figure 4.6. Estimates from the power cepstra exhibit lower RMSE, thereby demonstrating the higher accuracy and better noise robustness of the cepstral technique compared to the autocorrelation technique. When the SNR of the signals is high, accurate leak location and wave speed estimates can be obtained using either technique. At low SNR, only the power cepstrum gives a clear indication of the reflections in a signal, as can be observed from the ACFs and power cepstra of a -6 dB simulated S1 leak signal shown in Figure 4.7. The autocorrelation technique fails in this case due to the presence of many noise-induced peaks that are of comparable height with the true reflection peaks in the ACFs. In contrast, the power cepstrum retains distinct peaks corresponding to the reflections. By comparing the ACFs and power cepstra shown in Figure 4.5 above, it can be seen that even in a high-SNR situation, the peaks associated with the reflections are sharper and more distinct in the power cepstrum. The presented results are in complete agreement with the analysis in Section 4.4.3. In the rest of this section, only the results obtained for the power cepstrum are presented due to its vastly superior performance.

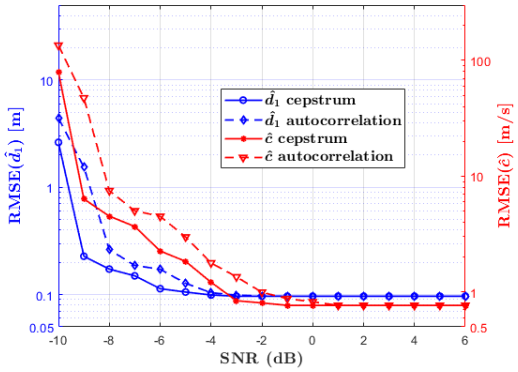

Figure 4.6: RMSE of autocorrelation and cepstral leak location and wave speed estimates obtained using the steady-state multipath identification leak localisation method for simulated leak signals. The SNR of the first signal varied between -10 and 6 dB.

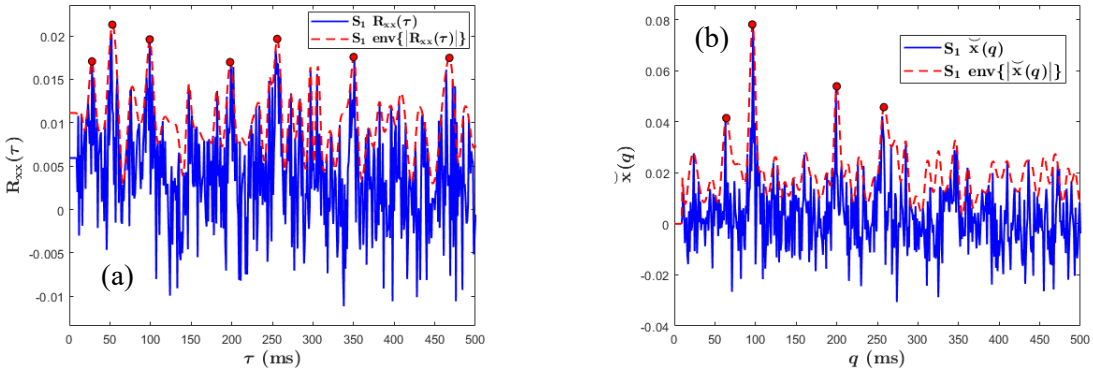

Figure 4.7: Comparison of the ACF and power cepstrum of simulated S1 leak signal with SNR of -6 dB. (a) ACF. (b) Power cepstrum.

4.5.3.2 Effects of pipe properties on multipath identification

To better understand the effects of pipe properties on the ability to locate leaks using the steady-state method, analytical examples are presented for a 'lossy' MDPE pipe with a higher attenuation factor. In this case, the loss factor of the pipe is set to be 10 times larger than the pipe in the leakage test rig. Figure 4.8 shows the ACF and power cepstrum of multipath leak signals simulated at S2 for the new MDPE pipe. White noise was added to the simulated leak signals so that they have an SNR of 3 dB. In this case, it becomes more difficult to identify real peaks corresponding to the reflections in the signals, thereby reducing the effectiveness of locating the leak. The effects of the higher pipe attenuation are more severe on the ACFs than on the cepstrum. In fact, it is almost impossible to detect the presence of reflections from the ACF. While the power cepstrum only exhibits peaks corresponding to a fewer number of reflections (compare Figures 4.8(b) and 4.5(b.ii)), it is still possible to estimate the leak location and wave speed using the cepstral technique, albeit with a lower accuracy compared to the case with a lower attenuation factor. In this case, the estimates are obtained as $\hat{d}_2$ = 33.9 metres and $\hat{c}_2$ = 328 m/s, which represent errors of -1.1 metres and 7% in the leak location and wave speed values, respectively. These results demonstrate that the proposed leak

localisation methodology based on multipath identification is more effective in pipes with lower attenuation. This is investigated further.

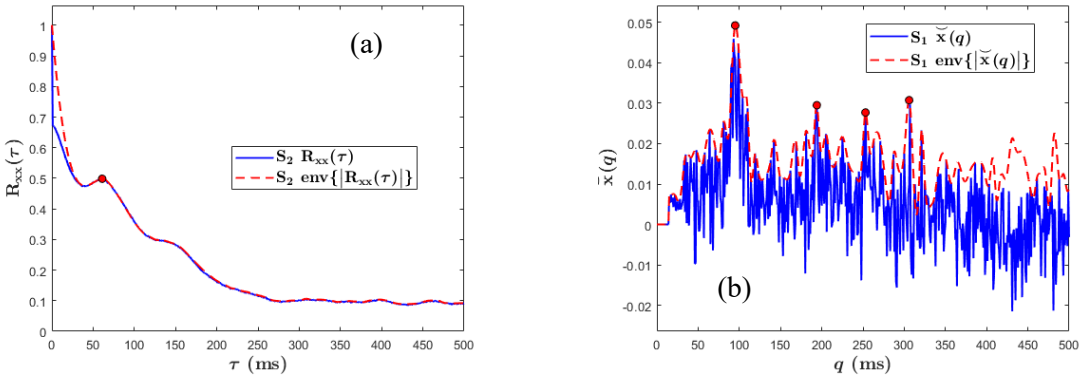

Figure 4.8: Multipath identification in the simulated S2 leak signal in an MDPE pipe with a loss factor of 0.2. (a) ACF. (b) Power cepstrum.

The study above was repeated with the SNR of the signals set at -4 dB while varying the attenuation factor of the MDPE pipe. Figure 4.9 compares the RMSE of the leak location and wave speed values obtained over 100 runs for different attenuation factors using the cepstral technique. It can be observed that the proposed method is indeed more robust and accurate in pipes with relatively low attenuation factors in agreement with the analysis in Section 4.4.3. As is characteristic of all acoustic methods, the performance of the method deteriorates in the presence of higher attenuation, substantially so when the attenuation factor exceeds 1.5×10^{-4} s/m.

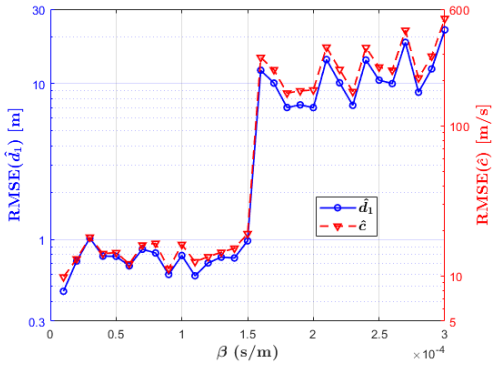

Figure 4.9: RMSE of leak location and wave speed estimates obtained in pipes of different attenuation factors using the cepstral technique.

In addition to interfering with the ability to detect and locate reflections in these pipes, high attenuation also limits the effective distance over which leaks can be located using the proposed method. Experimental evidence has shown that attenuation is high in pipes with diameter greater than 300 millimetres (Lowe et al., 2003; Hunaidi, 2012). Based on Equation (1.2), pipes with either high loss factor or high diameter to thickness ratio D_p/h_p (referred to as standard dimension ratio (SDR)) are generally characterised by higher attenuation. Therefore, based on the simulation results, two types of pipes for which the steady-state method is likely to be less effective are small-diameter pipes with

high loss factor and/or high SDR and large-diameter pipes. As a result, the proposed method is not likely to be effective on trunk mains or pipes made of 'lossy' materials such as PVC (compared to MDPE). Nonetheless, the method can be expected to perform well for typical distribution water pipes with low SDR (11 or less). It must, however, be emphasised that a low attenuation factor may not necessarily guarantee good performance since other factors affect multipath identification, including distance between sensor and discontinuities, noise, etc. Practical limitations of the proposed method will be discussed in Section 4.7.

The numerical simulation results in this section demonstrate that the proposed transient and steady-state multipath identification methods present viable means of locating leaks in a lot of water pipes without need for a priori knowledge of the wave speed. In the next section, these methods are further investigated using experimental leak signals.

4.6 Application of multipath identification leak detection methods to experimental data

The transient and steady-state methods presented in this chapter were used to locate leaks and determine the wave speed in the laboratory leakage test rig using the datasets described in Section 3.4. The representative results obtained for each method are presented in this section.

4.6.1 Experimental results for the active transient leak localisation method

Signals in five datasets with active transients were analysed using the matching method. Transients in these datasets were generated by hitting the pipe at the endcaps in the presence of a leak at L2. Only signals measured at X1 and X3 were considered because of the absence of a known in-bracket discontinuity between X1 and X2 and inability to simulate a leak between X2 and X3. The time histories and NSM outputs of the X1 and X3 signals from one of the datasets analysed were shown in Figures 3.8(c.i)–3.8(c.iii). The transients in the signals were induced by an impact with a metallic rod on the endcap close to X3. Based on the NSM outputs of the steady-state parts of the signals without the transient segments in Figure 3.8(c.iii) and the results of the Brown-Forsythe test in Table 3.2, it was confirmed that the transients in the signals are active transients. Only results obtained for the power cepstrum are reported, since they are vastly superior to the autocorrelation results. Based on the transient onsets (indicated with dots in Figure 3.8(c.ii), the transient source is located closer to X3 than X1. Hence, the only two feasible and applicable scenarios are: (i) an assumed out-of-bracket source closer to X3; and (ii) an assumed in-bracket source closer to X3. Due to absence of multiple discontinuities upstream of X1, the X1 signal is not considered except to determine the possible direction of propagation of the transient. In the first scenario with an assumed out-of-bracket source close to X3, the direction of transient propagation is inferred to be X3 to X1. From the schematic of the leakage test rig in Figure 2.1, there are 4 known discontinuities upstream of X3: the elbow,

measurement points at X2 and X1, and the end-cap close to X1. From the power cepstrum of the X3 signal shown in Figure 4.10(a), 10 TDOAs (marked with red dots) corresponding to reflections in the signal can be identified. There are 210 ways to assign the 4 known discontinuities to the 9 TDOAs. Figure 4.10 (b) shows the cost function $C\left(P_l,\tilde{c}\right)$ (Equation (4.1)) calculated for all possible 126 combinations P_l of the TDOAs and wave speed values between 200 and 450 m/s. The cost function attains its minimum value at $\tilde{c}$ = 363.5 m/s and the combination P_{opt} shown in Table 4.3. This estimated wave speed value differs from the true wave speed by 3%.

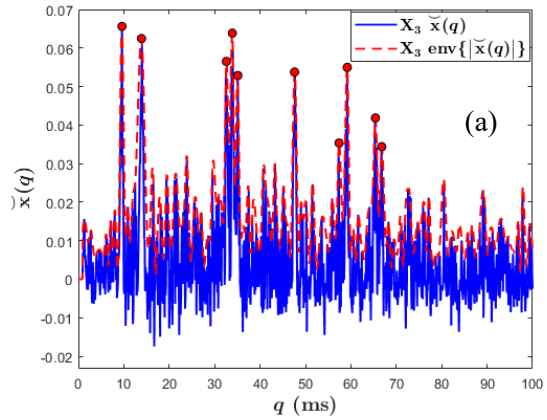

(a.) Power cepstrum of the signal.

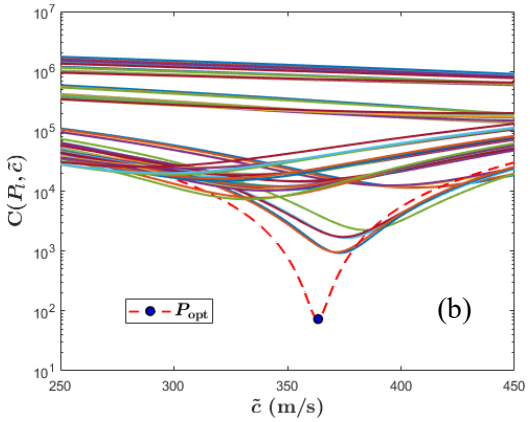

(b.) Cost function $C\left(P_l,\tilde{c}\right)$ in the case of an assumed out-of-bracket transient source.

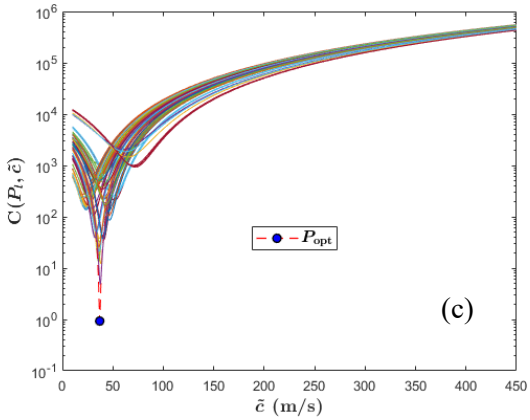

(c.) Cost function $C\left(P_l,\tilde{c}\right)$ in the case of an assumed in-bracket transient source.

Figure 4.10: Applying the matching method to the experimental signal measured at X3 when a transient is induced via impact at the endcap close to X3. Each line plot in (b.) and (c.) represents the cost function computed for a combination of the TDOAs, and the dotted line plot denotes the cost function computed for the optimal combination P_{opt}. The blue dot denotes the minimum of the cost function corresponding to P_{opt}.

Based on the estimated wave speed value, the 5 unmatched TDOAs correspond to discontinuities located at distances of 1.73, 2.58, 6.20, 6.36, 8.68, and 10.74 metres from X3, any of which may be a leak. To determine which corresponds to a leak, cross-correlation was applied to the

signal segments after the transient, giving the leak location as 8.13 metres from X3. It can thus be inferred that the discontinuity at 8.68 metres is indeed a leak. Compared to the actual distance of 8.49 metres, the error in the estimated leak location is 0.19 metres. The presence of a discontinuity at 6.2 metres from X3 possibly indicates a second reflection at the elbow (most likely at the point where it connects to the second pipe). The discontinuity at 10.74 metres appears to be the closed L1 leak valve. It is not clear where the remaining unmatched reflections originate from, but they are possibly reflections from discontinuities upstream of X3: the inlet valve, tee connector, and the endcap. This is very likely considering the early arrival times of these reflections and the relatively short distance between X3 and the upstream discontinuities. Alternatively, the wave speed can be determined as $c = d/\Delta T_{\text{onset}}$ = 359 m/s from the distance d = 11.74 metres between X1 and X3 and the time difference ΔT_{onset} = 32.7 ms between the transient onsets. Using this value of the wave speed yields the leak location as 8.44 metres from X3, which is more accurate than the estimate from the matching method.

Table 4.3: Optimal combination of TDOAs P_{opt} for the experimental signal acquired at X3 on the leakage test rig.

TDOA (ms)	9.5	14.2	32.3	34.1	35.0	47.8	57.3	59.1	64.4	65.4
Distance from X3 (m)	1.73	2.58	5.87	6.20	6.36	8.68	10.41	10.74	11.70	11.89
Matched discontinuity	-	-	Elbow	-	X2	**Leak**	-	-	X1	X1 endcap

In the scenario with an assumed in-bracket transient source, only leaks located upstream of X3 can be located. In this case, there are three known discontinuities upstream of X3: inlet valve, tee connector, and endcap. There are 84 ways to assign the 9 TDOAs identified in the power cepstrum of the X3 signal in Figure 4.10 (a) to these discontinuities. Figure 4.10 (c) shows the cost function obtained for all 84 possible combinations. In this case, the minimum value of the cost function occurs at $\tilde{c}$ = 37 m/s, an unusually low value for the wave speed. This estimate is considered implausible, and it is concluded that this scenario with an in-bracket transient source is infeasible. No further analysis is required. In contrast with the simulation example, in this case, not even a plausible value of the wave speed is obtained. This is because the direction of propagation was correctly assumed in the simulation example, whereas the assumption in this case contradicts the actual transient propagation direction. The X3 sensor does not capture primary reflections from the 3 discontinuities used in evaluating the cost function, resulting in an implausible estimate. This example confirms the soundness of the suggestion to evaluate the cost function for all possible scenarios and then select only the plausible estimates. Scenarios that do not correspond to the real situation will generally yield implausible estimates. Although evaluating the cost function for all possible scenarios increases the computational complexity of the method, it nonetheless helps to resolve the issue associated with

unknown location of the transient source. This makes the method particularly attractive for application with ambient transients, origin of which is usually unknown. In contrast, some fluid transient methods require the relative location of the transient source to be known a priori. Hence, the proposed method is more general in this regard.

The results obtained for the five datasets considered are summarised in Table 4.4. The presented leak location and wave speed estimates were obtained from the signal with the earlier onset. The matching method achieves a good performance for four of the five cases considered with the maximum leak localisation error less than 0.6 metres and wave speed estimates within 8% of the true value. While the method appears to perform well both for hydrophone and accelerometer signals, no definitive conclusions can be made about the effects of the choice of sensors due to the small number of datasets considered. It will be worthwhile to investigate this in further studies. The one case, Dataset 5, for which it fails is considered in more detail below. In this work, a leak localisation method is deemed to have failed if the estimates given by the method are implausible.

Table 4.4: Leak location and wave speed estimates obtained for the datasets.

Parameter	**Sensor**	**Transient source**	**Leak location (distance from X3)**	**Wave speed estimate**
True value			8.49 metres	354 m/s
Dataset				
1	Accelerometer	X3 endcap	8.68	363.5
2	Accelerometer	X1 endcap	8.28	383.5
3	Hydrophone	X1 endcap	8.92	367.5
4	Hydrophone	X3 endcap	7.94	373.0
5	Accelerometer	X1 endcap	10.91	730.5

Figure 4.11 shows the histories and the NSM of the X1 and X3 signals in Dataset 5. While the transients are not as obvious in the time histories compared to the case in Figure 3.8b(i), their presence as well as their active nature was successfully detected by the NSM. Insights into why the method fails for this dataset are revealed by the power cepstrum of the X3 signal shown in Figure 4.11(c). It can be observed that the real peaks corresponding to the reflections cannot be unambiguously determined from the power cepstrum, as there are a lot of noise-induced peaks, some of which are very close to the true TDOAs. As a result, difficulty arises in applying the cost function-based approach. This represents one shortcoming of the proposed method: it becomes unreliable when there many noise-induced peaks in the power cepstrum. The minimum of the cost function in this case occurs at 450 m/s, the set maximum value of the wave speed. After increasing the set maximum wave speed value to 1000 m/s, as shown in Figure 4.11(d), the minimum of the cost function shifts to 730.5 m/s, which is an unreasonably high value for an MDPE pipe. Therefore, it is concluded that the matching method

fails for this dataset. It is, however, still possible to obtain a fairly accurate wave speed estimate from the transient onsets. In this case, the wave speed calculated from the difference between transient onsets is 393 m/s, which differs from the true wave speed by 11%. In such a case where there are many noise-induced peaks in the power cepstrum, it is recommended to calculate the wave speed from the transient onsets and then apply cross-correlation to locate the leak. This recommended approach represents an example of a leak detection approach that combines transient and steady-state methods. Further details about such combined methods will be presented in Chapter 8.

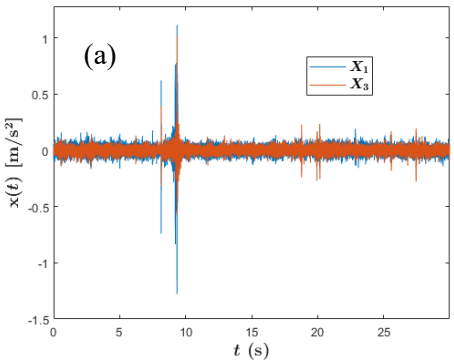

(a) Time histories.

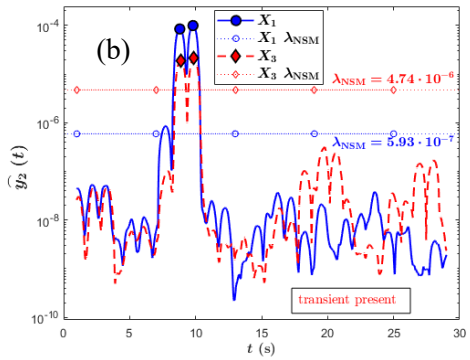

(b) NSM outputs.

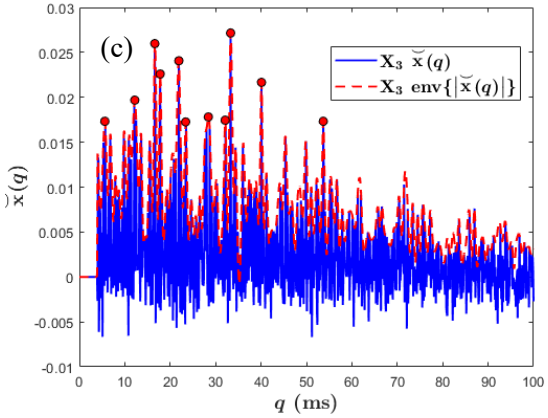

(c) Power cepstrum of the X

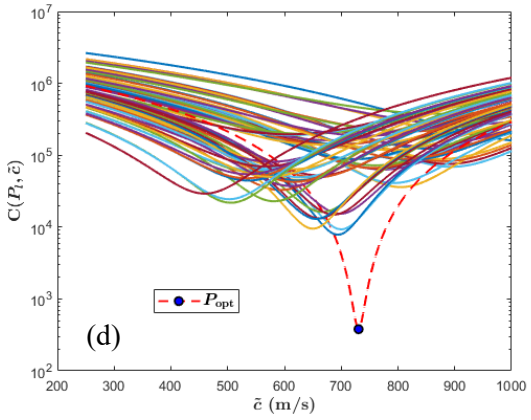

(d) Cost function $C\left(P_l, \tilde{c}\right)$.

Figure 4.11: Applying the matching method to X1 and X3 signals in Dataset 5.

The experimental results above demonstrate the capability of the proposed matching method to locate leaks in water pipes. Even in the one case among the five considered where it fails to accurately locate the leak, a fairly good estimate of the wave speed was obtained. This illustrates another advantage of the method: it can be used to complement the conventional cross-correlation technique by providing an estimate of the wave speed. It must be emphasised that the reported results have been obtained under controlled conditions that may differ substantially from real pipe systems. As a result, it is important to consider the limitations of the leakage test rig discussed in Section 2.5 when extending the results to real pipe systems. Such limitations are discussed in Section 4.7.

4.6.2 Experimental results for the steady-state leak localisation method

Signals measured at X1, X2, and X3 in 10 datasets with steady-state leak signals were analysed using the steady-state leak localisation method described in this chapter. The main information concerning the signals in each dataset was previously summarised in Table 3.4. Based on the schematic of the leakage test rig, the closest discontinuities to the sensors at X1, X2, and X3 are the endcap close to X1, the elbow, and the endcap close to X3, respectively. Hence, for any of the X1-X2 and X1-X3 pairs of signals in the datasets, the pipe configuration corresponds to the case with out-of-bracket discontinuities. Under this configuration, three independent estimates of the wave speed can be obtained for each dataset, one from each of X1, X2, and X3 signals. Note that the X2-X3 pair is not considered since the simulated leak at L1 or L2 is always out of bracket with respect to X2 and X3. The main features of the successful and unsuccessful results obtained for the 20 pairs, two from each dataset, are presented in this subsection.

Figure 4.12 shows the correlation functions and power cepstra of the accelerometer signals acquired at X1 and X2 in one of the successful cases (Dataset 5 in Table 3.4). The presence of multiple reflections in the measured signals is evident from the prominent peaks in their power cepstra. On the other hand, the ACFs fail to highlight the presence of a multipath situation. The signals measured on the leakage test rig represent one of the situations for which the autocorrelation method fails: when tonals or resonances are present in the signals. The presence of resonance in signals measured on the leakage test rig was previously highlighted in Section 2.3.3 (see Figure 2.5(b)). As indicated in the Figures 4.12(a.i) and 4.12(a.ii), the peaks associated with the resonances occur at approximately regular interval of 1.8 ms and 1.3 ms in the ACFs of X1 and X2 signals, respectively. This interval is given by the inverse of the dominant resonant frequency in the signals, 546 Hz in X1 and 767 Hz in X2, denoted with black dots in the normalised PSDs in Figure 4.12(d). As already stated in Section 4.4.3, logarithmic conditioning of the auto-power spectrum allows the cepstrum to detect multipaths in situations when tonal or resonant frequencies are present in the signals. By comparing the ACFs with the power cepstra in Figures 4.12(b.i) and 4.12(b.ii), it can be seen that while the peaks associated with the reflections in the X1 signals are still present in its ACF, the presence of resonance peaks makes it difficult to identify them unambiguously. The situation is even worse in the ACF of the X2 signal, in which the peaks associated with the reflections are completely masked. This example demonstrates that only the cepstral technique can be successfully employed to locate leaks in the test rig using the proposed steady-state method. Hence, only results obtained using this multipath identification technique is presented in the rest of this section.

From the power cepstra in Figure 4.12, the TDOAs of the primary reflections in the X1 and X2 signals were identified as $\tau_{11}[2,1]$ = 1.4 ms and $\tau_{22}[2,1]$ = 1.3 ms, respectively. Substituting these values in the expressions in Equation (4.6), the leak location and wave speed estimates are obtained as

$\hat{d}_1$ = 1.1 metres and $\hat{c}_1$ = 357 m/s from the X1 signal, and as $\hat{d}_2$ = 4.5 metres and $\hat{c}_2$ = 385 m/s from the X2 signal. In this case, even the less accurate leak location and wave speed estimates represent deviations of less than 9% from the true values. It is not clear why the estimates from the X1 signal are more accurate. It may be because the elbow 'scatters' the reflection more severely than the closed boundary condition at the endcap close to X1, thus making the TDOA of the reflection in the X2 signal harder to detect.

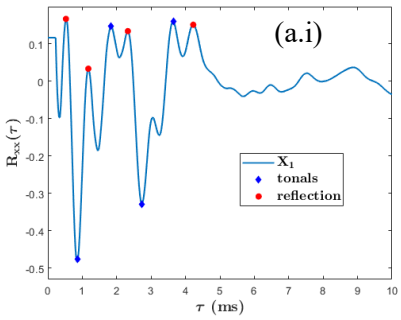

(a.i) ACF of X1 signal.

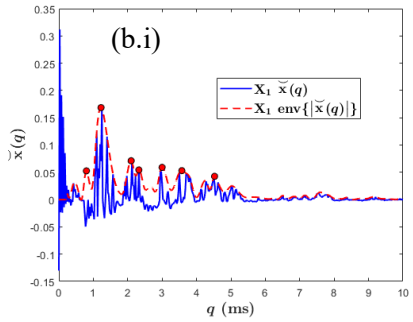

(b.i) Power cepstrum of X1 signal.

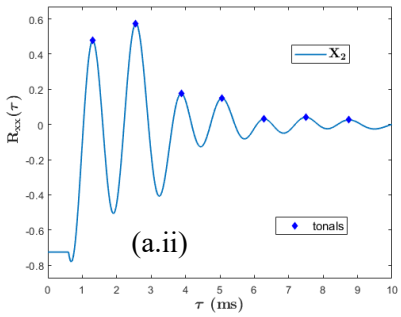

(a.ii) ACF of X2 signal.

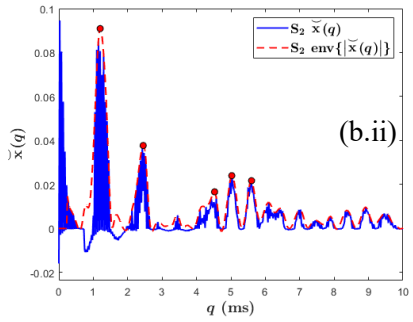

(b.ii) Power cepstrum of X2 signal.

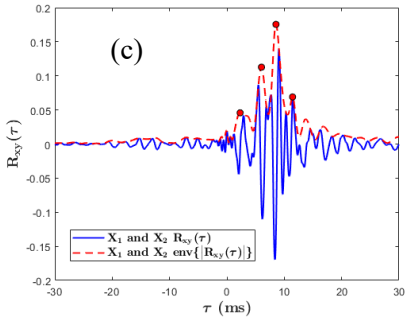

(c) CCF of X1 and X2 signals.

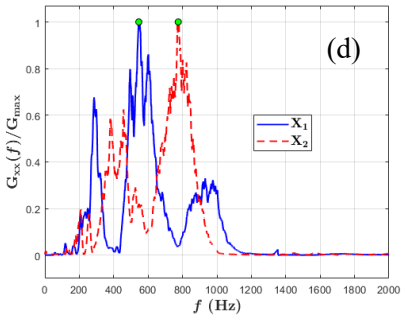

(d) PSDs of X1 and X2 signals.

Figure 4.12: Applying the steady-state multipath identification methods to experimental leak signals measured at X1 and X2.

Among the steady-state signals considered, the proposed method fails for one case of accelerometer signals. The results obtained for the successful cases are summarised in Figure 4.13. A couple of observations can be made about these results. The maximum absolute error in the plausible leak location estimates is 0.17 metres, while the plausible wave speed estimates differ by less than 15% from the true value. As shown by the annotations in Figure 4.13, the accelerometer signals

exhibit a lower RMSE for the leak location and wave speed estimates than the hydrophone signals, which suggests that the proposed method may be better suited for acceleration measurements. One possible reason for this is that the peaks in the correlation functions of acceleration signals are sharper than in those of acoustic pressure signals, as shown by Gao et al. (2005). This is also applicable to the cepstrum. Hence, the TDOAs are likely to be more precisely determined from accelerometer signals than hydrophone signals. However, just as for the matching method, no definite conclusions can be made due to the limited number of datasets considered. Further investigation in this regard is recommended.

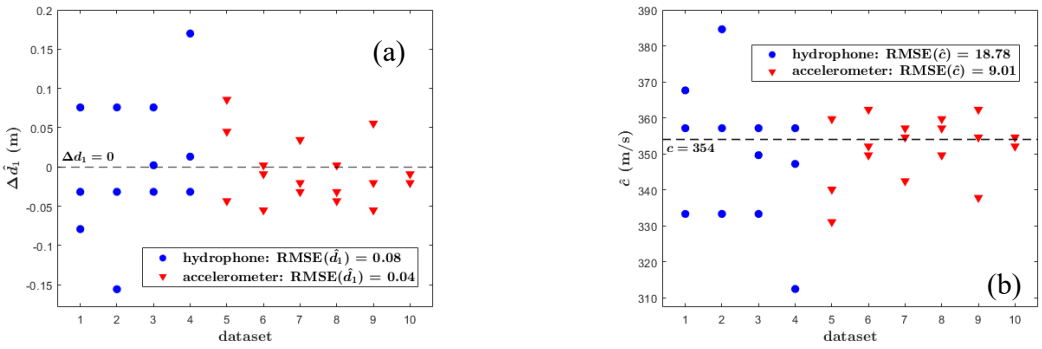

Figure 4.13: Summary of results for the experimental steady-state leak signals: (a) leak localisation error. (b) wave speed.

To gain further insights about the results, more details are presented for an example of an unsuccessful case. The power cepstrum of the X1 signal for a case where the steady-state method fails to give accurate estimates are shown in Figure 4.14. In this case, the presence of many noise-induced peaks in the cepstrum of the X1 signal makes it difficult to unambiguously distinguish the reflections in this signal, thereby causing both Spiesberger's algorithm and the leak localisation method to fail. In fact, if the location of the highest peak (3.025 ms) is used in the calculation, the steady-state method yields a wave speed estimate of 83 m/s, which is not a plausible value for the wave speed in an MDPE pipe. The steady-state method can only succeed when the reflection peaks can be identified in the cepstrum, so its performance will degrade in very noisy environments. Possible measures that can be employed to improve the effectiveness of the method include denoising or filtering the signals in the frequency region where leak noise is dominant prior to applying the method and averaging many realisations of the cepstrum.

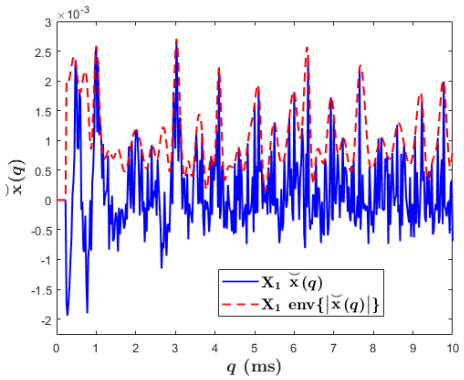

Figure 4.14: Power cepstrum of the X1 signal in an unsuccessful leak localisation case.

Due to the limitations of the rig layout, the proposed methods could not be experimentally investigated for a different pipe configuration. Nonetheless, the limited experimental results presented above demonstrate their potential applicability for locating leaks in water pipes. The ability to locate leaks directly from the measured signals without a priori knowledge of the wave speed is one of their big advantages. In the next section, the inherent limitations of these two methods as well as points that must be considered when generalising the reported experimental results are discussed.

4.7 Limitations of multipath identification leak detection methods

While only limited experimental results for 63-mm diameter in-vacuo MDPE pipes are available, based on theoretical analysis, multipath identification leak detection methods are expected to be a viable means of detecting and locating leaks in a lot of practical situations, especially in distribution pipes. However, some practical limitations of these methods can be identified. Firstly, like all reflectometry-based leak detection methods, they rely on knowledge of discontinuities in the pipe system. If reflections from an unknown discontinuity (such as deteriorated region in a pipe) are wrongly assigned to a known discontinuity, this may lead to the failure of the methods. Hence, the proposed methods can only be applied when an accurate schematic of the pipe system is available. Secondly, reflection-based methods in their current implementations are not capable of detecting leaks that occur at known discontinuities, for example, joint leaks, which represent a substantial proportion of leaks in water distribution networks (Farrow et al., 2017). This limits the scope of application of the proposed methods in real systems. Thirdly, reflection-based methods are only effective if the reflections in the measured signals can be reliably identified. As shown by the theoretical analysis and numerical simulation results, high levels of background noise and pipe attenuation make accurate multipath identification in leak signals considerably more difficult. As a result, the proposed methods may not be very effective in locating leaks in very noisy environments. In order to make the proposed methods more practically useful, it will be worthwhile to address the highlighted shortcomings in future studies.

It is important to note that the reported results have been obtained on a limited leakage test rig, which in many ways is certainly not representative of real water pipe systems. In fact, certain factors may make the leakage rig more favourable to reflectometry-based methodology compared to buried water pipes. First of all, the pipes in the test rig are new and so structurally uniform unlike old, buried water pipes which are likely to have undergo some level of deterioration. As stated above, the presence of unknown discontinuities, such as deteriorated sections and blockages, may affect the ability to locate leaks using multipath identification in real pipe systems. Secondly, as stated in Section 2.5, the relatively short length of the leakage test rig makes it easy to detect reflections and acoustic transients propagating in the pipe. Acoustic transients and reflected waves are likely to travel longer distances in real water pipes, thus decreasing their detectability in the measured signals. Thirdly, one

factor which has not been considered in this study is the possible effect of surrounding medium on acoustic wave reflections. As mentioned in Section 1.2.1, the presence of a surrounding medium heavily affects signal attenuation. The pipe-soil boundary is likely to have 'scattering' effects on transient and leak noise reflections or perhaps even be the source of new reflections in buried pipes (see Kokossalakis (2006)). It is worthwhile to consider such effects in further study of the proposed methods. Lastly, the reported results were only obtained for a relatively simple pipe configuration with few discontinuities. While theoretical results suggest that the methods are capable of detecting leaks in more complex configurations, this is yet to be confirmed experimentally. Further experimental validation is therefore required to investigate the effect of a high number of discontinuities. Because of the outlined limitations, the reported experimental results can be considered to be mostly valid for in-vacuo pipes. However, the good agreement of the results with the theoretical analysis and numerical simulations may provide some valid justification for extending or generalising the experimental results to real buried water pipes.

4.8 Summary and conclusion

An alternative methodology for performing acoustic leak detection and localisation based on multipath identification of reflections in acoustic/vibration signals measured on the pipe has been investigated. Two implementations of this methodology, one transient and the other steady-state, have been proposed and studied. The transient approach, referred to in this work as the matching method, is based on detecting acoustic transient reflections in the measured signals and corresponding them with the known discontinuities. The steady-state method relies on detecting the primary reflections of the leak noise in signals measured at two locations on the pipe. Two multipath identification methods based on the autocorrelation function (ACF) and power cepstrum were derived and analysed for detecting reflections in signals. Theoretical analysis showed that the cepstral method is vastly superior to the autocorrelation method for multipath identification in leak signals. Numerical simulations and experimental data obtained on the leakage test rig were used to investigate the effectiveness of the proposed leak detection methodology and compare with theoretical predictions. The results demonstrated that the methods are potentially viable means for detecting and locating leaks, although they are mostly effective for pipes with low attenuation factor. Possible benefits of the methods include the ability to locate leaks without knowledge of the wave speed as well as capability of estimating the wave speed simultaneously with the leak location. Moreover, the methods can be combined with existing acoustic methods in order to improve robustness of leak detection. Some inherent limitations of the methods were identified, including incapability of detecting leaks that occur at discontinuities such as joints, requirement of an accurate schematic of the pipe system, etc. Future works will focus on tackling the identified limitations, in order to improve the applicability of the methods to real pipe systems.

CHAPTER 5
ACOUSTIC LEAK DETECTION AS A SYSTEM IDENTIFICATION PROBLEM

Motivated by the frequency response and impulse response fluid transient methods described in Chapter 1, this chapter introduces an alternative leak detection approach based on system identification for locating leaks under the cross-correlation setup. The basic principles and implementation of this approach are presented, as well as techniques for dealing with challenges unique to the approach. Simulation and experimental results are provided to demonstrate the effectiveness of the proposed approach.

5.1 Recasting leak localisation as a system identification problem

Under the cross-correlation setup, the measured acoustic/vibration signals are driven by the same leak noise that propagates over different acoustic paths to the two measurement points. As such, the measured leak signals can be modelled as a single-input two-output (SITO) system

$$\begin{cases} x_1(t) = l(t) \otimes h_1 + n_1(t) \\ x_2(t) = l(t) \otimes h_2 + n_2(t) \end{cases} \tag{5.1}$$

where $l(t)$ is the signal generated at the leak location, h_i, $i = 1, 2$, is the IRF that expresses the relationship between $l(t)$ and the leak signal at the i th measurement point, and $n_i(t)$ is the background noise. As stated in Chapter 1, the pipe FRF or IRF encapsulates all information regarding wave propagation in the pipe, including the absolute propagation times from the acoustic source to either measurement point, propagation wave speed, and attenuation (Fuchs and Riehle, 1991). As such, the leak localisation problem under the cross-correlation setup can be viewed alternatively as a system identification problem of determining h_1 and h_2. However, since the input signal $l(t)$ is not available and cannot be measured in most practical situations, the IRFs can only be identified from the measured acoustic/vibration signals using BCI techniques. Hence, acoustic leak localisation can be considered a BCI problem, which with reference to the SITO system in Equation (5.1) can be stated as follows: given only the measured signals $x_1(t)$ and $x_2(t)$, determine the IRFs ('channels') h_1 and h_2. The term *'channels'* will be used throughout this chapter to refer to the IRFs h_1 and h_2 to emphasise that $l(t)$ propagates over two different acoustic paths.

Many techniques for solving the BCI problem have been developed, among which the most commonly used are those based on second-order statistics of the output signals, including time-domain

methods such as least mean squares (LMS) methods (Benesty, 2000), subspace methods (Moulines et al., 1995), least-squares algorithms (Xu et al., 1995a), and linear prediction methods (Abed-Meraim et al., 1997a), and frequency-domain methods such as the normalised multichannel frequency least mean squares (NMCFLMS) method and its variants (Haque and Hasan, 2008; Huang and Benesty, 2003b). While BCI techniques are widely used for applications, such as equalisation of digital communication channels (Tong et al., 1994), speech separation and dereverberation (Haque et al., 2011), and estimation of time delays in passive systems (Huang and Benesty, 2003a), the only relevant example of their application in leak detection available in the literature is the leak localisation method proposed by Yang et al. (2008). In this method, a BCI approach implemented with a genetic algorithm is employed for locating leaks in water pipes without knowledge of the pipeline length. Two main disadvantages of the method are requirement for a priori knowledge of the wave speed and high computational burden. An objective of this chapter is to demonstrate the viability of locating a leak using a BCI strategy without knowledge of the wave speed. The next section describes a technique for estimating the pipe channels blindly.

5.2 Normalised multichannel frequency least-mean squares blind channel identification

In the BCI techniques mentioned in the preceding section, the channels are represented using finite impulse response (FIR) filters of length L, each expressed in vector form as $\mathbf{h}_i = \left[h_{i,1}, h_{i,2}, \ldots, h_{i,L}\right]^T$, $i = 1, 2$. In order for the BCI problem stated above to have a unique solution (up to a scalar multiple), there are two conditions that must be satisfied (Abed-Meraim et al., 1997b). The first condition termed the distinct-channel condition is that the transfer functions of the two channels $H_1(z) = \mathrm{Z}\{\mathbf{h}_1\}$ and $H_2(z) = \mathrm{Z}\{\mathbf{h}_2\}$ must not contain any common zeros. Here, $\mathrm{Z}\{\bullet\}$ denotes the z-transform. If the distinct-channel condition is violated, it becomes impossible to distinguish if the common factor is associated with the input signal or the channels. The second condition is that the input signal must be rich or complex enough to excite all the modes in the channel dynamics. The linear complexity or richness of a finite sequence is analogous to the number of frequency components in an infinite data sequence, which is measured by the persistence of excitation of the signal (Ljung, 1999). Based on this second condition, the input signal cannot be a zero, a constant, or a single sinusoid, for example. In deriving the BCI algorithms, both conditions are assumed to be satisfied.

The most commonly employed methods for solving the BCI problem, i.e., methods based on second-order statistics, estimate the channel IRFs via the minimisation of a cost function defined in terms of the cross-relation (CR) error $\mathbf{e}$ given by

$$\mathbf{e} = x_1 \otimes \hat{\mathbf{h}}_2 - x_2 \otimes \hat{\mathbf{h}}_1 \tag{5.2}$$

where $\hat{\mathbf{h}}_i$ is an estimate of the i th channel IRF $\mathbf{h}_i$. Minimisation of the cost function can be achieved using different algorithms either in the time domain (for example, convex optimisation, LMS algorithm, subspace decomposition) or in the frequency domain (for example, LMS algorithm). For details about these algorithms, the reader is referred to the references given in the proceeding section. Among the available BCI techniques, the NMCFLMS is known to be computationally efficient as a result of computing the cost function in the frequency domain. Also, it provides the ability to incorporate spectral constraints, which is useful for locating the leak using the BCI technique, as will be shown in the next section. Based on these two reasons, the NMCFLMS is selected in this work for estimating the pipe IRFs.

The NMCFLMS estimates the IRFs by iteratively minimising a frequency-domain cost function over successive L -sample time blocks of the output signals in Equation (5.1). In the NMCFLMS algorithm, the cost function $J_{\mathrm{e}}(m)$ in the m th time blocks $\mathbf{x}_1(m)=\left[x_1(mL) \quad x_1(mL+1) \quad \cdots \quad x_1(mL+L-1)\right]^T$ and $\mathbf{x}_2(m)=\left[x_2(mL) \quad x_2(mL+1) \quad \cdots \quad x_2(mL+L-1)\right]$ is defined as

$$J_{\mathrm{e}}(m)=\underline{\mathbf{e}}(m)^H\,\underline{\mathbf{e}}(m) \tag{5.3}$$

$$\text{such that } \left\|\hat{\mathbf{h}}(L,m)\right\|_2=1 \tag{5.4}$$

where $(\bullet)^H$ denotes the Hermitian transpose, $\underline{\mathbf{e}}(m)=\mathbf{F}_L\mathbf{e}(m)$ is the frequency-domain CR error for the m th time blocks, $\mathbf{e}(m)$ is the CR error computed for $\mathbf{x}_1(m)$ and $\mathbf{x}_2(m)$ using Equation (5.2), $\mathbf{F}_L$ denotes a $L\times L$ discrete Fourier transform (DFT) matrix, $\hat{\mathbf{h}}(L,m)=\left[\hat{\mathbf{h}}_1^T(L,m) \quad \hat{\mathbf{h}}_2^T(L,m)\right]^T$ is the stacked vector of the channel estimates and $\|\bullet\|_2$ denotes the ℓ^2 norm. The update equations for minimising $J_{\mathrm{e}}(m)$ using the LMS algorithm are given by (Appendix E1)

$$\hat{\underline{\mathbf{h}}}_i^{10}(L,m+1)=\hat{\underline{\mathbf{h}}}_i^{10}(L,m)-\mu_{\mathrm{bci}}\nabla J_{\mathrm{e},i}(m) \tag{5.5}$$

where m , $m=1,2,\ldots,M$, is the signal frame index,

$$\nabla J_{\mathrm{e},i}(m)=\left[\underline{\mathbf{P}}_i(m)+\delta_{\mathrm{bci}}\mathbf{I}_{2L}\right]^{-1}\times\underline{\mathcal{D}}_k^*(m)\,\underline{\mathbf{e}}^{01}(m),\quad i\neq k \tag{5.6}$$

denotes the gradient of $J_{\mathrm{e}}(m)$ with respect to $\left(\hat{\underline{\mathbf{h}}}_i^{10}(m)\right)^*$;

$$\begin{aligned}\hat{\underline{\mathbf{h}}}_i^{10}(L,m)&=\left[\hat{\underline{\mathbf{h}}}_i^T(L,m) \quad \mathbf{0}_{L\times1}^T\right]^T=\left[\left(\mathbf{F}_L\hat{\mathbf{h}}_i(L,m)\right)^T \quad \mathbf{0}_{L\times1}^T\right]^T\\&=\left[\underline{h}_{i,1}^{10}(m),\underline{h}_{i,2}^{10}(m),\ldots,\underline{h}_{i,2L}^{10}(m)\right]\end{aligned} \tag{5.7}$$

is the zoomed frequency spectrum of the i th channel estimate with L zero padding;

$$\underline{\mathbf{e}}^{01}(m)=\mathbf{F}_{2L}\begin{bmatrix}\mathbf{0}_{L\times1}\\ \mathrm{F}_L^{-1}\,\underline{\mathbf{e}}(m)\end{bmatrix} \tag{5.8}$$

is the $2L$-point DFT of the zero-padded CR error $\mathbf{e}(m)$,

$$\underline{\mathcal{D}}_i(m) = \text{diag}\left\{\mathbf{F}_{2L}\tilde{\mathbf{x}}_i(m)\right\} \tag{5.9}$$

and

$$\underline{\mathbf{P}}_i(m) = \lambda_{\text{bci}}\underline{\mathbf{P}}_i(m-1) + (1-\lambda_{\text{bci}})\underline{\mathcal{D}}_k^*(m)\underline{\mathcal{D}}_k(m),\ k \neq i\ . \tag{5.10}$$

Here, $\hat{\underline{h}}_{i,k}^{10}$ denotes the k th element of $\hat{\underline{\mathbf{h}}}_i^{10}$; $\tilde{\mathbf{x}}_i(m) = \left[\mathbf{x}_i^T(m-1)\quad \mathbf{x}_i^T(m)\right]^T$; $\mathbf{0}_{K\times P}$ denotes a null matrix of size $K \times P$; $\mathbf{F}_L^{-1} = \frac{1}{L}\mathbf{F}_L^H$ is the $L \times L$ inverse DFT matrix; $\text{diag}\{\bullet\}$ creates a diagonal matrix with a given vector; $\lambda_{\text{bci}} = \left[1 - \frac{1}{3(L+1)}\right]^{L+1}$ is the forgetting (smoothing) factor; μ_{bci} is the step-size parameter; and δ_{bci} is the regularisation parameter (a small number) added to avoid singularities during matrix inversion. The frequency spectrum of the channels at the m th time block is zero padded to length $2L$ in order to alleviate the picket-fence effect associated with the discreteness of the DFT (i.e., frequency resolution bias error) (Cerna and Harvey, 2000). The dependency of the channel estimates on the selected channel length L has been explicitly expressed in Equation (5.5). The IRFs $\hat{\mathbf{h}}_1 = \mathbf{F}_L^{-1}\left\{\hat{\underline{\mathbf{h}}}_1\right\}$ and $\hat{\mathbf{h}}_2 = \mathbf{F}_L^{-1}\left\{\hat{\underline{\mathbf{h}}}_2\right\}$ are obtained by taking the $2L$-point inverse DFT of $\hat{\underline{\mathbf{h}}}_1^{10}$ and $\hat{\underline{\mathbf{h}}}_2^{10}$, and discarding the lower half, which will be all zeros when there is no noise. To avoid the all-zero trivial solution, it is necessary to initialise the coefficients of the FIR filters as non-zero vectors. Additionally, in place of the unit-norm constraint, another non-zero constraint, such as the singleton constraint, can be imposed on the channel estimates.

Since the NMCFLMS algorithm can be implemented using the fast Fourier transform (FFT), it is computationally efficient compared to time-domain methods. However, it has some shortcomings, the most serious of which is vulnerability to noise. In the presence of additive noise, the algorithm gives good initial estimate of the channels followed by rapid divergence from this good estimate (He et al., 2018). In order to improve the robustness of the method, additional constraints are usually imposed on the solution, for example, ℓ^p-norm constraint (He et al., 2018), spectral energy constraints (Haque and Hasan, 2008), and linear phase constraints (Jo and Calamia, 2021). The standard NMCFLMS update equation in Equation (5.5) uses a fixed step size, so its performance is highly dependent on the step size. Alternative versions that employ variable step sizes are available (Haque and Hasan, 2007). In the next section, procedures for estimating the wave speed and leak location from the channel estimates will be introduced.

5.3 Estimation of channel length and propagation times of the leak noise in the pipe channels

In order to calculate the wave speed in the pipe and the leak location from the channel estimates, knowledge of the absolute propagation times of the leak noise from the leak location to the two measurement points is required. In this chapter, the term 'propagation time' will be used to refer to the absolute travel time (in samples or seconds as specified) of the leak noise from the leak position to the measurement point(s). There are two difficulties associated with estimating the propagation times: the unknown channel length and possible violation of the distinct-zero condition. The latter can be illustrated as follows. Without loss of generality, it is assumed that the leak is closer to the first measurement point than the second. Let the propagation time in the first channel be D samples (this is also the common leading delay in the two channels). Then the outputs $x_1 = l \otimes h_1$ and $x_2 = l \otimes h_2$ in the SITO system in Equation (5.1) can be obtained from two different systems as shown in Figure 5.1. The first shown in Figure 5.1(a) corresponds to the situation in which the common leading delay D is embedded in the transfer functions, i.e., $H_1(z) = H_0(z)H_{d1}(z)$ and $H_2(z) = H_0(z)H_{d2}(z)$, where $H_0(z) = z^{-D}$ (delay operator in the z-domain) is the common factor shared by the two channels, while $H_{d1}(z)$ and $H_{d2}(z)$ are the distinct factors in the transfer functions. The second shown in Figure 5.1(b) represents the situation where the input signal is first delayed by D samples before being applied to a SITO system with distinct transfer functions $H_{d1}(z)$ and $H_{d2}(z)$. Given

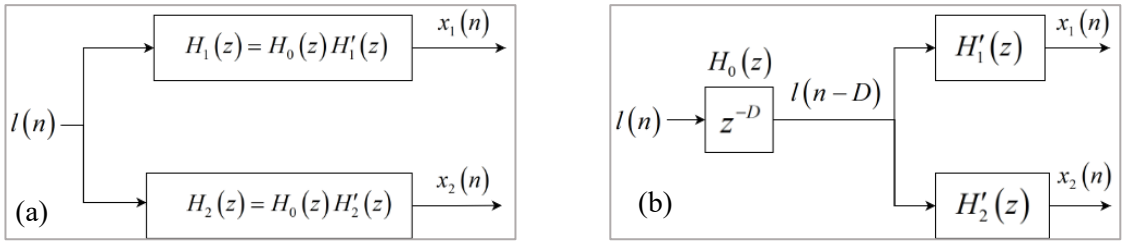

Figure 5.1: Representations of a SITO system with a leading delay. (a) Inherent delay in the transfer functions. (b) Delayed input.

the same input, these two systems have exactly the same outputs, but different channel dynamics. Only the first system is useful for estimating the propagation times in the channels. However, without additional information about the system dynamics, for example, the zero-input response of the system, the NMCFLMS algorithm identifies the IRFs corresponding to the second system. To make the NMCFLMS algorithm suitable for acoustic leak localisation, it must be *forced* to identify the first system instead. Measures for achieving this as well as addressing the challenges associated with unknown channel length and non-robustness to noise are described in this section.

To force the BCI algorithm to identify the first system in Figure 5.1(a), appropriate constraints based on additional knowledge about the pipe acoustic channels must be imposed on the channel estimates. Such information is provided by the FRF model of the pipe channels (Equation (2.5)). Experimental results in Section 2.3.4, as well as results from other studies (Gao et al., 2004; Gao, 2006; Gao and Liu, 2017; Almeida, 2013; Ayala Castillo, 2019) demonstrate that physical acoustic channels of water pipes are adequately described by this FRF model. Two important properties of this model that can be exploited for estimating the propagation times of the leak noise in the pipe channels are the linearity of the FRF phase and exponential decay of the FRF magnitude. Based on the first property, the IRFs h_1 and h_2 are essentially linear-phase FIR filters, the group delays of which correspond to the propagation times in the physical channels. These linear-phase FIR filters are uniquely defined by the distances d_1 and d_2 between the leak and the measurement points. Any change in d_1 or d_2 modifies both the phase and magnitude of the corresponding FRF. Since the pipe IRFs are represented using FIR filters, the propagation times in the channels are given by the group delays of the FIR filters. To ensure that the channel estimates provided by the NMCFLMS algorithm conform to the form dictated by the FRF model, appropriate spectral constraints need to be imposed on the estimates, as will be discussed in the next subsection. Additionally, the optimal channel length that best describes the FIR filters pair that best describes the pipe channels according to the FRF model must also be estimated. Afterwards, the BCI problem is solved for all feasible values of the leading delay D (i.e., the propagation time in the first channel), and then a cost function is defined to identify the best estimate among these. The next subsections concern the descriptions of these approaches.

5.3.1 Spectrally constrained blind channel identification method

According to the FRF model in Equation (2.5), the ideal pipe channel has a linear phase and a linear log-spectrum (this refers to the logarithm of the FRF magnitude), and accordingly, the second derivative of the phase and log-spectrum will be zero. However, in realistic cases, factors such as reflections, non-uniformity of pipes, and measurement noise, may cause these quantities to deviate from a linear form. Based on these, additional spectral constraints that penalise the deviation of the phase and log-spectrum of the channel estimates from a linear form are introduced in the NMCFLMS algorithm in order to ensure that the estimates conform to the form dictated by the FRF model. The modified cost function of the spectrally constrained algorithm that include these additional constraints is given by

$$\begin{aligned} \tilde{J}(m) &= J_{\mathrm{e}}(m) - \eta_{\mathrm{rb}}(m) J_{\mathrm{rb}}(m) + \eta_{\mathrm{ph}}(m) J_{\mathrm{ph}}(m) + \eta_{\mathrm{ls}}(m) J_{\mathrm{ls}}(m) \\ &\text{such that} \quad \left\| \hat{\mathbf{h}}(m) \right\|_2 = 1 \end{aligned} \tag{5.11}$$

where $J_{\mathrm{e}}(m)=\underline{\mathbf{e}}(m)^{H}\,\underline{\mathbf{e}}(m)$ is the cost function of the original NMCFLMS algorithm; $J_{\mathrm{ph}}(m)$ is the phase penalty term; $J_{\mathrm{ls}}(m)$ is the log-spectrum penalty term; $J_{\mathrm{rb}}(m)$ is the ℓ^{p}-norm penalty term defined by He et al. (2018) for faster convergence and improved noise-robustness of the NMCFLMS algorithm; and $\eta_{\mathrm{rb}}(m)$, $\eta_{\mathrm{ph}}(m)$, and $\eta_{\mathrm{ls}}(m)$ are the step sizes for the ℓ^{p}-norm, phase, and log-spectrum constraints, respectively. The phase $J_{\mathrm{ph},i}(m)$ and log-spectrum $J_{\mathrm{ls},i}(m)$ penalty terms for the i th channel are defined as

$$J_{\mathrm{ph},i}(m)=\sum_{k=2}^{2L-1}\left|\Omega_{i,k+1}(m)-2\Omega_{i,k}(m)+\Omega_{i,k-1}(m)\right|^{2} \tag{5.12}$$

and

$$J_{\mathrm{ls},i}(m)=\sum_{k=2}^{2L-1}\left|\Psi_{i,k+1}(m)-2\Psi_{i,k}(m)+\Psi_{i,k-1}(m)\right|^{2} \tag{5.13}$$

where $\Omega_{i,k}$ and $\Psi_{i,k}$ are the k th element of unwrapped phase vector $\mathbf{\Omega}_{i}=\mathrm{unwrap}\left\{\arg\left\{\left[\underline{\hat{h}}_{i,1}^{10}(m),\ \ldots,\ \underline{\hat{h}}_{i,2L}^{10}(m)\right]^{T}\right\}\right\}$ and log-spectrum vector $\mathbf{\Psi}_{i}(m)=\log\left\{\left[\left|\underline{\hat{h}}_{i,1}^{10}(m)\right|,\ \ldots,\ \left|\underline{\hat{h}}_{i,2L}^{10}(m)\right|\right]^{T}\right\}$, respectively, $\arg\{\bullet\}$ denotes the argument of a complex number, and $\mathrm{unwrap}\{\bullet\}$ denotes the phase unwrapping operation. These penalty terms represent the squared summations of the second-order numerical differentiation of the unwrapped phase and of the log-spectrum. The update equations for the spectrally constrained NMCFLMS algorithm are obtained as (Appendix E2)

$$\hat{\mathbf{h}}_{i}^{10}(L,m+1)=\hat{\mathbf{h}}_{i}^{10}(L,m)-\mu_{\mathrm{bci}}\nabla J_{\mathrm{e},i}(m)+\mu_{\mathrm{bci}}\begin{Bmatrix}\eta_{\mathrm{rb}}(m)\nabla J_{\mathrm{rb},i}(m)\\ -\eta_{\mathrm{ph}}(m)\nabla J_{\mathrm{ph},i}(m)\\ -\eta_{\mathrm{ls}}(m)\nabla J_{\mathrm{ls},i}(m)\end{Bmatrix} \tag{5.14}$$

where $\nabla J_{\mathrm{e},i}(m)$ is given in Equation (5.6);

$\nabla J_{\mathrm{rb},i}(m)=p\left[\underline{\mathbf{P}}_{i}(m)+\delta_{\mathrm{bci}}\mathbf{I}_{2L}\right]^{-1}\left|\hat{\mathbf{h}}_{i}^{10}(m-1)\right|^{p-1}\odot\exp\left\{j\arg\left(\hat{\mathbf{h}}_{i}^{10}(m)\right)\right\}$ is the gradient of the ℓ^{p}-norm term, $j=\sqrt{-1}$ is the imaginary unit, p $(1\le p<2)$ is the order of the ℓ^{p}-norm;

$\nabla J_{\mathrm{ph},i}(m)=\frac{j}{2}\mathbf{T}_{i}(m)\left\{\mathbf{Q}\mathbf{\Omega}_{i}(m)\right\}$ is the gradient of the phase-related penalty term;

$\nabla J_{\mathrm{ls},i}(m)=\frac{1}{2}\mathbf{T}_{i}(m)\left\{\mathbf{Q}\mathbf{\Psi}_{i}(m)\right\}$ is the gradient of the log-spectrum term;

$\mathbf{T}_{i}(m)=\mathrm{diag}\left[\dfrac{\hat{\mathbf{h}}_{i,1}^{10}(m)}{\left|\hat{\mathbf{h}}_{i,1}^{10}(m)\right|^{2}},\ \cdots,\ \dfrac{\hat{\mathbf{h}}_{i,2L}^{10}(m)}{\left|\hat{\mathbf{h}}_{i,2L}^{10}(m)\right|^{2}}\right]$; $\odot$ denotes element-wise multiplication; and

$$\mathbf{Q}=\left(\begin{array}{l}12\mathbf{I}_{2L\times 2L}-8\begin{bmatrix}\mathbf{0}_{(2L-1)\times 1} & \mathbf{I}_{(2L-1)\times(2L-1)}\\ 0 & \mathbf{0}_{1\times(2L-1)}\end{bmatrix}-8\begin{bmatrix}\mathbf{0}_{1\times(2L-1)} & 0\\ \mathbf{I}_{(2L-1)\times(2L-1)} & \mathbf{0}_{(2L-1)\times 1}\end{bmatrix}\\ +2\begin{bmatrix}\mathbf{0}_{(2L-2)\times 1} & \mathbf{I}_{(2L-2)\times(2L-2)}\\ \mathbf{0}_{2\times 1} & \mathbf{0}_{1\times(2L-2)}\end{bmatrix}+2\begin{bmatrix}\mathbf{0}_{1\times(2L-2)} & \mathbf{0}_{1\times 2}\\ \mathbf{I}_{(2L-2)\times(2L-2)} & \mathbf{0}_{(2L-2)\times 1}\end{bmatrix}\end{array}\right)\odot\begin{bmatrix}\mathbf{0}_{1\times 2L}\\ \mathbf{I}_{(2L-2)\times 2L}\\ \mathbf{0}_{1\times 2L}\end{bmatrix}.$$

The gradients in Equation (5.14) are taken with respect to the complex conjugates of the channel estimates, i.e., $\left(\hat{\underline{\mathbf{h}}}_i^{10}(m)\right)^*$ (see Appendix E2). The step sizes are given by

$$\left[\eta_{\mathrm{rb}}(m)\quad \eta_{\mathrm{ph}}(m)\quad \eta_{\mathrm{ls}}(m)\right]=\left|\left[\nabla J_{\mathrm{rb},i}(m)\quad -\nabla J_{\mathrm{ph},i}(m)\quad -\nabla J_{\mathrm{ls},i}(m)\right]^{\dagger}\nabla J_{\mathrm{e},i}(m)\right| \quad (5.15)$$

where † denotes the pseudoinverse. The spectrally constrained variant of the NMCFLMS in Equation (5.14) offers the computational advantages of the conventional NMCFLMS algorithm, while ensuring the estimated channels conform to the FRF model in Equation (2.5). Its robustness to noise is improved by the inclusion of the ℓ^p-norm constraint.

5.3.2 Estimation of channel length

In order to correctly identify the channel IRFs, it is necessary to ensure that the channel length L is accurately estimated. In other words, there is need to estimate the channel length L_{opt} of the FIR filters that best describe the pipe channels. If L is underestimated ($L<L_{\mathrm{opt}}$), the BCI algorithm gives inaccurate estimates, while in the case of overestimation ($L>L_{\mathrm{opt}}$), the BCI solution is no longer unique. The estimation of L_{opt} can be achieved using least sum of squared equation error (LSSE) method proposed by Gerstacker and Taylor (2003). This method is described as follows. As shown by Abed-Meraim et al. (1997a), the z-transforms $\hat{H}_1(z,L)$ and $\hat{H}_2(z,L)$ of the channel estimates obtained with an overestimated channel length $L>L_{\mathrm{opt}}$ will be of the form $\hat{H}_i(z,L)=R(z)H_i(z,L_{\mathrm{opt}})$, i.e., a product of the optimal ('true') channel transfer $H_i(z,L_{\mathrm{opt}})$ of degree L_{opt} with an unknown scalar polynomial $R(z)$ of degree $L-L_{\mathrm{opt}}$. As a result, the Diophantine equation in the coefficients of the scalar polynomials $\tilde{H}_1(z)$ and $\tilde{H}_2(z)$:

$$\hat{H}_1(z,L)\tilde{H}_2(z)-\hat{H}_2(z,L)\tilde{H}_1(z)=0 \quad (5.16)$$

will only have a solution for $L\geq L_{\mathrm{opt}}$ and no solution for $L<L_{\mathrm{opt}}$ (as the equation is underdetermined for these values). Under ideal conditions, the sum of the squares of the errors (denoted as $\mathrm{LSSE}(L)$) in the least-squares solution $\left[\tilde{H}_1(z)\quad \tilde{H}_2(z)\right]^T$ of Equation (5.16) will be zero if and only if

$L \geq L_{\text{opt}}$. For real conditions, it can be expected that $\text{LSSE}(L)$ decreases significantly at the transition point $L = L_{\text{opt}} - 1 \rightarrow L = L_{\text{opt}}$. Based on this, in the LSSE method, L_{opt} is given by the value of L that minimises the cost function

$$J_{\text{LSSE}}(L) = \frac{\text{LSSE}(L)}{\text{LSSE}(L-1)} \ . \tag{5.17}$$

A unit-norm constraint is imposed on the least-squares solution of Equation (5.16) to avoid the all-zero trivial solution. The range of possible values for the channel length $L_{\min} \leq L \leq L_{\max}$ is obtained by rearranging the cross-correlation equation:

$$\begin{cases} L_{\min} = 2\left\lfloor \left(\dfrac{d + c_{\min} \cdot \tau_{\text{peak}}}{2c_{\max}} \right) \cdot F_s \right\rfloor + 1 \\ L_{\max} = 2\left\lceil \left(\dfrac{d + c_{\max} \cdot \tau_{\text{peak}}}{2c_{\min}} \right) \cdot F_s \right\rceil + 1 \end{cases} \tag{5.18}$$

where F_s is the sampling rate; τ_{peak} is the time delay (in seconds) between the measured signals; $c_{\min}$ and $c_{\max}$ are the minimum and maximum values of the wave speed obtained by subtracting and adding some tolerance to a historical or calculated wave speed value; and $\lfloor \bullet \rfloor$ and $\lceil \bullet \rceil$ indicate the floor and ceiling functions, respectively. The inclusion of the factor of 2 and addition of 1 in the calculation of $L_{\min}$ and $L_{\max}$ is due to the fact that the group delay of a linear-phase filter of length L is $(L-1)/2$ samples. The channel estimates in the LSSE method are obtained with L set to $L_{\max}$, and the cost function $J_{\text{LSSE}}(L)$ is evaluated for values in the range $L_{\min} \leq L \leq L_{\max}$. Since the channel length must be long enough to accommodate the time delay $T_{\text{peak}} = \tau_{\text{peak}} \cdot F_s$ (in samples) between the signals, an alternative approach to determine the channel length is to estimate the channel IRFs for progressively increasing values of L until the difference between the propagation times becomes equal to T_{peak}. After the optimal channel length L_{opt} has been obtained, the propagation time in the first channel can then be estimated using the approach described in the next subsection.

5.3.3 Estimation of propagation times of the leak noise in the acoustic leak pipe channels

In order to estimate the leading delay D_{opt} in the first channel, the channel estimates are first obtained for all feasible values of the leading delay $0 \leq D \leq D_{\max} = \lceil d \cdot F_s / 2c_{\min} \rceil$ with the channel length L set to L_{opt}. The upper limit of the leading delay ($D_{\max}$) corresponds to a situation where the leak is exactly at the midpoint of the pipe. For each feasible value of D, a singleton constraint is imposed on

the first channel estimate by initialising the channel estimate as $\hat{\mathbf{h}}_1\left(L_{\text{opt}},0\right)=\left[\underbrace{0,0,\ldots 0}_{D-1},1,\underbrace{0,0,\ldots 0}_{L_{\text{opt}}-D-1}\right]$.

Note that it is assumed without loss of generality that the first measurement point is closer than the second measurement point to the leak. This constraint forces the BCI algorithm to assign the highest value in the channel FIR filter estimate to the D th coefficient. If the sign of τ_{peak} indicates that the second measurement point is closer, then the signals x_1 and x_2 should be swapped. The value of D_{opt} is then determined from the channel estimates via the two approaches described below.

The first approach is to determine D_{opt} as the value of D that minimises a cost function $J_\varepsilon\left(D,L_{\text{opt}}\right)$ constructed from the deconvolution errors of the channel estimates:

$$J_\varepsilon\left(D,L_{\text{opt}}\right)=\frac{\mathrm{E}\left\{e_1^2\left(D,L_{\text{opt}}\right)\right\}}{\mathrm{E}\left\{x_1^2\right\}}+\frac{\mathrm{E}\left\{e_2^2\left(D,L_{\text{opt}}\right)\right\}}{\mathrm{E}\left\{x_2^2\right\}} \tag{5.19}$$

where $\mathrm{E}\{\bullet\}$ denotes mathematical expectation or averaging, $e_i\left(D,L_{\text{opt}}\right)=x_i-\hat{l}\otimes\hat{h}_i$ is the deconvolution error for the i th channel estimate obtained with the channel length set to $L=L_{\text{opt}}$ and a singleton constraint set at the D th coefficient of the FIR filter of the first channel, and $\hat{l}$ denotes an estimate of the input signal, which can be recovered from the measured signals using either the multichannel input/output theory (MINT) (Miyoshi and Kaneda, 1988) or the multiple-error least mean squares (ME-LMS) method (Elliott and Nelson, 1985). In both MINT and ME-LMS methods, $\hat{l}$ is given by $\hat{l}=\hat{g}_1\otimes x_1+\hat{g}_2\otimes x_2$, where $\hat{g}_1$ and $\hat{g}_2$ are the multichannel inverse filters of the estimated channels $\hat{h}_1$ and $\hat{h}_2$. For SITO systems, the MINT and ME-LMS methods only differ in how the inverse filters are obtained. The cost function $J_\varepsilon\left(D,L_{\text{opt}}\right)$ evaluates how well the estimated pipe IRFs $\hat{h}_1$ and $\hat{h}_2$, and the recovered source signal $\hat{l}$ approximate the actual measured signals $x_1=l\otimes h_1$ and $x_2=l\otimes h_2$. It attains a value of zero if and only if $e_1=e_2=0$, which is only possible if the estimated channels are scalar multiples of the true channels. The value $D=D_{\text{opt}}$ that minimises $J_\varepsilon\left(D,L_{\text{opt}}\right)$ is considered the leading delay in the first physical pipe channel. A similar approach was employed by Furuya and Kaneda (1997) for recovering an unknown source signal in a two-channel system.

The second approach determines D_{opt} as the value of D that minimises a cost function $J_\beta\left(D,L_{\text{opt}}\right)$ constructed from estimates of the pipe attenuation factor:

$$J_\beta\left(D,L_{\text{opt}}\right)=\left|\frac{1}{2}\left(\frac{\hat{\beta}_1\left(D,L_{\text{opt}}\right)}{\hat{\beta}_2\left(D,L_{\text{opt}}\right)}+\frac{\hat{\beta}_2\left(D,L_{\text{opt}}\right)}{\hat{\beta}_1\left(D,L_{\text{opt}}\right)}\right)-1\right| \tag{5.20}$$

where $\hat{\beta}_1\left(D,L_{\text{opt}}\right)$ and $\hat{\beta}_2\left(D,L_{\text{opt}}\right)$ are estimates of the attenuation factor obtained from the magnitude of the first and second estimated channel FRFs, respectively, for channel length L_{opt} with a singleton constraint set at the D th coefficient of the FIR filter of the first channel. The attenuation factor is estimated via linear regression of the log-spectrum; specifically, $\hat{\beta}_i\left(D,L_{\text{opt}}\right)=-s_i/\hat{d}_i$, where s_i is the slope of the log-spectrum and $\hat{d}_i$ is the leak location estimate obtained using Equation (5.23) below. When the two pipe IRFs are accurately estimated (such that they conform to the FRF model), the values of $\hat{\beta}_1\left(D,L_{\text{opt}}\right)$ and $\hat{\beta}_2\left(D,L_{\text{opt}}\right)$ will be nearly equal, and $J_\beta\left(D,L_{\text{opt}}\right)$ will attain a small value. Conversely, if the channels are poorly estimated, then $J_\beta\left(D,L_{\text{opt}}\right)$ will be large.

The use of two different cost functions improves the robustness of the BCI technique, as they can be used to check consistency, and the optimal leading delay $\bar{D}_{\text{opt}}$ is taken as the average (approximated to the nearest integer) of the two estimates if they are close. Consequently, the propagation times t_1 and t_2 (in seconds) of the leak noise from the leak location to the first and second measurement points, respectively, are

$$\begin{cases} t_1=\bar{D}_{\text{opt}}/F_s \\ t_2=\dfrac{\bar{D}_{\text{opt}}}{F_s}+\tau_{\text{peak}} \end{cases}. \tag{5.21}$$

Since the group delay of a linear-phase FIR filter is given by the slope of its Fourier phase (Oppenheim et al., 1996), an alternative way to estimate the propagation times t_1 and t_2 is via linear regression of the unwrapped phase of the FT of the estimated channels. The leak location and wave speed values can be obtained in a straightforward manner from the propagation times, as described in the next section.

5.4 Acoustic leak localisation procedures using blind channel identification

The propagation wave speed in the pipe can be computed from the propagation times t_1 and t_2 as

$$\hat{c}=\frac{d}{t_1+t_2}=\frac{d\cdot F_s}{2\bar{D}_{\text{opt}}+\hat{\tau}_{\text{peak}}\cdot F_s}. \tag{5.22}$$

Substituting this wave speed value and the time delay $\hat{\tau}_{\text{peak}}=t_2-t_1$ in the cross-correlation equation (Equation (1.1)) gives the leak location as

$$\hat{d}_1 = \frac{t_1}{t_1 + t_2} d = \frac{\bar{D}_{\text{opt}}}{2\bar{D}_{\text{opt}} + \hat{\tau}_{\text{peak}} \cdot F_s} d \quad . \tag{5.23}$$

Locating the leak using Equation (5.23) does not require a priori knowledge of the wave speed in contrast with the conventional cross-correlation method. All necessary parameters are obtained from the measured leak signals exclusively. This leak localisation approach using a BCI technique can thus be considered *minimalistic* and *self-contained*. The procedures for locating a leak using the BCI technique are summarised as follows:

i. Pre-process the signals by passing them through a bandpass filter whose passband lie in the frequency region where the leak signal is dominant over the noise. This region can be determined using either the coherence-based criterion (Muggleton et al., 2011) or the CPS magnitude criterion (Almeida, 2013) mentioned in Section 1.2.3. Determine the time delay $\hat{\tau}_{\text{peak}}$ between the leak signals using any time delay estimator.

ii. Determine $L_{\min}$ and $L_{\max}$ using Equation (5.18). The value of $L_{\max}$ will be employed as the overestimated channel length. Using the spectrally constrained NMCFLMS algorithm, estimate the pipe channel for this overestimated channel length and determine the optimal channel length L_{opt} using the LSSE cost function in Equation (5.17) restricting the search to values of L between $L_{\min}$ and $L_{\max}$.

iii. Using the spectrally constrained NMCFLMS algorithm, estimate the pipe channels for the optimal channel length L_{opt} and all feasible values of the leading delay $0 \le D \le \lceil d \cdot F_s / 2c_{\min} \rceil$. Determine the optimal leading delay estimates D_{opt} using the deconvolution error and attenuation-based cost functions in (5.19) and (5.20). Take the final common delay estimates $\bar{D}_{\text{opt}}$ as the average (rounded to an integer) of the two estimates. The channel estimates corresponding to L_{opt} and $\bar{D}_{\text{opt}}$ are considered the best channel estimates. If the two estimates of D_{opt} given by the cost functions are inconsistent (more than 3 samples apart), then considering modifying the parameters of the NMCFLMS algorithm, for example, adjusting $c_{\min}$ and $c_{\max}$ or changing the frequency range for linear regression. If this does not lead to better results, then consider the method to have failed. The threshold of 3 samples is suggested based on simulation results.

iv. Finally, calculate the wave speed and leak location using Equations (5.22) and (5.23).

It is recommended that the spectral constraints be imposed only in the passband of the applied bandpass filter (if any). Also, the wave speed, leak location, and attenuation values obtained from

regressions in this frequency interval over multiple long signal segments can be averaged to reduce the effects of noise. In the next section, the viability of locating leaks using the proposed procedures is investigated using simulated and experimental leak signals.

5.5 Results and discussion

In this section, numerical simulations and experimental results are provided to investigate the effectiveness of the proposed system identification leak localisation approach and compare its performance with that of the conventional cross-correlation method. The code for the spectrally constrained NMCFLMS algorithm was implemented using functions provided in the Blind System Identification and Equalisation (BSIE) toolbox (Habets et al., 2011).

5.5.1 Simulation results for the blind channel identification leak localisation method

The BCI leak localisation technique was employed to locate a leak in a numerically simulated pipe, the properties of which are the same as the MDPE pipes in the leakage test rig (c = 354 m/s, β = 2.1×10^{-5} s/m.). With reference to the cross-correlation setup in Figure 1.1, the measurement points were arbitrarily set to be at distances of d_1 = 9 metres and d_2 = 25 metres from the leak. The simulation procedures were previously described in Section 4.5.1. With the sampling rate set at 1 kHz, the group delays of the simulated linear-phase FIR filters representing the pipe IRFs h_1 and h_2 in Equation (5.1) are 26 and 71 samples, respectively. Gaussian noise traces of the same power were added to the generated leak signals such that the first signal has an SNR of 6 dB. Prior to applying the BCI leak localisation algorithm, a random number of samples were removed from the start of the simulated signals.

Using the BCC, the time delay between the two simulated leak signals was determined to be $\hat{\tau}_{\text{peak}}$ = 45 ms. The minimum and maximum values of the wave speed were taken as $c_{\min}$ = 250 and $c_{\max}$ = 450 m/s, respectively, thereby yielding the minimum filter length $L_{\min}$ = 101 and maximum length $L_{\max}$ = 219. Figure 5.2(a) shows the plots of the LSSE cost function calculated for the channel estimates obtained for $L_{\max}$, with the value of the candidate channel length restricted to the interval $L_{\min} \le L \le L_{\max}$. It can be observed that this cost function achieves its minimum at L = 143, and hence this value is taken as the optimal channel length L_{opt}. The deconvolution error and attenuation-based cost functions calculated for channel estimates corresponding to this channel length and values of leading delays between 0 and $D_{\max}$ = 68 are also shown in Figure 5.2(b). Both cost functions are minimised at D = 26, thus giving the optimal leading delay as $\bar{D}_{\text{opt}}$ = 26. The channel estimates

obtained for the optimal filter length $L_{\text{opt}} = 143$ and leading delay $\bar{D}_{\text{opt}} = 26$ are compared with the simulated pipe IRFs in Figures 5.3(a)–5.3(d). Each IRF has been normalised by its maximum coefficient. Examination of the IRFs and their frequency-domain representations shows that they have been correctly identified by the spectrally constrained NMCFLMS algorithm.

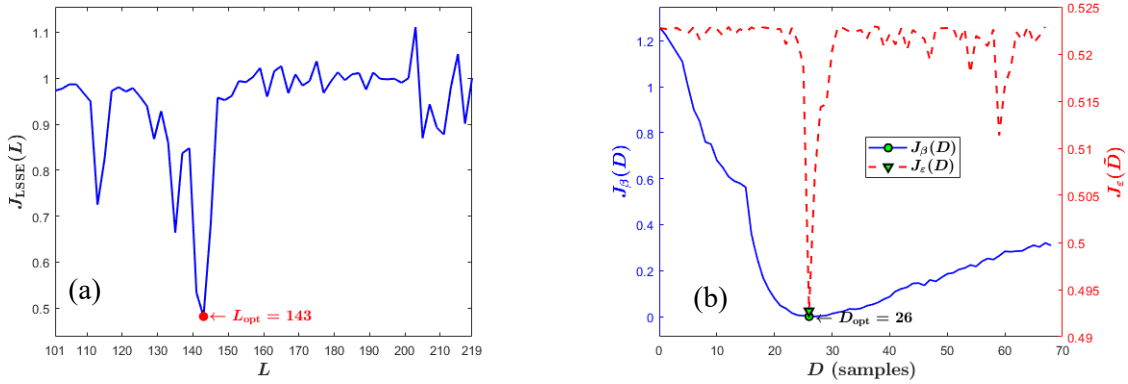

(a) LSSE cost function for estimating the channel length.

(b) Attenuation-based and deconvolution error cost functions for estimating the common delay.

Figure 5.2: Determining optimal channel length and common delay in the simulated channels. Simulation parameters: $c = 354$ m/s, $\beta = 2.1\times10^{-5}$ s/m, $d_1 = 9$ metres, $d_2 = 25$ metres, $F_s = 1$ kHz.

Substituting $\bar{D}_{\text{opt}} = 26$ and the time delay estimate $\hat{\tau}_{\text{peak}} = 45$ ms in Equations (5.22) and (5.23) yields the leak location and wave speed values as $\hat{d}_1 = 9.1$ metres and $\hat{c} = 351$ m/s. The leak location differs from the actual location by 0.1 metres, while the wave speed estimate is within 0.9% of the true value. The error in these estimates is related to the limited integer sample resolution of the propagation times. Alternatively, by performing linear regression of the unwrapped phase of the estimated FRFs (Figure 5.3(d)), the propagating times of the leak noise from the leak location to the measurement points are obtained as $t_1 = 25.2$ ms and $t_2 = 69.7$ ms. Note that the regression was restricted to frequencies up to 150 Hz in each FRF, i.e., the region where the unwrapped phase is approximately linear. Substituting these propagation times in Equations (5.22) and (5.23) results in leak location and wave speed estimates of $\hat{d}_1 = 9.03$ metres and $\hat{c} = 358$ m/s. The leak location is closer to the true value in this case since the estimates of the propagation times obtained via linear regression of the phase are not restricted to integer sample resolution. This numerical example demonstrates the validity of all aspects of the BCI leak localisation method, including the spectrally constrained NMCFLMS algorithm and the proposed cost functions.

It should be noted that the performance of the method is expected to degrade in the presence of any factor that distorts the form of the pipe channel from the FRF model or introduces channel estimation errors. Such factors interfere with the ability to accurately estimate the channels using BCI

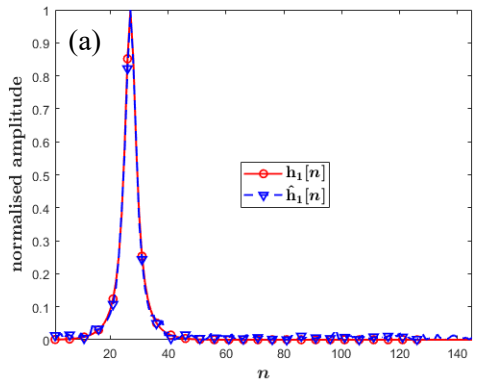

(a) Simulated and estimated IRFs of the first channel.

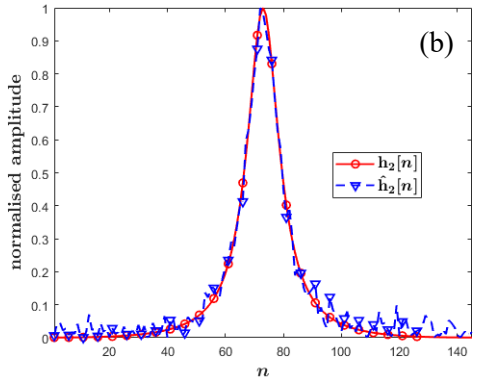

(b) Simulated and estimated IRFs of the second channel.

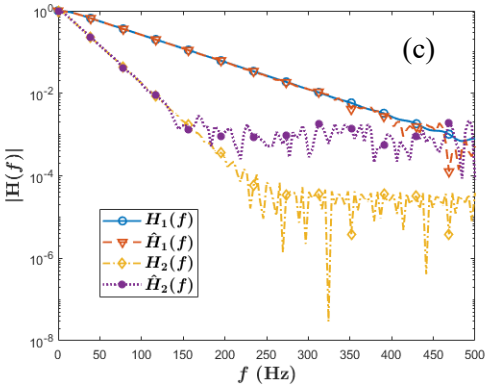

(c) FRF magnitude

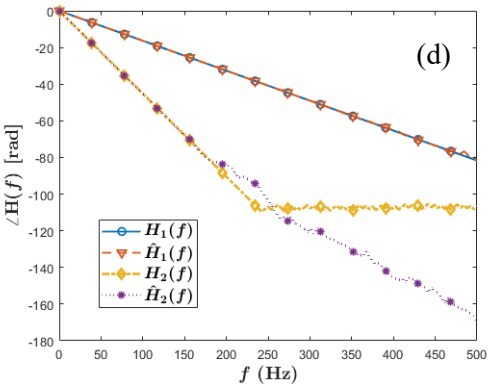

(d) Unwrapped FRF phase.

Figure 5.3: Comparison of the simulated pipe channels and the BCI channel estimates. Simulation parameters: $c = 354$ m/s, $\beta = 2.1\times10^{-5}$ s/m, $d_1 = 9$ metres, $d_2 = 25$ metres, $F_s = 1$ kHz.

techniques. Examples include noise, non-uniformity of the pipe, reflections, and high signal attenuation. Like for other acoustic methods, it is expected that the proposed BCI method will become less effective at long distances between the leak and the measurement locations due to signal attenuation. The effect of background noise on the performance of the BCI leak localisation method was investigated numerically. White Gaussian noise was added to the generated leak signals to achieve SNR between -3 and 6 dB for the first signal. Figure 5.4 shows the average leak location and wave speed estimates obtained over 100 runs for each SNR value. It can be observed that these estimates are close to the true values of 9 metres and 354 m/s (indicated with horizontal lines on the plot). Even at a SNR of -3 dB, the average wave speed estimate differs from the true value by 14%, while the absolute leak localisation error is 1.1 metres. For comparison, the average leak location estimates calculated using the BCC and GCC-ML time delay estimates and the true wave speed are also shown in Figure 5.4. At high SNR above 2 dB, both the BCI and GCC methods give accurate leak location estimates within 10 centimetres of the true leak location even though knowledge of the wave speed value is not assumed in the BCI. As the SNR decreases, the accuracy of the BCI leak location estimate degrades more substantially than the GCC estimates. In practice, however, the wave speed

used in the cross-correlation equation may differ substantially from the true wave speed. As a result, the error in the GCC estimates may exceed that of the BCI estimate, even at high SNR (see the quantitative analysis in Section 6.1). These simulation results demonstrate the ability of the proposed method to perform relatively well in the presence of noise. It is important to note that without applying spectral constraints, the NMCFLMS algorithm is very sensitive to the presence of even little noise in the signals. The robustness of the spectrally constrained algorithm can be explained by the inclusion of the spectral constraints and the robust constraints, thus allowing the channel estimates to conform to the expected form even in the presence of noise. The effectiveness of the method is investigated further in the next section using experimental data.

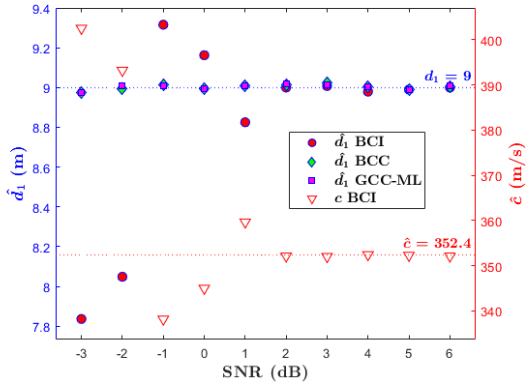

Figure 5.4: Average wave speed and leak location estimates obtained using the BCI and GCC for simulated leak signals.

5.5.2 Application to experimental leak signals

The BCI leak localisation technique was employed to locate leaks in the leakage test rig described in Chapter 2. The main information about the datasets containing steady-state leak signals, which are analysed in this subsection, has been provided previously in Section 3.4 (see Table 3.4). In order to reduce the computational burden of estimating the pipe IRFs, the measured signals were downsampled to 4 kHz prior to applying the BCI technique. At the original sampling rate of 40 kHz, setting $c_{\min}$ = 250 m/s and $c_{\max}$ = 450 m/s would require searching between $L_{\min}$ = 689 and $L_{\max}$ = 1529. On the other hand, with F_s = 4 kHz, the minimum and maximum feasible FIR filter lengths become $L_{\min}$ = 69 and $L_{\max}$ = 155. The downsampled signals were also passed through a bandpass filter whose cut-off frequencies correspond to the EB of the signals (as described in Section 2.3.2). Subsequent analyses including definition of spectral constraints and linear regression were restricted to this frequency region. A sample result is presented for the hydrophone signals measured at X1 and X2 in the Dataset 1 in Table 3.4. The time delay between the filtered X1 and X2 signals was estimated as $\hat{\tau}_{\text{peak}}$ = 9.025 ms using the BCC. Figure 5.5(a) shows the LSSE, deconvolution error, and attenuation-based cost functions obtained for these signals. The deconvolution error and attenuation-based cost

functions are calculated for common delay up to $D_{\max} = 44$. The optimal channel length can be determined to be $L_{\text{opt}} = 103$ given by the location of the minimum of the LSSE cost function, while the optimal leading delay is obtained as $\bar{D}_{\text{opt}} = 16$ given by the average (rounded to the nearest integer) of the locations and of the minima of the deconvolution cost function ($D_{\text{opt}} = 15$) and attenuation-based cost function ($D_{\text{opt}} = 16$).

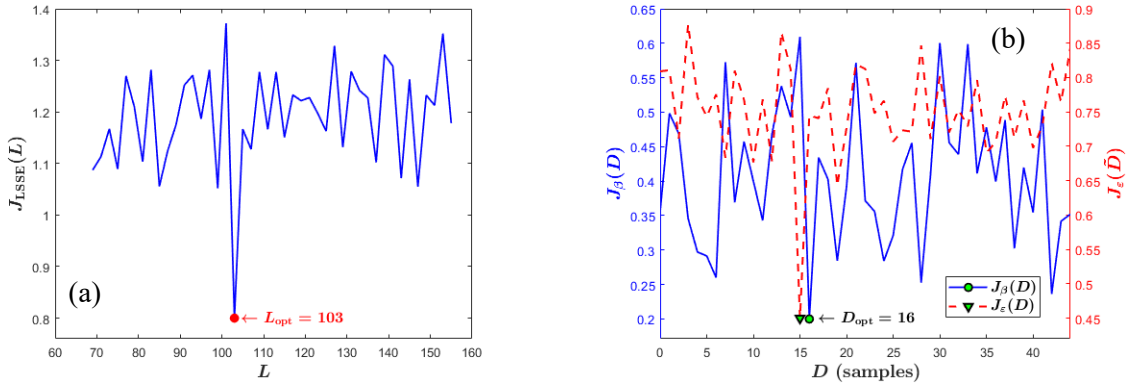

(a) LSSE cost function.

(b) Attenuation-based and deconvolution error cost functions.

Figure 5.5: Determining the optimal channel length and common delay in the pipe channels from the X1 and X2 hydrophone leak signals in Dataset 1 in Table 3.4.

Figure 5.6(a) shows the first and second pipe channel IRFs obtained for L_{opt} and D_{opt}. The amplitude of each IRF has been normalised by its maximum value. Compared to the simulated pipe IRFs in Figures 5.3(a) and 5.3(b), these IRFs have significant side lobes, which are likely due to the presence of reflections in the acquired signals. The presence of reflections, however, does not appear to drastically reduce the effectiveness of the BCI method. From the value $\bar{D}_{\text{opt}} = 16$ and $\hat{\tau}_{\text{peak}} = 9.025$ ms, the propagation times of the leak noise in the first and second pipe channels are estimated as $t_1 = 4.00$ ms and $t_2 = 13.03$ ms, respectively. The low-pass nature and linear phase property of the pipe channels at low frequencies are evident from the FRF magnitude and phase shown in Figures 5.6(c) and 5.6(d), respectively. Substituting the propagation times $t_1 = 4.00$ ms and $t_2 = 13.03$ ms in Equations (5.22) and (5.23) yields the wave speed and the leak location as $\hat{c} = 323$ m/s and $\hat{d}_1 = 1.3$ metres. These estimates differ from the true values by 9% and 0.14 metres, respectively. Again, it must be noted that the integer sample resolution of the propagation delay estimate limits the accuracy of the estimates. Alternatively, linear regression of the unwrapped phase of the FRF in Figure 5.6 (b) gives the propagation times as $t_1 = 3.95$ ms and $t_2 = 12.76$ ms. These correspond to wave speed estimate $\hat{c} = 328$ m/s and leak location estimate $\hat{d}_1 = 1.3$ metres. These estimates are close to the true

values, demonstrating the effectiveness of the BCI leak localisation method for the experimental signals.

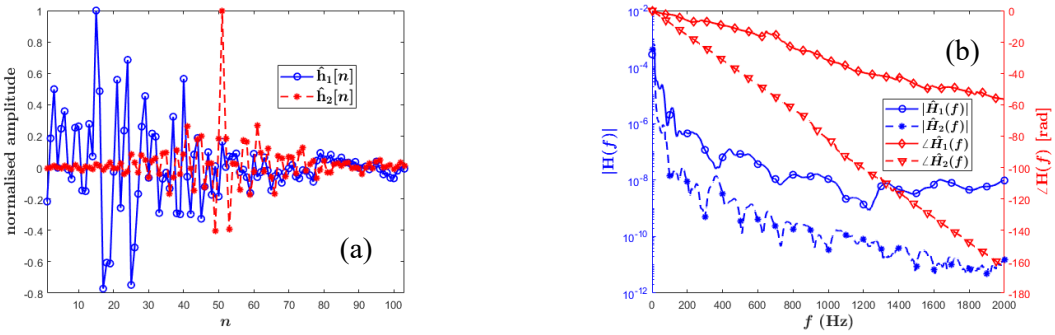

Figure 5.6: IRFs and FRFs blindly estimated from X1 and X2 hydrophone leak signals in Dataset 1 in Table 3.4. (a) Estimated IRFs of the pipe channels. (b) Magnitude and unwrapped phase of the estimated channel FRFs.

Table 5.1 presents a cross-section of results obtained from the available datasets. The first measurement point is at X1, while the second measurement point is indicated along with the leak location and wave speed estimates. Also shown are the mean and RMSE of the estimates obtained for the X1-X2 and X1-X3 signal pairs in all the datasets. For comparison, the leak location estimates obtained using the BCC and the GCC-ML time delay estimates are also shown in Table 5.1. As indicated by the RMSE of the leak location estimates, in general, the BCI method performs better than the BCC but worse than the GCC-ML. The maximum absolute leak location error in the BCI leak location estimates is 0.17 metres compared to 0.23 and 0.13 metres for the BCC and GCC-ML methods, respectively. It should, however, be noted that the true wave speed value has been used in calculating the GCC leak location estimates, while such information was not made available to the BCI leak localisation algorithm. Remarkably, the maximum discrepancy in the BCI wave speed estimate is 12%. This is lower than the 21% difference between the true wave speed and the value 279 m/s calculated from the wave speed equation if a typical value of E_p = 0.8 GPa is assumed for the Young's modulus of the MDPE pipe (see Section 2.3.2). Using this calculated wave speed value in the cross-correlation equation with the GCC-ML time delay estimate yields a maximum absolute leak localisation error of 0.52 metres, about thrice larger than the error in the BCI leak location estimate. This demonstrates the danger of using the calculated wave speed value when the pipe properties are not reliably known or when the wave speed cannot be conveniently measured in-situ. In such cases, the BCI method can provide a preferable alternative to the conventional cross-correlation method. Hence, the method may be particularly useful for inaccessible buried pipes, the material properties of which may be impossible to measure.

The experimental results presented in this section demonstrate that the proposed BCI method is capable of locating leaks under the cross-correlation setup without explicit knowledge of the wave speed or pipe material. Due to its inherent ability to estimate wave speed directly from the measured

leak signals, the method can achieve low leak localisation errors, even outperforming the conventional cross-correlation method in some cases. However, like for all results reported in this work, it is important to consider the limitations of the leakage test rig when generalising the experimental results to real pipe systems. In the next section, these along with the limitations of the proposed method and the current study are discussed.

Table 5.1: Cross-section of BCI wave speed estimates and BCI and GCC leak location estimates obtained for experimental leak signals in the datasets described in Table 3.4.

			Wave speed estimate $\hat{c}$ (m/s)	**Leak location estimate $\hat{d}_1$ (m)**		
		Method	**BCI**	**BCI**	**BCC**	**GCC-ML**
Dataset	**First measurement point**	**Second measurement point**				
1	X1	X2	328	1.31	1.29	1.14
2		X2	344	1.2	1.32	1.16
3		X3	355	1.15	1.23	1.23
4		X3	373	1.12	1.40	1.26
5		X2	319	1.29	1.30	1.21
6		X2	328	1.25	1.25	1.17
7		X2	328	1.23	1.40	1.26
8		X3	344	1.2	1.08	1.12
9		X3	367	1.1	1.17	1.17
10		X3	310	1.34	1.39	1.30
Mean			340	1.22	1.28	1.20
RMSE			24.3	0.09	0.15	0.06

5.6 Limitations of the system identification leak localisation method

Issues that can be highlighted for the proposed BCI method include high computational complexity and ineffectiveness in non-uniform pipes. Since the BCI leak detection procedures involve exhaustive search over all feasible values of the channel length, it is more computationally expensive than the conventional cross-correlation method. The effectiveness of leak localisation using the BCI approach depends on how adequately the physical pipe channels are described by the FRF model in Equation (2.5). As a result, factors such as non-uniformity of the pipe, that distort this form of the pipe channel can limit the ability to accurately estimate the wave speed and leak location from the blindly identified IRFs. Hence, the method may not be effective in pipes consisting of different materials or deteriorated sections. Since such pipes constitute a significant proportion of pipes in water distribution networks, this may limit the scope of application of the method in real pipe systems. Furthermore, the BCI method is not immune to some of the issues limiting the conventional cross-correlation technique, for example, signal attenuation and non-robustness of TDE. Pipe channels can only be reliably estimated

if the leak signals are not severely attenuated. Hence, like the conventional cross-correlation method, the BCI method may fail in plastic pipes when the distance between the leak and the measurement points is too large. Since calculating the absolute propagation times and setting the additional singleton constraint requires knowledge of the time delay between the measured signals, it follows that any factor that affects the accuracy of the time delay estimate will also affect the BCI method.

Like the multipath identification methods proposed in Chapter 4, certain properties of the leakage test rig makes it particularly favourable for the application of the system identification leak localisation method. The most important among these are the structural uniformity of the pipes and relatively short length of the rig. The former ensures that wave propagation in the rig is adequately described by the FRF model, while the latter implies that leak signals are not severely attenuated. Both of these factors make it easier to locate leaks in the leakage test rig using the proposed method.

In addition to these issues, it is also important to note that the study carried out in this chapter represents a rather limited and rudimentary introduction of the system identification leak detection strategy without an in-depth analysis of its performance. Certain factors that are likely to affect performance have not been considered, including pipe properties, surrounding medium, presence of reflections, and inter-sensor distance, mostly due to unavailability of suitable data. Despite the limited nature of the study, the available simulation and experimental results demonstrate the potential viability of the proposed method for locating leaks in water pipes. A more rigorous investigation of the method is recommended as well as a more comprehensive validation of the method in a variety of practical situations.

5.7 Summary and conclusion

An alternative method for locating leaks in water pipes using a system identification approach has been introduced in this chapter. In this method, the impulse response functions (IRFs) relating the signal at the leak location and the measured acoustic/vibration signals are estimated exclusively from the measured signals using a blind channel identification (BCI) technique known as the normalised multichannel frequency least mean squares (NMCFLMS) method. A simple analysis of the channel estimates yields the propagation times of the leak noise to the measurement points, thereby allowing the leak location and wave speed to be determined. To ensure that the estimated channels conform to the form given by a model of the frequency response function (FRF) of the pipe, spectral constraints based on linearity of the Fourier phase and log-spectrum of the IRFs were introduced in the NMCFLMS algorithm. Three different cost functions were defined to identify the channel estimates that best describe the physical pipe channels according to the FRF model. Numerical simulations and experimental results demonstrated the good performance of the system identification leak localisation methodology, albeit in idealised and controlled conditions. The main advantage of the method is that in contrast with the conventional cross-correlation approach, a priori knowledge of the wave speed is

no longer a prerequisite for leak localisation. Limitations of the method include high computational complexity, ineffectiveness in non-uniform pipes, and susceptibility to noise. Tackling these limitations can improve the applicability to real pipe systems.

CHAPTER 6
CORRELATION QUALITY ASSESSEMENT

As mentioned in Section 1.3, there are two aspects to the TDE problem in acoustic leak detection: improving the accuracy of the time delay estimate and quantifying the TDE error. Most of the existing research has focused mainly on the first aspect (see Gao et al. (2006), Almeida (2013), and references therein). However, it can be argued that the second aspect is just as important. Without a quantitative assessment of the accuracy of the time delay estimate, it is difficult to make informed inferences about the reliability of leak localisation results in a given situation. This chapter will therefore focus on this often-neglected aspect of the TDE problem. Alternative methods for improving the accuracy of the time delay estimate will be developed in Chapter 7. In this chapter, a quantitative analysis of the effect of the TDE error on leak localisation accuracy is first presented. Then metrics that are currently used for assessing the quality of TDE results are introduced, after which alternatives are proposed. Finally, the effectiveness of the proposed alternative metrics is investigated using experimental data.

6.1 Quantitative assessment of the impact of time delay estimation error on leak localisation

As discussed in Section 1.2, the accuracy of the time delay estimate is an important factor that determines the effectiveness of acoustic leak localisation using the cross-correlation technique. The effect of this factor can be assessed quantitatively as follows. Let $\hat{d}_1$ denote the leak location calculated using the time delay estimate $\hat{\tau}_{\text{peak}}$ and some wave speed value $\hat{c}$, which differ from the true time delay τ_{peak} and true wave speed c by $\Delta\tau_{\text{peak}} = \hat{\tau}_{\text{peak}} - \tau_{\text{peak}}$ and $\Delta c = \hat{c} - c$, respectively. Based on the cross-correlation equation (Equation (1.1)), the absolute error in leak location $\Delta d_1 = \left|\hat{d}_1 - d_1\right|$ is given by

$$\begin{aligned}\Delta d_1 &= \frac{1}{2}\left|\tau_{\text{peak}}\cdot\Delta c + c\cdot\Delta\tau_{\text{peak}} + \Delta c\cdot\Delta\tau_{\text{peak}}\right| \\ &= \left|d\cdot\left(\frac{1}{2}-\frac{d_1}{d}\right)\left(\frac{\Delta c}{c}+\frac{\Delta\tau_{\text{peak}}}{\tau_{\text{peak}}}\right)+\frac{\Delta c\cdot\Delta\tau_{\text{peak}}}{2}\right| = \frac{c\cdot\tau}{2}\left|\left(\frac{\Delta\tau_{\text{peak}}}{\tau_{\text{peak}}}+1\right)\left(\frac{\Delta c}{c}+1\right)-1\right|\end{aligned} \quad (6.1)$$

The last two expressions in Equation (6.1) are only valid for $\tau_{\text{peak}} \neq 0$, i.e., when the leak is not exactly at the midpoint of the pipe, while the first expression is valid for all cases. Equation (6.1) shows that the absolute leak localisation error is affected by the true time delay and wave speed values as well as the absolute errors in their estimated values. It can be observed that even when the wave speed is exactly known, error in the leak location value due to the error in the time delay can be large.

This is illustrated in Figure 6.1, which shows the leak localisation error for different locations of the leak due to TDE error only with the inter-sensor distance and true wave speed set to d = 100 metres and c = 354 m/s, respectively. The error in the leak location estimate becomes higher when the true leak location is closer to one end of the pipe. For a fixed leak location and a given wave speed error, the leak localisation error increases linearly with the absolute TDE error. Assuming the wave speed value is exact, it can be seen from this plot that for d_1/d = 0.2, a 10% error in the time delay estimate will result in an undesirable absolute leak localisation error of Δd_1 = 3 metres.

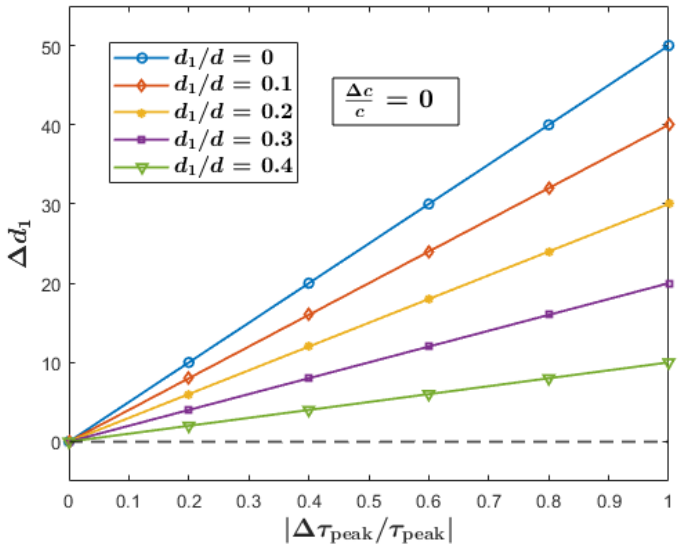

Figure 6.1: Leak localisation error due to TDE error for different relative leak locations in a cross-section measurement setup with c = 354 m/s and d = 100 metres

The simple illustration above underlines the practical importance of assessing the accuracy of the time delay during acoustic leak localisation. It should be noted that while in practice, the wave speed and inter-sensor distance are usually assumed to be known, these quantities can have errors as well. For example, locations calculated from Global Positioning System (GPS) maps may have errors of up to 2 metres (DoD, 2020). This is important to consider when assessing the overall uncertainty in the estimated leak location. This chapter only focuses on the time delay estimate. In the next section, quality metrics which have been proposed in the literature for assessing the quality of this quantity are briefly described. It is important to note that assessment of TDE accuracy is relevant not only in the conventional cross-correlation technique, but also in the alternative leak localisation methods proposed in the preceding two chapters.

6.2 Existing time delay quality assessment metrics

As stated above, there are very few research works dedicated to assessing the quality of the time delay estimate. Almeida (2013) proposed the ratio $\Delta\omega/\omega_c$ of the bandwidth of leak signals (or applied

bandpass filter) $\Delta\omega$ to the centre frequency of the bandwidth ω_c as a parameter for characterising the shape of the CCF. Based on the effects of $\Delta\omega$ and ω_c discussed in Section 1.2.3 (see the illustration in Figure 1.3), the ratio $\Delta\omega/\omega_c$, which is termed the bandwidth-to-centre-frequency ratio (BCFR) in this thesis, quantifies both the distance between the main and adjacent peaks in the CCF as well as the broadness of the CCF peak. A large value of the BCFR implies that the main CCF peak is sharp, while the adjacent peak is relatively small and is located far from the main peak. Conversely, in a CCF characterised by a low BCFR, the main peak may be wide and of comparable height with adjacent peaks, thus making it difficult making it difficult to unambiguously identify the time delay. No threshold was given by Almeida (2013), but the results in that work seemed to suggest that BCFR values greater than 0.3 indicate good quality of the time delay estimate. The BCFR can be calculated alternatively as (Almeida, 2013)

$$\mathrm{BCFR} \approx \frac{1}{\pi}\sqrt{6\left(1-\vartheta\right)} \tag{6.2}$$

where ϑ is the ratio of the heights of the adjacent and main peaks in the envelope of the CCF. The BCFR has certain drawbacks that may render it ineffective for assessing the quality of TDE results. Firstly, the formulation of the BCFR considers only the effects of the bandwidth of the signals or applied bandpass filter and ignores other factors, such as noise. Hence, a large BCFR does not necessarily guarantee a 'good' CCF shape, especially if the signals are corrupted by noise. In this work, a CCF is said to 'good' shape when the main peak associated with the time delay is sharp and the correlation values off from the peak are small. Such a 'good' CCF shape is desirable for accurate TDE using correlation-based methods. Secondly, the BCFR does not really characterise the shape of the whole CCF, since it considers only the main peak and the peak immediately adjacent to it. Thirdly, as pointed out by Almeida (2013), the presence of resonances in the analysed bandwidth of the signal can adversely affect the ability to accurately determine the time delay estimate. Since the BCFR does not take this into account, this metric will be ineffective for quantifying the accuracy of the time delay estimate in leak signals with resonances.

To denote the quality of the time delay estimate, Ayala Castillo (2019) proposed five indices: bandwidth index k_b, coherence index k_{co}, phase index k_{ph}, peak index k_{pk}, and shape index k_{sh}, which are calculated as follows:

$$\begin{aligned} &k_{\mathrm{b}} = 1 - R_{x_1x_2}\left(\tau\big|_{\text{second peak}}\right);\quad k_{\mathrm{co}} = \mathrm{E}\left\{\gamma^2_{x_1x_2}\left(\omega\right)\right\};\quad k_{\mathrm{ph}} = 1 - \sqrt{\mathrm{var}\left\{\left|\Delta_{\mathrm{ph}}\left(\omega\right) - 1\right|\right\}};\\ &k_{\mathrm{pk}} = \max\left\{\rho_{x_1x_2}\left(\tau\right)\right\};\quad k_{\mathrm{sh}} = 1 - R_{x_1x_2}\left(\tau\big|_{\text{second peak}}\right) \end{aligned} \tag{6.3}$$

where $R_{x_1x_2}\left(\tau\big|_{\text{second peak}}\right)$ denotes the second highest peak in the CCF $R_{x_1x_2}\left(\tau\right)$, $\rho_{x_1x_2}\left(\tau\right) = \frac{R_{x_1x_2}(\tau)}{\sigma_{x_1}\sigma_{x_2}}$ is the normalised CCF, $\Delta_{\mathrm{ph}}\left(\omega\right)$ is the ratio of the experimental unwrapped cross-spectral phase to its

least squares fit, $\mathrm{var}\{\bullet\}$ denotes variance, and $\max\{\bullet\}$ denotes the maximum value. The mean of the coherence $\gamma^2_{x_1x_2}(\omega)$ in the coherence index and variance of $\left|\Delta_{\mathrm{ph}}(\omega)-1\right|$ in the phase index are calculated for frequencies in the interval $\omega_1 \le \omega \le \omega_2$ where there is leak noise. Each of these indices assesses the impact of different factors on the CCF shape as follows: bandwidth of the leak noise (bandwidth index); external noise (coherence index); noise, structural dynamics of the pipe system, and wave reflections (phase index, peak index); correlated noise and reflections (shape index). To obtain a single parameter that quantifies the quality of the time delay estimate, Ayala Castillo (2019) proposed taking the geometric mean of the indices, i.e.,

$$\mathrm{CQI} = \sqrt[5]{k_{\mathrm{b}}k_{\mathrm{co}}k_{\mathrm{ph}}k_{\mathrm{pk}}k_{\mathrm{sh}}} \tag{6.4}$$

with values 0-0.2, 0.2-0.7, and 0.7-1.0 indicating poor, good, and excellent quality of the time delay estimate, respectively. This index defined in Equation (6.4) is termed CCF Quality Index (CQI) in this work. While the CQI considers many factors affecting the CCF shape unlike the BCFR, it is more cumbersome to calculate. For example, the phase index requires linear regression of the unwrapped cross-spectral phase. Another issue with the CQI is that most of the indices considered in its formulation are correlated, and hence, may not necessarily provide independent assessment of the time delay estimate quality, which defeats the purpose of integrating multiple indices. Also, there is no guarantee that the phase index is non-negative. In some cases, its value may be negative, resulting in a complex CQI value, interpretation of which is unclear. Moreover, the shape index cannot distinguish between uncorrelated and correlated signals, since it attains a high value for both the CCF of uncorrelated signals and the CCF of leak signals with a 'good' shape.

In the water industry, inferences about the reliability of leak localisation results are usually based on the peak-to-mean ratio (PMR) defined as the ratio of the CCF peak height $R_{\max} = \max\left\{R_{x_1x_2}(\tau)\right\}$ to the mean of the absolute CCF values:

$$\mathrm{PMR} = \frac{R_{\max}}{\frac{1}{N_{\mathrm{c}}}\sum\left|R_{x_1x_2}(\tau)\right|} \tag{6.5}$$

where N_{c} is the CCF size (number of lags in the CCF). The PMR describes how much the CCF peak 'sticks out' above the mean CCF level. It can be observed that PMR of a CCF with a 'good' shape will be large, tending towards a value of N_{c}. Conversely, a CCF characterised by a reduced main peak and relatively higher background correlation values will have a small PMR (tending towards unity). Although this measure has achieved some level of success in practice, its current use is purely based on heuristic principles and theoretical justification is currently lacking. An attempt to provide some theoretical foundation for this metric will be carried out in this chapter.

In addition to the drawbacks already highlighted above, one issue common to the existing assessment metrics is that they consider only the CCF shape, without taking into account the actual

value of the time delay estimate. Any factor that introduces a bias in the time delay estimate without changing the shape of the CCF is likely to result in incorrect inference about the TDE quality using these metrics. An example of such factors is the presence of resonances. Also, since they are mostly proposed based on heuristic considerations, they lack strong theoretical foundation. This results in lack of robust methodology for selecting appropriate thresholds for their effective application. For example, the PMR threshold is usually set based on historical data[1]. However, in practical applications, the optimal thresholds are likely to vary depending on signal properties and measurement environment.

From this discussion, it can be observed that the drawbacks of the existing metrics may render them practically ineffective for assessing the quality of the time delay estimate in some situations. Alternative approaches for assessing TDE quality are developed in the next section.

6.3 Alternative approaches for assessing accuracy of the time delay estimate

Assessing the accuracy of the time delay estimate is essentially a binary hypothesis problem, the end result of which is to infer whether there is *good correlation* between the measured signals. This chapter focuses only on the time delay estimate obtained using a correlation-based time delay estimator. The term *good correlation* or *high quality* will be used to indicate that the time delay estimate obtained from the CCF is accurate (close to the true value). Since the true delay is not known a priori, the accuracy of the time delay estimate can only be assessed *indirectly* by considering the properties of the CCF. Under the cross-correlation setup, the measured leak signals $x_1(t)$ and $x_2(t)$ can be represented as in Equation (5.1), which is repeated here for convenience

$$\begin{cases} x_1(t) = l(t) \otimes h_1 + n_1(t) = l_1(t) + n_1(t) \\ x_2(t) = l(t) \otimes h_2 + n_2(t) = l_2(t) + n_2(t) \end{cases} \tag{6.6}$$

where $l_i(t) = l(t) \otimes h_i$ is the noise-free component of $x_i(t)$. The biased CCF $R_{x_1x_2}(\tau)$ of the signals can be expressed as

$$R_{x_1x_2}(\tau) = R_{l_1l_2}(\tau) + R_{l_1n_2}(\tau) + R_{n_1l_2}(\tau) + R_{n_1n_2}(\tau) \tag{6.7}$$

where $R_{uv}(\tau) = \frac{1}{T}\int_0^T u(t)v(t+\tau)dt$, and T is the observation time. The properties of the CCF relevant for estimating the time delay are the location $\tau = \tau_{\text{peak}}$ and the value $R_{\max} = R_{x_1x_2}(\tau_{\text{peak}})$ of the highest peak in the CCF. The former gives the time delay estimate, while the latter affects the ability to unambiguously determine this time delay estimate. Three different approaches are considered in this section for *indirectly* assessing TDE accuracy based on these two properties. The

[1] Private communication with UK water companies

first is based on the probability distribution of $R_{\max}$, while the second is based on the processing gain (PG) defined in terms of $R_{\max}$ and background cross-correlation values. The third is a statistical approach that considers the time delay values estimated from multiple realisations of the CCF. For each approach, two extreme cases are considered: when the signals are uncorrelated and when there is good correlation between them.

6.3.1 Information criterion approach

This section presents an approach for assessing the quality of the time delay estimate by considering the probability distribution of cross-correlation values in cases of good and bad correlation.

6.3.1.1 Distribution of the cross-correlation function peak value

In the absence of a leak, the CCF in Equation (6.7) reduces to $R_{x_1x_2}(\tau) = R_{n_1n_2}(\tau)$. If the background noise signals are assumed to be uncorrelated and have zero mean, then based on the central limit theorem, the cross-correlation values $R_{n_1n_2}(\tau)$ are normally distributed with zero mean and variance $\frac{\sigma_{n_1}^2\sigma_{n_2}^2}{N}$, where σ_u^2 denotes the variance of u and N is the signal length (Hanson and Yang, 2008; Roe and White, 1961). In this work, this is written as $R_{n_1n_2}(\tau) \sim \mathcal{N}\left(0, \frac{\sigma_{n_1}^2\sigma_{n_2}^2}{N}\right)$, where the symbol $\sim$ reads as "has the probability distribution of". The probability distribution of $R_{\max} = \max\left\{R_{n_1n_2}(\tau)\right\}$ can be derived from the extreme value theorem (also known as the Fisher-Tippett-Gnedenko theorem), which can be stated as follows: the extremum of a very large collection of random observations from the same arbitrary distribution converges in distribution to a Type I, Type II, or Type III generalised extreme value (GEV) distribution (Haan and Ferreira, 2006). Specifically, let $Y = \max\{X_1, X_2, \ldots, X_N\}$ be the maximum value of N independent and identically distributed normal random variables $X_1, X_2, \ldots, X_N$ with a common cumulative distribution function (CDF) $F_{X_i}(u) = \Upsilon(u)$, $i = 1, 2, \ldots, N$. Then, $Y \sim \mathrm{GEV}_1\left(\mu_\Upsilon(N), s_\Upsilon(N)\right)$, where $\mathrm{GEV}_1\left(\mu_\Upsilon(N), s_\Upsilon(N)\right)$ is the Type I GEV or Gumbel distribution with location parameter

$$\mu_\Upsilon(N) = \Upsilon^{-1}\left(1 - \tfrac{1}{N}\right) \tag{6.8}$$

and scale parameter

$$s_\Upsilon(N) = \Upsilon^{-1}\left(1 - \tfrac{1}{N}\cdot e^{-1}\right) - \Upsilon^{-1}\left(1 - \tfrac{1}{N}\right) \tag{6.9}$$

where $\Upsilon^{-1}(\bullet)$ is the inverse of the CDF (Kotz and Nadarajah, 2000). The expected value and variance of Y are given by (Kotz and Nadarajah, 2000)

$$\begin{cases} \mathrm{E}\{Y\} = \mu_{\Upsilon}(N) + \gamma \cdot s_{\Upsilon}(N) \\ \mathrm{var}\{Y\} = \frac{\pi^2}{6} s_{\Upsilon}^2(N) \end{cases} \tag{6.10}$$

where $\gamma = 0.5772$ is the Euler-Mascheroni constant. Therefore, the distribution of $R_{\max}$ for uncorrelated signals is the Type I GEV distribution, i.e., $R_{\max} \sim \mathrm{GEV}_1\left(\mu_{F_{R_{\max}}}(N_c), s_{F_{R_{\max}}}(N_c)\right)$ with $F_{R_{\max}}(u) = \Phi\left(\frac{u}{\sigma_{n_1}\sigma_{n_2}/\sqrt{N}}\right)$, where $\Phi(\bullet)$ denotes the CDF of the standard normal distribution with mean 0 and variance 1. Note that the CDF of a normal random variable X with mean $\mu_X = \mathrm{E}\{X\}$ and variance $\sigma_X^2 = \mathrm{var}\{X\}$ is given by $F_X(u) = \Phi\left(\frac{u-\mu_X}{\sigma_X}\right)$, while the inverse of the CDF is given by $F_X^{-1}(\bullet) = \mu_X + \sigma_X \cdot \Phi^{-1}(\bullet)$ (Pishro-Nik, 2014). The expected value and variance of $R_{\max}$ can be evaluated using Equation (6.10).

In the case of correlated leak signals, based on Equation (6.7), $R_{\max} = \max\left\{R_{x_1x_2}(\tau)\right\}$ is the sum of the term $R_{l_1l_2}(\tau_{\text{peak}})$ and contributions from the noise terms $R_N = R_{l_1n_2}(\tau_{\text{peak}}) + R_{n_1l_2}(\tau_{\text{peak}}) + R_{n_1n_2}(\tau_{\text{peak}})$. The value of $R_{l_1l_2}(\tau_{\text{peak}})$ over multiple realisations of the CCF can be assumed to be approximately constant since it is not affected by noise. Note that this assumption is not *strictly* true, since the value of $R_{l_1l_2}(\tau_{\text{peak}})$ depends on the leak noise $l(t)$, a random signal. Since R_N is the sum of three normally distributed zero-mean random variables (CCFs of uncorrelated signals) in this case, $R_{\max} \sim \mathcal{N}\left(\mu_{R_{\max}}, \sigma_{R_{\max}}^2\right)$ with mean $\mu_{R_{\max}} = R_{l_1l_2}(\tau_{\text{peak}})$ and variance $\sigma_{R_{\max}}^2 = \frac{1}{N}\left(\sigma_{l_1}^2\sigma_{n_2}^2 + \sigma_{n_1}^2\sigma_{l_2}^2 + \sigma_{n_1}^2\sigma_{n_2}^2\right)$.

Figures 6.2(a) and 6.2(b) show the empirical PDFs of the CCF peak for white noise (an example of uncorrelated signals) and simulated leak signals, respectively, as well as the fitted GEV and normal distributions. The simulation procedures and parameters were outlined in Section 5.5.1 in Chapter 5. Also shown are the PDFs of the theoretical distributions $\mathrm{GEV}_1\left(\mu_{F_{R_{\max}}}(N_c), s_{F_{R_{\max}}}(N_c)\right)$ and $\mathcal{N}\left(\mu_{R_{\max}}, \sigma_{R_{\max}}^2\right)$ derived above. The empirical and fitted PDFs were estimated using the MATLAB function 'ksdensity', while the fitted PDFs were obtained using the MATLAB function 'fitdist' with required distribution (GEV or normal) specified as an input parameter. To quantify the relative agreement between the PDFs, the JD between the theoretical PDFs and the empirical and fitted PDFs were calculated using Equation (3.7). On Figures 6.2(a) and 6.2(b), the empirical and theoretical PDFs are denoted as P_{emp} and P_{th}, respectively, while the fitted normal and GEV PDFs are denoted as

P_{normal} and P_{GEV_I}, respectively. Based on the JD values, it can be observed that the CCF peak is best described by different distributions for uncorrelated noise (GEV) and leak signals (normal) as predicted by the analysis above. Hence, the assessment of the quality of cross-correlation between signals can be viewed as a model selection problem, or more specifically, as the problem of deciding whether the observed values of the CCF peak R_{max} are *best* described by a Type I GEV distribution or a normal distribution. It is, however, important to note that the extent to which these distributions fit the CCF peak in the cases of uncorrelated signals and leak signals differs. By visual inspection and from the values of the JD in Figure 6.2(a), the GEV fits the distribution of R_{max} for uncorrelated signals far better than the normal distribution, which is a much poorer fit as shown by the relatively high value of $\text{JD}(P_{\text{th}}, P_{\text{normal}}) = 0.245$. On the other hand, while the normal distribution is the better fit for the distribution of R_{max} for leak signals, the GEV appears to be a good fit as well in some regions, as shown by the relatively small value of $\text{JD}(P_{\text{th}}, P_{\text{GEV}_\text{I}}) = 0.010$ in Figure 6.2(b). This observation has important implication on how inference is made about the quality of the time delay estimate in the information criterion and processing gain approaches (as will be described in Sections 6.3.1.3 and 6.3.2). Information criteria are widely employed in model discrimination problems. They are briefly described in the next section.

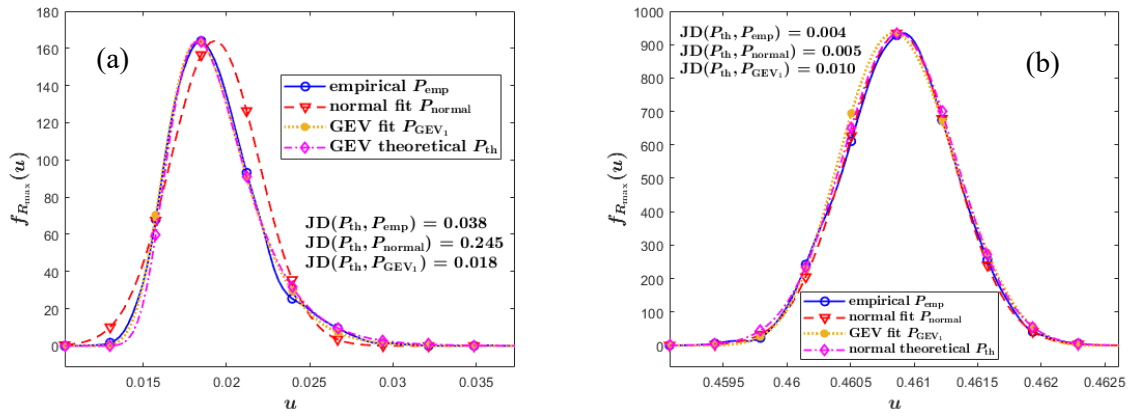

(a.) white Gaussian noise signals. (b.) simulated leak signals.

Figure 6.2: Comparison of the GEV and normal distributions for describing the PDF of the CCF peak in the case of: (a) uncorrelated noise. (b) correlated signals.

6.3.1.2 Description of information criteria

Two information criteria that can be used to infer the distribution of the CCF peak value are the Akaike Information Criterion (AIC) and the Bayesian Information Criterion (BIC). The AIC is defined as (Akaike, 1974)

$$\text{AIC}_M = 2k_M - 2\log\{L_M\} \tag{6.11}$$

while the BIC is given by (Schwarz, 1978; Wit et al., 2012)

$$\mathrm{BIC}_M = k_M \log\{N_\mathrm{R}\} - 2\log\{L_M\} \tag{6.12}$$

where L_M is the maximised value of the likelihood function of a model (distribution) M, i.e., $L_M = \Pr\left\{\hat{R}_{\max} \middle| \hat{\theta}, M\right\}$, where $\hat{\theta}$ are the parameter values that maximise the likelihood function, $\hat{R}_{\max}$ is the observed CCF peak data, N_R is the sample size (number of CCF peak values), and k_M is the number of parameters estimated by the model. The likelihood $\Pr\left\{\hat{R}_{\max} \middle| \hat{\theta}, M\right\}$ denotes the probability of observing the CCF peak value data $\hat{R}_{\max}$ assuming the underlying distribution is given by M. Note that if the sample size is small, some correction is often necessary to address potential overfitting by the AIC. The AIC with a correction for small sample sizes (denoted as AICc) is defined as (Burnham and Anderson, 2002)

$$\mathrm{AICc} = \mathrm{AIC} + \frac{2k_M^2 + 2k_M}{N_\mathrm{R} - k_M - 1}. \tag{6.13}$$

The AIC and BIC (and their variants) compare the likelihoods of the candidate models, balancing goodness of fit with simplicity. They reward goodness of fit (as assessed by the likelihood function) and penalise complexity of the model (i.e., the number of parameters in the distribution). Given a set of candidate models for the observed data, the preferred model is generally the one with the minimum AIC or BIC value. One critical difference between the AIC and BIC is the asymptotic property for well-specified and misspecified models (Ding et al., 2018). In contrast with the AIC, Bayesian analyses assume that one of the candidate models is the true model. To be specific, if the 'true model' that generated the observed data is in the set of candidates, then BIC will select the 'true model' with probability 1, as $N_\mathrm{R} \to \infty$, whereas the probability can be less than 1 when the AIC is used (Burnham and Anderson, 2002; Vrieze, 2012). In general, if the goal is prediction, AIC is preferred, while the BIC is preferred if the goal is selection, inference, or interpretation (Aho et al., 2014).

Note that AIC and BIC do not provide information about the absolute quality of a model, only its quality relative to other models. Candidate models can be compared using the relative likelihood (RL) defined for each model M as

$$\mathrm{RL}_M = \exp\left\{\frac{1}{2}\left(\mathrm{AIC}_{\min} - \mathrm{AIC}_M\right)\right\} \tag{6.14}$$

where $\mathrm{AIC}_{\min}$ is the minimum AIC or AICc value obtained for candidate models. The AIC and its variants estimate the relative amount of information lost by a given model (Burnham and Anderson, 2002), so RL_M can be interpreted as being proportional to the probability that the model M minimises the (estimated) information loss. The less information a model loses, the higher the quality of the model. Analogously, candidate models can be compared using the Bayes factor (BF) defined as

the ratio of the likelihoods of two statistical models integrated over the prior probabilities of their parameters (Gill, 2002). For a large sample size, the BF between two models M_1 and M_2 can be approximated from their BICs as (Wagenmakers et al., 2010)

$$\mathrm{BF}_{M_1,M_2} = \exp\left\{-\frac{1}{2}\left(\mathrm{BIC}_{M_1} - \mathrm{BIC}_{M_2}\right)\right\} . \tag{6.15}$$

Inference is generally made in favour of the model with the highest RL or BF. The main reason for comparing the models in terms of the RL and BF instead of comparing the JD, AIC, or BIC values directly is to allow an interpretation of the inference based on an appropriate scale. Two scales proposed by Kass and Raftery (1995) and Jeffreys (1998) for the interpretation of the BF are shown in Table 6.1. In both scales, inference is made in favour of M_1 only if BF_{M_1,M_2} is greater than $\sqrt{10} \approx 3.2$.

Table 6.1: Scales for the interpretation of the BF.

$\log_{10}\{\mathrm{BF}_{M_1,M_2}\}$	BF_{M_1,M_2}	**Strength of evidence in support of M_1**	
		Kass and Raftery (1995)	Jeffreys (1998)
<0	<1	Negative (supports M_2)	
0 to $1/2$	1 to 3.2	Barely worth mentioning	
$1/2$ to 1	3.2 to 10	Substantial	Substantial
1 to $3/2$	10 to 31.6	Strong	Strong
$3/2$ to 2	31.6 to 100		Very strong
>2	100	Decisive	

6.3.1.3 Steps in the information criterion approach

The process of assessing the quality of the time delay estimate using the RL or BF can be summarised as follows:

1. Divide the measured signals into sufficiently long non-overlapping segments. Overlapping segments may result in correlated and similar CCF peak values, distribution of which may not conform to either GEV or normal. In order to obtain a good CCF estimate, the length of each segment should be at least 10 times the maximum lag of interest in the CCF (Bendat and Piersol, 2010). For an accurate approximation of the AICc or BIC, it is important to ensure that the number of segments N_R is high (at least 30, see Lorah and Womack (2019)).

2. Compute the CCF between corresponding segments of the two signals and determine the CCF peak value in each CCF realisation. Alternatively, the CCFs can be computed from multiple measurements of the same leak under the same conditions.

3. Calculate the AICc and the BIC for the CCF peak values, assuming a Type I GEV distribution (M_1) and a normal distribution (M_2). Using the AICc and BIC, calculate the RLs (RL_{M_1}, RL_{M_2}) using Equation (6.14) and the BF (BF_{M_1,M_2}) using Equation (6.15).

4. If $\mathrm{RL}_{M_2} < 1$ or $\mathrm{BF}_{M_1,M_2} > 3.2$ (i.e., at least substantial evidence to support M_1), decide in favour of M_1; otherwise, decide in favour of M_2. In the first case, it is inferred that the time delay estimated from the CCF of the signals is incorrect, while it is considered accurate in the second case. Note that the inference has been formulated as accepting or rejecting the GEV distribution. This is because as mentioned above, difficulty may arise in distinguishing between normal and GEV distributions for CCF peak value of correlated signals. On the other hand, the distribution of CCF peak value for uncorrelated signals is more strongly described by the GEV. Hence, presence of substantial evidence in support of M_1 is expected when the signals are uncorrelated.

Two practical difficulties with the application of this approach are high computational complexity associated with fitting distribution functions to the observed data and the need for multiple realisations of the CCF. It may, therefore, be difficult to employ in situations where practical constraints preclude capability for multiple or long measurements. The effectiveness of assessing the quality of the time delay estimate using information criteria will be investigated in Section 6.4.

6.3.2 Processing gain approach

A parameter generally used for assessing the performance of a signal processor is the PG, which is defined as the ratio of the SNR of its output $\mathrm{SNR}_{\mathrm{out}}$ to the SNR of its input $\mathrm{SNR}_{\mathrm{in}}$ (Casasent et al., 1982). Signal processors with high PG are more robust to noise and other factors that may negatively impact performance. The input SNR $\mathrm{SNR}_{\mathrm{in}}$ is the ratio of the signal power to the noise power, while the output SNR $\mathrm{SNR}_{\mathrm{out}}$ of a correlation-based time delay estimator is the SNR of the CCF. For given signals, the input SNR is the same for all time delay estimators. Therefore, to compare the performance of different time delay estimators based on their PGs, it suffices to compare their output SNRs. The SNR of the CCF can be defined as the ratio of the 'useful' component to the 'noise' component in the CCF. Here, 'useful' components denote the parts of the CCF that contain information about the time delay. On the other hand, 'noise components' refer to the components that interfere with the ability to unambiguously determine the time delay in the CCF. Only the first term $R_{l_1 l_2}(\tau)$ in Equation (6.7), or specifically, the location of its peak value, contains information about the time delay. In contrast, the other three terms related to the presence of noise in the measured signals may give rise to spurious peaks or reduce the CCF peak. In addition, if the side lobes of

$R_{l_1 l_2}(\tau)$ are high, then it may become difficult to determine the time delay accurately. Hence, the 'useful' components are the CCF peak height $R_{\max}$ and its location $\hat{\tau}_{\text{peak}}$, while the 'noise components' include the side lobes of the CCF. Based on this, the SNR of the CCF can be defined as ratio of the CCF peak $R_{\max}$ to a statistical property of a 'noise component' in the CCF. Possible choices for the property of the 'noise component' are the mean or variance of correlation values away from the peak, the highest side lobe or secondary peak, etc. Among these, the variance of correlation values at lags *far* from the CCF peak is selected because of its analytical tractability and ease of analysis. The output SNR of the time delay estimator can be expressed as

$$\text{SNR}_{\text{out}} = \frac{R_{x_1 x_2}^2(\tau_{\text{peak}})}{\text{var}\left\{R_{x_1 x_2}(\tau_{far})\right\}} \tag{6.16}$$

where $\text{var}\left\{R_{x_1 x_2}(\tau_{far})\right\}$ denotes the variance of correlation values at lags τ_{far} at least $N_c/4$ samples away from τ_{peak} (the CCF $R_{x_1 x_2}(\tau)$ is computed in the lag interval $-(N_c-1)/2 \le \tau \le (N_c-1)/2$). In this work, the output SNR defined by Equation (6.16) will be referred to as the peak-to-side lobe ratio (PSR). It can be observed that the PSR in its definition is similar to the detection SNR defined for the ACF and the power cepstrum in Section 4.4.3. In fact, the PSR can be interpreted in the same way as the detection SNR, i.e., as an indication of noise tolerance, with higher values indicating better noise tolerance and higher ability to suppress side lobes resulting from noise and fluctuations of the leak noise in the CCF. It can also be interpreted as a quantitative measure of CCF peak detectability with a higher value indicating a CCF with a prominent peak and low values off from the peak, which is desirable for accurate TDE. In this sense, it characterises the CCF shape as the BCFR and PMR. The statistical properties of the PSR for uncorrelated and correlated signals will now be described.

6.3.2.1 Peak-to-side lobe ratio

Although the variance $\text{var}\left\{R_{x_1 x_2}(\tau_{far})\right\}$ is a random variable, it can be assumed to be *nearly* constant, since the CCF of bandlimited signals vanish at large lags (Jenkins and Watts, 1968), and the quantity $\frac{R_{n_1 n_2}(\tau)}{\sqrt{\text{var}\left\{R_{n_1 n_2}(\tau)\right\}}} \sim \mathcal{N}(0,1)$, i.e., a standard normal random variable. Thus, like the CCF peak value, in the case of uncorrelated signals, the square root of the PSR follows a Type I GEV distribution; specifically,

$$\sqrt{\text{PSR}} \sim \text{GEV}_1\left(\mu_\Phi(N_c), s_\Phi(N_c)\right) \tag{6.17}$$

where $\mu_\Phi(N_c)$ and $s_\Phi(N_c)$ are evaluated using Equation (6.10). Based on the properties of the CCF described in Section 6.3.1, the expected value of the PSR for uncorrelated signals is given by

$$\mathrm{PSR}=\left[(1-\gamma)\Phi^{-1}\left(1-\tfrac{1}{N_c}\right)+\gamma\cdot\Phi^{-1}\left(1-\tfrac{1}{N_c}\cdot e^{-1}\right)\right]^2 . \tag{6.18}$$

Since the CDF is an increasing function, larger CCF size corresponds to a higher PSR value, but for a fixed CCF size, the PSR will be constant and independent of the powers of the uncorrelated signals.

In the case of leak signals, the square root of the PSR is normally distributed, and assuming a flat leak noise spectrum in the analysed frequency interval, the PSR can be expressed as (Appendix F)

$$\mathrm{PSR}=\frac{2T}{\pi\beta d}\left(1+\frac{1}{\zeta_1}+\frac{1}{\zeta_2}+\frac{1}{\zeta_1}\frac{1}{\zeta_2}\right)^{-1} \tag{6.19}$$

where $\zeta_i \triangleq \dfrac{R_{l_i l_i}(\tau)}{R_{n_i n_i}(\tau)}$, $i=1,2$, are assumed to be nearly constant (i.e., the ACFs of the signal $l_i(t)$ and the noise $n_i(t)$ are very similar). The quantities ζ_1 and ζ_2 are proportional to the SNRs of the signals. The PSR of leak signals depends on the observation time, SNRs of the measured signals, pipe attenuation factor, and the inter-sensor distance. Its value increases as the SNR of leak signals increases as indicated by Equation (6.19). These observations are illustrated in Figure 6.3, which shows the PSR values obtained for simulated leak signals with SNR between -10 and 6 dB. The SNR values on the x-axis denote the SNR of the leak signal at the first measurement point. For each SNR, the 'noise PSR' indicate the PSR values calculated from the CCF of the white noise signals added to the leak signals to achieve the given SNR. The simulation procedures and parameters were outlined in Section 5.5.1 in Chapter 5. Equation (6.19) also indicates that indicates that TDE is less accurate for signals measured in pipes with large attenuation factor and at longer distances from the leak in agreement with theoretical and experimental results (see the analysis in Sections 7.1.1 and 7.4.1 in Chapter 7).

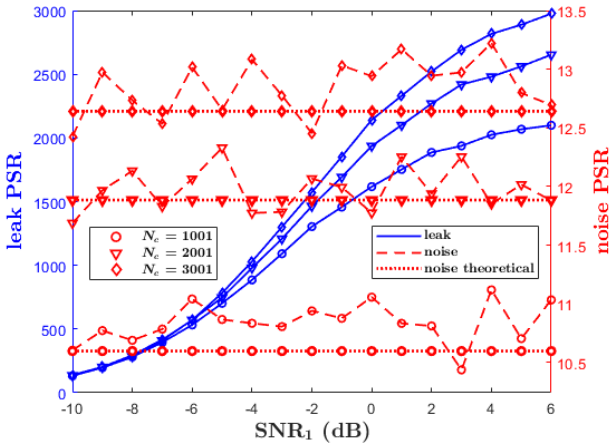

Figure 6.3: Comparison of the PSR for uncorrelated noise and correlated leak signals. The PSR is calculated for N_c = 1001, 2001, and 3001. The values on the x-axis are the SNR of the first leak signal. The noise PSR is calculated for the noise signals added to the leak signals to obtain the given SNR.

Inference about the quality of the time delay estimate is made by comparing the PSR value to a threshold λ_{PSR} that indicates the demarcation between good and bad correlation. The threshold can be calculated based on the distribution of the PSR for uncorrelated signals. The value of λ_{PSR} can be set using the approach employed for the NSM in Section 3.2.1.2 as

$$\lambda_{\mathrm{PSR}} = \left[F^{-1}_{\sqrt{\mathrm{PSR}}}\left(1-\xi\right)\right]^2 \tag{6.20}$$

where ξ is the AFPR, and $F^{-1}_{\sqrt{\mathrm{PSR}}}\left(\bullet\right)$ is the inverse of the CDF of the type I GEV distribution $\mathrm{GEV}_1\left(\mu_\Phi\left(N_\mathrm{c}\right), s_\Phi\left(N_\mathrm{c}\right)\right)$. In other words, λ_{PSR} is the value such that $\xi = \Pr\left\{\mathrm{PSR} > \lambda_{\mathrm{PSR}}\right\}$. If the PSR exceeds the threshold λ_{PSR}, then it is inferred that that the time delay estimate provided by the CCF is accurate. Otherwise, the time delay estimate is considered inaccurate.

An advantage of the processing gain approach over the information criterion approach (and the statistical approach described in the next subsection) is that the PSR can be calculated from a single CCF realisation, making it practically more convenient. Also, use of a threshold set based on the statistical distributions of the PSR for uncorrelated signals is likely to reduce the chances of incorrectly inferring good correlation when there is none (i.e., incidents of false alarms). It is, however, important to mention that since this threshold does not take the distributions for correlated signals into account, it may not necessarily result in ability of the metric to correctly infer high quality of the time delay estimate in cases of good correlation (i.e., high 'detection power'). Nonetheless, the threshold given by Equation (6.20) is likely to be more robust than the one set arbitrarily. The performance of the PSR for correlation quality assessment will be investigated in Section 6.4.

6.3.2.2 Peak-to-mean ratio

Based on its conceptual similarity to the PSR, the PMR can also be considered a measure of the output SNR of correlation-based time delay estimators. It can be shown that the PMR in the case of uncorrelated signals is distributed according to a Type I GEV distribution as follows. Since the cross-correlation values of uncorrelated signals are normally distributed, their absolute values $\left|R_{x_1x_2}\left(\tau\right)\right|$ follow a folded normal distribution with mean $\sqrt{\frac{2}{\pi}\cdot\mathrm{var}\left\{R_{x_1x_2}\left(\tau\right)\right\}} = \sqrt{\frac{2\sigma^2_{x_1}\sigma^2_{x_2}}{\pi N}}$ and variance $\left(1-\frac{2}{\pi}\right)\cdot\mathrm{var}\left\{R_{x_1x_2}\left(\tau\right)\right\} = \frac{\left(1-\frac{2}{\pi}\right)\cdot\sigma^2_{x_1}\sigma^2_{x_2}}{N}$ (Cooray and Ananda, 2008). Therefore, based on the central limit theorem (provided the CCF size N_c is large), the mean of the absolute cross-correlation values will be normally distributed with mean $\sqrt{\frac{2\sigma^2_{x_1}\sigma^2_{x_2}}{\pi N}}$ and variance $\sigma^2_{\mathrm{abs}} = \frac{\left(1-\frac{2}{\pi}\right)\cdot\sigma^2_{x_1}\sigma^2_{x_2}}{N\cdot N_\mathrm{c}}$. Approximating the mean of the absolute cross-correlation values by the expected value $\mu_{\mathrm{abs}} = \sqrt{\frac{2\sigma^2_{x_1}\sigma^2_{x_2}}{\pi N}}$ (this is justified by the

small value of the variance), the quantity $\kappa(\tau) = \dfrac{R_{n_1 n_2}(\tau)}{\mathrm{E}\left\{\left|R_{n_1 n_2}(\tau)\right|\right\}} \sim \mathcal{N}(0, \pi/2)$, i.e., a normal random variable with zero mean and variance $\dfrac{\pi}{2}$. Therefore, for uncorrelated signals,

$$\mathrm{PMR} \sim \mathrm{GEV}_1\left(\mu_\kappa(N_\mathrm{c}), s_\kappa(N_\mathrm{c})\right) \tag{6.21}$$

where $\mu_\kappa(N_\mathrm{c})$ and $s_\kappa(N_\mathrm{c})$ are evaluated using Equation (6.10) with $F_\kappa(u) = \Phi\left(\dfrac{u}{\sqrt{\pi/2}}\right)$ In this case, the PMR can be expressed analytically as

$$\begin{aligned}\mathrm{PMR} &= \left[(1-\gamma)\cdot F_\kappa^{-1}\left(1-\tfrac{1}{N_\mathrm{c}}\right) + \gamma\cdot F_\kappa^{-1}\left(1-\tfrac{1}{N_\mathrm{c}}\cdot e^{-1}\right)\right]\cdot\sqrt{\tfrac{\pi N}{2\sigma_{n_1}^2\sigma_{n_2}^2}} \\ &= \left[(1-\gamma)\Phi^{-1}\left(1-\tfrac{1}{N_\mathrm{c}}\right) + \gamma\cdot\Phi^{-1}\left(1-\tfrac{1}{N_\mathrm{c}}\cdot e^{-1}\right)\right]\cdot\sqrt{\tfrac{\pi}{2}}\end{aligned} . \tag{6.22}$$

This equation shows that the PMR and PSR are closely related for uncorrelated signals—the PSR is a squared value of the PMR scaled by a factor of $2/\pi$. Like the PSR, the PMR is dependent on the CCF size and independent of the powers of the uncorrelated signals.

In the case of correlated leak signals, the PMR cannot be expressed analytically since there is no closed form expression for the absolute correlation value $\left|R_{x_1 x_2}(\tau)\right|$ of leak signals. Inability to express the PMR in an analytical form impairs further theoretical analysis and represents a disadvantage of the PMR (compared to the PSR). However, it can be easily observed that like the PSR, the PMR of leak signals will be normally distributed and will increase as the SNR of the signals increases. Following the same procedures used for the PSR, the PMR threshold λ_{PMR} for assessing the quality of the time delay estimate can be set as the value such that the AFPR $\xi = \Pr\{\mathrm{PMR} > \lambda_{\mathrm{PMR}}\}$, i.e.,

$$\lambda_{\mathrm{PMR}} = F_{\mathrm{PMR}}^{-1}(1-\xi) \tag{6.23}$$

where $F_{\mathrm{PMR}}^{-1}(\bullet)$ is the inverse of the CDF of the type I GEV distribution $\mathrm{GEV}_1\left(\mu_\kappa(N_\mathrm{c}), s_\kappa(N_\mathrm{c})\right)$.

6.3.3 Statistical approach

One issue with the information criterion and processing gain approaches described above is that they do not explicitly take the location of the CCF peak (i.e., the time delay estimate) into account while inferring TDE accuracy. Since the CCF peak may not occur at the correct time delay due to the effects of noise, resonances, and reflections, possible error in the value of the time delay estimate has to be considered when assessing its quality. To achieve this, a quality assessment criterion, referred to as the *inconsistency score* (ICS) C_s in this work, is proposed:

$$C_s = \sqrt{\frac{1}{N_R}\sum_{k=1}^{N_R}\left(\hat{\tau}_{\text{peak},i} - \tilde{\tau}_{\text{peak}}\right)^2} \tag{6.24}$$

where N_R is the number of CCF realisations (obtained from signal segments or multiple measurements), $\hat{\tau}_{\text{peak},i}$ is the time delay estimate from the i th CCF realisation, and $\tilde{\tau}_{\text{peak}}$ is the *assumed* true delay taken as the statistical mode of the time delay estimates. Here, the term *assumed* is used to emphasise that the true delay is not known a priori. The ICS is similar to the standard deviation but defined in terms of the mode instead of the mean. A justification for the choice of the statistical mode over the statistical mean in the definition of the ICS is that the effects of outliers are less pronounced on the mode. When there is good correlation between the signals, the time delay estimates obtained from multiple CCF realisations will be nearly equal and close to the assumed true delay, thus resulting in a small ICS value. Conversely, a high ICS indicates large variability in the estimates. Note that it in employing the ICS, it is implicitly assumed that the time delay remains constant throughout the measurement period. In this work, a time delay estimate is said to be *inconsistent* if it differs from the *assumed* true time delay by more than some given value. The ICS assesses the overall *inconsistency* of time delay estimates obtained from multiple CCF realisations. Figure 6.4 shows the plots of the average ICS values and the proportion of inconsistent estimates (PiCE) obtained over 100 runs for simulated leak signals and white noise signals used in calculating the PSR in Figure 6.3 in the preceding section and for the same SNR values between -10 and 6 dB. The white noise signals are used as an example to illustrate the properties of the ICS for uncorrelated signals. A time delay estimate is considered inconsistent in the simulation if it differs from the *assumed* true time delay by more than 2 samples. For each SNR, the ICS and PiCE values calculated from the CCF of the white noise signals added to the leak signals are also given. An important observation that can be made from the plots is that like the PSR, the ICS and PiCE are practically constant and independent of the noise power in the case of uncorrelated signals. On the other hand, their values decrease as the SNR of the leak signals increases, tending towards zero.

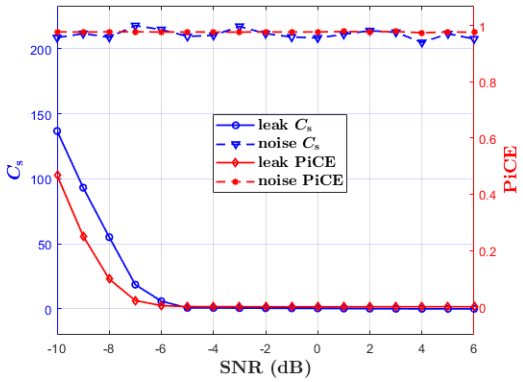

Figure 6.4: Comparison of the ICS and PiCE for uncorrelated noise and leak signals.

The workflow for the statistical approach is the same as that of the information criterion approach in Section 6.3.1 with the exception that the ICS is used in place of the RL and BF. In this

case, good quality of the time delay estimate is inferred if the value of C_s is *less* than some selected threshold λ_{ICS}. Based on simulation results, an inconsistency threshold of 1 is suggested. This value may, however, be adjusted if necessary, depending on the properties of the signals being considered. Additionally, to avoid situations with a lot of outliers, it is required that the proportion of inconsistent estimates be small (for example, less than 20%).

A benefit of the statistical approach over the two approaches described above is that it explicitly takes the value of the time delay estimate into account when assessing its quality. However, like the information criterion approach, it requires the computation of multiple CCF realisations either from many signal segments or many measurements of the same leak. This makes it computationally expensive as well as limits its applicability in situations where long measurements are not possible. In the next section, the viability of the proposed quality assessment approaches will be evaluated, and their performance compared with the existing quality metrics.

6.4 Evaluation of quality assessment metrics using experimental leak signals

In this section, the performances of the three approaches described in the preceding section are investigated using experimental signals.

6.4.1 Comparative study of quality assessment metrics in leak signals

The effectiveness of the proposed quality assessment metrics (RL, BF, PSR, ICS) is evaluated in terms of the true positive rate (TPR) and false positive rate (FPR), i.e., the proportion of correct positive inferences and the proportion of incorrect positive inferences, respectively. Good quality assessment metrics are characterised by a high TPR and a low FPR. Their performance are assessed for background noise and steady-state leak signals from the datasets previously described in Section 3.4. The CCFs of the X1-X2, X1-X3, and X1-X4 pairs of signals in the datasets were computed using the BCC with a maximum time lag of 8192 samples (205 ms). Each CCF of leak signals was classified either as ‘high-quality’ if it is characterised by a ‘good’ shape and gives an accurate time delay estimate, or as ‘low-quality’ otherwise. While this classification is somewhat subjective, it suffices for the purpose of this study. In this section, a time delay estimate is considered *accurate* if it is within one sample of the true delay and considered *inconsistent* if it differs from the assumed true delay by more than 2 samples (or 0.05 ms). A CCF that does not give an accurate time delay estimate is considered ‘low-quality’ regardless of its shape. There are a total of 31 high-quality CCFs, 14 low-quality CCFs, and 20 noise-only cases. An example of a high-quality CCF of signals measured at X1 and X2 is shown in Figure 6.5(a). This CCF is characterised by a prominent peak that occurs close to the correct time delay of 9 ms and low correlation values away from the peak. The slight error in the

time delay estimate is due to the limited integer resolution of the BCC method. Smaller peaks due to reflections in the signals can be observed close to the main CCF peak. However, these peaks do not interfere with the ability to unambiguously determine the time delay in this case. Figure 6.5(b) depicts a low-quality CCF calculated from signals acquired at X1 and X3 signals. This CCF is characterised by relatively low CCF peak that does not occur close to the correct time delay value (26 ms). It is impossible to obtain an accurate estimate of the time delay without first filtering the signals in this case.

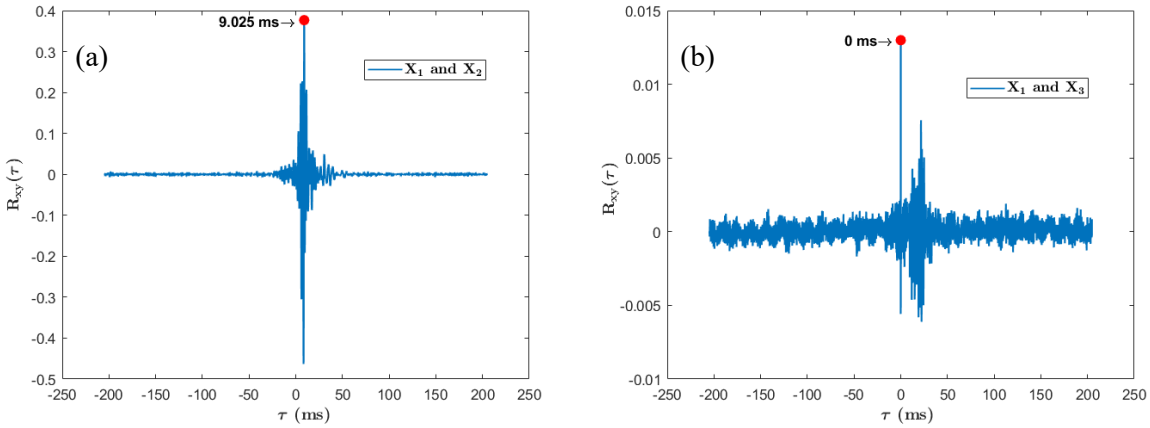

Figure 6.5: Examples CCFs obtained from accelerometer signals measured on the leakage rig in the presence of a leak at L1. (a) High-quality CCF of the X1 and X2 signals. (b) Low-quality CCF of the X1 and X3 signals.

Table 6.2 shows the values of the existing and proposed quality metrics obtained for the two representative examples shown in Figure 6.5 as well as the values for noise signals measured at X1 and X2. The RL, BF, and ICS were calculated from the CCFs of 1-second signal segments. Orange cells are used to highlight positive inference (i.e., values that exceed, or in the case of the ICS is less than, the corresponding threshold). The PSR and PMR thresholds were calculated with an AFPR of 0.001 using the approach outlined in Section 3.2.1.2. All metrics correctly infer high quality for the first CCF and low quality for the CCF of the noise signals. Only the BCFR and CQI fail to correctly infer low quality for the second CCF. Their failure is associated with the presence of resonances and reflections in the signals acquired on the leakage test rig, which results in a high value for the BCFR and the bandwidth index (more details about resonances in the signals will be given in Section 7.5). The values of the BF indicate substantial and strong evidence to infer that the CCF peak values are distributed according to a type I GEV in the low-quality and noise-only cases, respectively. On the other hand, the evidence supports rejecting this distribution in the high-quality case, thus allowing one to infer good correlation in this case. Similarly, the RL supports a normal distribution in the high-quality case and GEV distribution in the other two cases. It can be observed that all signal segments in the high-quality case yield consistent time delay estimates (as evidenced by the zero PiCE value). The high PiCE values in the low-quality and noise-only cases suggests high variability in the time delay

estimates obtained from the signal segments in these two cases. The assumed true delay is very close to the true delay in the high-quality case, in contrast with the low-quality cases. These observations demonstrate the soundness of the information criterion and statistical approaches. Based on the relative change in the values of the metrics, the ICS and PSR appear to be the most sensitive to change in correlation quality. These results indicate the ability of the proposed quality metrics to differentiate between high- and low-quality time delay estimates better than the BCFR and CQI.

Table 6.2: TDE quality assessment results for experimental leak signals.

Metric	**Threshold**	**High-quality CCF**	**Low-quality CCF**	**Noise-only CCF**
True delay τ_{peak} (ms)		9	26	-
Assumed true delay $\tilde{\tau}_{\text{peak}}$ (ms)		9.025	0	-103.7
PiCE	0.2	0.0	0.91	0.98
C_s		0.38	225.0	5854
BF_{M_1,M_2}	3.2	0.1	9.5	22.7
$[\text{RL}_{M_1}, \text{RL}_{M_2}]$		[0.17,1]	[1,0.09]	[1,0.001]
PMR	7.3	49.9	5.8	5.01
BCFR	0.3	0.54	0.33	0.053
CQI	0.2	0.45	0.39	0.17
PSR	33.6	13626	23.1	16.07

Summary of the results obtained for the CCFs from the available datasets is presented in Table 6.3 The results are presented for three categories: high-quality leak CCFs, low-quality leak CCFs, and CCFs of noise-only signals. Along with the average values for each metric, the proportion of cases correctly identified by the metric is shown in brackets. In addition to the TPR and FPR, the proportion of correct negative inferences, referred to as the true negative rate (TNR), and the proportion of incorrect negative inferences, referred to as the false negative rate (FNR) are also reported for each metric in Figure 6.6. Brighter colours are used to indicate values closer to unity, while darker shades of blue indicate values closer to zero. Note that the TNR and FPR have been calculated for low-quality leak CCFs without including the noise-only CCFs. It can be observed that on average all metrics are capable of distinguishing between accurate and inaccurate time delay estimates. However, they vary in their effectiveness, as shown by the TPR and FPR in Figure 6.6. From the proportion of correctly identified cases, It can be observed that the metrics achieve good performance in detecting high-quality CCFs but are less efficient in differentiating low-quality CCFs. Among the metrics, the ICS is the most effective as it has the highest TPR and lowest FPR. The PSR and BF also achieve very good performance, vastly outperforming the other metrics (except the ICS). The least effective in terms of detecting low-quality CCFs are the BCFR and the CQI, which also exhibits the worst FPR. These two metrics are vastly inferior to the alternative metrics, especially the ICS, PSR, and BF.

Examining the two CCFs shown in Figure 6.5 reveals a possible reason for the bad performance of the CQI and the BCFR. Reflections present in the signals measured on the test rig manifest as

additional peaks close to the main peak in the CCF. As can be observed from Equations (6.2) and (6.3), reflection peaks immediately adjacent to the main CCF peak results in a low values for the BCFR and the bandwidth index even in CCFs with a 'good' shape, possibly leading to an incorrect inference. These additional peaks will tend to increase the mean of the absolute values of the correlation values, whereas they have no effect on the variance of the far points. As a result, the PSR will outperform the PMR for such signals, especially when the CCF size is small. The high FPR of the BCFR and CQI may be related to the choice of their thresholds. Since the PSR and PMR thresholds are set based on their probability distribution for uncorrelated signals, these metrics exhibit lower FPR than the BCFR and CQI whose thresholds are set heuristically without rigorous analysis. Increasing the BCFR and CQI thresholds to 0.4 lowers their FPR to almost zero; however, this also decreases their TPR. Note that to avoid getting complex CQI values, the absolute value of the phase index is taken prior to calculating the geometric mean in the CQI. This may have contributed to the higher FPR of this metric.

Table 6.3: Summary of TDE quality assessment results for experimental leak signals measured on the leakage test rig at X1, X2, and X3. The leak signals are from the datasets described in Table 3.4.

Metric	Threshold	High quality	Low quality	Noise-only
PiCE	0.2	0.03	0.84	0.97
C_s	1.0	0.55 (1.0)	332.8 (0.93)	3626 (1.0)
BF_{M_1,M_2}	3.2	0.76 (0.97)	5.8 (0.86)	31.4 (1.0)
$[\mathrm{RL}_{M_1}, \mathrm{RL}_{M_2}]$	-	[0.31, 1] (0.94)	[1, 0.62] (0.79)	[1, 0.042] (1.0)
PMR	7.3	33.4 (0.97)	6.8 (0.79)	4.9 (1.0)
BCFR	0.3	0.69 (0.90)	0.24 (0.21)	0.036 (1.0)
CQI	0.2	0.76 (0.94)	0.31 (0.36)	0.15 (1.0)
PSR	33.6	9835 (1.0)	28.2 (0.86)	14.7 (1.0)

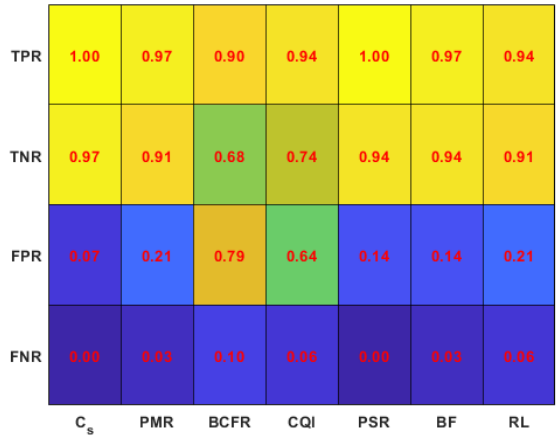

Figure 6.6: Summary of correlation quality assessment metrics for experimental signals acquired on the leakage test rig at X1, X2, and X3. The leak signals are from the datasets described in Table 3.4.

The BF achieves a better performance than the RL as can be inferred from its higher TPR and lower FPR. As stated in Section 6.3.1.2, the BF is known to be better for inference, which is the goal

in the TDE quality assessment problem. The lower TPR of the RL indicates that the AICc overfits the distribution of the CCF peak, deciding more frequently than the BIC in favour of the more complex GEV distribution in correlated leak signals. The slightly inferior performance of the BF compared to the ICS and PSR may be related to the small sample size. For each signal, 30 CCF realisations were used in calculating the BIC. Improvement in the performance of the BF and RL is possible with a larger sample size but at the cost of higher computational burden and longer computation time. However, the sample size is restricted by the signal length, since CCFs calculated from short signal segments may be inaccurate. This represents one disadvantage of the information criterion metrics: they are effective mostly when applied to long signals.

Based on these results, it can be concluded that the ICS, PSR, and BF are the best-performing metrics for assessing the quality of the time delay estimate. Their TNR is, however, less than unity, implying that they sometimes fail to recognise bad correlation between signals. Also, non-zero FPR shows that they sometimes infer good correlation when there is none. It is suggested to combine the metrics so that good correlation is inferred only when the ICS and at least one of PSR or BF give positive inferences. Unlike the use of a single approach, this combined approach considers both CCF shape and the time delay values in making an inference, possibly improving performance. It is interesting to observe that while very good results were reported for the CQI by Ayala Castillo (2019) and BCFR by Almeida (2013), their performances are less satisfactory for the signals being considered in this section. This seems to suggest that performance of quality metrics may be system specific. As already stated above, the poor performance of the BCFR and CQI in this case may be related to the choice of threshold, so refinement of the threshold selection methodology may improve their performance. The next subsection explores a relevant practical application of the proposed quality assessment metrics for selecting good TDE parameters.

6.4.2 Selection of time delay estimation parameters using quality assessment metrics

Owing to their capability for assessing the accuracy of the time delay estimate (as demonstrated above), the quality metrics can be used to assess the effectiveness of available choices for TDE parameters, including bandpass filters and GCC weighting functions. To illustrate the effectiveness of using the metrics for this purpose, they were applied to leak signals acquired in a buried 200-metre long 150-mm diameter PVC pipe system located in a leakage test facility in Ottawa Canada. A detailed description of the test site and measurement procedures has been given by Hunaidi et al. (2000). The schematic of the test site is shown in Figure 6.7(a). Leak signals from a leaky joint were measured using hydrophones installed on risers connected to two hydrants 109.5 metres apart, one 32.8 metres upstream and the other downstream of the joint. These distances include the lengths of the upstream and downstream risers: 3.2 metres and 3.7 metres, respectively. During data acquisition, the hydrophone-measured signals were each passed through an anti-aliasing filter with the cut-off frequency set at 200 Hz and sampled at a frequency of 500 Hz for duration of 66 seconds. With the

acoustic wave speed in the pipe experimentally estimated to be 484 m/s (Gao et al., 2006), based on the distances between the leak position and the measurement points, the true time delay between the leak signals is 90.7 ms. Figures 6.7(b)–6.7(d) show the CPS (magnitude and unwrapped phase) and MSC of the measured hydrophone signals, while their CCF calculated with a maximum time lag of 2048 samples (4 s) is shown in Figure 6.8(a). This CCF is characterised by a 'bad shape', and its peak does not occur at the correct time delay value. The low quality of the time delay estimate in this case can be attributed to the presence of tonal components and resonances in the measured signals as indicated by peaks in their cross-spectral magnitude shown in Figure 6.7(b) (see Almeida (2013)). The presence of tonals in the raw signals can also be inferred from the periodic shape of the CCF and the presence of additional phase jumps in the unwrapped cross-spectral phase in Figure 6.7(c).

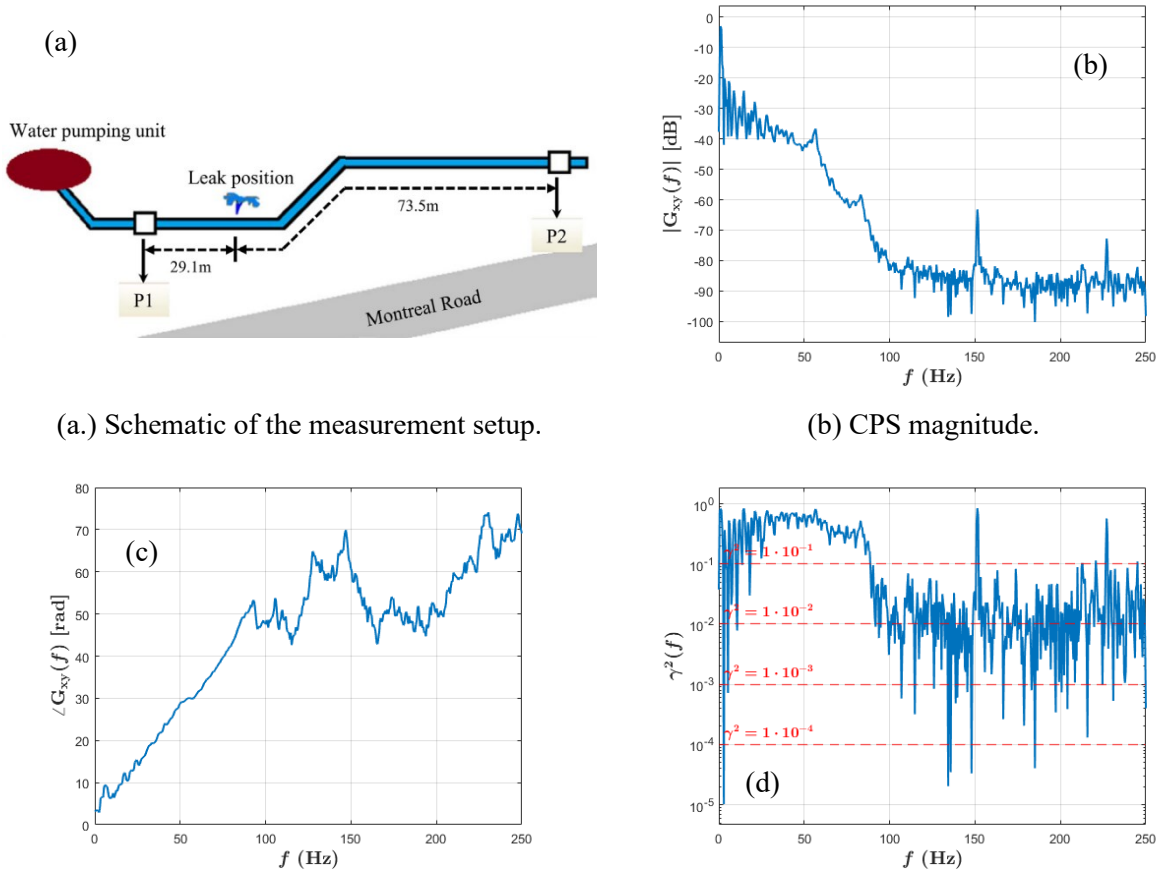

(a.) Schematic of the measurement setup.

(b) CPS magnitude.

(c) Unwrapped CPS phase.

(d) Magnitude-squared coherence.

Figure 6.7. Schematic of the Ottawa leakage test facility and spectral properties of the experimental hydrophone signals acquired at the facility.

Figures 6.8(b)–6.8(e) show the CCFs obtained after passing the signals through different bandpass filters. The cut-off frequencies shown on the plots encompass frequencies where the coherence of the signals exceeds the indicated threshold. Application of the filters leads to noticeable improvement in both the shape of the CCF and the accuracy of the time delay estimate. However, only the third and fourth filters (Figures 6.8(d)–6.8(e)) lead to the correct time delay estimate. In practice, since the true time delay is not known a priori, it may be difficult to know which of the filters yields

good results. Use of the proposed quality assessment metrics provides a simple way to resolve this issue. Figure 6.8(f) shows the values of the quality metrics for the filtered signals. Values that exceed the quality threshold are highlighted with yellow cells and red font, while values below the threshold are indicated by blue cells and white font.

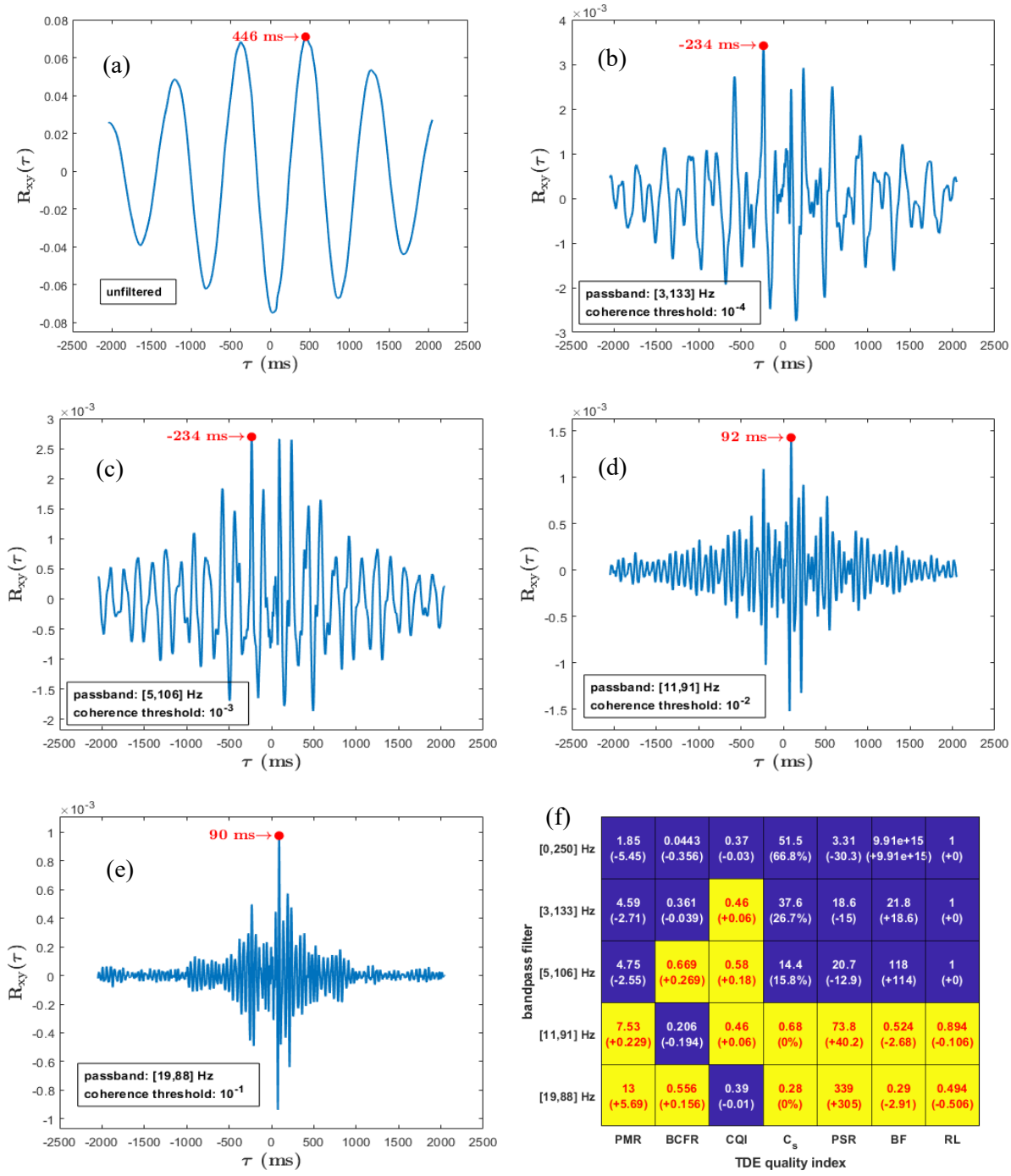

Figure 6.8: Quality assessment of CCFs of raw and filtered hydrophone leak signals acquired at the Ottawa facility. (a) Raw signals. (b)-(e) Filtered signals. (f) Quality assessment metrics.

The proposed alternative metrics and the PMR correctly infer the quality of the time delay estimate in all five cases considered. These metrics attain higher values for the filtered signals characterised by higher TDE accuracy and better CCF shape. On the other hand, the BCFR and the CQI leads to

incorrect inference in 2 and 3 cases, respectively. This example demonstrates the sensitivity of the BCFR and CQI to the presence of resonances in the analysed signal bandwidth. In comparison with the PMR, the ICS, PSR, and BF appear to be more sensitive to changes in the quality of the time delay estimate. Hence, by comparing the values of these metrics, one can select the best among possible choices of bandpass filters. This helps to resolve the issue associated with selection of bandpass filters and weighting functions in the GCC methods, identified in Chapter 1. The PSR will be used to select best parameters for accurate TDE results in the alternative TDE methods proposed in Chapter 7.

The best GCC weighting function for given leak signals be determined in the same fashion, as can be illustrated using the PMR and PSR. Figure 6.9 shows the CCFs of the unfiltered hydrophone signals, which were obtained using the GCC-PHAT and GCC-ML methods. The PMR and PSR values obtained for each CCF are also shown, as well as the quality threshold for each metric. Comparison of the CCFs and the corresponding values of the quality metrics shows that the metrics attain higher values for weighting functions that give a more accurate time delay estimate. Their values get closer to the threshold as TDE accuracy increases. A large difference between the values obtained for the basic CCF in Figure 6.8(a) and generalised CCFs in Figure 6.9 reflects the noticeable improvement in the time delay accuracy and CCF shape. In this case, the highest value is attained by the GCC-ML, whose estimate is the most accurate, differing from the true delay by one sample (2 ms). In terms of the relative change in quality metric values, the PSR appears to be more sensitive to change in CCF quality than the PMR. Based on these results, the PSR is recommended for the purpose of selecting best TDE parameters.

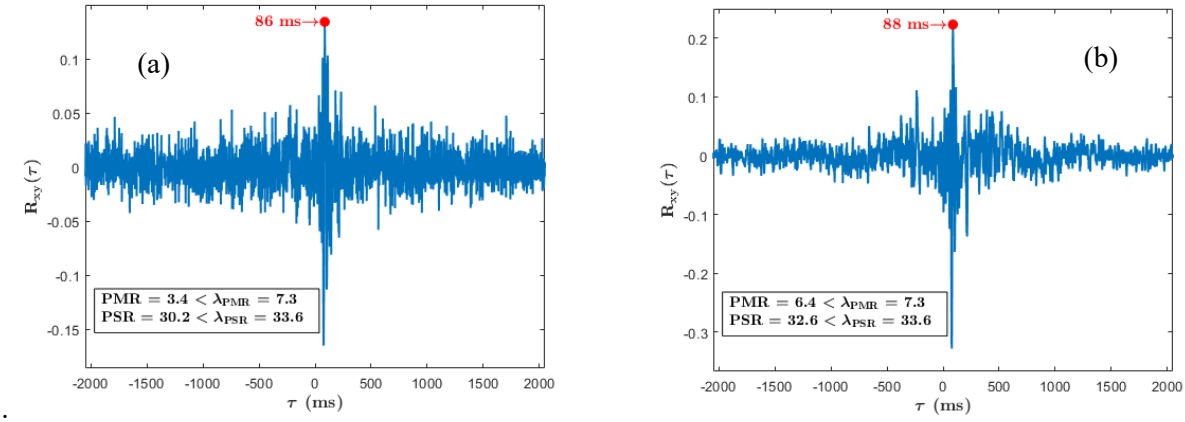

(a) GCC-PHAT. (b) GCC-ML.

Figure 6.9: Weighted CCFs of raw hydrophone signals.

It is important to note that the quality assessment metrics can only be used to assess the relative quality of available options of bandpass filters and weighting functions. In order words, they only present a means for selecting the best option among available choices which have been designed using some other approaches. Hence, they are only useful for this purpose if good choices are among the available choices; otherwise, the quality assessment metrics simply select the best one among the bad choices.

The experimental results obtained in this section show that the proposed quality assessment metrics can discriminate between low-quality and high-quality time delay estimates, thereby providing a means for partially assessing the reliability of cross-correlation results and selecting parameters for accurate TDE in leak signals. Based on the results of the comparative study above, the ICS, PSR, and BF perform well in terms of sensitivity to correlation quality. These metrics are recommended as robust options for assessing the quality of the time delay estimate in acoustic leak detection practice. To summarise this chapter, possible limitations of the proposed quality metrics are discussed in the next section.

6.5 Limitations of the correlation quality assessment metrics

The first issue that can be highlighted for the quality assessment metrics is that they determine the cross-correlation quality *a posteriori*. In other words, the quality of the time delay estimate can only be determined after the TDE process has already been completed. This may make the approaches computationally demanding when they are used to compare a large number of TDE parameter options, as the CCF must be computed for each option considered.

The second issue is that the proposed information criterion and PG approaches do not assess the accuracy of the time delay estimate *per se*, but rather assume that CCFs that have a 'good' shape or follow some given distribution must necessarily give accurate time delay estimate. This may not be true in practice. For example, the presence of a large bias in the CCF peak location will result in a poor time delay estimate, even when the CCF has a 'good' shape. Any definition of time delay quality that does not explicitly take the time delay value into account is inadequate. While the ICS deals with this issue, it has drawbacks of its own, including effects of large outliers and requirement for a large number of CCF realisations. A few abnormally large or small erroneous time delay estimates among otherwise accurate estimates can substantially increase the ICS. The suggested combined approach with a majority rule can mitigate the second issue to some extent. As already stated, an issue common to the information criterion and statistical approaches is that they require a sufficiently high number of CCF realisations for accurate results. Hence, they may be difficult to employ in situations where there is limited capacity for multiple measurements or long recordings.

The third issue is associated with the definition of the proposed quality metrics. Only two extreme cases were considered in deriving the metrics: when the signals are uncorrelated and when the correlation between them is good. Hence, the metrics may fail for cases where the background noise signals are correlated, in which they are likely to incorrectly infer the presence of accurate time delay estimate. Since this situation may be encountered in practice, it is necessary to investigate measures for detecting the presence of correlated noise in the measured signals in order to distinguish between whether the positive inference is caused by good correlation between leak signals or correlation between the background noise. Another related issue concerns the selection of the quality assessment

thresholds. Since the threshold has been set based on the assumption that 'bad' CCFs only result from uncorrelated signals, it may not be robust for cases where the background noise is correlated. Setting appropriate thresholds should be based on rigorous analysis, and properties of the measured signals and measurement environment must be considered.

To address the highlighted issues, there is need for further in-depth analysis of the quality metrics and their experimental validation in different measurement environments. Nevertheless, the present study represents an important step in providing a means to objectively assess the quality of cross-correlation results.

6.6 Summary and conclusion

In this chapter, three approaches were considered for assessing the quality of the time delay estimate. In each approach, quality metrics were derived based on properties of the cross-correlation function (CCF) of uncorrelated noise and correlated leak signals. The first metrics are the Bayesian Factor (BF) and relative likelihood (RL) derived from the Bayesian Information Criterion (BIC) and a variant of the Akaike Information Criterion (AIC). These metrics assess the time delay quality by considering the probability distribution of the CCF peak values. The second metric referred to as the Peak-to-Side lobe ratio (PSR) quantitatively describes the detectability of the CCF peak relative to the variance of the background correlation values. It is derived based on the processing gain (PG) of correlation-based time delay estimators. The third metric termed the inconsistency score (ICS) describes the time delay accuracy in terms of root-mean square of deviations of the time delay estimates from their statistical mode. Numerical simulations and experimental results demonstrated the viability of the proposed quality assessment approaches. Among the metrics, the ICS and PSR achieved the best performance. Certain issues affecting the effectiveness of the proposed approaches were highlighted. The results of the study have shown that the proposed approaches provide viable means of assessing the accuracy of the time delay estimate in acoustic leak detection applications. Also, the proposed metrics can be employed as figures of merit for selecting the best parameters for the TDE process.

CHAPTER 7
ALTERNATIVE TIME DELAY ESTIMATION METHODS

The aspect of the TDE problem in acoustic leak detection, involving assessment of the accuracy of the time delay estimate was investigated in Chapter 6. This chapter focuses on the aspect of the TDE problem concerning improvement of accuracy of the time delay estimate. Specifically, the aim of this chapter is to address the issues identified in Chapter 1 regarding selection of cut-off frequencies of the bandpass filter and GCC weighting functions. This is important for acoustic leak localisation using the conventional cross-correlation technique or any method where the time delay plays an integral role, including the multipath identification and system identification techniques proposed in Chapters 4 and 5. Instead of proposing means to improve selection of the cut-off frequencies and weighting function, a different approach is taken in this work: development of TDE methods where the choice of either is not required. Two such alternatives are presented in this chapter, the first based on transforms with inherent filtering capability and the second based on cepstral analysis. The basic principles, performance analysis, and implementation of these two approaches are outlined in this chapter.

7.1 Time delay estimators with inherent filtering property

This section introduces the general principles of the TDE method based on transforms with inherent filtering property and analyses its performance for leak signals. For convenience, this method will be referred to as *inherent bandpass* TDE method (abbreviated as IB-TDE). As a subset of the GCC method, the IB-TDE estimates the time delay τ_{peak} between the measured leak signals from the CCF $R_{\tilde{x}_1\tilde{x}_2}(\tau)$ of $\tilde{x}_1(t) = w(t) \otimes x_1(t)$ and $\tilde{x}_2(t) = w(t) \otimes x_2(t)$, where $w(t)$ is a function constructed from an appropriate transform. In contrast with the commonly used GCC weighting functions which are constructed based solely on signal and noise properties (see Table 1.1), $w(t)$ is designed using the wavelet transform (WT) and data-adaptive decompositions. An important advantage of using these transforms is that there is no longer any need to explicitly filter the leak signals prior to estimating the time delay as will be demonstrated in Section 7.5. The variance of the time delay estimate $\hat{\tau}_{\text{peak}}$ given by the location of the peak of $R_{\tilde{x}_1\tilde{x}_2}(\tau)$ is derived and analysed for leak signals in terms of pipe and signal properties in the next subsection, while the implementations of the wavelet-based and data-adaptive IB-TDE methods are described in Sections 7.2 and 7.3, respectively.

7.1.1 Variance of the time delay estimate

The variance of the IB-TDE time delay estimate is derived under the following assumptions:

A1. The signals $l(t)$, $n_1(t)$, and $n_2(t)$ in Equation (6.6) are stationary bandlimited zero-mean signals, uncorrelated with each other. The signal $l(t)$ is ergodic.

A2. The spectrum of $l(t)$ is flat with power spectral density S_0. The noise signals $n_1(t)$ and $n_2(t)$ have identical double-sided bandwidths $2B_0$ and power spectral densities N_0. Additionally, the leakage of the autospectra of $l_i(t)$ and $n_i(t)$ outside their bandwidths is negligible, and the bandwidth of $l_i(t)$ is smaller than B_0.

Assuming the time delay estimate $\hat{\tau}_{\text{peak}}$ given by the location of the peak of $R_{\tilde{x}_1\tilde{x}_2}(\tau)$ lies in the neighbourhood of the true delay τ_{peak}, the estimate $\hat{\tau}_{\text{peak}}$ can be shown to be unbiased and its variance $\sigma^2_{\hat{\tau}_{\text{peak}},\text{IB}}$ is derived as (Appendix G1)

$$\sigma^2_{\hat{\tau}_{\text{peak}},\text{IB}} = \frac{2\pi}{T}\frac{\int_{-\infty}^{\infty}\omega^2 W^2(\omega)\begin{bmatrix}G_{n_1n_1}(\omega)G_{l_2l_2}(\omega)+G_{n_2n_2}(\omega)G_{l_1l_1}(\omega)\\+G_{n_1n_1}(\omega)G_{n_2n_2}(\omega)\end{bmatrix}d\omega}{\left[\int_{-\infty}^{\infty}\omega^2 W(\omega)\left|G_{l_1l_2}(\omega)\right|d\omega\right]^2} \tag{7.1}$$

where $W(\omega)$ is the IB-TDE weighting function given by $W(\omega)=\left|\text{F}\{w(t)\}\right|^2$. If the magnitude of the IB-TDE weighting function is approximated as $|W(\omega)|=1$ in the analysed frequency band $\omega_1 \le \omega \le \omega_2$, i.e., the frequency region in which the leak noise is considered to be significant relative to the background noise, then Equation (7.1) can be expressed as (Appendix G1)

$$\sigma^2_{\hat{\tau}_{\text{peak}},\text{IB}} = \frac{\pi}{T}\frac{\sigma^2_{l_1}\sigma^2_{l_2}}{B_0}\frac{\left[\dfrac{B^2_{l_2}}{\text{SNR}_1}+\dfrac{B^2_{l_1}}{\text{SNR}_2}+\dfrac{1}{2B_0}\dfrac{1}{\text{SNR}_1}\dfrac{1}{\text{SNR}_2}\dfrac{\omega_2^3-\omega_1^3}{3}\right]}{\left[\int_{\omega_1}^{\omega_2}\omega^2 G_{l_1l_2}(\omega)d\omega\right]^2} \tag{7.2}$$

where $B^2_{l_i}$ denotes the effective bandwidth of l_i. In this chapter, the effective bandwidth of a signal is defined as the RMS radian frequency in its spectrum (see Equation (G.16) in Appendix G1). The variance of the time delay estimate in Equation (7.2) has been expressed in terms of the analysed bandwidth and properties of the signals and noise. It is worthwhile to examine the effects of pipe properties as well. By substituting the FRF model (Equation (2.5)) in Equation (7.2) and evaluating the resulting expression, the variance of the time delay estimate for acoustic pressure signals is obtained as (Appendix G1)

$$\sigma^2_{\hat{\tau}_{\text{peak}},\text{IB}} \approx \frac{\pi}{T}\frac{\sigma^2_{l_1}\sigma^2_{l_2}}{B_0}\frac{1}{S_0^2}\frac{(\beta d)^6}{2}\left[\begin{array}{l}\dfrac{1}{\text{SNR}_1}\dfrac{1}{(\beta d_1)^2}+\dfrac{1}{\text{SNR}_2}\dfrac{1}{(\beta d_2)^2}\\ +\dfrac{1}{3B_0}\dfrac{1}{\text{SNR}_1}\dfrac{1}{\text{SNR}_2}\omega_2^3\end{array}\right]. \tag{7.3}$$

The expression in Equation (7.3) is valid for small ω_1, $\omega_2 \gg \omega_1$, and $d_i \neq 0$. The variance of the time delay estimate is affected by the SNRs of the measured signals, the bandwidth of the weighting function, pipe attenuation, inter-sensor distance, and actual leak location as well as measurement time and leak noise spectrum. Effects of these factors are considered in the next subsection.

7.1.2 Factors affecting the variance of the time delay estimate

In this subsection, the effects of the SNRs, bandwidth of the leaks, pipe attenuation, and inter-sensor distance on the variance of the time delay estimate are discussed. When SNR_1 and SNR_2 are large, the third term in the numerator of Equation (7.3) can be neglected, and the variance of the time delay estimate can be approximated as

$$\sigma^2_{\hat{\tau}_{\text{peak}},\text{IB}}\Big|_{\text{high}} \approx \frac{\pi\sigma^2_{l_1}\sigma^2_{l_2}}{8B_0S_0^2T}(\beta d)^4\left[\frac{1}{\text{SNR}_1}\left(\frac{d}{d_1}\right)^2+\frac{1}{\text{SNR}_2}\left(\frac{d}{d_2}\right)^2\right]. \tag{7.4}$$

In the case where SNR_1 and SNR_2 are small, the first two terms in the square brackets in the numerator of Equation (7.3) can be neglected for typical values of pipe attenuation factor and distances (assuming the leak is not very close to one end of the pipe), and $\sigma^2_{\hat{\tau}_{\text{peak}},\text{IB}}$ can be approximated as

$$\sigma^2_{\hat{\tau}_{\text{peak}},\text{IB}}\Big|_{\text{low}} \approx \frac{\pi\sigma^2_{l_1}\sigma^2_{l_2}}{12B_0^2S_0^2T}(\beta d)^6\cdot\frac{\omega_2^3}{\text{SNR}_1\cdot\text{SNR}_2} = \frac{\pi}{3T}\frac{N_0^2}{S_0^2}(\beta d)^6\cdot\omega_2^3. \tag{7.5}$$

The variance of the time delay estimate is inversely proportional to the product of the SNRs of the signals in low-SNR conditions, whereas it varies inversely as each of the SNRs in the high-SNR case. This implies the existence of a thresholding phenomenon, i.e., there is an SNR value below which the low-SNR expression is a better approximation of the variance, and above which, the high-SNR approximation is more accurate. This can be observed in Figure 7.1, where the approximation in Equations (7.5) and (7.4) are compared with the full expression in Equation (7.3). The SNRs of the first and second signals have been set to be equal.

In both low and high-SNR cases, high values of the attenuation factor and inter-sensor distance result in a large variance of the time delay estimate. The variance in the high-SNR case is minimised when the leak is equidistant from both sensors (i.e., $d_1/d_2 = 1$) and becomes larger as the leak gets closer to any one end of the pipe. This agrees with the results obtained from the quantitative analysis

of the effects of TDE error on leak localisation in Section 6.1 (see Figure 6.1). On the other hand, the actual location of the leak does not affect the variance when the SNR is low. The cut-off frequency ω_2 is polynomially proportional to the variance in the low-SNR case but has little effect in the high-SNR case. This direct relationship between the variance and the analysed bandwidth of the signals in the low-SNR case contrasts with the result obtained for systems without frequency-dependent attenuation by Quazi (1981). In such systems, the low-SNR approximation of the variance of the time delay estimate is proportional to $1/\left(\omega_2^3-\omega_1^3\right)\approx 1/\omega_2^3$. Since the noise spectrum is assumed to be flat, increase in the analysed bandwidth effectively increases the contributions of the noise. On the other hand, frequency-dependent attenuation (represented by the monotonically decreasing term $e^{-|\omega|\beta d}\leq 1$ in the denominator of Equation (7.2) essentially reduces the contributions of the leak noise at higher frequencies. These two factors result in the observed increase in variance, which becomes more substantial when ω_2 is increased way above the frequency region where the leak noise is dominant.

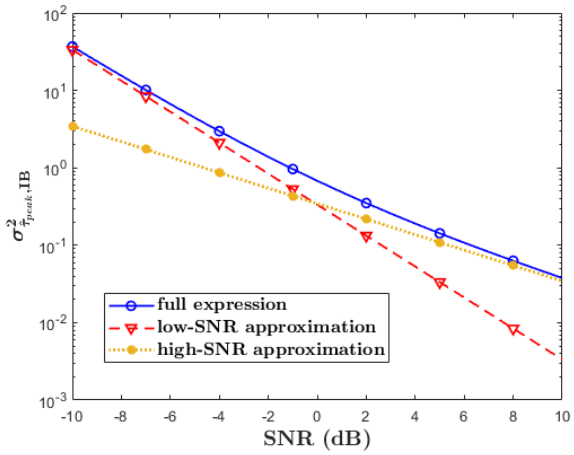

Figure 7.1: Comparison of the low-SNR and high-SNR approximations of the variance. Parameters: $\beta = 2.1\times10^{-5}$ s/m, $d = 100$ metres, $d_1 = 20$, $T = 1$, $\omega_2 = 2\pi\times100$ rad/s.

Among the parameters that affect the time delay estimate, only the measurement time and cut-off frequency can be adjusted by the operator, so the only possible measures for reducing the TDE variance in a given measurement setup are increasing the measurement time T and properly selecting the cut-off frequency ω_2. The latter is automatically facilitated by the choice of transforms used in implementing the IB-TDE method. The next two sections introduce two such transforms: the WT and data-adaptive decompositions.

7.2 Wavelet transform-based time delay estimator

The main motivation for considering the WT in the implementation of the IB-TDE method is its ability to decompose signals by scale (Xu et al., 1995b). This property makes the WT particularly attractive for analysing bandlimited signals, including acoustic leak signals. In the WT-based

implementation of the IB-TDE method, $w(t)$ is selected as a wavelet $\psi(t)$ at an *appropriate* scale, and thus, the modified signals $\tilde{x}_1(t)$ and $\tilde{x}_2(t)$ are the WTs $W_\psi x_1$ and $W_\psi x_2$ with respect to $\psi(t)$. The WT $W_\psi x$ of a signal $x(t)$ is defined as (Mallat, 2008)

$$W_\psi x(s,b) = \int_{-\infty}^{\infty} x(t)\psi^*\left(\tfrac{t-b}{s}\right)dt \tag{7.6}$$

where $\psi_{s,b}(t) = |s|^{-1/2}\psi\left(\tfrac{t-b}{s}\right)$ consists of a family of normalised dilations (controlled by scale parameter s) and translations in time (controlled by translation parameter b) of $\psi(t)$.

An important property that must be satisfied by the WT used in implementing the IB-TDE method is *shift-invariance*. A shift-invariant WT preserves any delay present in the signals. In other words, a shift in the input signal manifests as an equivalent shift in the WT coefficients at *all* scales (Bradley, 2003). Two choices for shift-invariant WTs are the continuous wavelet transform (CWT) and the maximal overlap discrete wavelet transform (MODWT). The MODWT is a non-decimated version of the conventional discrete wavelet transform (DWT) that operates over dyadic scales $s = 2^{-k}$, $k \in \mathbb{Z}$, and integer translations $b = n \in \mathbb{Z}$ (Percival and Walden, 2000). Since the MODWT is more computationally efficient than the CWT, it is preferred for implementing the IB-TDE method. For a given scale $s = 2^{-k}$, the CCF $R_{\tilde{x}_1\tilde{x}_2}(\tau)$ can be defined in terms of the MODWTs of the signals as

$$R_{\tilde{x}_1\tilde{x}_2}(\tau) = R^{\psi}_{x_1x_2}(\tau,k) = \sum_n W_\psi x_1\left(2^{-k},n\right)W_\psi x_2\left(2^{-k},n+\tau\right) \tag{7.7}$$

where the parameter $k = 1,2,3,\ldots$ is referred to as the decomposition level. In this work, this method of computing the time delay using Equation (7.7) is termed wavelet transform cross-correlation (WTCC), and when necessary, denoted as *WTCC-wav*, where 'wav' indicates the wavelet used.

The weighting function $W(\omega)$ in the WTCC method is the squared magnitude of the FT of the selected wavelet at the given decomposition level $\underline{\psi}_k(\omega)$

$$\underline{\psi}_k(\omega) = \left|\mathrm{F}\left\{\psi_{2^{-k},n}(t)\right\}\right|^2 = 2^k\left|\underline{\psi}\left(2^{-k}\omega\right)\right|^2 \tag{7.8}$$

where $\underline{\psi}(\omega) = \mathrm{F}\{\psi(t)\}$. An important observation is that the bandwidth of $\underline{\psi}_k(\omega)$ depends on the decomposition level. Like all variants of the DWT, the MODWT is efficiently implemented using a quadrature filter bank (Mallat, 2008). Each level of the filter bank consists of a low-pass filter and a high-pass filter, which provide the approximation and the detail coefficients of the signal, respectively. The detail coefficients from the k th level of the filter bank encompass frequencies in the interval $\left[F_s/2^{k+1}, F_s/2^k\right)$. Hence, the decomposition levels represent a set of bandpass filters with different frequency windows. Lower decomposition levels correspond to higher frequencies and larger

bandwidths while higher decomposition levels correspond to lower frequencies and smaller bandwidths. Therefore, the variance of the WTCC time delay estimate will depend on the decomposition level, especially when the SNR is low (see Equation (7.5)). Implementing the WTCC involves the selection of two parameters: the wavelet and the decomposition level. Their selection can be based on important properties of wavelets, discussed below. For efficiency, only discrete wavelets will be considered.

7.2.1 Selection of wavelet function and decomposition level

The selection of discrete wavelets for any application is governed by properties such as orthogonality, vanishing moments, regularity, support length, and symmetry (Guo et al., 2022). Among these properties, the most important for TDE are the number of vanishing moments and orthogonality. The former has a direct effect on the bandwidth of wavelets, while the latter determines the efficiency of computing the WT (Dremin et al., 2001). The computational burden of the MODWT implemented using an orthogonal wavelet is the same as that of the FFT algorithm (Percival and Walden, 2000). Examples of orthogonal wavelets include Daubechies ('db N'), symlet ('sym N'), coiflet ('coif N'), and Fejer-Korovkin wavelets ('fk N'). Here, N denotes the number of vanishing moments. For a description of these wavelets, see Mallat (2008). The frequency responses of different orthogonal wavelets (haar, db4, sym8, fk22) at various decomposition levels are shown in Figure 7.2. The Haar wavelet (denoted as 'haar') is the same as 'db1'.

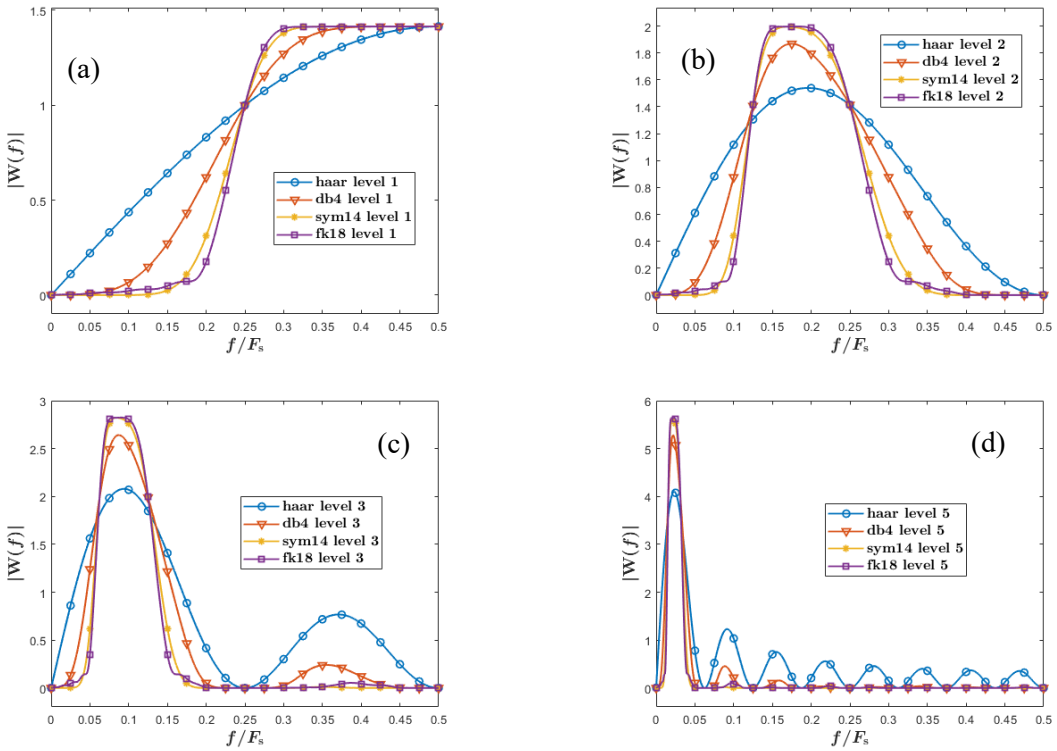

Figure 7.2: Frequency responses of haar, db4, sym14, fk18 wavelets at different decomposition levels. (a) Level 1. (b) Level 2. (c) Level 3. (d) Level 5.

It can be observed that wavelets with more vanishing moments have lower centre frequencies and smaller bandwidths, generally resulting in better frequency localisation (Guo et al., 2022). On the other hand, wavelets with fewer vanishing moments have larger bandwidth (but smaller responses) and larger side lobes. High side lobes imply that the WT may spread frequency information between frequency windows, thereby showing contents outside the frequency range of interest. However, since these sidelobes are much smaller than the main lobes, this is not likely to be a serious issue in the WTCC. Since wavelets with fewer vanishing moments are less computationally expensive and allow more low-frequency contents to pass, they are a good choice for analysing leak signals. Using wavelets with high number of vanishing moments increases the computational burden of the WTCC. Thus, the best choice of wavelets in the TDE method is orthogonal wavelets with fewer vanishing moments.

For accurate TDE results, it is desirable for the bandwidth of the weighting function to be located in the frequency region where the leak noise spectrum is significant relative to the noise (Almeida, 2013). Hence, when implementing the WTCC, it is important to avoid wavelet decomposition levels whose bandwidth include very low-frequency regions dominated by noise or high-frequency regions that have been severely attenuated by the filtering effects of the pipe. To select the best decomposition level(s), the relative wavelet energy (RWE) criterion can be employed. The RWE for each decomposition level k is defined as (Rosso et al., 2001)

$$\mathrm{RWE}_k = \frac{E_{1,k}}{E_{1,\mathrm{tot}}} + \frac{E_{2,k}}{E_{2,\mathrm{tot}}} \tag{7.9}$$

where $E_{i,k} = \sum_n W_\psi^2 x_i\left(2^{-k}, n\right)$ represents the energy encompassed by the k th decomposition level in the WT of the i th signal, and $E_{i,\mathrm{tot}} = \sum_n x_i^2\left(n\right)$ is the total energy in the signal. A justification for using this criterion is that the MODWT partitions signal variance or energy by scale (Percival and Walden, 2000). Hence, decomposition levels where the leak signal energy is significant will have higher energy compared to those with only noise, so the best decomposition levels are those with the highest RWE. The PSR proposed in Chapter 6 can also be used to select the best decomposition levels. Because of the shift-invariant property of the MODWT, an approach that may be useful for improving TDE accuracy with very little increase in computational complexity is to estimate the time delay from the sum of the wavelet coefficients at the decomposition levels with high RWE or PSR.

Figure 7.3(a) shows the variance of the time delay estimate calculated using Equation (7.1) for the first 10 decomposition levels of haar, db4, sym8, and fk22 wavelets and simulated leak signals with SNRs of 3 dB. The details of the simulation procedures are described in Section 4.5.1. An important observation that can be made from the plot is that the wavelets all achieve the smallest variance at the same decomposition levels. Also, wavelets with fewer vanishing moments achieve smaller variance at a given decomposition level than more complex wavelets. Based on the plot, these

wavelets are also more likely to give good results over a larger number of decomposition levels. As stated above, the higher side lobes in these wavelets do not seem to have substantial effects on the variance. It can also be observed from Figure 7.3(b) that the RWE and PSR attain their highest values at the decomposition levels where the smallest variance is achieved, thus confirming the soundness of employing these criteria for selecting the best decomposition levels. These results suggest that the accuracy of the time delay estimate is determined primarily by the selected decomposition level rather than the wavelet used. As shown by the higher variance achieved at these levels in Figure 7.3(a), the very low and high decomposition levels are likely to be unsuitable for TDE in noisy signals. This is because these decomposition levels have their bandwidths either in the low-frequency region dominated by noise or include frequency regions where the leak noise is severely attenuated. In the next subsection, the performance of the WTCC for leak signals is evaluated further using numerical simulations.

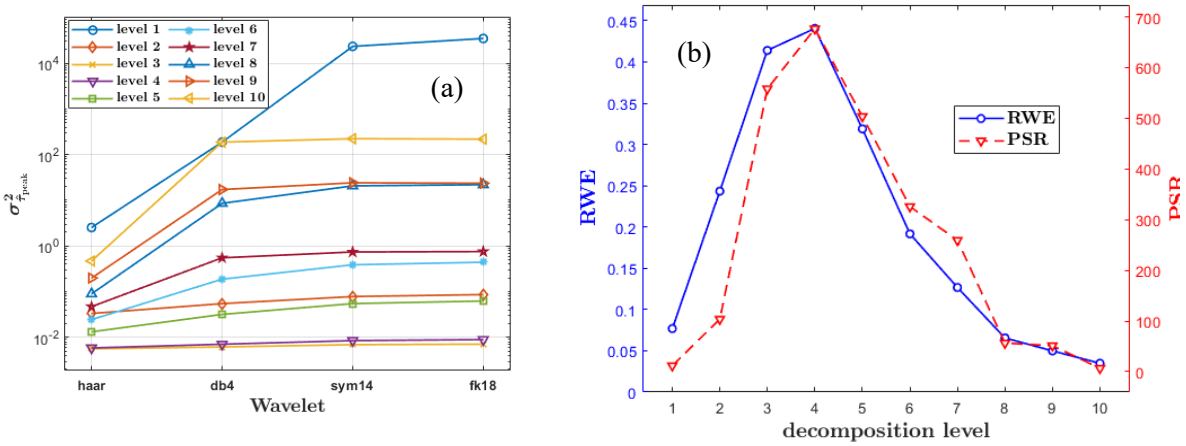

Figure 7.3: Simulation results for the WTCC. (a) Variance of the time delay estimate. (b) RWE and PSR for the db4 wavelet.

7.2.2 Simulation results for the wavelet transform-based time delay estimator

The RMSE (Equation (3.8)) of the WTCC time delay estimates obtained over 1000 Monte Carlo simulation runs for acoustic pressure signals is compared with that of the BCC, GCC-PHAT, and GCC-ML estimates for SNR values between -9 dB and 6 dB in Figure 7.4. The simulation procedures are as described in Section 4.5.1, and the simulation parameters are shown in the caption of Figure 7.4. For each run, a different realisation of the added noise was used. Regardless of the wavelet used, the WTCC achieves the lowest RMSE and outperforms the GCC methods at the third and fourth decomposition levels. However, its performance degrades significantly outside these levels, becoming worse than the GCC estimators especially at low SNR. In particular, the very low decomposition levels especially in wavelets with high number of vanishing moments are essentially useless for estimating the time delays as shown by the large variance. This again confirms the more crucial role of the decomposition level relative to the type of wavelet. Since the choice of wavelet is not crucial, one

can use the simplest orthogonal wavelet, the Haar wavelet in computing the CCF $R^{\psi}_{x_1x_2}(\tau,k)$ in order to reduce the computational load of the WTCC. Thus, the WTCC effectively requires the choice of only one parameter—the decomposition level, which can be easily selected using the RWE or PSR. Since the very low frequencies in leak signals are usually dominated by noise (Gao et al., 2006), it is suggested to restrict the number of decomposition levels considered to $\left\lfloor \log_2\left(\frac{F_s}{5}\right)\right\rfloor - 1$, where $\log_2\{\bullet\}$ denotes binary logarithm. This ensures that only decomposition levels whose lower cut-off frequencies are above 5 Hz are considered in the WTCC. For example, the suggested maximum levels to consider when estimating delays in signals sampled at 500 Hz and 1 kHz will be 5 and 6, respectively. The performance of the WTCC will be further investigated using experimental leak signals in Section 7.5.

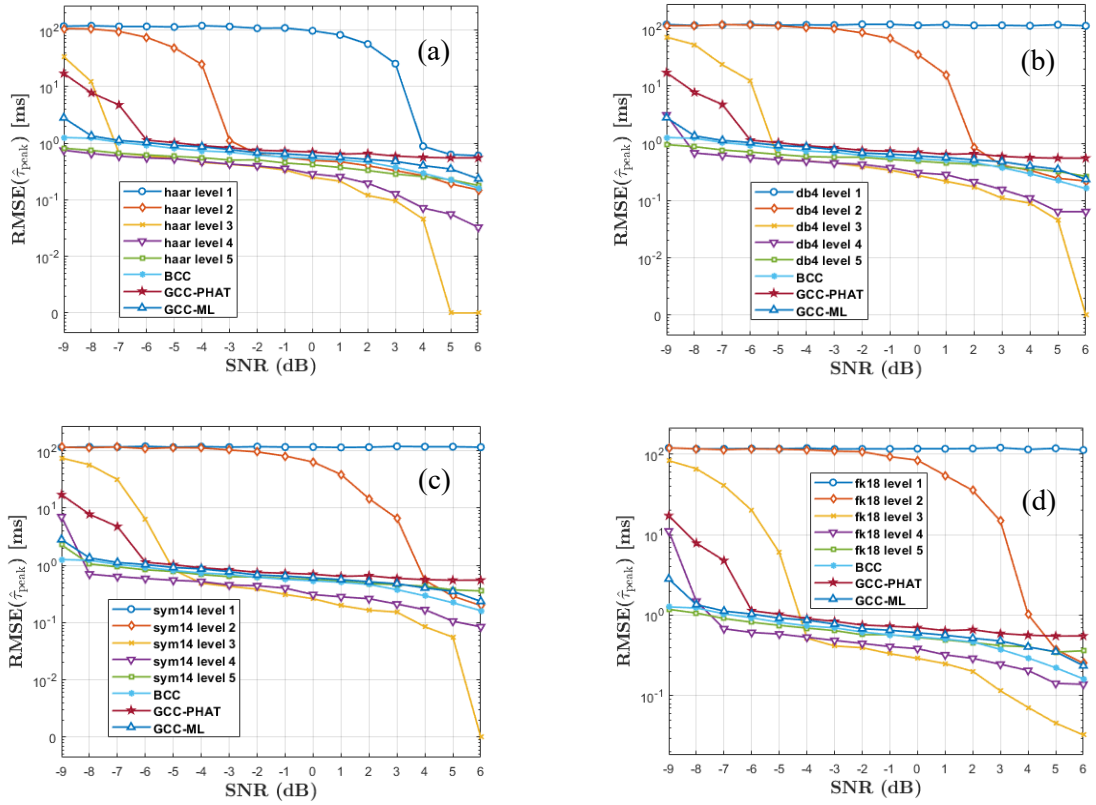

Figure 7.4: RMSE of the WTCC and GCC time delay estimates for different wavelets: (a) haar. (b) db4. (c) sym14. (d) fk18. Simulation parameters: $c = 354$ m/s, $\beta = 2.1\times10^{-5}$ s/m, $d_1 = 9$ metres, $d_2 = 25$ metres, $F_s = 500$ Hz.

7.3 Data-adaptive time delay estimator

The second approach for implementing the IB-TDE method is based on the use of data-adaptive decompositions. Data-adaptive decompositions are heuristic analysis tools which resolve signals into their multi-resolution components in the time domain. Unlike the WT, they do not use fixed basis

functions but instead extract different resolutions from the signals directly. Examples include the empirical mode decomposition (EMD) (Huang et al., 1998), variational mode decomposition (VMD) (Dragomiretskiy and Zosso, 2014), and empirical wavelet transform (EWT) (Gilles, 2013). These data-adaptive decompositions separate a signal $x(t)$ into a set of complete and almost orthogonal components $\mathrm{IMF}_k(t)$, known as intrinsic mode functions (IMFs):

$$x(t) = \sum_{k=1}^{N_{\mathrm{imf}}} \mathrm{IMF}_k(t) + res(t) \tag{7.10}$$

where N_{imf} is the number of IMFs, and $res(t)$ is the residual. They achieve the decomposition of signals in very different ways. The EMD works recursively on the time-domain signal to extract progressively lower frequency IMFs via a sifting operation, whereas the VMD starts by identifying signal peaks in the frequency domain and extracts all modes concurrently. The sifting operation in the EMD basically involves the calculation of the moving average of the envelopes connecting extrema of the signal. On the other hand, the EWT extracts the IMFs by designing an adaptive wavelet filter bank based on segmentation of Fourier spectrum of the signal, achieved by detecting the local maxima in the spectrum. In contrast with the VMD and EWT, which have theoretical foundations, the EMD is purely algorithmic. As a result, the filters used in the VMD and EWT decompositions are available to the user.

The EMD is used in this section to illustrate some properties of data-adaptive decompositions relevant to the implementation of the IB-TDE method. Due to the lack of a theoretical description for the EMD, extensive numerical simulations were used to study its properties for leak signals. The simulation process and parameters are the same as in Section 4.5.1. Figure 7.5 shows the PSDs of the first 5 IMFs of the simulated leak signal and the binary logarithm of the number of zeros crossing N_{zcross} in the IMFs. The PSDs and the number of zero crossings were averaged over 1000 simulation runs. Different realisations of white Gaussian noise was added during each simulation run so that the simulated leak signal has an SNR of -3 dB. The PSDs have been normalised by their maximum value. The number of zero crossings is a rough measure of the centre frequency of each IMF. It can be observed that the PSDs of the IMFs are very similar to the weighting functions obtained at the decomposition levels of the MODWT (compare Figures 7.5 and 7.2). Furthermore, the centre frequency of the IMFs decreases on a dyadic scale just like that of the decomposition levels in the MODWT. This implies that the EMD recursively separates the signal into approximations (low-frequency components) and details (high-frequency components), essentially a bandpass filtering operation just like the MODWT. Similar results were obtained for white noise (Wu and Huang, 2004) and fractional Gaussian signals (Flandrin et al., 2004). Like the EMD, the VMD and EWT can also be viewed as a set of bandpass filters. However, the centre frequencies of VMD and EWT IMFs do not necessarily change on a dyadic scale (this is mainly related to the way the signals are decomposed by these data-adaptive decompositions). Among the data-adaptive decompositions, only the EWT shares

the energy-preserving property of the MODWT. In other words, the sum of the energy in all the decomposition levels in the MODWT and EWT is equal to the energy in the original signal, whereas this property is not found in the EMD and VMD techniques (Huang et al., 2008). Another important difference to note is that unlike the EMD IMFs, the contents of individual VMD and EWT IMFs are dependent on the number of IMFs being extracted (Wu et al., 2020; Shi et al., 2017). One important consequence of these differences is that IMFs of two signals from the same decomposition level obtained using the VMD or EWT do not necessarily have similar frequency content. These differences have important consequence when the IB-TDE method is implemented using these data-adaptive decompositions as described below.

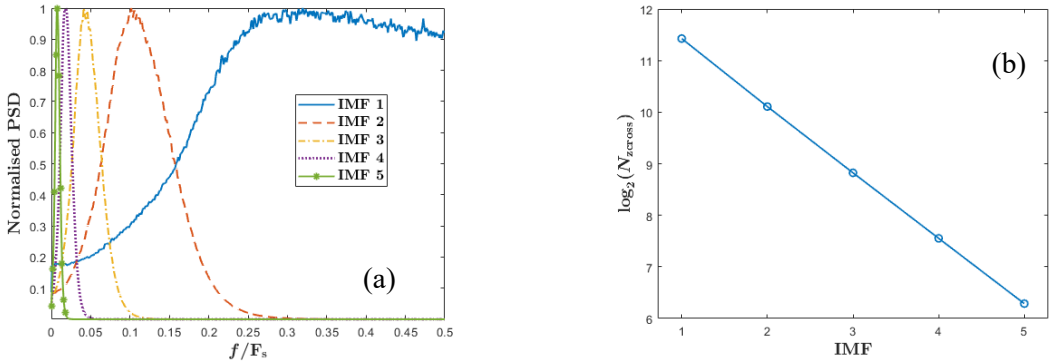

Figure 7.5: EMD of simulated leak signals. (a) Auto-power spectra of the IMFs. (b) Binary logarithm of the number of zero crossings.

The IB-TDE CCF $R_{\tilde{x}_1\tilde{x}_2}(\tau)$ can be implemented as the discrete CCF of the IMFs $\mathrm{IMF}_{k,1}$ and $\mathrm{IMF}_{\tilde{k},2}$ of signals $x_1(t)$ and $x_2(t)$, i.e.,

$$R_{\tilde{x}_1\tilde{x}_2}(\tau) = R^{DD}_{x_1x_2}(\tau,k) = \sum_n \mathrm{IMF}_{k,1}(n)\cdot \mathrm{IMF}_{\tilde{k},2}(n+\tau) \tag{7.11}$$

where $\mathrm{IMF}_{\tilde{k},2}$ denotes the IMF of $x_2(t)$ that encompasses the same frequency range as the IMF $\mathrm{IMF}_{k,1}$ of $x_1(t)$. As in the WTCC, the parameter $k = 1, 2, \ldots$ will also be referred to as the decomposition level. Due to the dyadic decomposition scheme inherent in the EMD, $\mathrm{IMF}_{\tilde{k},2} = \mathrm{IMF}_{k,2}$ when the IB-TDE is implemented using the EMD, i.e., the IMFs used in computing $R_{\tilde{x}_1\tilde{x}_2}(\tau)$ correspond to the same decomposition level. This is not necessarily the case for the VMD and EWT. In the case of implementation of the IB-TDE using these decompositions, $\mathrm{IMF}_{\tilde{k},2}$ has to be selected as the IMF whose centre frequency is closest to that of $\mathrm{IMF}_{k,1}$. This presents very little difficulty in practice as the filters used in the VMD and EWT decompositions are available to the user (in contrast with the EMD). This method of estimating the time delay from $R^{DD}_{x_1x_2}(\tau,k)$ defined in Equation (7.11) will be denoted in this work as '*DD*-CC', where '*DD*' denotes the type of data-adaptive decomposition employed. It requires the choice of only one parameter—the decomposition level k. Since the EMD

and VMD do not preserve energy of the signals, the proportion of energy in the IMFs is not an appropriate criterion for selecting the best decomposition level in the EMD-CC and VMD-CC. As a result, only the PSR can be used to facilitate the selection of the best decomposition levels in the EMD-CC and VMD-CC. On the other hand, analogously to the WTCC, the selection of the best IMF in the EWT-CC can be achieved using either the PSR or the Relative IMF Energy (RIE) criterion defined as

$$\mathrm{RIE}_k = \frac{E_{2,\mathrm{IMF}_k}}{E_{1,\mathrm{tot}}} + \frac{E_{2,\mathrm{IMF}_{\tilde{k}}}}{E_{2,\mathrm{tot}}} \tag{7.12}$$

where $E_{1,\mathrm{IMF}_k} = \sum_n \mathrm{IMF}_{k,1}^2(n)$ and $E_{2,\mathrm{IMF}_{\tilde{k}}} = \sum_n \mathrm{IMF}_{\tilde{k},2}^2(n)$ represent the energies in the selected IMFs. Like in the WTCC, an improvement in the TDE process may be achieved by summing the best IMFs in each signal prior to calculating the CCF.

The performance of the DD-CC was investigated using the EMD for the same simulated leak signals used in Section 7.2.2. Figure 7.6(a) shows the RMSE of the time delay estimates obtained for the first 5 IMFs. The first two IMFs achieve a substantially lower RMSE than higher IMFs, considerably outperforming the GCC estimators. The average RIE and PSR values are also maximum for these IMFs as shown in Figure 7.6(b). In contrast with the first wavelet decomposition level (which essentially defines a high-pass filter), the first IMF appears to be useful for TDE in leak signals. This is because the first IMF allows a higher proportion of low-frequency components to pass (compare Figures 7.5(a) and 7.2(a)). Since the bandwidth and centre frequency of the EMD IMFs become progressively smaller at higher decomposition levels, the search for the best IMF may be restricted to the first few decomposition levels. Based on the differences noted above, the best EMD IMFs will be contiguous and correspond to the lower decomposition levels, whereas that may not be the case with the VMD and EWT. Further experimental investigation of the DD-CC will be conducted in Section 7.5.

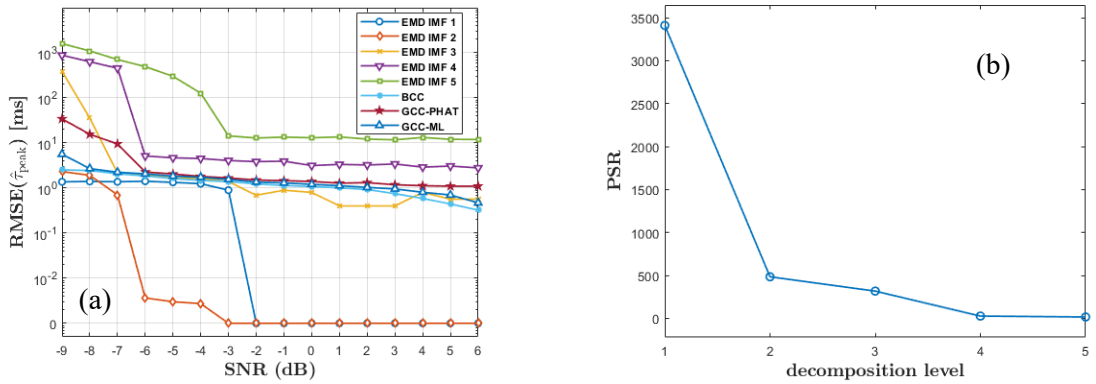

Figure 7.6: Simulation results for the EMD-CC. (a) RMSE of time delay estimate. (b) RIE and PSR. Simulation parameters: c = 354 m/s, β = 2.1×10^{-5} s/m, d_1 = 9 metres, d_2 = 25 metres, F_s = 500 Hz.

7.4 Cepstral time delay estimator

An interesting filtering property of the cepstrum is that it converts signals combined by convolution into sums of their cepstra for possible linear separation (Oppenheim et al., 1968). From the third term in Equation (4.12), it can be observed that the power cepstrum of a multipath leak signal contains impulses of alternating signs at integer multiples of the TDOA of the reflection. The inherent filtering ability and structure of the power cepstrum suggest an alternative approach for estimating time delays in leak signals, which is described as follows.

The sum $z_1(t)$ and difference $z_2(t)$ of the measured signals $x_1(t)$ and $x_2(t)$ in Equation (6.6)can be expressed as

$$\begin{cases} z_1(t) = x_1(t) + x_2(t) = \left[h_1(t) + h_2(t)\right] \otimes l(t) + v_1(t) \\ z_2(t) = x_1(t) - x_2(t) = \left[h_1(t) - h_2(t)\right] \otimes l(t) + v_2(t) \end{cases} \tag{7.13}$$

where $v_1(t) = n_1(t) + n_2(t)$ and $v_2(t) = n_1(t) - n_2(t)$. The signals $z_1(t)$ and $z_2(t)$ are composite signals consisting of attenuated copies of $l(t)$ corrupted by additive noise signals $v_1(t)$ and $v_2(t)$. If in addition to Assumption A1 in Section 7.1.1, $n_1(t)$ and $n_2(t)$ are assumed to be Gaussian, then $v_1(t)$ and $v_2(t)$ are both zero-mean identically distributed Gaussian random signals with the same true auto-power spectra: $G_{v_1v_1}(\omega) = G_{v_2v_2}(\omega) = G_{vv}(\omega)$. Using the procedures in Appendix C, the power cepstra of $z_1(t)$ and $z_2(t)$ are then obtained as

$$\begin{cases} \breve{z}_1(q) = R_1(q) + \sum_{m=1}^{\infty} \frac{(-1)^{m-1}}{m} g_{1,m}(q) + \frac{1}{2} \sum_{k=1}^{\infty} (-1)^{k+1} Q_k(q) \otimes \delta\left(q \pm k\tau_{\text{peak}}\right) \\ \breve{z}_2(q) = R_2(q) + \sum_{m=1}^{\infty} \frac{(-1)^{m-1}}{m} g_{2,m}(q) - \frac{1}{2} \sum_{k=1}^{\infty} Q_k(q) \otimes \delta\left(q \pm k\tau_{\text{peak}}\right) \end{cases} \tag{7.14}$$

where $R_1(q) = R_2(q) = \mathrm{F}^{-1}\left\{\log\left\{G_S(\omega)\right\}\right\}$, $G_S(\omega) = G_{l_1l_1}(\omega) + G_{l_2l_2}(\omega) + G_{vv}(\omega)$,

$g_{i,m}(q) = \mathrm{F}^{-1}\left\{\left\{v_i(\omega)\right\}^m\right\}$, $v_i(\omega) = \dfrac{\varepsilon_i(\omega)}{G_{z_iz_i}(\omega)}$, $\varepsilon_i(\omega)$ denotes the random fluctuations in the spectral estimate of $G_{z_iz_i}(\omega)$; $Q_k(q) = \mathrm{F}^{-1}\left\{M_k(\omega)\right\}$, $M_k(\omega)$ are polynomial functions of $A(\omega) = a(\omega)B(\omega) = 2\dfrac{G_{ll}(\omega)}{G_S(\omega)}e^{-|\omega|\beta d}$, defined in Appendix C; $a(\omega) = \dfrac{2e^{-|\omega|\beta\Delta d}}{1+e^{-2|\omega|\beta\Delta d}}$, $\Delta d = d_2 - d_1$,

$B(\omega) = \left[1 + 1/\chi(\omega)\right]^{-1}$, and $\chi(\omega) = \dfrac{G_{l_1l_1}(\omega)}{G_{vv}(\omega)} + \dfrac{G_{l_2l_2}(\omega)}{G_{vv}(\omega)}$ denotes the sum of the SNRs (in the frequency domain) of the measured leak signals. It can be observed that the signs of the impulses at

the quefrencies corresponding to the time delay τ_{peak} and its odd harmonics differ in $\breve{z}_1(q)$ and $\breve{z}_2(q)$. Therefore, only the impulses at the quefrencies corresponding to the time delay and its odd harmonics are preserved in the 'residual cepstrum' $z(q)=\breve{z}_1(q)-\breve{z}_2(q)$:

$$z(q)=\sum_{m=1}^{\infty}\frac{(-1)^{m-1}}{m}g_{12,m}(q)+\sum_{k=1}^{\infty}Q_k(q)\otimes\delta\left(q\pm(2k-1)\tau_{\text{peak}}\right) \tag{7.15}$$

where $g_{12,m}=g_{1,m}(q)-g_{2,m}(q)$. Based on the properties of $Q_k(q)$, the height of the impulses reduces as k increases, so the highest peak will be observed at $k=1$. Hence, an estimate of the time delay $\hat{\tau}_{\text{peak}}$ between $x_1(t)$ and $x_2(t)$ can be obtained as the location of the highest peak in the residual cepstrum. Due to the symmetry of the power cepstrum (Mandava, 1992), only the first half of $z(q)$ is considered when estimating the time delay. This method of estimating the time delay is referred to as *cepstral TDE method* in this work (abbreviated as 'CEPS-TDE'). The CEPS-TDE is similar to a TDE approach algorithmically described by Choudhary et al. (2015) for an underwater multipath environment. Since $v_i(\omega)$ is a zero-mean process, the effects of the terms $g_{12,m}$ in Equation (7.15) can be reduced by averaging many realisations of $z(q)$ obtained from segments of the signals. To avoid cepstral aliasing, the length of the segments should be sufficiently long or zero-padded as discussed by Bolton and Gold (1984). In the next subsection, the performance of CEPS-TDE for leak signals is analysed in terms of pipe and signal properties.

7.4.1 Variance of the cepstral time delay estimate

The variance $\sigma^2_{\hat{\tau}_{\text{peak,CEPS}}}$ of the cepstral time delay estimate can be expressed as (Appendix G2)

$$\sigma^2_{\hat{\tau}_{\text{peak,CEPS}}}=\frac{\pi}{3T}\left(\omega_2^3-\omega_1^3\right)\left[\int_{\omega_1}^{\omega_2}\omega^2 a(\omega)\chi(\omega)e^{\chi(\omega)}\,\mathrm{E}_1\{\chi(\omega)\}\,d\omega\right]^{-2} \tag{7.16}$$

where the first-order exponential function $\mathrm{E}_1\{u\}$ is related to the exponential integral $\mathrm{Ei}\{u\}$ by $\mathrm{E}_1\{u\}=-\mathrm{Ei}\{-u\}$ (Gradshteyn and Ryzhik, 2007). The expression $\chi(\omega)e^{\chi(\omega)}\,\mathrm{E}_1\{\chi(\omega)\}$ tends towards unity as $\chi(\omega)\to\infty$ and towards zero as $\chi(\omega)\to 0$ (Abramowitz and Stegun, 1964, page 242). Hence, when the SNRs of the signals are high ($\chi(\omega)\gg 1$ for $\omega_1\le\omega\le\omega_2$), the variance of the time delay estimate $\sigma^2_{\hat{\tau}_{\text{peak,CEPS}}}$ can be approximated as

$$\sigma^2_{\hat{\tau}_{\text{peak,CEPS}}}\Big|_{\text{high}} \approx \frac{4\pi}{3T}\omega_2^3\left[\int_{\omega_1}^{\omega_2}\omega^2\frac{2e^{-|\omega|\beta\Delta d}}{1+e^{-2|\omega|\beta\Delta d}}d\omega\right]^{-2} \approx \frac{\pi}{3T}\omega_2^3\left[\int_{\omega_1}^{\omega_2}\omega^2 e^{-|\omega|\beta\Delta d}d\omega\right]^{-2} \approx \frac{\pi}{12T}\left(\beta\Delta d\right)^6\omega_2^3 \quad . \tag{7.17}$$

In the interval $0 < u \le 1$, the exponential function $\mathrm{E}_1\{u\}$ can be approximated as (Abramowitz and Stegun, 1964, page 231)

$$\mathrm{E}_1\{u\} \approx -\log\{u\} - \gamma + a_1u + a_2u^2 + a_3u^3 + a_4u^4 + a_5u^5 \tag{7.18}$$

where γ is Euler-Mascheroni constant, and $a_1, a_2, \ldots, a_5$ are real constants. Noting that $e^{\chi(\omega)} \approx 1$ for $\chi(\omega) \ll 1$ and $G_{vv}(\omega) = 2N_0$ under Assumption A2 above, $\sigma^2_{\hat{\tau}_{\text{peak,CEPS}}}$ can be approximated in low-SNR conditions as

$$\sigma^2_{\hat{\tau}_{\text{peak,CEPS}}}\Big|_{\text{low}} \approx \frac{\pi}{3T}\frac{N_0^2}{S_0^2}\omega_2^3\left[\int_{\omega_1}^{\omega_2}\omega^2 e^{-|\omega|\beta d}\cdot\left(\log\{\chi(\omega)\}+\gamma\right)d\omega\right]^{-2} \tag{7.19}$$

where the first-order and higher monomial terms in Equation (7.18) have been neglected.

In both high and low-SNR conditions, the variance of the cepstral time delay estimate varies polynomially as the analysed bandwidth and pipe attenuation factor. In high-SNR case, for a given pipe and analysed bandwidth, the variance of the cepstral time delay estimate is essentially a constant independent of signal properties. Like in the IB-TDE method, the variance does not depend on the actual leak location when SNR is low. Possible measures for reducing the variance are increasing the observation time and adjusting the value of ω_2. However, this frequency cannot be set arbitrarily; pipe attenuation and signal properties must be considered. In the next section, the performance of the cepstral time delay estimate is compared with that of the IB-TDE method.

7.4.2 Comparison of cepstral and inherent bandpass time delay estimators

It can be shown that the CEPS-TDE always achieves a lower variance than the IB-TDE method in low-SNR conditions as follows. To facilitate the comparison of the two methods, the expressions for the variance are expressed in alternative forms. Since $\chi(\omega)$ can be neglected in low-SNR conditions, the low-SNR approximation of the IB-TDE time delay estimate variance in Equation (7.2) can be expressed as

$$\sigma^2_{\tau_{\text{peak}},\text{IB}}\Big|_{\text{low}} \approx \frac{\pi}{T}\frac{\int_{\omega_1}^{\omega_2}\omega^2\left[2\chi(\omega)+\frac{N_0^2}{S_0^2}\right]d\omega}{\left[\int_{\omega_1}^{\omega_2}\omega^2 e^{-|\omega|\beta d}d\omega\right]^2} \approx \frac{\pi}{3T}\frac{N_0^2}{S_0^2}\omega_2^3\left[\int_{\omega_1}^{\omega_2}\omega^2 e^{-|\omega|\beta d}d\omega\right]^{-2} \quad . \tag{7.20}$$

The ratio of $\sigma^2_{\tau_{\text{peak}},\text{IB}}\Big|_{\text{low}}$ in Equation (7.20) to $\sigma^2_{\tau_{\text{peak,CEPS}}}\Big|_{\text{low}}$ in Equation (7.19) is obtained as

$$\frac{\sigma^2_{\tau_{\text{peak}},\text{IB}}\Big|_{\text{low}}}{\sigma^2_{\tau_{\text{peak,CEPS}}}\Big|_{\text{low}}} \approx \left[\frac{\int_{\omega_1}^{\omega_2} \omega^2 e^{-|\omega|\beta d}\cdot\left(\log\left\{\chi(\omega)\right\}+\gamma\right)d\omega}{\int_{\omega_1}^{\omega_2} \omega^2 e^{-|\omega|\beta d}\,d\omega}\right]^2 > 1 \qquad (7.21)$$

where the inequality follows from $\left|\mathrm{E}_1\left\{\chi(\omega)\right\}\right| \approx \left|\log\left\{\chi(\omega)\right\}+\gamma\right| > 1$ for small values of $\chi(\omega)$.

The superior performance of the CEPS-TDE is associated with the logarithmic conditioning in the cepstrum, as previously discussed in Section 4.4.3.

Figure 7.7 shows the RMSE of the CEPS-TDE time delay estimate for the simulated leak signals used in Section 7.2.2. It can be observed that the CEPS-TDE outperforms the conventional GCC methods at all SNR values considered. The superiority of the CEPS-TDE over the IB-TDE method can be verified by comparing the RMSE in Figures 7.4, 7.6(a), and 7.7. Apart from exhibiting a lower TDE variance than the IB-TDE method, another advantage of the CEPS-TDE is simplicity, as it does not require the selection of any parameter. One disadvantage that can be highlighted for the CEPS-TDE is inability to determine the sign of the time delay estimate. However, if necessary, the sign may be determined by considering the relative attenuation of the signals or inferred from their CCF.

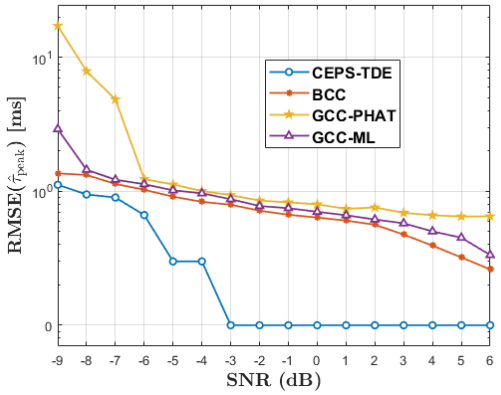

Figure 7.7: RMSE of the CEPS-TDE time delay estimate for simulated leak signals. Simulation parameters: $c = 354$ m/s, $\beta = 2.1\times10^{-5}$ s/m, $d_1 = 9$ metres, $d_2 = 25$ metres, $F_s = 500$ Hz.

7.5 Experimental results

The performance of the proposed IB-TDE and CEPS-TDE methods is investigated in this section using experimental data. The main features of the methods are illustrated with steady-state leak signals measured with accelerometers at X1 and X2 with a leak simulated at L1 in the leakage test rig described in Chapter 2. The sampling rate of the signals is 40 kHz, and the time delay between them is 9 ms. Figures 7.8(a)–7.8(c) show the CPS (magnitude and unwrapped phase) and MSC of the two signals. The signals have high coherence and approximately linear cross-spectral phase in the

frequency range 154-1048 Hz. The BCC and GCC-ML methods yield time delay estimates of 9.025 and 8.975 ms, respectively, while the GCC-PHAT method yields an estimate of 0 ms. Two possible reasons can be highlighted for the bad performance of the GCC-PHAT in this case. The first reason is the presence of resonances in the signals, as indicated by the peaks in the CPS magnitude (Figure

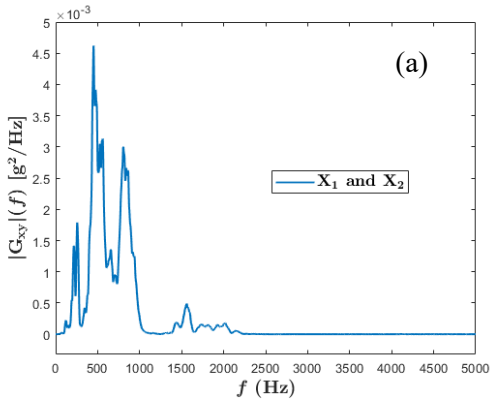

(a) Cross-spectral magnitude.

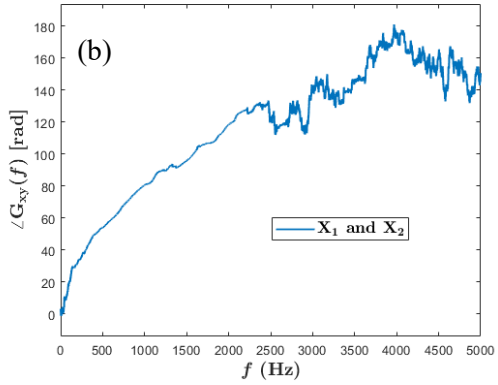

(b) Unwrapped cross-spectral phase.

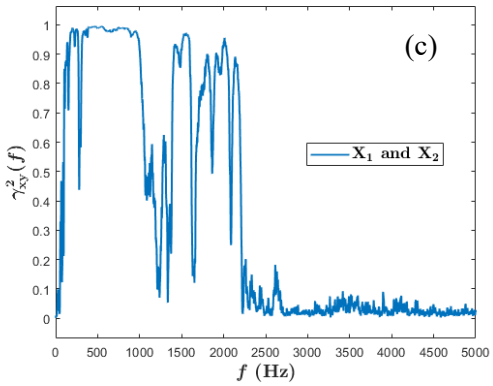

(c) Magnitude-squared coherence.

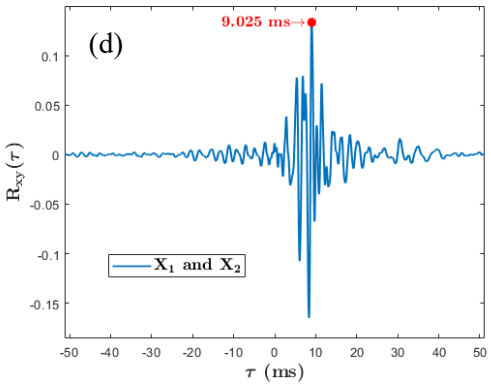

(d) Cross-correlation function.

Figure 7.8: Spectral properties and CCF of the X1 and X2 experimental leak signals.

7.8(a)) and the appearance of a large negative peak in the CCF in Figure 7.8(d) (Almeida, 2013). The second reason is that the cross-spectral phase is extremely noisy above 2.2 kHz indicating that it cannot be successfully unwrapped above this frequency. Because the GCC-PHAT estimates the time delay from the phase only, it is severely affected by the presence of resonances and noisy phase (Almeida, 2013). These factors are mitigated to some extent in the BCC and GCC-ML due to weighting of the phase by the CPS magnitude and coherence, respectively, both of which are very small in the frequency region with noisy phase. When the signals are first filtered in the frequency range with a linear phase, the GCC-PHAT estimate improves to 8.925 ms. As illustrated by this example and the results obtained in Section 6.4.2, the effectiveness of estimating time delays in leak signals using the conventional GCC approach is affected by the type of weighing function employed as well as the cut-off frequencies of any applied filter. Incorrect selection of any of these parameters may result in inaccurate time delay estimates. As will be demonstrated in this section, the proposed alternative TDE methods do not have such limitation.

The RWE, RIE, and PSR values obtained for the unfiltered signals for the first 10 decomposition levels of different wavelets and data-adaptive decompositions are shown in Figure 7.9. All wavelets achieve their highest RWE values at exactly the same decomposition levels, in this case, at decomposition levels 4-6. There is a good correlation between the PSR and the RWE for wavelets with high number of vanishing moments at all decomposition levels. In contrast with the RWE, the PSR achieves high values at the decomposition levels 1-3 for the Haar wavelet and levels 2-3 for the 'db4' wavelet. This implies that even though the proportion of signal energy at the low levels is relatively small, they may still be useful for estimating time delays using wavelets with small number of vanishing moments. This agrees with the simulation results in Section 7.2.1 (see Figure 7.3(a)). It can be observed from Figure 7.9(b) that the few IMFs that have a high proportion of signal energy also achieve the highest PSR values: IMFs 2-3 for the EMD, IMF 9 for the VMD, and IMFs 7 and 10 for the EWT. As expected from the discussion in Section 7.3, the best decomposition levels are contiguous in the EMD and MODWT, while the situation is different for the EWT.

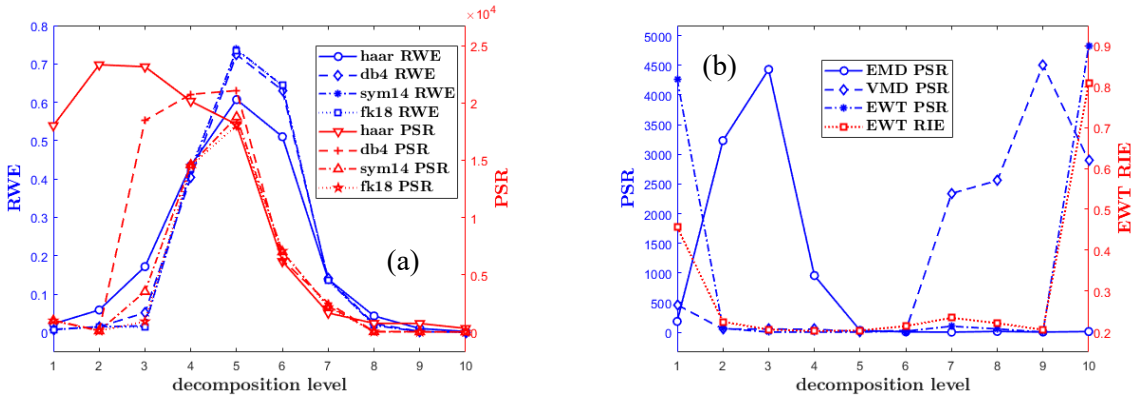

Figure 7.9: Selection of best decomposition levels for X1 and X2 experimental leak signals. (a) RWE and PSR. (b) RIE and PSR.

The WTCC and DD-CC time delay estimates obtained at all 10 decomposition levels are shown in Figure 7.10(a). It can be observed that the most accurate time delay estimates are obtained at the decomposition levels that yield the highest value of the RWE, RIE, and PSR. In agreement with simulation results, all the wavelets yield fairly accurate estimates at these decomposition levels, again confirming that the choice of decomposition level is more crucial than the type of wavelet employed. It should be noted, however, that the WTCC and DD-CC fail to give accurate time delay estimates if implemented using a decomposition level with low RWE, RIE, and PSR values, as shown by the estimates in Figure 7.10(a). In agreement with the conclusion from Figure 7.9 above, unlike more complex wavelets, the Haar wavelet yields accurate time delay even at the lowest decomposition levels. The CEPS-TDE yields the time delay estimate as 8.975 ms given by the location of the peak in the residual power cepstrum of the two signals shown in Figure 7.10(b).

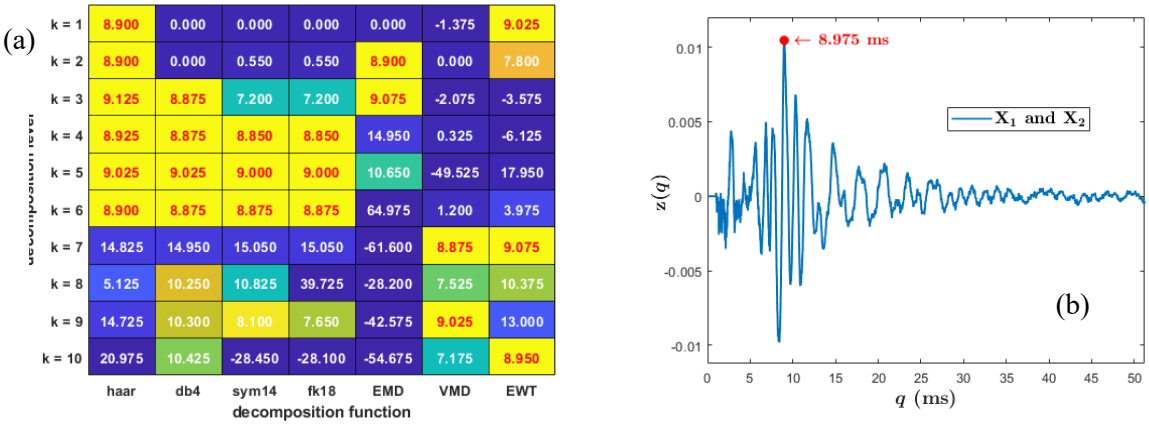

Figure 7.10: Time delay estimates for unfiltered leak signals. (a) WTCC and DD-CC. (b) Residual power cepstrum.

As stated in Sections 7.2.1 and 7.3, improvement in the performance of the time delay estimator may be achieved by computing the time delay from the sum of the WT coefficients or IMFs at the decomposition levels with high RWE, PSR, or RIE. This is illustrated using the EMD-CC in Figure 7.11, where the CCFs obtained from the best IMF (IMF 3) and the sum of the IMFs with high PSR (IMFs 2 and 3) are compared. It can be observed that the CCF computed from the sum of the IMFs provides a slightly higher peak as well as a more accurate estimate of the time delay (9.0 ms) than the value 9.075 ms provided by the third IMF only.

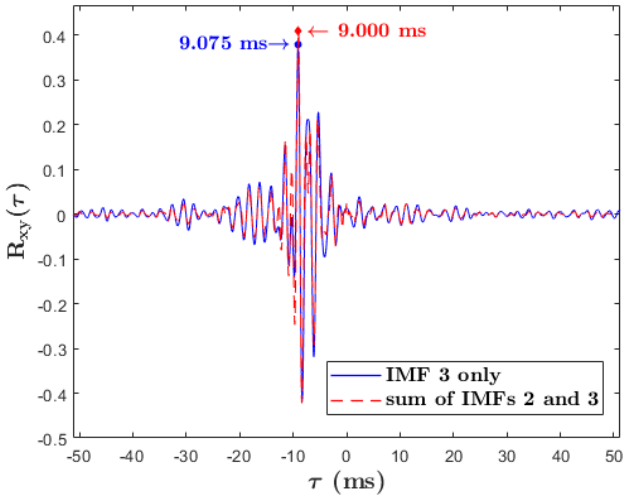

Figure 7.11: CCFs obtained from the EMD IMFs for the X1 and X2 signals: (a) IMF 3 only. (b) Sum of IMFs 2 and 3.

In order to demonstrate the ability of the proposed methods to estimate the time delay without pre-processing in situations where existing GCC methods fail, they were applied to the Ottawa hydrophone leak signals used for investigating quality assessment metrics in Section 6.4.2. As shown in that section, without first filtering the signals with a properly selected bandpass filter, the BCC, GCC-PHAT, and GCC-ML methods yield estimates of 448, 88, and 86 ms (see Figure 6.8(a) and Figure 6.9), which differ from 90 ms the value of the true time delay. Figures 7.1(a)–7.1(b) show the

RWE, RIE, and PSR calculated for the first 5 decomposition levels of the hydrophone signals. Since the sampling rate of the signals is 500 Hz, only the first 5 decomposition levels are considered in the WTCC and DD-CC as suggested in Section 7.2.1. With the exception of the PSR for the Haar wavelet, the criteria attain their maximum values at the following decomposition levels: 3 (wavelet), 1 (EMD), 5 (VMD), and 1 (EWT). While the PSR achieves its maximum at the first decomposition level of the Haar wavelet, it still has a high value at the third decomposition level of this wavelet.

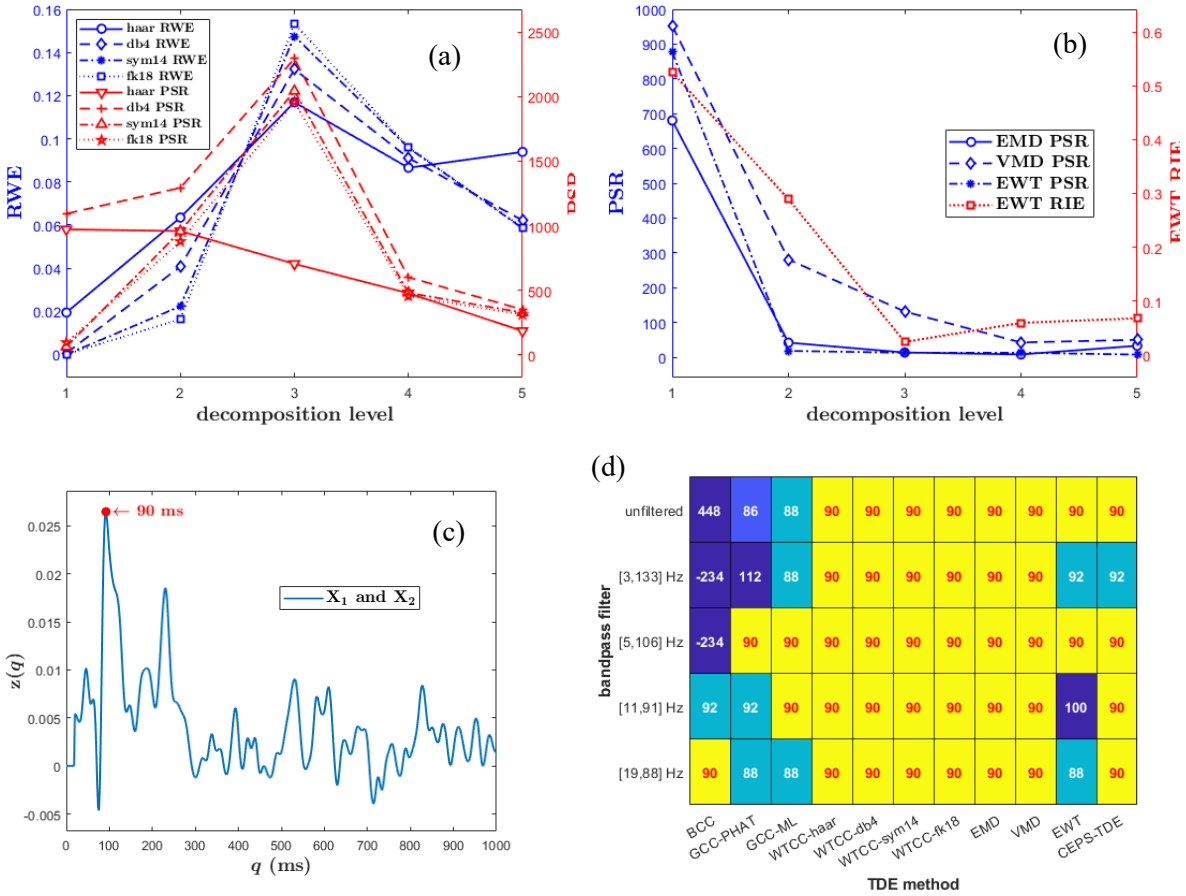

Figure 7.12: Estimating time delay in the Ottawa hydrophone signals. (a) RWE and PSR. (b) RIE and PSR. (c) Residual cepstrum. (d) Time delay estimates for raw and filtered signals.

Figure 7.12(d) shows the WTCC and DD-CC time delay estimates obtained at the above-mentioned decomposition levels with and without the application of bandpass filters, the cut-off frequencies of which are indicated on the plot. The selection of these filters was described in Section 6.4.2. Also presented are the GCC and CEPS-TDE results. Time delay estimates that correspond to the correct time delay value of 90 ms are indicated with yellow cells and red font. Estimates that deviate from the true value are indicated with white font. The further an estimate deviates from the true value, the darker the shade of blue used to denote its cell. Without first filtering the signals, the GCC methods fail to correctly estimate the time delay in the signals. On adjusting the cut-off frequencies of the filter to the frequency region 11-91 Hz where the leak noise dominates and coherence is high, the BCC, GCC-PHAT, and GCC-ML estimates improve to 92, 92, and 90 ms, respectively, which are closer to the actual time delay. In contrast with the GCC methods, the alternative TDE methods all provide

accurate time delay estimates even without first filtering the signals. In fact, the application of a bandpass filter has little or no effect on the WTCC, EMD-CC, VMD-CC, and CEPS-TDE time delay estimates. The residual power cepstrum of the unfiltered signals is shown in Figure 7.12(c), where it can be observed that the peak occurs at 90 ms. In complete agreement with the analysis in Section 7.2, practically the same time delay estimate is obtained for different wavelets at the selected decomposition level, thus confirming that only the choice of the decomposition level is important, not the type of wavelet used. Bandpass filtering appears to affect the EWT-CC, with the EWT-CC estimate becoming inaccurate with the application of the filters with the smallest bandwidths. Based on this, it is recommended not to apply any bandpass filter when estimating time delays using the EWT-CC.

These results demonstrate that in contrast with the conventional GCC method, the effectiveness proposed IB-TDE (except the EWT-CC) and CEPS-TDE methods in providing accurate time delay estimates are not affected by the cut-off frequencies of any applied filter. Based on their performances, the WTCC, EMD-CC, and CEPS-TDE methods are recommended as effective alternatives to conventional GCC methods. They provide practically convenient and effective means of estimating delays in acoustic leak detection. These methods can be implemented in leak noise correlators for more robust leak localisation performance. To conclude this study, the benefits and limitations of the proposed time delay estimators are briefly discussed in the next section.

7.6 Benefits and limitations of the time delay estimators

One obvious advantage of the proposed IB-TDE and CEPS-TDE methods is that the time delay can be obtained without requiring spectral information of the noise and leak signals or first filtering the signals. Due to their inherent filtering and denoising capabilities, the proposed methods achieve good performance when GCC methods fail as shown by the simulation and experimental results. They can be adopted as an effective way to accurately determine time delays between leak signals when the spectral characteristics of the signals and noise cannot be reliably estimated. Also, since these methods require the choice of not more than one parameter, their application simplifies the TDE process. This contrasts with the GCC approach where success is dependent on the selection of cut-off frequencies and choice of weighting function. The single parameter required in the WTCC and DD-CC methods, namely the decomposition level, can be effectively and easily selected using the RWE, RIE, and PSR, as demonstrated in this chapter. Ease of automation is another benefit of the proposed TDE methods, as they can be employed without need for any user input. In contrast, the coherence-based criterion (Muggleton et al., 2011) and cross-power spectrum-based criterion (Almeida, 2013) for selecting cut-off frequencies in the conventional GCC approach are generally difficult to apply without user interaction. The possibility for automated operation makes the proposed methods suitable for use by people who may lack the technical expertise required to select appropriate weighting functions and

cut-off frequencies in leak localisation systems. These advantages make the proposed methods practically attractive for estimating time delays in acoustic leak detection.

The only serious disadvantage that can be highlighted for the IB-TDE and CEPS-TDE methods is higher computational complexity compared to the conventional GCC methods. For example, the CEPS-TDE method involves calculation of multiple cepstra, while the IB-TDE methods require additional decomposition of the signals as well as selection of best decomposition level. As already stated, the computational burden of the WTCC can be reduced by using the simplest orthogonal wavelet, the Haar wavelet. The fast EMD algorithm (Myakinin et al., 2014; Zhang et al., 2021) can be employed to reduce the computational burden of the EMD-CC. Further works will focus on refinement of the methods in terms of reducing their computational complexity.

7.7 Summary and conclusion

This chapter focused on the aspect of time delay estimation (TDE) problem in acoustic leak detection concerning the improvement of the accuracy of the time delay estimate. To achieve this, two alternative methods that do not require explicit selection of cut-off frequencies and weighting functions were introduced. The first referred to as inherent bandpass filtering method (IB-TDE) applies transforms with inherent filtering capability, namely the wavelet transform (WT) and data-adaptive decompositions, to leak signals and then completes the cross-correlation processing on the decomposed signals. The second referred to as the cepstral method (CEPS-TDE) calculates the power cepstra of the sum and difference of the leak signals and then estimates the time delay from the location of the highest peak in the difference of the resulting two cepstra.

While the proposed methods are more computationally expensive compared to conventional generalised cross-correlation (GCC) methods, numerical simulations and experimental results show that they have fewer failures and lower estimate errors than the GCC methods. Their superiority over the GCC is due to their feature of inherently filtering the signals prior to calculating the time delay. An important conclusion is that the accuracy of the wavelet-based and data-adaptive methods is determined primarily by the selected wavelet decomposition level rather than the wavelet or data decomposition employed. The selection of best decomposition levels is facilitated using simple criteria, such as the relative wavelet energy (RWE), relative IMF energy (RIE), and the peak-to-side lobe ratio (PSR). By eliminating the need for preliminary filtering and choice of weighting functions, these methods provide an attractive alternative for robust TDE in acoustic leak detection without the limitations of the conventional GCC methods.

CHAPTER 8
COMBINING TRANSIENT AND STEADY-STATE METHODS FOR ACOUSTIC LEAK DETECTION

An important conclusion from the results in the preceding chapters in this thesis is that each acoustic leak detection method, transient or steady-state, offers practical benefits but suffers from issues that limit its applicability in some situations. Moreover, each method is suitable only for specific leak detection tasks. As a result, no one method is adequate for detecting and locating leaks in all application scenarios. Robust and reliable performance can only be achieved through a systematic synergy of different methodologies. The primary aim of this chapter is to explore the possibility of employing this strategy in order to improve acoustic leak detection. To achieve this aim, different acoustic leak detection methodologies are compared, and an approach for their simultaneous application is developed. Experimental results are provided to investigate the effectiveness of the proposed approach.

8.1 Comparison of acoustic leak detection methods

In this section, the acoustic leak detection methods are compared in terms of cost, ease of implementation and data analysis, and suitability for leak detection tasks. Table 8.1 summarises the use, advantages, and shortcomings of transient and steady-state methods, including those proposed in Chapters 3–5. Use of listening devices is suitable for routine acoustic leak surveys and pinpointing of discovered leaks. This technique is the least expensive among acoustic methods in terms of hardware cost. However, it is labour-intensive and so inefficient for regularly inspecting a large pipe network. Moreover, analysis and interpretation of results require a trained and experienced technician to distinguish between sounds from leaks and extraneous noise. Modern electroacoustic listening devices that include features such as digital filters and electronic displays improve leak detection effectiveness and aid objective interpretation of results (Sewerin, 2023).

Compared to use of listening devices, acoustic noise logging and cross-correlation incur substantially higher equipment cost but less labour costs (Hunaidi et al., 2004). While acoustic noise logging is applicable for discovering leaks, cross-correlation can only be used to locate leaks after their discovery. They are effective options for discovering and locating leaks in busy or inaccessible areas where manual surveys may not be feasible or effective. Practical application of these methods requires technical expertise to set appropriate data analysis parameters, for example, filters in leak noise cross-correlators. Depending on the capabilities of the employed leak detection devices, a trained technician may be needed to interpret the data acquired by the devices, especially lower-end

Table 8.1: Summary of steady-state and transient methods.

Method	Suitable tasks	Advantages	Shortcomings
Steady-state methods			
Listening devices	Leak detection and pinpointing	Simplicity and ease of use. Relatively inexpensive. Minimal system interruption. Needs no calibration or further analysis.	Labour-intensive. Infrequent surveys. Possibly significant water loss before leak discovery. Subjective results. Small leak detection range.
Acoustic noise logging	Leak awareness	Suitable for busy areas. Provides long-term record. Automated operations. May be used with other loggers to quantify leaks. Can detect old and new leaks.	Not suitable for locating leaks. High false alarm rates and questionable hardware reliability. (Van Der Kleij and Stephenson, 2002) Takes a long time to detect and confirm leaks.
Passive steady-state detection		Faster than acoustic noise logging. Only a single measurement required. Simple to implement.	Requires initial calibration for robust operation. Cannot locate leak. May be ineffective for detecting 'weak' leaks.
Conventional cross-correlation	Leak localisation	Simple to deploy and use. Suitable for pipes in inaccessible routes. Minimal system interruption.	Requires knowledge of wave speed. Relatively high equipment cost. Inefficient for plastic and large-diameter metallic pipes (Hunaidi, 2012). Technical knowledge required to set appropriate parameters.
Blind Channel Identification		Knowledge of wave speed is not required. Suitable for buried pipes with unknown properties. Capability to estimate the wave speed.	Affected by channel estimation errors. Susceptibility to noise. May be ineffective in non-uniform pipe sections. Less expensive than conventional cross-correlation
Multipath identification		A priori knowledge of wave speed not required. Capability to estimate the wave speed.	Requires accurate pipe system schematic and presence of known discontinuities. Affected by multipath identification errors and noise. Not effective in pipes with high attenuation, for example, large-diameter pipes. Reduced leak detection range.

Transient methods			
Method	**Suitable tasks**	**Advantages**	**Shortcomings**
Passive transient detection	Leak awareness	Fast, real-time detection. Simple to implement. Requires only a single recording.	Continuous sensor operation. Cannot locate leak. Can only detect new leaks.
Active transient (matching method)	Leak awareness, Leak localisation	Fast, real-time detection. Knowledge of wave speed is not required. Capability to estimate the wave speed. Can detect old and new leaks.	Requires accurate pipe system schematic and presence of known discontinuities. Effectiveness depends on ability to locate reflections. Lack extensive experimental validation on real systems.

models (EPA, 2010). Higher-end devices include additional features such as frequency filtering, digital readouts, and correlating analysis, thereby providing more 'automated' interpretation of data (Kilinski, 2019). However, their use increases the cost of leak detection. It should be noted that devices that combine the functionalities of acoustic noise logging and leak cross-correlation (the so-called correlating leak noise loggers) are commercially available (Hamilton and Charalambous, 2020). The use of such devices can reduce the overall hardware cost of acoustic leak detection. Another measure for reducing cost is to employ cross-correlation systems that use personal computers instead of dedicated leak noise correlator hardware devices. Acoustic noise logging and cross-correlation can be implemented either using permanently installed devices or employed in an ad-hoc manner using a 'lift and shift' scheme. Data from permanently installed devices are generally downloaded during a 'drive-by' survey. In the *'drive by'* scheme, at regular interval, the devices are driven past by an operative with a leak detection system in their van. The devices transmit data via radio to the leak detection system during the 'drive-by' survey (Bykerk and Valls Miro, 2022).

The passive steady-state leak awareness method proposed in Chapter 3 offers the possibility of discovering leaks from a short-term measurement in a timelier manner than is possible with acoustic noise logging. In fact, only a single measurement is required to identify the presence of a leak in the pipe using this method. While this method is simple to apply, it may not be effective for detecting 'weak' leaks that do not exhibit clearly distinguishable features in their signal spectrum. Furthermore, it requires the availability of leak-free reference signals to set the LDM normalisation factor for robust performance. The steady-state system identification and multipath identification methods proposed in Chapters 4 and 5, respectively, can locate leaks without knowledge of pipe properties or wave speed unlike the leak noise correlation method. They are also relatively less expensive than cross-correlation techniques that use dedicated leak noise correlators. However, both methods are susceptible to noise and any factor that adversely affects TDE accuracy. The system identification method may not be effective in pipes with non-uniform sections. Compared to other steady-state acoustic leak localisation methods, the range of the multipath identification method is reduced. Also, this method is not likely to be effective in pipes with high attenuation, for example, large-diameter pipes used in transmission

applications. Furthermore, it can only be applied in the presence of known discontinuities close to the sensor location.

In contrast with most steady-state methods, transient methods by their nature are suitable for identifying leaks in real time. They, however, require permanently installed sensor systems that operate and transmit data continuously to a central server. The passive transient leak awareness method proposed in Chapter 3 is only capable of discovering new leaks that trigger 'strong' acoustic transients. Also, this method may issue false alarms in the presence of a new persistent non-leak signal source. Among all the methods listed in Table 8.1, only the active transient (matching) method is capable of both detecting and locating old and new leaks. All the other methods are suitable for either leak awareness or for locating discovered leaks. Unlike other leak localisation methods, the matching method can be implemented using only one sensor. It offers the capability of estimating the wave speed. However, like the multipath identification steady-state method, it requires accurate pipe system schematic and presence of known discontinuities in the pipe. Since its effectiveness generally depends on the ability to locate reflections in measured leak signals, it is affected by multipath identification errors and noise. Due to the additional cost associated with battery, data storage, and data transmission, transient methods are likely to incur higher hardware cost than steady-state methods. Hence, these methods may not be cost effective in large pipe systems, and it may be more appropriate to limit their application to critical sections with multiple leak possibilities. It should be noted that steady-state methods, acoustic noise logging in particular, can also be used for continuous monitoring of the pipe system if the acoustic noise loggers are programmed to operate continuously. Since transient methods do not require the presence of an operator after the initial set-up (for example, for 'drive by' or manual data download), they are less labour intensive. Transient methods are generally more computationally expensive than steady-state methods due to complexity involved in processing and interpreting transient data.

It can be seen acoustic leak detection methods differ in terms of cost, ease of implementation and data analysis, suitability for leak detection tasks, and the level of expertise required to translate the inspection data into a more comprehensive format for interpretation. Each leak detection method can only be applied when certain conditions are satisfied. Apart from the active transient (matching) method which can be implemented using only one sensor, the other leak localisation methods in Table 8.1 require two sensors bracketing the suspected leak. Any method that employs reflectometry principles can only be employed when multiple known discontinuities are present not far (< 100 metres) from the sensor locations. Otherwise, the reliability of such methods reduces significantly. These conditions limit the application scenarios under which the acoustic methods can be applied. The reliability of any acoustic method depends on a number of factors, particularly, the pipe material and size, measurement environment, and mode of deployment. Acoustic methods are generally less reliable in non-metallic pipes and in large-diameter pipes (greater than 300 millimetres) due to high level of acoustic attenuation (Hunaidi, 2012). Due to signal attenuation, all acoustic methods can only

be used to detect and locate leaks not too far (< 100 metres for plastic pipes) from the sensor location. Their reliability is also reduced in very noisy environments, such as city centres.

An important conclusion from the comparison of the results in Table 8.1 is that both transient and steady-state methods can potentially play crucial roles in acoustic leak detection practice. Based on their advantages and shortcomings, each method is suitable for some situations but not others. A synergy of these two categories of methods is likely to improve reliability of acoustic leak detection, compared to the use of a single method. Such a possibility is explored in the next section.

8.2 Combined acoustic leak detection approach

This section concerns the development of an acoustic leak detection approach that combines different transient and steady-state leak detection methods. In addition to the requirements outlined in Section 1.5 in Chapter 1, such a combined approach must also satisfy the following:

- Capability for simultaneous acquisition and processing of acoustic transients and steady-state leak signals under a common (existing) measurement and data acquisition setup.
- Capability for fast and possibly real-time leak detection.
- Suitability for essential leak detection tasks, namely, leak awareness and leak localisation.
- Ability to provide and systematically combine independent estimates of the leak location.
- Ability to infer all required parameters from readily available data.

In developing such an approach, several important factors must be considered, including selection of leak detection methods, choice of data acquisition system and measurement setup, and techniques for combining results. The selection of acoustic leak detection methods and sensors is briefly discussed in the next subsection, while data fusion techniques are outlined in Section 8.2.2.

8.2.1 Selection of leak detection methods and sensors in the combined approach

Generally, selection of leak detection methods for a water pipe system ultimately depends upon the performance requirements specific to the pipe system and involves a trade-off between various criteria, such as cost, effectiveness, maintenance requirements, and computational complexity (ADEC, 1999). Effectiveness deals primarily with the performance related aspects of a leak detection method and is evaluated in terms of sensitivity, accuracy, reliability, and robustness. Focus on attaining ideal performance in one area usually results in some degradation of the other criteria. For example, a sensitive leak detection method is normally very reliable but will frequently generate alarms during normal pipeline operations.

Selection of appropriate methods for a pipe system can be achieved via multi-criteria decision analysis (MCDA), which is concerned with solving decision and planning problems involving

multiple conflicting criteria (Saaty, 1987). Each criterion is assigned a weight that denotes its relative importance in the decision making. Such weightings can vary depending on the application scenario being considered, for example, material, size, and criticality of the pipe. They can be derived either from multi-parameter studies or based on synthesis of past reported performances in field trials. Cost is typically the most important criterion considered when selecting methods for small-diameter pipes with diameter less than 300 mm (Yazdekhasti et al., 2018). Reliability and robustness are crucial in the case of critical large-diameter pipes used in transmission applications. It is challenging to derive set of representative weightings when there is a wide range of application scenarios and criteria. Therefore, instead of employing the MCDA approach to select specific methods for each possible application scenario, all the steady-state and transient methods listed in Table 8.1 (except use of listening devices) are considered for inclusion in the combined approach. The use of listening devices is excluded because it does not have capability for data storage and advanced signal processing. Another reason for considering all available methods in the combined approach is that all acoustic methods considered in this thesis can be realised using existing measurement setup and sensors. The methods can be implemented using simple algorithms on a personal computer and do not require high technical expertise for interpretation of results. Hence, there is no substantial difference in cost (hardware, software, labour, and data analysis) between the methods. The only criteria that may vary vastly between the methods are suitability for a given pipe system and leak detection task.

In the combined approach, one algorithm involving the available methods is developed, and then all methods applicable to the pipe system under consideration are '*activated'* during leak detection. The term 'activated' is used to indicate that the measured data can be analysed using the given method. For example, cross-correlation can only be employed when there are two sensors on either side of the suspected leak. On the other hand, multipath identification methods require knowledge of locations of discontinuities in the pipe system. Including all available methods and then 'activating' the applicable ones maximises the scope of the combined approach and ensures that essential leak detection tasks can be performed in a lot of application scenarios. It should be noted that due to the inherent inability of acoustic methods to directly estimate leak intensity, leak size estimation is not considered in the combined approach. It is, however, possible to incorporate additional signal processing techniques in order to estimate leak size from acoustic/vibration data, for example, using machine learning tools (see Butterfield (2018)). This is outside the scope of this research.

As stated in previous chapters, any acoustic pressure or vibration sensor can be employed for acoustic leak detection (Gao et al., 2005; Almeida, 2013). In addition to cost, the important factors that must be considered when choosing a sensor system are pipeline access requirements, mode of deployment, communication protocols, and maintenance requirements. Hydrophones must be inserted into the water via openings on fire hydrants or other outlets along the pipeline. In contrast, accelerometers are mounted directly on the surface of the pipe or on any fixture in contact with it. Use of hydrophones is therefore more restrictive compared to accelerometers. More importantly, it should

be noted that in most acoustic methods, the type of sensor used does not make a substantial difference (as shown by the similarity of results obtained for hydrophone and accelerometer signals by Almeida (2013)). It is more important to ensure that any sensors employed have good metrological characteristics, including high accuracy, consistency, validity, uniqueness, and data completeness (Romano, 2012). Also, the sensor system must be capable of operating in the mode required by the included leak detection methods. Transient methods can only be deployed with a sensor system capable of operating and transmitting data in real time. On the other hand, intermittent operation and manual data collection may be employed for steady-state methods without impacting reliability.

8.2.2 Description of combined leak detection approach

A combined approach that fulfils the requirements outlined above is depicted by the algorithm shown in Figure 8.1. The algorithm consists of major steps geared towards specific signal processing or leak detection tasks, most of which can be accomplished using multiple approaches: data acquisition, transient detection, transient extraction, leak awareness, leak localisation, and data fusion. Apart from the measured signals, the input data may also include metadata about the pipe system layout, pipe materials, mode of sensor operation, and sensor locations. The additional input information is required to determine what methods are applicable. Each step of the algorithm is briefly described.

The data acquisition step is responsible for the acquisition of transient and steady-state data. This is accomplished using a sensor system consisting of one or multiple acoustic/vibration sensors installed at strategic locations in the pipe system. The next task after data acquisition is transient detection, the aim of which is to detect and locate acoustic transients in the measured signals. This can be achieved using the NSM transient detector proposed in Chapter 3. Further analysis with transient methods is only possible in case of positive transient detection inference.

The leak awareness step can be accomplished using four independent methods: passive transient method (Chapter 3), passive steady-state method (Chapter 3), active transient (matching) method (Chapter 4), and acoustic noise logging. In contrast with the other methods, passive transient method requires continuous sensor operation in order to detect new leaks. The applicability of the matching method is dependent on the presence of known discontinuities in the pipe, as discussed in Chapter 4. To improve robustness of leak detection, a majority rule may be employed to reduce the chances of a false positive: a leak alert is only given if at least two of the ‘activated’ leak awareness methods give positive inferences about the presence of leaks in the pipe. Otherwise, it is classified as a false alarm.

If the presence of a leak is confirmed, the signals are further analysed to locate the leak. Four methods are available for leak localisation: matching method (Chapter 4), steady-state multipath identification (Chapter 4), and steady-state blind channel identification (Chapter 5), and conventional cross-correlation. In contrast with the conventional cross-correlation, the other three methods calculate the leak location exclusively from the measured signals without a priori knowledge of the wave speed.

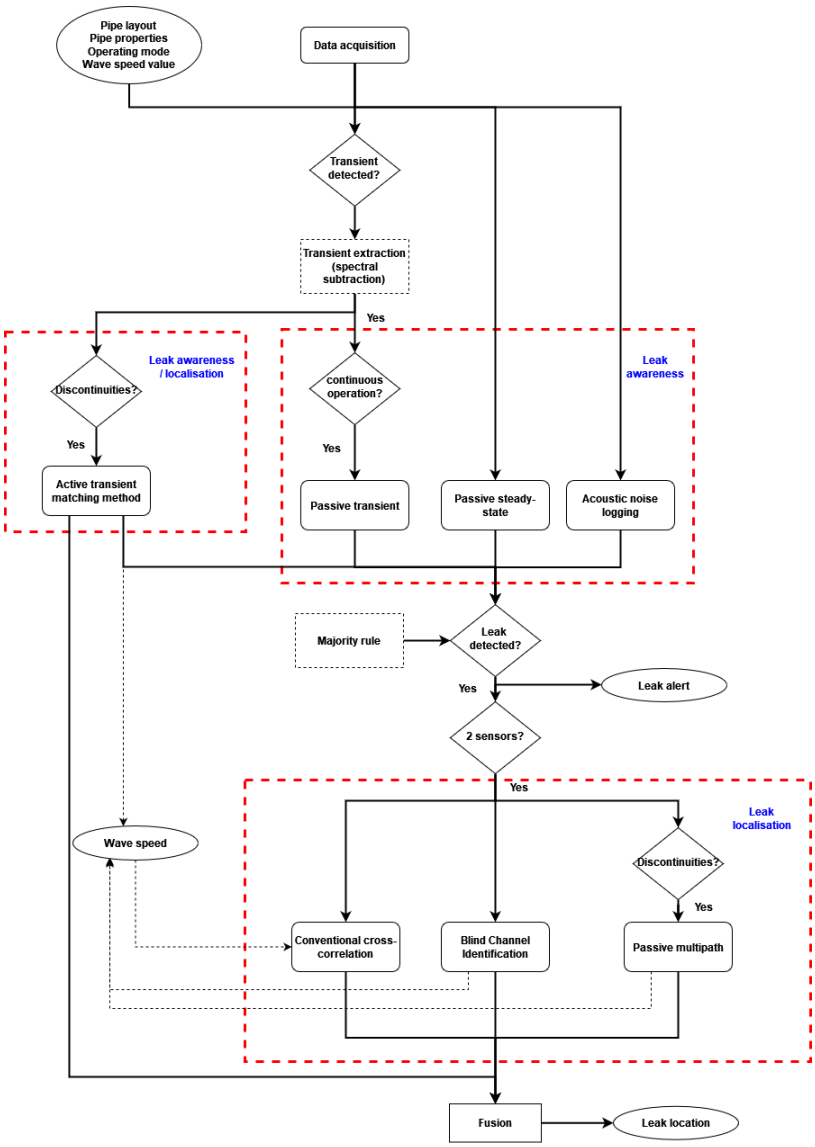

Figure 8.1: Combined acoustic leak detection approach.

They also provide estimates of the wave speed, which can be used to obtain additional leak location estimates via the cross-correlation technique. In case none of the alternative methods is activated, the leak can only be located with the cross-correlation method using the calculated wave speed value. Like the matching method, the condition required to 'activate' the steady-state multipath identification method is knowledge of discontinuities in the pipe. While the matching method is feasible with only one sensor, the other leak localisation methods require two sensors bracketing the detected leak.

In the last step of the algorithm, the leak location estimates from the 'activated' leak localisation methods are systematically combined to produce the final leak location value. Two ways to achieve this are simple averaging and inverse-variance weighting (Hartung et al., 2008). In the former, the final value is simply the average of the leak location estimates, while in the latter, it is their weighted average using the inverse variance of the 'activated' methods as weights. Inverse-variance weighting is preferable if the variances of historical estimates obtained on the same pipe or similar measurement

environments are available. A majority rule can be employed such that the final leak location estimate is taken as the (weighted) average of the two most *consistent* estimates.

In order to improve performance when transient and steady-state methods are 'activated' simultaneously, an optional step of transient extraction using spectral subtraction (Vaseghi, 1996) can be carried out after an acoustic transient has been detected. This step separates transient and steady-state components of the measured signal. In the spectral subtraction method, the time-averaged spectrum of the steady-state component (assumed to be stationary during the measurement period) is subtracted from the spectrum of the composite signal ('total' spectrum) in order to obtain the 'residual spectrum', which is considered the spectrum of the transient component. The time-averaged spectrum of the steady-state component is estimated from the portion of the measurement preceding the transient onset. To restore the transient component, the 'residual spectrum' is combined with the phase of the whole signal and then transformed via IFT to the time domain. The extracted transient and steady-state components are then analysed further using appropriate transient and steady-state methods, respectively.

The practical advantages of the combined approach as well as its limitations will be discussed at the end of this chapter. In the next section, its effectiveness is investigated using experimental data.

8.3 Experimental results

The combined approach described in the preceding section was applied to three categories of datasets acquired on the leakage test rig. These datasets have been previously described in Section 3.4. The first dataset category contains leak transients generated when a leak was simulated by opening the valve at L1, while the second category contains transients generated by pipe impacts in the presence of an ongoing leak at L1. The third category comprises steady-state leak signals. The reason for selecting three different datasets is to illustrate the ability of the combined approach to detect and locate leaks in a 'self-contained' manner by automatically 'activating' applicable transient and steady-state methods depending on the signals and the input information. Note that the results presented in this section is somewhat a concatenation of previous results, so for brevity, only the results for signals measured with a leak at L1 are presented. The only input information available to the proposed algorithm are the measured signals, inter-sensor distance d = 5.5 metres, and locations of the known discontinuities (endcaps, elbow, inlet valve, inlet tee connection).

To assess the effectiveness of the combined approach, the cross-validation technique usually used in machine learning applications was employed. The available datasets described in Section 3.4 were considered the training subset, while new datasets not previously analysed, one from each category, was considered the validation subset. Table 8.2 shows the summary of the results obtained for the training datasets in Chapters 3-5, including the success rate of the leak awareness methods, and

the average value and standard error (standard deviation) of the leak location estimate for the leak localisation methods.

Table 8.2: Leak location estimates using the combined approach.

Input to algorithm:	• X1 and X2 signals • Continuous sensor operation • Inter-sensor distance d = 5.5 metres • Location of known discontinuities				
Dataset			**Leak transients**	**Active transients**	**Steady-state signals**
Method					
		Proportion of correct inferences			
Passive transient		0.89	✓	✓	×
Passive steady-state		1.00	✓	✓	✓
Acoustic noise logging		-	-	-	-
		Leak location estimate $\hat{d}_1$ (m)			
		Mean ± standard error (m)	**(Wave speed estimate $\hat{c}$ (m/s))**		
Active transient (matching method)		1.65±0.41	-	1.29 (371.5)	-
Passive multipath identification		1.16 ±0.06	1.05 (349)	1.12 (349)	1.18 (349)
Blind channel identification		1.21 ±0.08	1.10 (367)	1.04 (367)	1.10 (367)
Conventional cross-correlation	calculated wave speed	1.69 ±0.04	1.45 (279)		
	matching method wave speed		-	1.01	-
	passive multipath identification wave speed		1.05	1.12	1.18
	BCI wave speed		1.10	1.04	1.10
Final estimate $\hat{d}_1$ (m)	**Simple averaging**		1.08	1.10	1.14
	Inverse-variance weighting		1.07	1.06	1.14

The passive transient and steady-state leak detection methods exhibit good performance with a success rate of 89% and 100%, respectively. While the conventional cross-correlation method achieves a lower standard error than the alternative leak localisation methods proposed in this thesis (namely, the matching, passive multipath identification, and BCI methods), it can be observed that it has a higher bias in the leak location estimate due to the systematic error in the calculated wave speed. Note that the time delay estimate in the cross-correlation method was accurately obtained using the WTCC proposed in Chapter 7, which explains the low standard error of the estimates. In practical situations where there certainly exists some error in the wave speed (due to uncertainties in pipe material

properties and environmental conditions), the alternative methods are likely to provide a more accurate leak location value closer to the actual leak location in the pipe. Among these methods, the passive multipath identification approach appears to be the most accurate for the leakage test rig, as it exhibits the lowest variance in the leak location estimates. This is perhaps not surprising, since the reflections from the endcap close to X1 are very easily detectable in the X1 signals given its proximity to the X1 access point. The matching method exhibits the largest standard error because of the very small sample size used to calculate the error. As can be seen in Section 4.6.1, only 4 successful cases were available.

The results obtained for the X1 and X2 signals from the validation subset are reported in Table 8.2. This validation set contains signals measured with a leak simulated at L1 and an active transient introduced by hitting the endcap close to X3. If a given method is 'activated' for a dataset, the results are indicated with orange cells, while inapplicable methods are indicated with blue cells. Where necessary, the wave speed estimate is also presented. A checkmark ✓ is used to indicate a positive leak detection result, while the symbol ✗ indicates a negative result. It can be observed that the matching method was only successfully 'activated' for the signals with active transients. On the other hand, all the leak localisation methods were 'activated' for the three datasets. In all three cases, the conventional cross-correlation using calculated wave speed value was not 'activated' as the 'activated' multipath identification and BCI methods provide the required wave speed information. The results obtained for different methods exhibit varying level of accuracy in spite of being calculating from the same input signals. This is related to the reliability of the extra information available to each method and the precision of the adopted signal processing methods. For example, error in the location of the known discontinuities or TDOAs of reflections reduces the accuracy of the estimates in the multipath identification methods. The BCI method exhibits the highest leak localisation error of 0.13 metres compared to 0.12 metres for the matching and passive multipath identification methods. It can be noted that the cross-correlation leak location estimates are identical to the estimates of the method supplying the wave speed value (except the matching method). This is because the passive multipath identification and BCI methods are formulated based on the cross-correlation equation. Only the leak location estimate obtained using the wave speed estimated by the matching method is independent. Simple averaging gives more accurate final leak location estimates than inverse-variance weighting in this case. As already stated, this is because of the large variance attributed to the matching method. Nonetheless, the largest error in final estimates obtained via inverse-variance weighting is less than the largest leak localisation error for the individual methods. The maximum absolute error in the leak location estimates are 0.09 metres for simple averaging and 0.11 metres for inverse-variance weighting. Both are less than the maximum error observed for the single methods (0.13 metres for the BCI method and 0.12 metres for the matching and passive multipath identification methods). Despite the varying accuracy of results from individual methods, the final estimates obtained via simple averaging and inverse-variance weighting are fairly accurate, thus demonstrating the effectiveness of

these fusion approaches. This shows that the ability to combine independent estimates from multiple methods indeed improves the robustness and reliability of acoustic leak detection.

This experimental example demonstrates the potential viability of detecting and locating leaks in a practically convenient 'self-contained' manner directly from the measured signals using the proposed combined approach. The benefits and limitations of the approach are discussed in the next section.

8.4 Benefits and limitations of the combined leak detection approach

A couple of advantages can be highlighted for the combined approach. One big advantage is that acoustic leak detection is carried out using only readily available data. The 'self-contained' nature of the approach ensures that all parameters required by one method can be inferred from another method even when pipe properties are unknown. For instance, the matching method can estimate the wave speed, which can then be used in the cross-correlation method, thereby eliminating the need to rely on 'third-party' wave speed value. Conversely, results from steady-state methods can be used to 'calibrate' or adjust settings in the transient methods. By including most of the available acoustic methods, the combined approach presents a holistic approach that ensures that essential leak detection tasks, namely, leak awareness and leak localisation, can be accomplished in a lot of application scenarios. Applicable leak detection methods for each task are automatically selected based on the available input information, making the approach more universal and practically convenient than use of a single method. Independent estimates from applicable methods can also be combined to provide more accurate results. This redundancy makes the combined approach more robust. As stated previously, all methods considered in the combined approach operate on the same input acoustic/vibrations signals, thus eliminating the need for multiple data acquisition systems, measurement setup, or sensor types. Another benefit offered by the combined approach is the reduced time required for leak detection and localisation. Instead of relying on acoustic logging that may take days to detect the presence of leaks in the pipe systems, the integration of transient methods allows for near real-time leak detection. Furthermore, transient methods can help in highlighting possible leak locations in the network, thereby reducing the search area to pinpoint leaks using steady-state methods.

There are certain issues that may affect the practical application of the combined approach. Firstly, the combined method is not immune to the physical limitations of the component acoustic methods, especially as regards pipe attenuation. Severe signal attenuation results in inaccurate leak location estimates no matter how computationally sound the applied signal processing tools are. The range at which leaks can be effectively detected is still limited by the maximum range of the component methods. To cover a large extent of the pipe system, it is necessary to install many sensors at strategic locations, which may increase the cost of the leak detection system. Secondly, the

assumption about independence of estimates from different methods is *not* strictly true since all included methods analyse the same data. Hence, any error in the measured signals is likely to affect all estimates, thereby skewing the final result. Also, error can potentially propagate from one method to the other due to use of wave speed estimate from one method in the other. Since the final leak location estimate is a (weighted) average of the obtained estimates, a large error in one estimate may skew the final result. Thirdly, the computational complexity of the combined approach is higher compared to use of a single method since it involves very different signal processing methodologies. As a result, the implementation of the approach in hardware is likely to be practically challenging. Apart from computational considerations, other practical issues which may also limit hardware implementation are suitability for real-time operation, space requirements, frequency of operation, etc. Lastly, like most acoustic methods, the combined approach in the current form is incapable of estimating leak size. As noted above, it is possible to incorporate this functionality by employing a machine learning technique. It could be worthwhile to investigate this possibility in future studies.

It is necessary to tackle the identified issues to improve the practical applicability of the combined approach. Further validation in a variety of practical application scenarios is also required. Nonetheless, despite the highlighted limitations, the results obtained in this chapter have demonstrated that a combined approach that involves simultaneous application of multiple leak detection methodologies is an attractive and potentially viable way to improve acoustic leak detection process in the water industry.

8.5 Summary and conclusion

In order to overcome the limitations of individual acoustic methods, an approach that combines transient and steady-state leak detection methodologies has been presented in this chapter. The combined approach included most of the existing acoustic methods and the alternative methods proposed in this thesis, allowing leaks to be detected and located in a variety of practical scenarios. Based on the available input data, all applicable leak detection methods are automatically selected, and the independent leak detection results are then combined in a systematic way. The advantages of the combined approach were discussed, including suitability for real-time operation, ability to detect and locate leaks in a 'self-contained' manner directly from the measured signals, and improved robustness compared to use of a single method. Its limitations were also identified, in particular, effect of systematic data errors, high computational burden, and limited range due to pipe attenuation. This method was experimentally validated using data from the leakage test rig, with the results showing the proposed method presents a potentially viable approach to achieve more robust and effective acoustic leak detection in water pipes.

CHAPTER 9
CONCLUSIONS AND RECOMMENDATIONS FOR FUTURE WORK

In this chapter, the main conclusions of this thesis are summarised together with suggestions for future work.

9.1 Conclusions

In this thesis, possible strategies for tackling some issues limiting the effectiveness of detecting and locating leaks in water pipes (especially in plastic pipes) using acoustic methods have been investigated. These strategies were developed by considering acoustic leak detection through a number of alternative perspectives: as a transient/signal detection, as a multipath identification, and as a system identification problem. The main conclusions of the work in this thesis can be summarised as follows:

1. Leak occurrence is accompanied by acoustic transients that can be detected using acoustic/vibration sensors installed in the fluid or on the pipe. In contrast with acoustic transients induced by normal pipeline operations, acoustic transients generated by leak occurrence introduce sustained changes in the temporal and spectral properties of the signals resulting in a new steady state. The presence of a new leak can thus be inferred by detecting acoustic transients and identifying the type of change they introduce in the measured signals as outlined in Chapter 3.
2. It has been found that signal properties that characterise the shape and variation of signal spectrum are sensitive to the presence of a leak, with their values differing vastly for background noise and leak signals. Hence, leaks can be discovered by defining a leak detection metric (LDM) that quantifies spectral shape and spectral variation in acoustic/vibration signals. This approach is able to detect leaks that do not generate strong transients or cause substantial changes in the time-domain properties of the measured signals.
3. Acoustic transients can be detected by quantifying the local non-stationarity of the signal with respect to a statistical parameter as described in Chapter 3. It was found that such a transient detector is more general than those based on a generalised likelihood ratio test (GRLT) since it makes no assumption about the distribution of the background noise and the transient. Also, it has a high detection power and can precisely locate the onset and end of acoustic transients in signals.

4. The phenomenon of acoustic wave reflection at discontinuities provides a viable means for detecting and locating leaks as demonstrated in the transient and steady-state methods developed in Chapter 4. In the transient method, the wave speed and location of leaks in a pipe is estimated by minimising a cost function that matches the times difference of arrival (TDOAs) of reflections of acoustic transients in acoustic/vibration signals with the location of known discontinuities in the pipe. It was also shown that the wave speed and leak location can be obtained from steady-state leak signals in a variety of practical scenarios by solving a system of two equations formulated from the TDOAs of leak noise reflections.

5. The TDOA of a reflected wave with reference to a direct-path wave in an acoustic/vibration signal can be estimated from the autocorrelation function (ACF) and cepstrum of the signal, as was shown in Chapter 4. It was found that the effectiveness of detecting and estimating the TDOA is lower in pipes with high attenuation and in the presence of high background noise level. Numerical and experimental results showed that the cepstral method is vastly superior to the autocorrelation method. Unlike the autocorrelation method, the cepstral method can detect reflections even in the presence of tonal components or resonances in the signals.

6. The impulse response functions (IRFs) of the pipe that relate the signals generated at the leak location and the signals acquired at the measurement points can be estimated from the measured signals exclusively using a blind channel identification (BCI) technique as demonstrated in Chapter 5. By introducing spectral constraints on the estimated pipe IRFs, the propagation times of the leak noise in the physical channels can be estimated. Using this information, the leak location can be determined without knowledge of the wave speed or pipe material properties.

7. A quantitative analysis of the cross-correlation equation in Chapter 6 showed that even a small error in the time delay estimate can result in a large leak localisation error, especially if both the wave speed and time delay are simultaneously over-estimated. The quality of the time delay estimate in correlation-based time delay estimation (TDE) methods can be inferred from the statistical properties of the cross-correlation function (CCF), including probability distribution, processing gain (PG), and deviations of time delay estimates from their statistical mode. It was found that quality assessment metrics based on these properties can also be used to evaluate the effectiveness of possible choices of filters and weighting functions for TDE.

8. Two alternative methods, one based on wavelet transform (WT) and data-adaptive decompositions, and the other based on cepstral analysis, were developed in Chapter 7 for TDE in acoustic leak detection. It was found that the accuracy of the time delay estimate is determined primarily by the decomposition level of the WT or data-adaptive decomposition, and the choice of wavelet function or type of data-adaptive decomposition scheme is less crucial. Selection of best decomposition level is facilitated using simple criterion like the

relative wavelet energy (RWE), relative IMF energy (RIE), or the quality metrics proposed in Chapter 6. An advantage of these methods is that they are capable of estimating time delays without need to first filter the signals unlike the conventional generalised cross-correlation (GCC) methods.

9. Improved acoustic leak detection can be achieved by combining different leak detection methods as demonstrated in Chapter 8. It was found that such a combined approach presents an effective way to carry out acoustic leak detection in a 'self-contained' and 'automated' manner directly from the measured signals. Based on the input data, appropriate methods applicable for a given leak detection task, for example, leak awareness and leak localisation, can be automatically selected, and parameters (for example wave speed) required by one method can be provided by another. The independent leak detection results from the different component methods can then combined in a systematic way.

The methods proposed in this thesis were validated using experimental data acquired on an in-vacuo laboratory pipe leakage test rig, which is described in Chapter 2. Overall, test results generally agreed with numerical simulation results. They demonstrated the effectiveness of the leak detection methods based on transient/signal detection, multipath identification, and system identification principles as well as the combined approach. The experimental results indicate that the alternative TDE methods and the metrics proposed for assessing the quality of the time delay estimate are generally robust and achieve good performance for leak signals.

9.2 Recommendations for future work

One major limitation of this work is that the proposed alternative leak detection and signal processing methods have only been validated using data from a limited leakage test rig that differs from real water distribution systems in a lot of ways. The reported results can only be generalised after a thorough investigation in real pipe systems. A more representative database of signals can be collected from different pipe systems to compare with the results reported in this thesis. This would allow for the possibility of investigating important factors that may have negligible effects on signals from the test rig but substantial effects on signals from real systems, for example, surrounding medium and high number of discontinuities. In addition, this could be useful for validating some observations made in this thesis but from which no definite conclusions could be drawn. An important example is the effects of the type of sensor on the multipath identification leak detection methods. This could be investigated further with the availability of signals acquired using different sensors in real pipe systems.

As indicated throughout the thesis, some of the studies have been limited mostly due to constraints associated with unavailability of suitable data and hardware. One particularly relevant

research direction that has been hindered by this constraint is investigating the possibility of extracting acoustic signals from data acquired by transient loggers. This can be considered with availability of suitable data, as it may be a viable means of improving acoustic leak detection. Another recommended research direction is investigating the possibility of incorporating acoustic/vibration sensors in transient loggers to allow for the continuous sensor operation required in the acoustic transient methods. These two directions were mentioned as possible measures for tackling the challenge associated with real-time applicability of the active acoustic transient leak detection method.

In some of the methods investigated, it has been indicated that performance may be highly dependent on the selected parameters. While the current implementation of the methods is considered adequate for analysing the data acquired on the leakage test rig, a more general and robust methodology is required to select the necessary parameters in the methods. Two particularly important examples are the selection of statistical features and inference thresholds for the non-stationarity measure (NSM) transient detector and the leak detection metric (LDM). More general and robust alternatives for defining the LDM and setting the parameters could be explored. The possibility of employing the LDM for leak detection without need for noise-free template can also be investigated.

The results obtained during the investigation of the passive acoustic transient leak detection method seem to suggest that the strength of leak transients does not necessarily correlate with the amount of change introduced by the leak in the subsequent steady-state signals. The relationship between leak transients and the amount of change introduced by the subsequent steady-state signals generated by the leak can be studied. An interesting and potentially useful direction is investigating the possibility of inferring more information about a leak, for example, its size, from the detected acoustic transients.

The alternative methods presented in this thesis could be implemented in practical acoustic leak detection systems. However, to achieve this, the various issues highlighted for the methods have to be addressed, particularly those related to computational complexity and robustness issues. Possible measures for refining the proposed methods and dealing with the identified issues could be investigated, for example, optimised pre-processing and denoising. The quality metrics are only valid for assessing the accuracy of time delay estimates obtained using a correlation-based method. More universal metrics capable of assessing the quality of estimates obtained using other time delay estimators could be developed.

Apart from the brief comparison between transient and steady-state methods, the methods proposed in this work have all been studied mostly in isolation. This represents another limitation of the research project. A more comprehensive comparative study of the methods is recommended, as it may provide more insights into their applicability for practical leak detection. The possibility of employing more complex data fusion techniques in obtaining the final leak location estimate in the combined approach could be explored instead of simple averaging and inverse-variance weighting.

Also, more functionalities, leak size estimation in particular, could be included in the combined approach.

The current research has focused on detecting only one leak in the pipe. Research into the applicability of the proposed methods (especially the reflection-based methods) in multi-leak situations could be conducted in future studies.

APPENDICES

Appendix A. Formulae for time-domain and spectral features

In Table A.1, $\bar{x}$ is the mean of x, σ_x^2 is the variance of x, N is the signal length, f_k and s_k are the frequency and spectral value (magnitude or power spectrum) at frequency bin k, respectively; K_1 and K_2 are the band edges, in bins, over which to calculate the spectral descriptor; $\Delta K = K_2 - K_1$; μ_f is the mean frequency, μ_s is the mean spectral value, p is the norm order, υ is the specified energy threshold (usually 0.95 or 0.85).

Table A.1: Formulae for time-domain and frequency-domain features.

Feature	Equation	Feature	Equation
Time-domain features			
RMS	$x_{\text{rms}} = \sqrt{\frac{1}{N}\sum_{n=1}^{N} x^2(n)}$	Skewness	$\frac{\sum_{n=1}^{N}\left(x(n)-\bar{x}\right)^3}{(N-1)\cdot\sigma_x^3}$
Standard deviation	$\sigma_x = \sqrt{\frac{1}{N-1}\sum_{n=1}^{N}\left(x(n)-\bar{x}\right)^2}$	Kurtosis	$\frac{\sum_{n=1}^{N}\left(x(n)-\bar{x}\right)^4}{(N-1)\sigma_x^4}$
Signal power	$\frac{1}{N}\sum_{n=1}^{N} x^2(n)$	Crest factor	$\frac{\max\{\lvert x\rvert\}}{x_{\text{rms}}}$
Shape factor	$\frac{x_{\text{rms}}}{\frac{1}{N}\sum_{n=1}^{N}\lvert x(n)\rvert}$	Clearance factor	$\frac{\max\{x\}}{\left(\frac{1}{N}\sum_{n=1}^{N}\lvert x(n)\rvert\right)^2}$
Entropy	$\sum_{n=1}^{N} x^2(n)\log\{x^2(n)\}$	Impulse factor	$\frac{\max\{x\}}{\frac{1}{N}\sum_{n=1}^{N}\lvert x(n)\rvert}$
Spectral descriptors			
Spectral centroid	$\varpi_{\text{centroid}} = \frac{\sum_{k=K_1}^{K_2} f_k s_k}{\sum_{k=K_1}^{K_2} s_k}$	Spectral skewness	$\frac{\sum_{k=K_1}^{K_2}\left(f_k-\varpi_{\text{centroid}}\right)^3 s_k}{\left(\varpi_{\text{spread}}\right)^3\sum_{k=K_1}^{K_2} s_k}$
Spectral spread	$\varpi_{\text{spread}} = \sqrt{\frac{\sum_{k=K_1}^{K_2}\left(f_k-\varpi_{\text{centroid}}\right)^2 s_k}{\sum_{k=K_1}^{K_2} s_k}}$	Spectral kurtosis	$\frac{\sum_{k=K_1}^{K_2}\left(f_k-\varpi_{\text{centroid}}\right)^4 s_k}{\left(\varpi_{\text{spread}}\right)^4\sum_{k=K_1}^{K_2} s_k}$
Spectral flatness	$\frac{1}{\frac{1}{\Delta K}\sum_{k=K_1}^{K_2} s_k}\cdot\left(\prod_{k=K_1}^{K_2} s_k\right)^{\frac{1}{\Delta K}}$	Spectral crest	$\frac{\max\{s_k\}}{\frac{1}{\Delta K}\sum_{k=K_1}^{K_2} s_k}$

Feature	Equation	Feature	Equation
Spectral flux	$\varpi_{\text{flux}} = \mathrm{E}\{\text{flux}(t)\}$ where $\text{flux}(t) = \left(\sum_{k=K_1}^{K_2} \left\| s_k(t) - s_k(t-1) \right\|^p \right)^{1/p}$	Spectral rolloff point	f_m such that $\sum_{k=K_1}^{m} \left\| s_k \right\| = \upsilon \cdot \sum_{k=K_1}^{K_2} s_k$
Spectral slope	$\frac{\sum_{k=K_1}^{K_2} (f_k - \mu_f)(s_k - \mu_s)}{\sum_{k=K_1}^{K_2} (f_k - \mu_f)^2}$	Spectral entropy	$\frac{-\sum_{k=K_1}^{K_2} s_k \log\{s_k\}}{\log\{\Delta K - 1\}}$
Spectral decrease	$\frac{\sum_{k=K_1+1}^{K_2} \frac{s_k - s_{K_1}}{k-1}}{\sum_{k=K_1+1}^{K_2} s_k}$		

Appendix B. Deriving the distribution of the non-stationarity measure

The probability distribution of the second-order NSM $\hat{y}_r$ given in Equation (3.3) is derived as follows. For a large window length L_g, the r th moment m_r of signal x approximately follows the Gaussian distribution according to the Central Limit Theorem. This is denoted as $m_r \sim \mathcal{N}\left(\bar{m}_r, \sigma^2_{m_r}\right)$, where $\bar{m}_r$ and $\sigma^2_{m_r}$ are the expectation and variance of m_r, respectively. Specifically for the second moment, $\bar{m}_2 \approx \frac{\sigma_x^2}{L_g}\left\{L_g + \frac{\bar{x}^2 \cdot L_g}{\sigma_x^2}\right\} = \sigma_x^2 + \bar{x}^2$ and $\sigma^2_{m_2} \approx 2\frac{\sigma_x^4}{L_g^2}\left\{L_g + 2\frac{\bar{x}^2}{\sigma_x^2} \cdot L_g\right\} = \frac{2\sigma_x^2}{L_g}\left\{\sigma_x^2 + 2\bar{x}^2\right\}$, where $\bar{x}$ and σ_x^2 are the mean and the variance of x, respectively. This follows from the normal approximation to a scaled chi-squared distribution with $L_g - 1$ degrees of freedom (Douillet, 2009; Lee, 2009).

Denoting $\theta_i = m_r(i)$, it can be observed that $\hat{y}_r$ calculated in Equation (3.3) with a rectangular window is the biased sample variance of the multivariate normal variable $\boldsymbol{\theta} = \left(\theta_1, \theta_2, \cdots, \theta_{L_g}\right)^T \sim \mathcal{N}\left(\bar{\mathbf{m}}_r, \boldsymbol{\Sigma}_r\right)$, where the expectation vector $\bar{\mathbf{m}}_r$ is the $L_g \times 1$ vector with elements all equal to $\bar{m}_r$, and the covariance matrix $\boldsymbol{\Sigma}_r$ is given by the symmetric Toeplitz matrix

$$\boldsymbol{\Sigma}_r = \frac{\sigma^2_{m_r}}{L_g^2}\begin{bmatrix} 1 & \frac{L_g-1}{L_g} & \cdots & \frac{1}{L_g} \\ \frac{L_g-1}{L_g} & 1 & \cdots & \frac{2}{L_g} \\ \vdots & \vdots & \ddots & \vdots \\ \frac{1}{L_g} & \frac{2}{L_g} & \cdots & 1 \end{bmatrix}. \tag{B.1}$$

This matrix is derived by observing that the covariance $\operatorname{cov}\left\{\theta_n, \theta_{n+k}\right\}$ between the n th component θ_n and the $(n+k)$th component θ_{n+k} of $\boldsymbol{\theta}$ is given by

$$\operatorname{cov}\left\{\theta_n, \theta_{n+k}\right\} = \operatorname{cov}\left\{\frac{1}{L_g}\sum_{i=n-L_g}^{n+L_g} x^r(i), \frac{1}{L_g}\sum_{i=n+k-L_g}^{n+k+L_g} x^r(i)\right\} = \frac{\left(L_g - k\right)\sigma^2_{m_r}}{L_g^2}. \tag{B.2}$$

Let $\mathbf{M}$ be a matrix such that $\mathbf{M}\boldsymbol{\theta} = \boldsymbol{\theta} - \bar{\theta}$, where $\bar{\theta}$ is the mean of the vector $\boldsymbol{\theta}$. This matrix is given by $\mathbf{M} = \mathbf{I}_{L_g} - \mathbf{1}\left(\mathbf{1}^T\mathbf{1}\right)^{-1}\mathbf{1}^T = \mathbf{I}_{L_g} - \frac{1}{L_g}\mathbf{J}_{L_g}$, where $\mathbf{I}_{L_g}$ denotes an $L_g \times L_g$ identity matrix, $\mathbf{1}$ is the L_g -length column vector of ones, and $\mathbf{J}_{L_g}$ denotes an $L_g \times L_g$ matrix of ones. Since $\mathbf{M}^T = \mathbf{M}$ and $\mathbf{MM} = \mathbf{M}$, the sum of squares $Y_r = \sum_{i=1}^{L_g}\left(\theta_i - \bar{\theta}\right)^2$ is given by the quadratic form of $\boldsymbol{\theta}$:

$$Y_r = \sum_{i=1}^{L_g} \left(\theta_i - \bar{\theta}\right)^2 = \left(\mathbf{M\theta}\right)^T \left(\mathbf{M\theta}\right) = \boldsymbol{\theta}^T \mathbf{M}^T \mathbf{M\theta} = \boldsymbol{\theta}^T \mathbf{M\theta} \ . \tag{B.3}$$

The distribution of the quadratic form of a normally distributed multivariate variable is given by the weighted sum of independent, potentially non-central, chi-squared random variables (Mathai and Provost, 1992). Specifically,

$$Y_r = \boldsymbol{\theta}^T \mathbf{M\theta} = \sum_{i=1}^{L_g} \lambda_i U_i^2 \tag{B.4}$$

where $\lambda_1, \ldots, \lambda_{L_g}$ are the eigenvalues $\boldsymbol{\Sigma}_r^{1/2} \mathbf{M} \boldsymbol{\Sigma}_r^{1/2} = \boldsymbol{\Sigma}_r \mathbf{M}$. It is easy to verify that $\mathbf{M}$ is of rank $L_g - 1$ with one eigenvalue equal to zero and $L_g - 1$ eigenvalues equal to one (see Paolella (2019)). Hence, $\boldsymbol{\Sigma}_r \mathbf{M}$ is positive definite with positive eigenvalues, and the PDF f_{Y_r} of Y_r can be calculated based on Equation (B.4). A simple scale transformation yields the PDF $f_{\hat{y}_r}$ of the NSM output $\hat{y}_r$ as $f_{\hat{y}_r}(u) = L_g \cdot f_{Y_r}\left(L_g u\right)$. Likewise, the SDF of $\hat{y}_r$ is obtained as $\Pr\left\{\hat{y}_r > u\right\} = 1 - \Pr\left\{Y_r \le L_g u\right\}$.

Appendix C. Power cepstrum of leak signals

The estimated auto-power spectrum $\hat{G}_{xx}(\omega)$ of the composite leak signal with a signal reflection given in Equation (4.8) can be expressed as the sum of the true auto-power spectrum $G_{xx}(\omega)$ given in Equation (4.10) and random fluctuations $\varepsilon(\omega)$ due to the finite signal length:

$$\begin{aligned}\hat{G}_{xx}(\omega) &= G_{xx}(\omega)+\varepsilon(\omega)\\ &= G_d(\omega)\left\{1+\Gamma^2 e^{-2|\omega|\beta\Delta d}\right\}+G_{nn}(\omega)+2\Gamma G_d(\omega)e^{-|\omega|\beta\Delta d}\cos(\omega\tau_{\mathrm{PR}})+\varepsilon(\omega)\end{aligned} \tag{C.1}$$

where $\Delta d = d_{\mathrm{PR}} - d_{\mathrm{PW}}$, $\tau_{\mathrm{PR}} = \Delta d/c$ is the time delay between the direct and reflected signals, and $G_d = G_{ll}(\omega)e^{-2\omega\beta d_{\mathrm{PW}}}$ is the auto-spectrum of the direct-path signal. Equation (C.1) can be rewritten as

$$\begin{aligned}\hat{G}_{xx}(\omega) &= G_I(\omega)\left\{1+\frac{2\Gamma\cdot e^{-|\omega|\beta\Delta d}\cos(\omega\tau_{\mathrm{PR}})}{1+\Gamma^2 e^{-2|\omega|\beta\Delta d}+G_{nn}(\omega)/G_d(\omega)}\right\}\left\{1+\frac{\varepsilon(\omega)}{G_{xx}(\omega)}\right\}\\ &= G_I(\omega)\left\{1+a(\omega)B(\omega)\cos(\omega\tau_{\mathrm{PR}})\right\}\left\{1+\nu(\omega)\right\}\end{aligned} \tag{C.2}$$

where $G_I(\omega) = G_d(\omega)\left\{1+\Gamma^2 e^{-2|\omega|\beta\Delta d}\right\}+G_{nn}(\omega)$, $\nu(\omega)=\dfrac{\varepsilon(\omega)}{G_{xx}(\omega)}$, $a(\omega)=\dfrac{2\Gamma\cdot e^{-|\omega|\beta\Delta d}}{1+\Gamma^2 e^{-2|\omega|\beta\Delta d}}$, $B(\omega)=\left(1+\dfrac{1}{\chi(\omega)}\right)^{-1}$, and $\chi(\omega)=\dfrac{G_{nn}(\omega)/G_d(\omega)}{1+\Gamma^2 e^{-2|\omega|\beta\Delta d}}$. The logarithm of $\hat{G}_{xx}(\omega)$ is then given by

$$\log\left\{\hat{G}_{xx}(\omega)\right\} = \log\left\{G_I(\omega)\right\}+\log\left\{1+a(\omega)B(\omega)\cos(\omega\tau_{\mathrm{PR}})\right\}+\log\left\{1+\nu(\omega)\right\}\ . \tag{C.3}$$

The last two terms in Equation (C.3) can be expanded using the logarithmic expansion $\log(1+u)=\sum_{k=1}^{\infty}(-1)^{k+1}\dfrac{u^k}{k}$ for $|u|\le 1$. Since $|B(\omega)|\le 1$ and by the AM-GM inequality, $|a(\omega)|\le 1$, the second term can be expanded as

$$\log\left\{1+a(\omega)B(\omega)\right\} = \sum_{k=1}^{\infty}(-1)^{k+1}M_k(\omega)\cos(k\omega\tau_{\mathrm{PR}}) \tag{C.4}$$

where $M_k(\omega)$ is the coefficient of $\cos(k\omega\tau_{\mathrm{PR}})$ obtained by applying the trigonometric identity (Beyer, 1987)

$$\cos^k\theta = \begin{cases}\dfrac{1}{2^{k-1}}\displaystyle\sum_{n=0}^{k-1/2}\binom{k}{n}\cos\left((n-2k)\theta\right) & \text{for odd } k\\ \dfrac{1}{2^k}\binom{k}{k/2}+\dfrac{1}{2^{k-1}}\displaystyle\sum_{n=0}^{k/2-1}\binom{k}{n}\cos\left((n-2k)\theta\right) & \text{for even } k\end{cases}. \tag{C.5}$$

The values of the coefficients of $M_k(\omega)$ for the first few integers k are

$$M_0(\omega) = \frac{A^2(\omega)}{4} + \frac{3A^4(\omega)}{32} + \frac{5A^6(\omega)}{96} + \cdots$$

$$M_1(\omega) = A(\omega) + \frac{A^3(\omega)}{4} + \frac{A^5(\omega)}{8} + \cdots$$

$$M_2(\omega) = \frac{A^2(\omega)}{4} + \frac{A^4(\omega)}{8} + \frac{5A^6(\omega)}{64} + \cdots$$

…

where $A(\omega) = a(\omega)B(\omega)$. To expand the last expression in Equation (C.3), it will be assumed that the fluctuations in the spectral estimate are small such that $|\nu(\omega)| \le 1$. It then follows that

$$\log\{1+\nu(\omega)\} = \sum_{k=1}^{\infty}(-1)^{k+1}\frac{\nu^k(\omega)}{k} \quad . \tag{C.6}$$

Substituting Equations (C.4) and (C.6) into Equation (C.3) and taking the IFT of the resulting expression yields the power cepstrum as

$$\breve{x}(q) = R(q) + \sum_{m=1}^{\infty}\frac{(-1)^{m-1}}{m}g_m(q) + \frac{1}{2}\sum_{k=1}^{\infty}(-1)^{k+1}Q_k(q)\otimes\delta(q \pm k\tau_{\mathrm{PR}}) \tag{C.7}$$

where $R(q) = \mathrm{F}^{-1}\{\log\{G_I(\omega)\}\}$; $g_m(q) = \mathrm{F}^{-1}\{\nu^m(\omega)\} = \underbrace{g_1(q)\otimes\cdots\otimes g_1(q)}_{\text{m times}}$;

$Q_k(q) = \mathrm{F}^{-1}\{M_k(\omega)\}$; and $\delta(\bullet)$ denotes the Dirac delta function.

Appendix D. Deriving the performance metrics of the autocorrelation and cepstral multipath identification methods

Appendix D1. Time delay resolution

The time delay resolution is given by the width of the ACF or cepstral peak that corresponds to the time delay estimate. The time delay resolution $\tau_{\text{res,ACF}}$ of the ACF can thus be calculated as

$$\begin{aligned}\tau_{\text{res,ACF}} &= \frac{\int_{-\infty}^{\infty} R_d^2(\tau)\,d\tau}{R_d^2(\tau_{PR})} = \frac{\frac{1}{2\pi}\int_{-\infty}^{\infty}\left[\Gamma G_{ll}(\omega)e^{-|\omega|\beta d_\Sigma}\right]^2 d\omega}{\left[\frac{1}{2\pi}\int_{-\infty}^{\infty}\Gamma G_{ll}(\omega)e^{-|\omega|\beta d_\Sigma}d\omega\right]^2} \\ &= 2\pi\frac{2\int_0^{\infty}\left[e^{-|\omega|\beta d_\Sigma}\right]^2 d\omega}{\left[2\int_0^{\infty}e^{-|\omega|\beta d_\Sigma}d\omega\right]^2} = \frac{\pi\beta d_\Sigma}{2}\end{aligned} \tag{D.1}$$

where $R_d = \Gamma\cdot R_{ll}(\tau-\tau_{PR})\otimes\psi_r(\tau)$ denotes the component of the ACF in Equation (4.11) that contains the time delay peak and the leak noise spectrum $G_{ll}(\omega)$ is assumed to be flat. The second equality in Equation (D.1) results from Parseval's theorem.

The time delay resolution of the power cepstrum is given by

$$\begin{aligned}\tau_{\text{res,CEPS}} &= \frac{\int_{-\infty}^{\infty} Q_1^2(q)\,dq}{Q_1^2(0)} = \frac{\frac{1}{2\pi}2\int_0^{\infty}\left[\frac{2\Gamma\cdot e^{-|\omega|\beta\Delta d}}{1+\Gamma^2e^{-2|\omega|\beta\Delta d}+G_{nn}(\omega)/G_d(\omega)}\right]^2 d\omega}{\left[\frac{1}{2\pi}2\int_0^{\infty}\frac{2\Gamma\cdot e^{-|\omega|\beta\Delta d}}{1+\Gamma^2e^{-2|\omega|\beta\Delta d}+G_{nn}(\omega)/G_d(\omega)}d\omega\right]^2} \\ &\approx \pi\frac{\int_0^{\infty}e^{-2|\omega|\beta\Delta d}d\omega}{\left[\int_0^{\infty}e^{-|\omega|\beta\Delta d}d\omega\right]^2} = \frac{\pi\beta\cdot\Delta d}{2}\end{aligned} \tag{D.2}$$

where it has been assumed that all the terms except $Q_1(q)$ in Equation (4.12) as well as the subsequent higher-order peaks in $Q_1(q)$ are negligible at the time delay $q=\tau_{PR}$, $\zeta_d \triangleq \frac{G_d(\omega)}{G_{nn}(\omega)}$ is negligible (i.e., high SNR) or nearly constant, and $\Gamma e^{-2|\omega|\beta\Delta d}$ is small

Appendix D2. Detection signal-to-noise ratio

The variance $\text{var}\left\{\hat{R}_{xx}(\tau)\right\}$ of the ACF estimate $\hat{R}_{xx}(\tau)$ is given by (Bendat and Piersol, 2010)

$$\begin{aligned}\operatorname{var}\left\{\hat{R}_{xx}(\tau)\right\} &= \frac{1}{T}\int_{-T}^{T}\left(R_{xx}^2(\xi)+R_{xx}(\tau+\xi)R_{xx}(\tau-\xi)\right)d\xi \\ &= \frac{1}{2\pi T}\int_{-\infty}^{\infty}\left(1+e^{2j\omega\tau}\right)G_{xx}^2(\omega)\,d\omega \approx \frac{1}{2\pi T}\int_{-\infty}^{\infty}G_I^2(\omega)\,d\omega\end{aligned} \tag{D.3}$$

where $G_I(\omega)$ is as defined in Appendix C, and T is the observation time. The second expression in Equation (D.3) results from Parseval's theorem, and the last approximation is valid for lags much greater than the correlation time of the signal. Thus, the detection SNR for the autocorrelation method is given by

$$\begin{aligned}D_{\text{snr,ACF}} &= \frac{R_{xx}^2(\tau_{\text{PR}})}{\operatorname{var}\left\{\hat{R}_{xx}(\tau)\right\}} = \frac{\left[\frac{1}{2\pi}2\int_0^{\infty}\Gamma G_{ll}(\omega)e^{-|\omega|\beta d_{\Sigma}}d\omega\right]^2}{\frac{1}{2\pi T}2\int_0^{\infty}G_d^2(\omega)\left[1+\Gamma e^{-2|\omega|\beta\Delta d}+G_{nn}(\omega)/G_d(\omega)\right]^2 d\omega} \\ &\approx \frac{\Gamma^2 T}{\pi\left(1+1/\zeta_d\right)^2}\frac{\left[\int_0^{\infty}e^{-|\omega|\beta d_{\Sigma}}d\omega\right]^2}{\int_0^{\infty}\left[e^{-2|\omega|\beta d_{PW}}\right]^2 d\omega} = \frac{4\Gamma^2 T}{\pi\left(1+1/\zeta_d\right)^2(\beta d_{\Sigma})^2}\frac{1}{B_d}\end{aligned} \tag{D.4}$$

where $\Gamma e^{-2|\omega|\beta\Delta d}$ is assumed to be small, and B_d is the statistical bandwidth of the direct-path signal, which is defined as (Bendat and Piersol, 2010)

$$B_d = \frac{\left[\int_0^{\infty}G_d(\omega)d\omega\right]^2}{\int_0^{\infty}G_d^2(\omega)d\omega} \approx \frac{\left[\int_0^{\infty}e^{-2|\omega|\beta d_{PW}}d\omega\right]^2}{\int_0^{\infty}e^{-4|\omega|\beta d_{PW}}d\omega} = \frac{1}{\beta d_{\text{PW}}}\ . \tag{D.5}$$

The cepstral peak at $q=\tau_{PR}$ (Equation (4.12)) must be detected in a background noise given by the term $\varepsilon_{\text{CEP}} = \sum_{m=1}^{\infty}\frac{(-1)^{m-1}}{m}g_m(q)$. For large observation time T, the spectral noise $\varepsilon(\omega)$ in the auto-power spectrum estimate can be approximated as a zero-mean white noise process with the property (Lindgren and Gong, 1974)

$$\mathrm{E}\left\{\varepsilon(\omega_m)\varepsilon(\omega_n)\right\} \cong \frac{2\pi}{T}G_{xx}^2(\omega)\delta(\omega_m+\omega_n)\ . \tag{D.6}$$

Based on this property, the variance of the background noise ε_{CEP} is evaluated as

$$\sigma_{\varepsilon_{\text{CEP}}}^2 = \mathrm{E}\left\{\left|\frac{1}{2\pi}2\int_0^{\infty}\frac{\varepsilon(\omega)}{G_{xx}(\omega)}e^{j\omega\tau_{\text{PR}}}d\omega\right|^2\right\} = \frac{1}{\pi T}\int_{\omega_1}^{\omega_2}1\,d\omega = \frac{\Delta\omega}{\pi T}\ . \tag{D.7}$$

where $\Delta\omega=\omega_2-\omega_1$, and $\omega_1\le\omega\le\omega_2$ is the analysed frequency region, i.e., the frequency region in which the leak noise is considered to be significant relative to the noise. This yields the detection SNR as

$$D_{\text{snr,CEPS}} = \frac{Q_1^2(0)}{\sigma^2_{\varepsilon_{CEP}}} = \frac{\pi T}{\Delta\omega}\left[2\,\tfrac{1}{2\pi}\int_0^\infty \frac{2\Gamma\cdot e^{-|\omega|\beta\Delta d}}{1+\Gamma^2 e^{-2|\omega|\beta\Delta d}+1/\zeta_d}\,d\omega\right]^2$$
$$\approx \frac{4\Gamma^2 T}{\pi\Delta\omega}\frac{1}{\left(1+1/\zeta_d\right)^2}\left[\int_0^\infty e^{-|\omega|\beta\Delta d}\,d\omega\right]^2 = \frac{4\Gamma^2 T}{\pi\left(1+1/\zeta_d\right)^2\left(\beta\Delta d\right)^2}\frac{1}{\Delta\omega} \quad . \qquad \text{(D.8)}$$

Appendix E. Deriving the spectrally constrained normalised multichannel frequency least-mean squares (NMCFLMS) blind channel identification algorithm

Appendix E1. Deriving the blind channel identification update equation

The bulk of the derivation in this appendix is based on the documentation for BSIE toolbox (Habets et al., 2011). Each output signal x_i, $i=1,2$, is first divided into M time blocks of L samples ($\mathbf{x}_i(m)=\left[x_i(mL) \quad x_i(mL+1) \quad \cdots \quad x_i(mL+L-1)\right]^T$, $m=1,2,\ldots,M$). The time-domain cross-relation (CR) $x_2 \otimes h_1 - x_1 \otimes h_2$ in the m th time blocks is given by $\mathbf{e}(m)=\mathbf{y}_{12}(m)-\mathbf{y}_{21}(m)$, where $\mathbf{y}_{ij}(m)=\mathbf{x}_i(m)\otimes\mathbf{h}_j$. The linear convolution $\mathbf{y}_{ij}(m)$ can be obtained using the overlap-save technique from the last L samples of the circular convolution $\tilde{\mathbf{y}}_{ij}(m)$ (Rabiner and Gold, 1975)

$$\tilde{\mathbf{y}}_{ij}(m)=\mathbf{C}_{x_i(m)}\hat{\mathbf{h}}_j^{10}(m) \tag{E.1}$$

where $\hat{\mathbf{h}}_j^{10}(m)=\left[\hat{\mathbf{h}}_j^T(m) \quad \mathbf{0}_{L\times 1}^T\right]^T$ is the j th channel estimate with L zero padding, $\mathbf{0}_{K\times P}$ denotes a null matrix of size $K\times P$, and

$$\mathbf{C}_{x_i(m)}=\begin{bmatrix} x_i(mL-L) & x_i(mL+L-1) & \cdots & x_i(mL-L+1) \\ x_i(mL-L+1) & x_i(mL-L) & \cdots & x_i(mL-L+2) \\ \vdots & \vdots & \ddots & \vdots \\ x_i(mL+L-1) & x_i(mL+L-2) & \cdots & x_i(mL-L) \end{bmatrix}$$ is the $2L\times 2L$ circulant matrix constructed from $\tilde{\mathbf{x}}_i(m)=\left[\mathbf{x}_i^T(m-1) \quad \mathbf{x}_i^T(m)\right]^T=\left[x_i(mL-L) \quad x_i(mL-L+1) \cdots x_i(mL+L-1)\right]^T$. It should be noted that the channel estimates $\underline{\hat{\mathbf{h}}}_1(m)$ and $\underline{\hat{\mathbf{h}}}_2(m)$ depend on the selected block size L, but this dependency will be omitted in this derivation for brevity. Note that the first column of $\mathbf{C}_{x_i(m)}$ is given by $\tilde{\mathbf{x}}_i(m)$, and subsequent columns are shifted versions of $\tilde{\mathbf{x}}_i(m)$. A 50% overlap has been employed such that previous L samples of $\mathbf{x}_i(m-1)$ are included in $\tilde{\mathbf{x}}_i(m)$. Thus, $\mathbf{y}_{ij}(m)$ can be extracted from $\tilde{\mathbf{y}}_{ij}(m)$ as

$$\mathbf{y}_{ij}(m)=\mathbf{W}_{L\times 2L}^{01}\tilde{\mathbf{y}}_{ij}(m)=\mathbf{W}_{L\times 2L}^{01}\mathbf{C}_{x_i(m)}\hat{\mathbf{h}}_j^{10}(m)=\mathbf{W}_{L\times 2L}^{01}\mathbf{C}_{x_i(m)}\mathbf{W}_{2L\times L}^{10}\hat{\mathbf{h}}_j(m) \tag{E.2}$$

where $\mathbf{W}_{L\times 2L}^{01}=\left[\mathbf{0}_{L\times L} \quad \mathbf{I}_{L\times L}\right]$, $\mathbf{W}_{2L\times L}^{10}=\left[\mathbf{I}_L \quad \mathbf{0}_{L\times L}\right]^T$, and $\mathbf{I}_K$ is the $K\times K$ identity matrix. The circulant matrix $\mathbf{C}_{x_i(m)}$ can be diagonalised by a DFT (Davis, 2012) as $\mathbf{C}_{x_i(m)}=\mathbf{F}_{2L}^{-1}\mathcal{D}_i(m)\mathbf{F}_{2L}$, where

$\mathbf{F}_K$ denotes a $K \times K$ DFT matrix, while the corresponding inverse DFT matrix is denoted as $\mathbf{F}_K^{-1} = \frac{1}{K}\mathbf{F}_K^H$, $(\bullet)^H$ denotes the Hermitian transpose, and $\underline{\mathcal{D}}_i(m)$ is a diagonal matrix with diagonal elements being given by the $2L$-point DFT of $\tilde{\mathbf{x}}_i(m)$. In this appendix, an underscore is used to indicate a frequency-domain parameter. Hence, the frequency-domain CR error $\underline{\mathbf{e}}(m)$ can be written as

$$\underline{\mathbf{e}}(m) = \mathbf{F}_L\left\{\mathbf{y}_{12}(m) - \mathbf{y}_{21}(m)\right\} = \boldsymbol{\mathcal{W}}_{L\times 2L}^{01}\left\{\underline{\mathcal{D}}_1(m)\boldsymbol{\mathcal{W}}_{2L\times L}^{10}\underline{\hat{\mathbf{h}}}_2(m) - \underline{\mathcal{D}}_2(m)\boldsymbol{\mathcal{W}}_{2L\times L}^{10}\underline{\hat{\mathbf{h}}}_1(m)\right\} \quad \text{(E.3)}$$

where $\underline{\hat{\mathbf{h}}}_i(m) = \mathbf{F}_L\hat{\mathbf{h}}_i(m)$, $\boldsymbol{\mathcal{W}}_{L\times 2L}^{01} = \mathbf{F}_L\mathbf{W}_{L\times 2L}^{01}\mathbf{F}_{2L}^{-1}$, and $\boldsymbol{\mathcal{W}}_{2L\times L}^{10} = \mathbf{F}_{2L}\mathbf{W}_{2L\times L}^{10}\mathbf{F}_L^{-1}$. Estimates of the two channels $\underline{\hat{\mathbf{h}}}_1$ and $\underline{\hat{\mathbf{h}}}_2$ are obtained by minimising the cost function $J_{\mathrm{e}}(m)$ given by the mathematical expected of the instantaneous error $J_{\mathrm{e}}(m) = \underline{\mathbf{e}}(m)^H\,\underline{\mathbf{e}}(m)$ using the LMS algorithm. For $m = 1, 2, \ldots, M$, the LMS channel estimates are given by (Huang and Benesty, 2003b)

$$\underline{\hat{\mathbf{h}}}_i^{10}(m+1) = \underline{\hat{\mathbf{h}}}_i^{10}(m) - \mu_{\mathrm{bci}}\nabla J_{\mathrm{e},i}(m) \quad \text{(E.4)}$$

where

$$\nabla J_{\mathrm{e},i}(m) = \left[\underline{\mathbf{P}}_i(m) + \delta_{\mathrm{bci}}\mathbf{I}_{2L}\right]^{-1} \times \underline{\mathcal{D}}_k^*(m)\,\underline{\mathbf{e}}^{01}(m), \quad i \neq k, \quad \text{(E.5)}$$

denotes the gradient of $J_e(m)$ with respect to $\left(\underline{\hat{\mathbf{h}}}_i^{10}(m)\right)^*$; $\underline{\mathbf{e}}^{01}(m) = \boldsymbol{\mathcal{W}}_{L\times 2L}^{01}\underline{\mathbf{e}}(m) = \mathbf{F}_{2L}\begin{bmatrix} 0_{L\times 1} \\ \mathbf{F}_L^{-1}\underline{\mathbf{e}}(m) \end{bmatrix}$, μ_{bci} is the step-size parameter for the LMS algorithm, δ_{bci} is the regularisation parameter (a small number) to avoid singularities during matrix inversion, and $\underline{\mathbf{P}}_i(m) = \underline{\mathcal{D}}_i^*(m)\underline{\mathcal{D}}_i(m)$ is computed using a recursive scheme

$$\underline{\mathbf{P}}_i(m) = \lambda_{\mathrm{bci}}\underline{\mathbf{P}}_i(m-1) + (1-\lambda_{\mathrm{bci}})\underline{\mathcal{D}}_k^*(m)\underline{\mathcal{D}}_k(m), \quad i \neq k \quad \text{(E.6)}$$

where $\lambda_{\mathrm{bci}} = \left[1 - \frac{1}{3(L+1)}\right]^{L+1}$ is the forgetting (smoothing) factor.

Appendix E2. Deriving the update equation for the spectrally constrained NMCFLMS

The modified NMCFLMS cost function that includes phase and log-spectrum spectral constraints is shown in Equation (5.11). Minimisation of this cost using the LMS algorithm and derivation of the update equation for the channel estimates require the computation of the gradient of each penalty term with respect to the complex conjugate $\left(\underline{\hat{\mathbf{h}}}_i^{10}(m)\right)^*$ of each channel estimate (see the LMS procedures in He et al. (2018)). The gradient $\nabla J_{\mathrm{e},i}(m)$ of the cost function in the original NMCFLMS algorithm is given in Equation(E.5). The gradient $\nabla J_{\mathrm{rb},i}(m)$ of $J_{\mathrm{rb},i}(m)$ has been derived by He et al. (2018) as

$$\nabla J_{\mathrm{rb},i}(m)=\frac{\partial J_{\mathrm{rb},i}(m)}{\partial\left(\underline{\hat{\mathbf{h}}}_i^{10}(m)\right)^*}=p\left[\underline{\mathbf{P}}_i(m)+\delta\mathbf{I}_{2L}\right]^{-1}\left|\hat{\mathbf{h}}_i^{10}(m-1)\right|^{p-1}\odot\exp\left\{j\arg\left(\hat{\mathbf{h}}_i^{10}(m)\right)\right\} \quad \text{(E.7)}$$

where $j=\sqrt{-1}$ is the imaginary unit, p $(1\le p<2)$ is the order of the ℓ^p-norm, and $\odot$ denotes the Hadamard (element-wise) product. The derivative $\nabla J_{\mathrm{ph},i}(m)$ of the phase penalty term $J_{\mathrm{ph},i}(m)$ in Equation (5.12) is calculated as

$$\nabla J_{\mathrm{ph},i}(m)=\frac{\partial J_{\mathrm{ph},i}(m)}{\partial\left(\underline{\hat{\mathbf{h}}}_i^{10}(m)\right)^*}=\frac{\partial\boldsymbol{\Omega}_i(m)}{\partial\left(\underline{\hat{\mathbf{h}}}_i^{10}(m)\right)^*}\frac{\partial J_{\mathrm{ph},i}(m)}{\partial\boldsymbol{\Omega}_i(m)}\ . \quad \text{(E.8)}$$

The k th element of the first term in this equation can be evaluated using the Wirtinger derivative $\frac{\partial}{\partial u^*}=\frac{1}{2}\left(\frac{\partial}{\partial\mathrm{Re}\{u\}}+j\frac{\partial}{\partial\mathrm{Im}\{u\}}\right)$ (Petersen and Pedersen, 2012) as

$$\frac{\partial\Omega_{i,k}(m)}{\partial\left(\underline{\hat{h}}_{i,k}^{10}(m)\right)^*}=\frac{\partial}{\partial\left(\underline{\hat{h}}_{i,k}^{10}(m)\right)^*}\arctan\left(\frac{\mathrm{Im}\left\{\underline{\hat{h}}_{i,k}^{10}(m)\right\}}{\mathrm{Re}\left\{\underline{\hat{h}}_{i,k}^{10}(m)\right\}}\right)=\frac{j}{2}\frac{\underline{\hat{h}}_{i,k}^{10}(m)}{\left|\underline{\hat{h}}_{i,k}^{10}(m)\right|^2}\ . \quad \text{(E.9)}$$

Here, $\mathrm{Re}\{u\}$ and $\mathrm{Im}\{u\}$ denote the real and imaginary parts of the complex number u, respectively. The k th element of the second term in Equation (E.8) is evaluated as

$$\begin{aligned}\frac{\partial J_{\mathrm{ph},i}(m)}{\partial\Omega_{i,k}(m)}&=\frac{\partial}{\partial\Omega_{i,k}(m)}\sum_{k=2}^{2L-1}\left|\Omega_{i,k-1}(m)-2\Omega_{i,k}(m)+\Omega_{i,k+1}(m)\right|^2\\&=2\cdot\Omega_{i,k-2}(m)-8\cdot\Omega_{i,k-1}(m)+12\cdot\Omega_{i,k}(m)\\&\quad-8\cdot\Omega_{i,k+1}(m)+2\cdot\Omega_{i,k+2}(m)\end{aligned} \quad \text{(E.10)}$$

for $2\le k\le 2L-1$. By substituting Equations (E.9) and (E.10) in Equation (E.8), $\nabla J_{\mathrm{ph},i}(m)$ is obtained in matrix form as

$$\nabla J_{\mathrm{ph},i}(m)=\tfrac{j}{2}\mathbf{T}_i(m)\{\mathbf{Q}\boldsymbol{\Omega}_i\} \quad \text{(E.11)}$$

where $\mathbf{T}_i(m)=\mathrm{diag}\left\{\left[\frac{\underline{\hat{h}}_{i,1}^{10}(m)}{\left|\underline{\hat{h}}_{i,1}^{10}(m)\right|^2},\ \cdots,\ \frac{\underline{\hat{h}}_{i,2L}^{10}(m)}{\left|\underline{\hat{h}}_{i,2L}^{10}(m)\right|^2}\right]\right\}$ is a diagonal matrix whose k th diagonal element is given by $\frac{\underline{\hat{h}}_{i,k}^{10}(m)}{\left|\underline{\hat{h}}_{i,k}^{10}(m)\right|^2}$; and

$$\mathbf{Q}=\left(\begin{array}{l}12\mathbf{I}_{2L\times 2L}-8\begin{bmatrix}\mathbf{0}_{(2L-1)\times 1} & \mathbf{I}_{(2L-1)\times(2L-1)}\\ 0 & \mathbf{0}_{1\times(2L-1)}\end{bmatrix}-8\begin{bmatrix}\mathbf{0}_{1\times(2L-1)} & 0\\ \mathbf{I}_{(2L-1)\times(2L-1)} & \mathbf{0}_{(2L-1)\times 1}\end{bmatrix}\\ +2\begin{bmatrix}\mathbf{0}_{(2L-2)\times 1} & \mathbf{I}_{(2L-2)\times(2L-2)}\\ \mathbf{0}_{2\times 1} & \mathbf{0}_{1\times(2L-2)}\end{bmatrix}+2\begin{bmatrix}\mathbf{0}_{1\times(2L-2)} & \mathbf{0}_{1\times 2}\\ \mathbf{I}_{(2L-2)\times(2L-2)} & \mathbf{0}_{(2L-2)\times 1}\end{bmatrix}\end{array}\right)\odot\begin{bmatrix}\mathbf{0}_{1\times 2L}\\ \mathbf{I}_{(2L-2)\times 2L}\\ \mathbf{0}_{1\times 2L}\end{bmatrix}\ .$$

In a similar manner, the gradient $\nabla J_{\mathrm{ls},i}(m)$ of the log-spectrum penalty term $J_{\mathrm{ls},i}(m)$ in Equation (5.13) is given by

$$\nabla J_{\mathrm{ls},i}(m) = \frac{\partial J_{\mathrm{ls},i}(m)}{\partial\left(\underline{\hat{\mathbf{h}}}_i^{10}(m)\right)^*} = \frac{\partial \boldsymbol{\Psi}_i(m)}{\partial\left(\underline{\hat{\mathbf{h}}}_i^{10}(m)\right)^*}\frac{\partial J_{\mathrm{ls},i}(m)}{\partial \boldsymbol{\Psi}_i(m)} \ . \tag{E.12}$$

The k th element in the first term of this equation can be evaluated as

$$\frac{\partial \Psi_{i,k}(m)}{\partial\left(\underline{\hat{h}}_{i,k}^{10}(m)\right)^*} = \frac{1}{2}\frac{\underline{\hat{h}}_{i,k}^{10}(m)}{\left|\underline{\hat{h}}_{i,k}^{10}(m)\right|^2} \tag{E.13}$$

while the elements in the second term have the same form as the terms in Equation (E.10). Consequently, $\nabla J_{\mathrm{ls},i}(m)$ is obtained in matrix form as

$$\nabla J_{\mathrm{ls},i}(m) = \tfrac{1}{2}\mathbf{T}_i(m)\{\mathbf{Q}\boldsymbol{\Psi}_i\} \ . \tag{E.14}$$

Employing the same LMS algorithm procedures as He et al. (2018), the update equations for the spectrally constrained NMCFLMS algorithm can be expressed as

$$\underline{\hat{\mathbf{h}}}_i^{10}(L,m+1) = \underline{\hat{\mathbf{h}}}_i^{10}(L,m) - \mu_{\mathrm{bci}}\nabla J_{\mathrm{e},i}(m) + \mu_{\mathrm{bci}}\begin{Bmatrix}\eta_{\mathrm{rb}}(m)\nabla J_{\mathrm{rb},i}(m)\\ -\eta_{\mathrm{ph}}(m)\nabla J_{\mathrm{ph},i}(m)\\ -\eta_{\mathrm{ls}}(m)\nabla J_{\mathrm{ls},i}(m)\end{Bmatrix} \tag{E.15}$$

where the step sizes are calculated analogously to the step size in variable step multichannel frequency LMS method (Haque and Hasan, 2007) as

$$\begin{bmatrix}\eta_{\mathrm{rb}}(m) & \eta_{\mathrm{ph}}(m) & \eta_{\mathrm{ls}}(m)\end{bmatrix} = \left|\begin{bmatrix}\nabla J_{\mathrm{rb}}(m) & -\nabla J_{\mathrm{ph}}(m) & -\nabla J_{\mathrm{ls}}(m)\end{bmatrix}^{\dagger}\nabla J_{\mathrm{e}}(m)\right| \tag{E.16}$$

where ∇J_{rb}, ∇J_{ph}, ∇J_{ls}, and ∇J_{e} are stacked column vectors for the respective gradients in the two channels ($i=1$ and $i=2$); and † denotes the pseudoinverse. Finally, substituting Equations (E.5), (E.7), (E.11), (E.14), and (E.16) in Equation (E.15) yields the required update equations.

Appendix F. Deriving the expressions for the peak-to-side lobe ratio

If the leak noise spectrum is assumed to be flat, $G_{ll}(\omega)=S_0$, the expected value of the CCF peak $R_{\max}=R_{x_1x_2}(\tau_{\text{peak}})$ is given by

$$\mathrm{E}\{R_{\max}\}=R_{l_1l_2}(\tau_{\text{peak}})=\frac{S_0}{\pi\beta d} \tag{F.1}$$

where $R_{l_1l_2}(\tau)=\mathrm{F}^{-1}\{G_{l_1l_2}(\omega)\}=\mathrm{F}^{-1}\left\{G_{ll}(\omega)e^{-|\omega|\beta d}e^{-j\omega\tau_{\text{peak}}}\right\}$ is the biased CCF of the noise-free components of measured leak signals (i.e., the first term in Equation (6.7)). For a long measurement time T, the variance of the cross-correlation value at an arbitrary lag τ is given by (Bendat and Piersol, 2010)

$$\begin{aligned}\mathrm{var}\{R_{x_1x_2}(\tau)\}&\approx\frac{1}{T}\int_{-\infty}^{\infty}\left(R_{x_1x_1}(\varsigma)R_{x_2x_2}(\varsigma)+R_{x_1x_2}(\varsigma+\tau)R_{x_2x_1}(\varsigma-\tau)\right)d\varsigma\\&=\frac{1}{T}\int_{-\infty}^{\infty}\begin{pmatrix}R_{l_1l_1}(\varsigma)R_{l_2l_2}(\varsigma)+R_{l_1l_1}(\varsigma)R_{n_2n_2}(\varsigma)\\+R_{n_1n_1}(\varsigma)R_{l_2l_2}(\varsigma)+R_{n_1n_1}(\varsigma)R_{n_2n_2}(\varsigma)\\+R_{l_1l_2}(\varsigma+\tau)R_{l_2l_1}(\varsigma-\tau)\end{pmatrix}d\varsigma\end{aligned}. \tag{F.2}$$

The cross-correlation values of bandlimited signals approaches zero at lags τ much greater than the correlation time of the signals, which implies that $R_{x_1x_1}(\varsigma)R_{x_2x_2}(\varsigma)\gg R_{x_1x_2}(\varsigma+\tau)R_{x_2x_1}(\varsigma-\tau)$ for $\tau\gg 0$ (Bendat and Piersol, 2010). Thus, for a large $\tau=\tau_{far}$, the variance can be approximated as

$$\mathrm{var}\{R_{x_1x_2}(\tau_{far})\}\approx\frac{1}{T}\int_{-\infty}^{\infty}\begin{pmatrix}R_{l_1l_1}(\varsigma)R_{l_2l_2}(\varsigma)+R_{l_1l_1}(\varsigma)R_{n_2n_2}(\varsigma)\\+R_{n_1n_1}(\varsigma)R_{l_2l_2}(\varsigma)+R_{n_1n_1}(\varsigma)R_{n_2n_2}(\varsigma)\end{pmatrix}d\varsigma\ . \tag{F.3}$$

Assuming similar correlation functions (Gaussian) for the leak signals and noise, and defining $\zeta_i=\dfrac{R_{l_il_i}(\tau)}{R_{n_in_i}(\tau)}$ as being nearly constant, then the variance at the far point can be rewritten as

$$\begin{aligned}\mathrm{var}\{R_{x_1x_2}(\tau_{far})\}&=\left(1+\frac{1}{\zeta_1}+\frac{1}{\zeta_2}+\frac{1}{\zeta_1}\frac{1}{\zeta_2}\right)\frac{1}{T}\int_{-\infty}^{\infty}R_{l_1l_1}(\varsigma)R_{l_2l_2}(\varsigma)d\varsigma\\&=\left(1+\frac{1}{\zeta_1}+\frac{1}{\zeta_2}+\frac{1}{\zeta_1}\frac{1}{\zeta_2}\right)\frac{1}{2\pi T}\int_{-\infty}^{\infty}G_{l_1l_1}(\omega)G_{l_2l_2}(\omega)d\omega\end{aligned} \tag{F.4}$$

where the last expression follows from Parseval's theorem. Rewriting the auto-power cepstra in terms of the pipe FRF (Equation (2.5)), the PSR is obtained as

$$\mathrm{PSR}=\frac{\mathrm{E}^2\{R_{\max}\}}{\mathrm{var}\{R_{x_1x_2}(\tau_{far})\}}=\frac{2T}{\pi\beta d}\left(1+\frac{1}{\zeta_1}+\frac{1}{\zeta_2}+\frac{1}{\zeta_1}\frac{1}{\zeta_2}\right)^{-1}. \tag{F.5}$$

Appendix G. Deriving the variance of the time delay estimate

Appendix G1. Inherent bandpass filtering time delay estimate

The derivation in this appendix follows the approach used by Azaria and Hertz (1984). The biased CCF $\hat{R}_{\tilde{x}_1\tilde{x}_2}(\tau)$ of filtered leak signals $\tilde{x}_1(t) = w(t) \otimes x_1(t)$ and $\tilde{x}_2(t) = w(t) \otimes x_2(t)$ can be separated into two parts: a signal term $\hat{R}_{\tilde{l}_1\tilde{l}_2}(\tau)$ and a noise term $\hat{R}_{\tilde{N}}(\tau)$

$$\hat{R}_{\tilde{x}_1\tilde{x}_2}(\tau) = \hat{R}_{\tilde{l}_1\tilde{l}_2}(\tau) + \hat{R}_{\tilde{N}}(\tau) \tag{G.1}$$

where

$$\hat{R}_{\tilde{l}_1\tilde{l}_2}(\tau) = \int_0^T \tilde{l}_1(t)\tilde{l}_2(t+\tau)\,dt \tag{G.2}$$

and

$$\hat{R}_{\tilde{N}}(\tau) = \int_0^T \tilde{l}_1(t)\tilde{n}_2(t+\tau)\,dt + \int_0^T \tilde{n}_1(t)\tilde{l}_2(t+\tau)\,dt + \int_0^T \tilde{n}_1(t)\tilde{n}_2(t+\tau)\,dt \tag{G.3}$$

where T is the measurement duration. The symbol $\hat{}$ is used to denote a single realisation or estimate of a parameter, while its expected or true value will be written without any embellishment. The estimate $\tau = \hat{\tau}_{\text{peak}}$ is found by setting the first derivative $\hat{R}'_{x_1x_2}(\hat{\tau}_{\text{peak}}) = \left(\frac{\partial \hat{R}_{x_1x_2}(\tau)}{\partial \tau}\right)_{\tau=\hat{\tau}_{\text{peak}}} =$ $\hat{R}'_{\tilde{l}_1\tilde{l}_2}(\hat{\tau}_{\text{peak}}) + \hat{R}'_{\tilde{N}}(\hat{\tau}_{\text{peak}}) = 0$. In the neighbourhood of the true delay $\tau = \tau_{\text{peak}}$, the signal term $\hat{R}_{\tilde{l}_1\tilde{l}_2}(\tau)$ can be expanded in a Taylor series up to second order as

$$\hat{R}_{\tilde{l}_1\tilde{l}_2}(\tau) \approx \hat{R}_{\tilde{l}_1\tilde{l}_2}(\tau_{\text{peak}}) + \tfrac{1}{2}(\tau - \tau_{\text{peak}})^2 \hat{R}''_{\tilde{l}_1\tilde{l}_2}(\hat{\tau}_{\text{peak}}) \tag{G.4}$$

where $\hat{R}''_{\tilde{l}_1\tilde{l}_2}(\tau) = \dfrac{\partial^2 \hat{R}_{\tilde{l}_1\tilde{l}_2}(\tau)}{\partial \tau^2}$. Note that $\hat{R}'_{\tilde{l}_1\tilde{l}_2}(\tau_{\text{peak}}) \approx 0$ based on Assumption A1 in Section 7.1.1. Using the approximation in Equation (G.4) yields

$$\hat{\tau}_{\text{peak}} - \tau_{\text{peak}} = \frac{-\hat{R}'_{\tilde{N}}(\hat{\tau}_{\text{peak}})}{\hat{R}''_{\tilde{l}_1\tilde{l}_2}(\tau_{\text{peak}})}\,. \tag{G.5}$$

To calculate the expectation $\mathrm{E}\{\hat{\tau}_{\text{peak}} - \tau_{\text{peak}}\}$, the unknown $\hat{\tau}_{\text{peak}}$ in the numerator in Equation (G.5) can further be approximated by its true value τ_{peak} to make the resulting expressions independent of individual estimates. Since $\tilde{l}(t)$, $\tilde{n}_1(t)$, and $\tilde{n}_2(t)$ are all uncorrelated based on

Assumption A1 in Section 7.1.1, it follows that $\mathrm{E}\left\{\hat{R}'_{\tilde{N}}\left(\tau_{\text{peak}}\right)\right\}=0$, and hence, $\mathrm{E}\left\{\hat{\tau}_{\text{peak}}-\tau_{\text{peak}}\right\}\approx 0$, indicating that $\hat{\tau}_{\text{peak}}$ is an unbiased estimate of the time delay.

In order to compute $\sigma^2_{\hat{\tau}_{\text{peak}}}=\mathrm{E}\left\{\left(\hat{\tau}_{\text{peak}}-\tau_{\text{peak}}\right)^2\right\}$, note that since l_1 and l_2 are ergodic (based on Assumption A1 in Section 7.1.1), for a large $T>>\left|\tau_{\text{peak}}\right|$, the fluctuation $\delta R_{\tilde{l}_1\tilde{l}_2}\left(\tau_{\text{peak}}\right)\triangleq\frac{1}{T}\left(\hat{R}_{\tilde{l}_1\tilde{l}_2}\left(\tau_{\text{peak}}\right)-T\cdot R_{\tilde{l}_1\tilde{l}_2}\left(\tau_{\text{peak}}\right)\right)$ is negligible compared to $R_{\tilde{l}_1\tilde{l}_2}\left(\tau_{\text{peak}}\right)$. By neglecting the fluctuation $\delta R_{\tilde{l}_1\tilde{l}_2}\left(\tau_{\text{peak}}\right)$, the second derivative $\hat{R}''_{\tilde{l}_1\tilde{l}_2}\left(\tau_{\text{peak}}\right)$ can be approximated as $\hat{R}''_{\tilde{l}_1\tilde{l}_2}\left(\tau_{\text{peak}}\right)\approx T\cdot R''_{\tilde{l}_1\tilde{l}_2}\left(\tau_{\text{peak}}\right)$. Therefore, it also follows that the time delay estimation variance $\sigma^2_{\hat{\tau}_{\text{peak}}}$ is

$$\sigma^2_{\hat{\tau}_{\text{peak}}}\approx\frac{\mathrm{E}\left\{\left(\hat{R}'_{\tilde{N}}\left(\tau_{\text{peak}}\right)\right)^2\right\}}{T^2\left(R''_{\tilde{l}_1\tilde{l}_2}\left(\tau_{\text{peak}}\right)\right)^2}\ . \tag{G.6}$$

The expression $\mathrm{E}\left\{\left(\hat{R}'_{\tilde{N}}\left(\tau_{\text{peak}}\right)\right)^2\right\}$ can be expressed as

$$\begin{aligned}\mathrm{E}\left\{\left(R'_{\tilde{N}}\left(\tau_{\text{peak}}\right)\right)^2\right\}=&\,\mathrm{E}\left\{\int_0^T\tilde{l}_1\left(t\right)\tilde{n}'_2\left(t+\tau_1\right)dt\int_0^T\tilde{l}_1\left(u\right)\tilde{n}'_2\left(u+\tau_1\right)dt\right\}\\&+\mathrm{E}\left\{\int_0^T\tilde{n}_1\left(t\right)\tilde{l}'_2\left(t+\tau_1\right)dt\int_0^T\tilde{n}_1\left(u\right)\tilde{l}'_2\left(u+\tau_1\right)dt\right\}\\&+\mathrm{E}\left\{\int_0^T\tilde{n}_1\left(t\right)\tilde{n}'_2\left(t+\tau_1\right)dt\int_0^T\tilde{n}_1\left(u\right)\tilde{n}'_2\left(u+\tau_1\right)dt\right\}\end{aligned} \tag{G.7}$$

where the expectations of the cross products of the three integrals in Equation (G.7) are set to zero due to Assumption A1 in Section 7.1.1. To simplify Equation (G.7), it can be noted that the variance of the integral of a zero-mean stochastic process $g\left(t\right)$ is given by (Papoulis and Pillai, 2014)

$$\mathrm{var}\left\{\int_0^T g\left(t\right)dt\right\}=T\cdot\int_{-T}^{T}\left(1-\tfrac{|\zeta|}{T}\right)R_{gg}\left(\zeta\right)d\zeta\approx\int_{-\infty}^{\infty}R_{gg}\left(\zeta\right)d\zeta \tag{G.8}$$

where the approximation is valid for observation time T much larger than the correlation duration of $g\left(t\right)$. Using this property, $\mathrm{E}\left\{\left(\hat{R}'_{\tilde{N}}\left(\tau_{\text{peak}}\right)\right)^2\right\}$ can be simplified as

$$\begin{aligned}\mathrm{E}\left\{\left(\hat{R}'_{\tilde{N}}\left(\tau_{\text{peak}}\right)\right)^2\right\}=&\,T\cdot\int_{-\infty}^{\infty}R_{\tilde{l}_1\tilde{l}_1}\left(\tau\right)R_{\tilde{n}_2'\tilde{n}_2'}\left(\tau\right)d\tau+T\cdot\int_{-\infty}^{\infty}R_{\tilde{n}_1\tilde{n}_1}\left(\tau\right)R_{\tilde{l}_2'\tilde{l}_2'}\left(\tau\right)d\tau\\&+T\cdot\int_{-\infty}^{\infty}R_{\tilde{n}_1\tilde{n}_1}\left(\tau\right)R_{\tilde{n}_2'\tilde{n}_2'}d\tau\end{aligned}\ . \tag{G.9}$$

The first and second derivatives of the ACF of a zero-mean stationary process $g\left(t\right)$ are given by (Bendat and Piersol, 2010)

$$\begin{aligned} R'_{gg}(\tau) &= R_{gg'}(\tau) = -R_{g'g}(\tau) \\ R''_{gg}(\tau) &= R_{g''g}(\tau) = -R_{g'g'}(\tau) \end{aligned} . \quad \text{(G.10)}$$

By integrating the first and third terms in Equation (G.9) by parts and using Equation (G.10), the expression for $\mathrm{E}\left\{\left(\hat{R}'_{\tilde{N}}\left(\tau_{\text{peak}}\right)\right)^2\right\}$ can be simplified further as

$$\begin{aligned} \mathrm{E}\left\{\left(R'_{\tilde{N}}\left(\tau_{\text{peak}}\right)\right)^2\right\} = &-T\cdot\int_{-\infty}^{\infty} R''_{\tilde{l}_1\tilde{l}_1}(\tau) R_{\tilde{n}_2\tilde{n}_2}(\tau)\,d\tau - T\cdot\int_{-\infty}^{\infty} R''_{\tilde{l}_2\tilde{l}_2}(\tau) R_{\tilde{n}_1\tilde{n}_1}(\tau)\,d\tau \\ &+T\cdot\int_{-\infty}^{\infty} R'_{\tilde{n}_1\tilde{n}_1}(\tau) R'_{\tilde{n}_2\tilde{n}_2}(\tau)\,d\tau \end{aligned} . \quad \text{(G.11)}$$

Finally, the variance of the time delay estimate can be obtained by substituting Equation (G.11) in Equation (G.6) to obtain

$$\sigma^2_{\hat{\tau}_{\text{peak}}} \approx \frac{1}{T^2\left(R''_{\tilde{l}_1\tilde{l}_2}\left(\tau_{\text{peak}}\right)\right)^2}\begin{bmatrix} -T\cdot\int_{-\infty}^{\infty} R''_{\tilde{l}_1\tilde{l}_1}(\tau) R_{\tilde{n}_2\tilde{n}_2}(\tau)\,d\tau - T\cdot\int_{-\infty}^{\infty} R''_{\tilde{l}_2\tilde{l}_2}(\tau) R_{\tilde{n}_1\tilde{n}_1}(\tau)\,d\tau \\ +T\cdot\int_{-\infty}^{\infty} R'_{\tilde{n}_1\tilde{n}_1}(\tau) R'_{\tilde{n}_2\tilde{n}_2}(\tau)\,d\tau \end{bmatrix}. \quad \text{(G.12)}$$

By applying Wiener–Khinchin theorem, Equation (G.12) can be expressed in the frequency domain as

$$\sigma^2_{\hat{\tau}_{\text{peak}}} \approx \frac{2\pi}{T}\frac{\int_{-\infty}^{\infty}\omega^2\left[G_{\tilde{n}_1\tilde{n}_1}(\omega)G_{\tilde{l}_2\tilde{l}_2}(\omega)+G_{\tilde{n}_2\tilde{n}_2}(\omega)G_{\tilde{l}_1\tilde{l}_1}(\omega)+G_{\tilde{n}_1\tilde{n}_1}(\omega)G_{\tilde{n}_2\tilde{n}_2}(\omega)\right]d\omega}{\left[\int_{-\infty}^{\infty}\omega^2\left|G_{\tilde{l}_1\tilde{l}_2}(\omega)\right|d\omega\right]^2} \quad \text{(G.13)}$$

or in terms of the IB-TDE weighting function $W(\omega)$ as

$$\sigma^2_{\hat{\tau}_{\text{peak}},\text{IB}} = \frac{2\pi}{T}\frac{\int_{-\infty}^{\infty}\omega^2 W^2(\omega)\begin{bmatrix} G_{n_1n_1}(\omega)G_{l_2l_2}(\omega)+G_{n_2n_2}(\omega)G_{l_1l_1}(\omega) \\ +G_{n_1n_1}(\omega)G_{n_2n_2}(\omega)\end{bmatrix}d\omega}{\left[\int_{-\infty}^{\infty}\omega^2 W(\omega)\left|G_{l_1l_2}(\omega)\right|d\omega\right]^2} . \quad \text{(G.14)}$$

To simplify and analyse the variance, the magnitude of $W(\omega)$ is approximated without loss of generality as $|W(\omega)|=1$ in the analysed frequency band $\omega_1 \le \omega \le \omega_2$, i.e., the frequency region in which the leak noise is considered to be significant relative to the background noise. Two important quantities relevant to the analysis are now defined: SNR_i is defined as

$$\mathrm{SNR}_i \triangleq \frac{\sigma^2_{l_i}}{\sigma^2_{n_i}} = \frac{R_{l_il_i}(0)}{2B_0N_0}, \quad i=1,2 \quad \text{(G.15)}$$

where σ^2_u denotes the variance of $u(t)$, while the effective bandwidth B_{l_i} of $l_i(t)$ is defined as (Stein, 1981)

$$B^2_{l_i} = \int_{-\infty}^{\infty}\omega^2 G_{l_il_i}(\omega)\,d\omega \Big/ \int_{-\infty}^{\infty} G_{l_il_i}(\omega)\,d\omega . \quad \text{(G.16)}$$

Substituting Equations (G.15) and (G.16) into Equation (G.14) and using Assumptions A1 and A2 in Section 7.1.1, the variance of the time delay estimate is obtained as

$$\sigma^2_{\hat{\tau}_{\text{peak}},\text{IB}} = \frac{\pi}{T}\frac{\sigma^2_{l_1}\sigma^2_{l_2}}{B_0}\frac{\left[\dfrac{B^2_{l_2}}{\text{SNR}_1}+\dfrac{B^2_{l_1}}{\text{SNR}_2}+\dfrac{1}{2B_0}\dfrac{1}{\text{SNR}_1}\dfrac{1}{\text{SNR}_2}\dfrac{\omega_2^3-\omega_1^3}{3}\right]}{\left[\int_{\omega_1}^{\omega_2}\omega^2\left|G_{l_1l_2}(\omega)\right|d\omega\right]^2}. \qquad \text{(G.17)}$$

Equation (G.17) can be rewritten in terms of pipe properties for acoustic pressure measurements by expressing the auto-spectra of $l_i(t)$ in terms of the FRF $H(\omega,d_i)$ in Equation (2.5). By evaluating the resulting integrals in the expression have been evaluated using the relation (Gradshteyn and Ryzhik, 2007)

$$\int_0^b \omega^n e^{-a\omega}d\omega = \frac{n!}{a^{n+1}}\left[1-e^{-ab}\sum_{k=0}^{n}\frac{(ab)^k}{k!}\right], \quad a>0 \qquad \text{(G.18)}$$

the effective bandwidth B_{l_i} can be calculated under Assumption A2 in Section 7.1.1 as $B^2_{l_i}\approx\dfrac{1}{2(\beta d_i)^2}$. This value is valid for small ω_1 and $\omega_2 \gg \omega_1$. Assuming a flat spectrum for the leak noise $G_{ll}(\omega)=S_0$, the integral in the denominator of Equation (G.17) is evaluated as $\int_{\omega_1}^{\omega_2}\omega^2 G_{l_1l_2}(\omega)d\omega \approx \dfrac{2S_0}{(\beta d)^3}$. Finally, the variance of the time delay estimate can be expressed in terms of the pipe and signal properties as

$$\sigma^2_{\hat{\tau}_{\text{peak}},\text{IB}} \approx \frac{\pi}{T}\frac{\sigma^2_{l_1}\sigma^2_{l_2}}{B_0}\frac{1}{S_0^2}\frac{(\beta d)^6}{2}\left[\begin{array}{l}\dfrac{1}{\text{SNR}_1}\dfrac{1}{(\beta d_1)^2}+\dfrac{1}{\text{SNR}_2}\dfrac{1}{(\beta d_2)^2}\\ +\dfrac{1}{3B_0}\dfrac{1}{\text{SNR}_1}\dfrac{1}{\text{SNR}_2}\omega_2^3\end{array}\right]. \qquad \text{(G.19)}$$

Appendix G2: Cepstral time delay estimate

The residual cepstrum in Equation $z(q)$ in Equation (7.15) is the sum of two parts:

$$z(q) = z_s(q)+z_N(q) \qquad \text{(G.20)}$$

where $z_s(q)=\sum_{k=1}^{\infty}Q_k(q)\otimes\delta\left(q\pm(2k-1)\tau_{\text{peak}}\right)$ denotes the part that contains the time delay information, and $z_N(q)=\sum_{m=1}^{\infty}\dfrac{(-1)^{m-1}}{m}g_{12,m}(q)$ denotes the contribution from the background noise.

Note that in separating $z(q)$ this way, the contribution of the term $B(\omega)$ to the background noise

has been neglected. However, as noted by Hassab and Boucher (1976), the contributions of this term to be background noise in low-SNR conditions is negligible compared to that of the other noise terms. Since $\mathrm{E}\left\{g_{12,m}\left(q\right)\right\}=0$, it follows that $\mathrm{E}\left\{\hat{\tau}_{\text{peak}}-\tau_{\text{peak}}\right\}\approx 0$, which implies that the cepstral time delay estimator is unbiased. Following the same procedures as in **Appendix G1**, $\sigma^2_{\hat{\tau}_{\text{peak}},\text{ceps}}=\mathrm{E}\left\{\left(\hat{\tau}_{\text{peak}}-\tau_{\text{peak}}\right)^2\right\}$ is approximated as

$$\sigma^2_{\hat{\tau}_{\text{peak}},\text{ceps}}\approx\frac{\mathrm{E}\left\{\left(z'_N\left(\tau_{\text{peak}}\right)\right)^2\right\}}{\left(\mathrm{E}\left\{z''_s\left(\tau_{\text{peak}}\right)\right\}\right)^2}\ . \tag{G.21}$$

Based on Equation (D.6), $\mathrm{E}\left\{\nu_i\left(\omega_1\right)\nu_j\left(\omega_2\right)\right\}$ can be evaluated as

$$\mathrm{E}\left\{\nu_i\left(\omega_1\right)\nu_j\left(\omega_2\right)\right\}=\frac{1}{G^2_{xx}\left(\omega\right)}\mathrm{E}\left\{\varepsilon_i\left(\omega_1\right)\varepsilon_j\left(\omega_2\right)\right\}=\begin{cases}\dfrac{2\pi}{T}\delta\left(\omega_1+\omega_2\right) & \text{for}\quad i=j\\ 0 & \text{otherwise}\end{cases}\ . \tag{G.22}$$

Consequently, the term $\mathrm{E}\left\{\left(z'_N\left(\tau_{\text{peak}}\right)\right)^2\right\}$ in the numerator of Equation (G.21) can be evaluated as

$$\mathrm{E}\left\{\left(z'_N\left(\tau_{\text{peak}}\right)\right)^2\right\}=\mathrm{E}\left\{\left|\frac{1}{2\pi}\int_{-\infty}^{\infty}\omega\left\{\nu_1\left(\omega\right)-\nu_2\left(\omega\right)\right\}d\omega\right|^2\right\}=\frac{1}{\pi T}\int_{\omega_1}^{\omega_2}\omega^2 d\omega\ . \tag{G.23}$$

To further simplify the evaluation of the term $\left(\mathrm{E}\left\{z''_s\left(\tau_{\text{peak}}\right)\right\}\right)^2$, the higher-order terms in the second summation as well as higher-order terms in $Q_1\left(q\right)$ in the residual cepstrum in Equation (7.15) are neglected. This is a good approximation particularly for low SNRs or when the relative attenuation between the measured signals is high (see Hassab and Boucher (1976)). The term $\left(\mathrm{E}\left\{z''_s\left(\tau_{\text{peak}}\right)\right\}\right)^2$ can be approximated in the frequency domain as

$$\left(\mathrm{E}\left\{z''_s\left(\tau_{\text{peak}}\right)\right\}\right)^2=\left(\frac{1}{2\pi}2\int_{\omega_1}^{\omega_2}\omega^2 a\left(\omega\right)\mathrm{E}\left\{B\left(\omega\right)\right\}d\omega\right)^2\ . \tag{G.24}$$

Substituting Equations (G.23) and (G.24) into Equation (G.21) and noting that $\mathrm{E}\left\{B\left(\omega\right)\right\}=\chi\left(\omega\right)e^{\chi(\omega)}\,\mathrm{E}_1\left\{\chi\left(\omega\right)\right\}$ (Hassab and Boucher, 1976) gives the expression for the variance of the cepstral time delay estimate as

$$\sigma^2_{\hat{\tau}_{\text{peak}},\text{ceps}}=\frac{\pi}{3T}\frac{\left(\omega_2^3-\omega_1^3\right)}{\left(\int_{\omega_1}^{\omega_2}\omega^2 a\left(\omega\right)\chi\left(\omega\right)e^{\chi(\omega)}\,\mathrm{E}_1\left\{\chi\left(\omega\right)\right\}d\omega\right)^2} \tag{G.25}$$

where $\mathrm{E}_1\left\{\bullet\right\}$ denotes the first-order exponential function.

REFERENCES

1. Abed-Meraim, K., Moulines, E., and Loubaton, P. (1997a). Prediction error method for second-order blind identification. *IEEE Transactions on Signal Processing*, *45*(3), 694-705. https://doi.org/10.1109/78.558487

2. Abed-Meraim, K., Qiu, W., and Hua, Y. (1997b). Blind system identification. *Proceedings of the IEEE*, *85*(8), 1310-1322. https://doi.org/10.1109/5.622507

3. Abramowitz, M., and Stegun, I.A. (1964). *Handbook of Mathematical Functions with Formulas, Graphs, and Mathematical Tables* (9 ed.). Dover: New York.

4. ADEC. (1999). *Technical Review of Leak Detection Technologies* (Vol. I). Alaska Department of Environmental Conservation:

5. Adegboye, M.A., Fung, W.-K., and Karnik, A. (2019). Recent Advances in Pipeline Monitoring and Oil Leakage Detection Technologies: Principles and Approaches. *Sensors (Basel, Switzerland)*, *19*(11), 2548. https://doi.org/10.3390/s19112548

6. Aho, K., Derryberry, D., and Peterson, T. (2014). Model selection for ecologists: the worldviews of AIC and BIC. *Ecology*, *95*(3), 631-636. https://doi.org/10.1890/13-1452.1

7. Akaike, H. (1974). A new look at the statistical model identification. *IEEE Transactions on Automatic Control*, *19*(6), 716-723. https://doi.org/10.1109/TAC.1974.1100705

8. Akay, M. (2012). *Biomedical Signal Processing*. Elsevier Science:

9. Almeida, F.C.L. (2013). *Improved Acoustic Methods for Leak Detection in Buried Plastic Water Distribution Pipes* [PhD, University of Southampton]. Southampton, UK.

10. Almeida, F.C.L., Brennan, M.J., Joseph, P.F., Dray, S., Whitfield, S., and Paschoalini, A.T. (2015). Towards an in-situ measurement of wave velocity in buried plastic water distribution pipes for the purposes of leak location. *Journal of Sound and Vibration*, *359*, 40-55. https://doi.org/10.1016/j.jsv.2015.06.015

11. API. (1996). *A Guide to Leak Detection for Aboveground Storage Tanks* (Vol. 334). American Petroleum Institute:

12. Ayala Castillo, P.C. (2019). *An investigation into some signal processing techniques for the development of a low-cost acoustic correlator to detect and locate leaks in buried water pipes* [PhD, São Paulo State University]. São Paulo, Brazil.

13. Azaria, M., and Hertz, D. (1984). Time delay estimation by generalized cross correlation methods. *IEEE Transactions on Acoustics, Speech, and Signal Processing*, *32*(2), 280-285. https://doi.org/10.1109/tassp.1984.1164314

14. Bartlett, M.S. (1937). Properties of Sufficiency and Statistical Tests. *Proceedings of the Royal Society of London. Series A, Mathematical and Physical Sciences*, *160*(901), 268-282. http://www.jstor.org/stable/96803

15. Beck, S.B., Curren, M.D., Sims, N.D., and Stanway, R. (2005). Pipeline Network Features and Leak Detection by Cross-Correlation Analysis of Reflected Waves. *Journal of Hydraulic Engineering*, *131*(8), 715-723. https://doi.org/10.1061/(asce)0733-9429(2005)131:8(715)

16. Becker, D. (2015). *Leak detection in water distribution networks by correlation: sound velocity as a possible source of error*. Herman Sewerin Gmbh: Guetersloh, Germany.

17. Bendat, J.S., and Piersol, A.G. (2010). *Random Data*. Wiley:

18. Benesty, J. (2000). Adaptive eigenvalue decomposition algorithm for passive acoustic source localization. *The Journal of the Acoustical Society of America*, *107*(1), 384-391. https://doi.org/10.1121/1.428310

19. Beyer, W.H. (1987). *CRC standard mathematical tables. 28th ed*. CRC Press: Boca Raton, Fla.

20. Bimpas, M., Amditis, A., and Uzunoglu, N. (2010). Detection of water leaks in supply pipes using continuous wave sensor operating at 2.45GHz. *Journal of Applied Geophysics*, *70*(3), 226-236. https://doi.org/10.1016/j.jappgeo.2010.01.003

21. bin Md Akib, A., bin Saad, N., and Asirvadam, V. (2011). Pressure point analysis for early detection system. *7th IEEE International Colloquium on Signal Processing and its Applications*, 103-107. https://doi.org/10.1109/CSPA.2011.5759852

22. Blevins, R.D., and Plunkett, R. (1980). Formulas for Natural Frequency and Mode Shape. *Journal of Applied Mechanics*, *47*(2), 461-462. https://doi.org/10.1115/1.3153712

23. Bodenham, D.A., and Adams, N.M. (2015). A comparison of efficient approximations for a weighted sum of chi-squared random variables. *Statistics and Computing*, *26*(4), 917-928. https://doi.org/10.1007/s11222-015-9583-4

24. Bogert, B.P., Healy, M.J., and Tukey, J.W. (1963). The Quefrency Analysis of time series for echoes: Cepstrum, Pseudo-Autocovariance, Cross-Cepstrum and Saphe-Cracking. In Rosenblatt, M. (Ed.), *Time Series Analysis* (pp. 209-243). Wiley.

25. Bolton, J.S., and Gold, E. (1984). The application of cepstral techniques to the measurement of transfer functions and acoustical reflection coefficients. *Journal of Sound and Vibration*, *93*(2), 217-233. https://doi.org/10.1016/0022-460x(84)90309-2

26. Bradley, A.P. (2003). Shift-invariance in the Discrete Wavelet Transform. *Proceedings of the 7th International Conference on Digital Image Computing: Techniques and Applications*, 29-38.

27. Brennan, M.J., Chapman, D.N., Joseph, P.F., Metje, N., Muggleton, J.M., and Rustighi, E. (2017). *Achieving Zero Leakage by 2050: Detection and Location Methods Acoustic Leak Detection*. UK Water Industry Research (UKWIR): London, United Kingdom.

28. Brown, M.B., and Forsythe, A.B. (1974). Robust Tests for the Equality of Variances. *Journal of the American Statistical Association*, *69*(346), 364-367. https://doi.org/10.1080/01621459.1974.10482955

29. Brunone, B., and Ferrante, M. (2001). Detecting leaks in pressurised pipes by means of transients. *Journal of Hydraulic Research*, *39*(5), 539-547. https://doi.org/10.1080/00221686.2001.9628278

30. Burnham, K.P., and Anderson, D.R. (2002). *Model Selection and Multimodel Inference: A practical information-theoretic approach* (2 ed.). Springer: New York.

31. Butterfield, J. (2018). *Deriving further information from the leak signal in water distribution pipes* [EngD, University of Sheffield]. https://etheses.whiterose.ac.uk/22850/

32. Bykerk, L., and Valls Miro, J. (2022). Detection of Water Leaks in Suburban Distribution Mains with Lift and Shift Vibro-Acoustic Sensors. *Vibration*, *5*(2), 370-382. https://doi.org/10.3390/vibration5020021

33. Carter, G.C., Nuttall, A.H., and Cable, P.G. (1973). The smoothed coherence transform. *Proceedings of the IEEE*, *61*(10), 1497-1498. https://doi.org/10.1109/proc.1973.9300

34. Casasent, D., Silbershatz, G., and Vijaya Kumar, B.V.K. (1982). Acoustooptic matched filter correlator. *Applied Optics*, *21*(13), 2356-2364. https://doi.org/10.1364/AO.21.002356

35. Cerna, M., and Harvey, A.F. (2000). The fundamentals of FFT-based signal analysis and measurement. https://www.sjsu.edu/people/burford.furman/docs/me120/FFT_tutorial_NI.pdf

36. Chen, C.H. (1984). On a segmentation algorithm for seismic signal analysis. *Geoexploration*, *23*(1), 35-40. https://doi.org/10.1016/0016-7142(84)90022-x

37. Chien, H.I. (1967). *Transients Analysis in the Water Pipeline* [PhD, University of Houston].

38. Choudhary, H., Bahl, R., and Kumar, A. (2015). Inter-sensor time delay estimation using cepstrum of sum and difference signals in underwater multipath environment. *2015 IEEE Underwater Technology (UT)*, 1-7. https://doi.org/10.1109/UT.2015.7108308

39. Cooray, K., and Ananda, M. (2008). A Generalization of the Half-Normal Distribution with Applications to Lifetime Data. *Communications in Statistics-theory and Methods*, *37*, 1323-1337. https://doi.org/10.1080/03610920701826088

40. Covas, D., Jacob, A., and Ramos, H. (2006). Bottom-Up Analysis for Assessing Water Losses: A Case Study. *Eighth Annual Water Distribution Systems Analysis Symposium (WDSA)*, 1-19. https://doi.org/10.1061/40941(247)34

41. Cramer, R., Shaw, D., Tulalian, R., Angelo, P., and van Stuijvenberg, M. (2015). Detecting and correcting pipeline leaks before they become a big problem. *Marine Technology Society Journal*, *49*(1), 31-46. https://doi.org/10.4031/mtsj.49.1.1

42. Cremer, L., Heckl, M., and Petersson, B.A.T. (2010). *Structure-Borne Sound: Structural Vibrations and Sound Radiation at Audio Frequencies*. Springer Berlin: Heidelberg.

43. Davis, P.J. (2012). *Circulant matrices* (2nd ed.). AMS Chelsea Publishing: Providence, Rhode Island.

44. Delgado, M.R., and Begovich Mendoza, O. (2017). A comparison between leak location methods based on the negative pressure wave. *Proceedings of the 14th International Conference on Electrical Engineering, Computing Science and Automatic Control (CCE)*, 1-6. https://doi.org/10.1109/iceee.2017.8108841

45. Demirci, S., Yigit, E., Eskidemir, I.H., and Ozdemir, C. (2012). Ground penetrating radar imaging of water leaks from buried pipes based on back-projection method. *NDT & E International*, *47*, 35-42. https://doi.org/10.1016/j.ndteint.2011.12.008

46. Derrick, B., Ruck, A., Toher, D., and White, P. (2018). Tests for equality of variances between two samples which contain both paired observations and independent observations. *Journal of Applied Quantitative Methods*, *13*, 36-54.

47. Digulescu, A., Candel, I., Ioana, C., Vasile, G., Dunca, G., Bucur, D.M., and Serbanescu, A. (2015). Water hammer effect characterization using an acoustic signal processing approach. *Proceedings of the 9th International Symposium on Advanced Topics in Electrical Engineering (ATEE)*, 5-8. https://doi.org/10.1109/ATEE.2015.7133666

48. Ding, J., Tarokh, V., and Yang, H. (2018). Model selection techniques: an overview. *IEEE Signal Processing Magazine*, *35*(6), 16-34. https://doi.org/10.1109/MSP.2018.2867638

49. DoD. (2020). *Global positioning system standard positioning service performance standard* (5 ed.). Office of the Department of Defense: https://www.gps.gov/technical/ps/2020-SPS-performance-standard.pdf

50. Douillet, P.L. (2009). Sampling distribution of the variance. *Proceedings of the 2009 Winter Simulation Conference (WSC)*, 403-414. https://doi.org/10.1109/wsc.2009.5429351

51. Dragomiretskiy, K., and Zosso, D. (2014). Variational Mode Decomposition. *IEEE Transactions on Signal Processing*, *62*(3), 531-544. https://doi.org/10.1109/tsp.2013.2288675

52. Dray, S., Loveday, M., Tooms, S., and Stephen, T. (2012). *Leak detection on plastic pipes.* (Vol. 12/WM.08/47). UK Water Industry Research (UKWIR): London, UK.

53. Dremin, I.M., Ivanov, O.V., and Nechitailo, V.A. (2001). Wavelets and their uses. *Uspekhi Fizicheskih Nauk*, *171*(5), 465. https://doi.org/10.3367/ufnr.0171.200105a.0465

54. El-Zahab, S., and Zayed, T. (2019). Leak detection in water distribution networks: an introductory overview. *Smart Water*, *4*(1), 5. https://doi.org/10.1186/s40713-019-0017-x

55. Elliott, S.J., and Nelson, P.A. (1985). Algorithm for multichannel LMS adaptive filtering. *Electronics Letters*, *21*(21), 979. https://doi.org/10.1049/el:19850693

56. EPA. (2010). *Control and Mitigation of Drinking Water Losses in Distribution Systems*. US Environmental Protection Agency, Office of Water (4606M), EPA 816-R-10-019.

57. Ewins, D.J., and Saunders, H. (1986). Modal Testing: Theory and Practice. *Journal of Vibration and Acoustics*, *108*(1), 109-110. https://doi.org/10.1115/1.3269294

58. Fantozzi, M., and Lambert, A.O. (2012). Residential night consumption—Assessment, Choice of Scaling Units and Calculation of Variability. *Proceedings of the IWA Water Loss Conference*, 26-29.

59. Farrow, J., Jesson, D., Mulheron, M., Nensi, T., and Smith, P. (2017). *Achieving Zero Leakage By 2050: The Basic Mechanisms of Bursts and Leakage*. UK Water Industry Research (UKWIR): London, UK.

60. Flandrin, P., Rilling, G., and Goncalves, P. (2004). Empirical mode decomposition as a filter bank. *IEEE Signal Processing Letters*, *11*(2), 112-114. https://doi.org/10.1109/lsp.2003.821662

61. Fuchs, H.V., and Riehle, R. (1991). Ten years of experience with leak detection by acoustic signal analysis. *Applied Acoustics*, *33*(1), 1-19. https://doi.org/10.1016/0003-682x(91)90062-j

62. Fuller, C.R., and Fahy, F.J. (1982). Characteristics of wave propagation and energy distributions in cylindrical elastic shells filled with fluid. *Journal of Sound and Vibration*, *81*(4), 501-518. https://doi.org/10.1016/0022-460x(82)90293-0

63. Furuya, K., and Kaneda, Y. (1997). Two-channel blind deconvolution for non-minimum phase impulse responses. *Proceedings of the IEEE International Conference on Acoustics, Speech, and Signal Processing*, *2*, 1315-1318. https://doi.org/10.1109/icassp.1997.596188

64. Gao, Y. (2006). *Leak detection in plastic water pipes* [PhD, University of Southampton]. Southampton, UK.

65. Gao, Y., Brennan, M.J., and Joseph, P.F. (2006). A comparison of time delay estimators for the detection of leak noise signals in plastic water distribution pipes. *Journal of Sound and Vibration*, *292*(3-5), 552-570. https://doi.org/10.1016/j.jsv.2005.08.014

66. Gao, Y., Brennan, M.J., and Joseph, P.F. (2009). On the effects of reflections on time delay estimation for leak detection in buried plastic water pipes. *Journal of Sound and Vibration*, *325*(3), 649-663. https://doi.org/10.1016/j.jsv.2009.03.037

67. Gao, Y., Brennan, M.J., Joseph, P.F., Muggleton, J.M., and Hunaidi, O. (2004). A model of the correlation function of leak noise in buried plastic pipes. *Journal of Sound and Vibration*, *277*(1-2), 133-148. https://doi.org/10.1016/j.jsv.2003.08.045

68. Gao, Y., Brennan, M.J., Joseph, P.F., Muggleton, J.M., and Hunaidi, O. (2005). On the selection of acoustic/vibration sensors for leak detection in plastic water pipes. *Journal of Sound and Vibration*, *283*(3-5), 927-941. https://doi.org/10.1016/j.jsv.2004.05.004

69. Gao, Y., and Liu, Y. (2017). Theoretical and experimental investigation into structural and fluid motions at low frequencies in water distribution pipes. *Mechanical Systems and Signal Processing*, *90*, 126-140. https://doi.org/10.1016/j.ymssp.2016.12.018

70. Geiger, G. (2008). *Principles of Leak Detection*. Krohne Oil and Gas: Breda, The Netherlands.

71. Geiger, G., Werner, T., and Matko, D. (2003). Leak Detection And Locating - A Survey. *Annual Pipeline Simulation Interest Group (PSIG) Meeting*, PSIG-0301.

72. Gerstacker, W.H., and Taylor, D.P. (2003). Blind channel order estimation based on second-order statistics. *IEEE Signal Processing Letters*, *10*(2), 39-42. https://doi.org/10.1109/lsp.2002.807866

73. Ghazali, M.F., Beck, S.B.M., Shucksmith, J.D., Boxall, J.B., and Staszewski, W.J. (2012). Comparative study of instantaneous frequency based methods for leak detection in pipeline networks. *Mechanical Systems and Signal Processing*, *29*, 187-200. https://doi.org/10.1016/j.ymssp.2011.10.011

74. Gill, J. (2002). Bayesian Hypothesis Testing and the Bayes Factor. In *Bayesian Methods : A Social and Behavioral Sciences Approach* (pp. 199–237). Chapman & Hall.

75. Gilles, J. (2013). Empirical Wavelet Transform. *IEEE Transactions on Signal Processing*, *61*(16), 3999-4010. https://doi.org/10.1109/tsp.2013.2265222

76. Gradshteyn, I.S., and Ryzhik, I.M. (2007). *Table of Integrals, Series, and Products* (7th ed.). Academic Press: USA.

77. Guo, T., Zhang, T., Lim, E., Lopez-Benitez, M., Ma, F., and Yu, L. (2022). A Review of Wavelet Analysis and Its Applications: Challenges and Opportunities. *IEEE Access*, *10*, 58869-58903. https://doi.org/10.1109/access.2022.3179517

78. Haan, L., and Ferreira, A. (2006). *Extreme Value Theory: An Introduction*. Springer: New York. https://doi.org/10.1007/0-387-34471-3

79. Habets, E.A.P., Lin, X., Zhang, W., Khong, A., Gaubitch, N.D., and Naylor, P.A. (2011). *Blind System Identification and Equalization Toolbox*. https://github.com/patrickanaylor/BSIE_toolbox

80. Hamilton, S., and Charalambous, B. (2020). *Leak Detection: Technology and Implementation* (2nd ed.). IWA Publishing: London, UK. https://doi.org/10.2166/9781789060850

81. Hannan, E.J., and Thomson, P.J. (1973). Estimating group delay. *Biometrika*, *60*(2), 241-253. https://doi.org/10.1093/biomet/60.2.241

82. Hanson, J.A., and Yang, H. (2008). Quantitative evaluation of cross correlation between two finite-length time series with applications to single-molecule FRET. *Journal of Physical Chemistry B*, *112*(44), 13962-13970. https://doi.org/10.1021/jp804440y

83. Haque, M.A., and Hasan, M.K. (2007). Variable step-size multichannel frequency-domain LMS algorithm for blind identification of finite impulse response systems. *IET Signal Processing*, *1*(4), 182-189. https://doi.org/10.1049/iet-spr:20070022

84. Haque, M.A., and Hasan, M.K. (2008). Noise Robust Multichannel Frequency-Domain LMS Algorithms for Blind Channel Identification. *IEEE Signal Processing Letters*, *15*, 305-308. https://doi.org/10.1109/lsp.2008.917803

85. Haque, M.A., Islam, T., and Hasan, M.K. (2011). Robust Speech Dereverberation Based on Blind Adaptive Estimation of Acoustic Channels. *IEEE Transactions on Audio, Speech, and Language Processing*, *19*(4), 775-787. https://doi.org/10.1109/tasl.2010.2064306

86. Hartung, J., Knapp, G., and Sinha, B.K. (2008). *Statistical Meta-Analysis with Applications*. John Wiley & Sons, Inc.: Hoboken, New Jersey. https://doi.org/10.1002/9780470386347

87. Hassab, J., and Boucher, R. (1976). A probabilistic analysis of time delay extraction by the cepstrum in stationary Gaussian noise. *IEEE Transactions on Information Theory*, *22*(4), 444-454. https://doi.org/10.1109/tit.1976.1055580

88. He, H., Chen, J., Benesty, J., and Yang, T. (2018). Noise Robust Frequency-Domain Adaptive Blind Multichannel Identification With Lp-Norm Constraint. *IEEE/ACM Transactions on Audio, Speech, and Language Processing*, *26*(9), 1608-1619. https://doi.org/10.1109/taslp.2018.2835729

89. Hero, A., and Schwartz, S. (1985). A new generalized cross correlator. *IEEE Transactions on Acoustics, Speech, and Signal Processing*, *33*(1), 38-45. https://doi.org/10.1109/tassp.1985.1164515

90. HMFSI. (1998). *Fire Service Manuals Volume 1: Fire Service Technology, Equipment and Media.* Stationery Office, HM Fire Service Inspectorate: London, UK.

91. Hoskins, A.J. (2015). *Monitoring the hydraulic dynamics in water distribution systems* [PhD, Imperial College London]. London, UK.

92. Hossein, R., Ivan, S., Joe, S., Michael, H., and Robert, W. (2022). *The Occurrence and Causes of Pressure Transients in Distribution Networks* (Vol. 22/WM/04/14). UK Water Industry Research (UKWIR): London, UK. https://ukwir.org/the-occurrence-and-causes-of-pressure-transients-in-distribution-networks

93. Huang, N.E., Shen, Z., Long, S.R., Wu, M.C., Shih, H.H., Zheng, Q., Yen, N.-C., Tung, C.C., and Liu, H.H. (1998). The empirical mode decomposition and the Hilbert spectrum for nonlinear and non-stationary time series analysis. *Proceedings of the Royal Society of London. Series A: Mathematical, Physical and Engineering Sciences*, *454*(1971), 903-995. https://doi.org/10.1098/rspa.1998.0193

94. Huang, T.-L., Ren, W.-X., and Lou, M. (2008). *The orthogonal Hilbert-Huang transform and its application in earthquake motion recordings analysis* 14th World Conference on Earthquake Engineering, Beijing, China.

95. Huang, Y., and Benesty, J. (2003a). Adaptive Multichannel Time Delay Estimation Based on Blind System Identification for Acoustic Source Localization. In *Adaptive Signal Processing* (pp. 227-247): Springer Berlin Heidelberg.

96. Huang, Y., and Benesty, J. (2003b). A class of frequency-domain adaptive approaches to blind multichannel identification. *IEEE Transactions on Signal Processing*, *51*(1), 11-24. https://doi.org/10.1109/tsp.2002.806559

97. Hunaidi, O. (2012). Acoustic leak detection survey strategies for water distribution pipes. *Construction Technology Update*, *79*, 1-5.

98. Hunaidi, O., Chu, W., Wang, A., and Guan, W. (2000). Detecting leaks in plastic pipes. *Journal - American Water Works Association*, *92*(2), 82-94. https://doi.org/10.1002/j.1551-8833.2000.tb08819.x

99. Hunaidi, O., and Chu, W.T. (1999). Acoustical characteristics of leak signals in plastic water distribution pipes. *Applied Acoustics*, *58*(3), 235-254. https://doi.org/10.1016/s0003-682x(99)00013-4

100. Hunaidi, O., Wang, A., Bracken, M., Gambino, T., and Fricke, C. (2004). Acoustic methods for locating leaks in municipal water pipe networks. *Proceedings of the International Conference on Water Demand Management*, 1-14.

101. IEA. (2017). *Water-Energy Nexus*. https://www.iea.org/reports/water-energy-nexus

102. Jeffreys, H. (1998). *The Theory of Probability* (3rd ed.). Clarendon Press: Oxford, UK.

103. Jenkins, G.M., and Watts, D.G. (1968). *Spectral Analysis and its Applications* (3rd ed.). Holden-Day: USA.

104. Jo, B., and Calamia, P. (2021). Robust Blind Multichannel Identification based on a phase constraint and different ℓp-norm constraints. *Proceedings of the 2020 28th European Signal Processing Conference (EUSIPCO), Amsterdam, Netherlands*, 1966-1970. https://doi.org/10.23919/eusipco47968.2020.9287710

105. Kampelopoulos, D., Karagiorgos, N., Kousiopoulos, G.-P., Porlidas, D., Konstantakos, V., and Nikolaidis, S. (2021). An RMS-based Approach for Leak Monitoring in Noisy Industrial Pipelines. *Proceedings of the IEEE International Instrumentation and Measurement Technology Conference (I2MTC)*, 1-6. https://doi.org/10.1109/I2MTC50364.2021.9460014

106. Kass, R.E., and Raftery, A.E. (1995). Bayes Factors. *Journal of the American Statistical Association*, *90*(430), 773-795. https://doi.org/10.1080/01621459.1995.10476572

107. Kavazanjian, E., Jr., Matasovic, N., Hadj-Hamou, T., and Sabatini, P.J. (1997). *Geotechnical Engineering Circular No. 3: Design Guidance. Geotechnical Earthquake Engineering for Highways. Volume I - Design Principles*. Department of Transportation, Federal Highway Administration: USA. https://rosap.ntl.bts.gov/view/dot/13897

108. Kilinski, M.A. (2019). *Overview of Leak Detection Technologies A Summary of Capabilities and Costs* (PNNL-28885). Pacific Northwest National Laboratory. https://www.osti.gov/servlets/purl/1571292

109. Knapp, C., and Carter, G. (1976). The generalized correlation method for estimation of time delay. *IEEE Transactions on Acoustics, Speech, and Signal Processing*, *24*(4), 320-327. https://doi.org/10.1109/tassp.1976.1162830

110. Kokossalakis, G. (2006). *Acoustic data communication system for in-pipe wireless sensor networks* [PhD, Massachusetts Institute of Technology]. Boston, MA, USA.

111. Kotz, S., and Nadarajah, S. (2000). *Extreme Value Distributions: Theory and Applications*. Imperial College Press: London, UK. https://doi.org/10.1142/p191

112. Kullback, S., and Leibler, R.A. (1951). On Information and Sufficiency. *The Annals of Mathematical Statistics*, *22*(1), 79-86, 78. https://doi.org/10.1214/aoms/1177729694

113. Kuonen, D. (1999). Saddlepoint Approximations for Distributions of Quadratic Forms in Normal Variables. *Biometrika*, *86*(4), 929-935. http://www.jstor.org/stable/2673596

114. Lee, P.J. (2005). *Using system response functions of liquid pipelines for leak and blockage detection* [PhD, University of Adelaide]. Adelaide, Australia.

115. Lee, P.J., Lambert, M.F., Simpson, A.R., Vítkovsky, J.P., and Misiunas, D. (2007). Leak location in single pipelines using transient reflections. *Australasian Journal of Water Resources*, *11*(1), 53-65. https://doi.org/10.1080/13241583.2007.11465311

116. Lee, P.M. (2009). *Bayesian Statistics: An Introduction* (3rd ed.). John Wiley & Sons, Inc.: New York.

117. Levene, H. (1961). Robust tests for equality of variances. In Olkin, I. and Hotelling, H. (Eds.), *Contributions to Probability and Statistics: Essays in Honor of Harold Hotelling* (pp. 278–292). Stanford University Press.

118. Li, Y. (2011). *Study on vibration and noise and its characteristics of pipeline systems considering fluid–structure interaction* [PhD, Harbin Engineering University]. Harbin, China.

119. Liemberger, R., and Wyatt, A. (2018). Quantifying the global non-revenue water problem. *Water Supply*, *19*(3), 831-837. https://doi.org/10.2166/ws.2018.129

120. Liggett, J.A., and Chen, L.C. (1994). Inverse Transient Analysis in Pipe Networks. *Journal of Hydraulic Engineering*, *120*(8), 934-955. https://doi.org/10.1061/(asce)0733-9429(1994)120:8(934)

121. Lin, W., and Zhang, X. (2006). A Novel Approach for Dynamic Pressure Transducer Based Pipeline Leak Detection. *Proceedings of the 2010 8th International Pipeline Conference, Calgary, Alberta, Canada*, *3*, 501-506. https://doi.org/https://doi.org/10.1115/IPC2010-31159

122. Lindgren, A., and Gong, K. (1974). Measurement of the relative delay between signals propagating in a multipath environment. *Proceedings of the IEEE International Conference on Engineering in the Ocean Environment (Ocean '74)*, 293-298. https://doi.org/10.1109/oceans.1974.1161438

123. Liu, W.Y. (1994). *Détection de rupture par mesure de non stationnarité locale : application à la segmentation de signaux multidimensionnels* [PhD, Institut National des Sciences Appliquées (INSA)]. Lyon, France.

124. Liu, W.Y., Magnin, I.E., and Gimenez, G. (1995). Un Nouvel Opérateur pour la Détection de Ruptures dans des Signaux Bruités [A New Operator for the Detection of Transitions in Noisy Signals]. *Traitement du signal*, *12*(3), 226-236.

125. Liu, Z., Kleiner, Y., Rajani, B., Wang, L., and Condit, W. (2012). *Condition Assessment Technologies for Water Transmission and Distribution Systems* (Vol. EPA/600/R-12/017). EPA: USA.

126. Ljung, L. (1999). *System Identification: Theory for the User*. Prentice Hall PTR: Hoboken, New Jersey.

127. Lorah, J., and Womack, A. (2019). Value of sample size for computation of the Bayesian information criterion (BIC) in multilevel modeling. *Behavior Research Methods*, *51*(1), 440-450. https://doi.org/10.3758/s13428-018-1188-3

128. Lord, J.D., and Morrell, R.M. (2006). *Measurement Good Practice Guide No. 98: Elastic Modulus Measurement*. National Physical Laboratory: Middlesex, UK.

129. Mallat, S. (2008). *A Wavelet Tour of Signal Processing* (3rd ed.). Academic Press: Boston, MA, USA.

130. Mandava, M. (1992). *Fast and robust cepstral techniques for digital image registration* [M.Sc., Texas Tech University]. Texas, USA.

131. Marple, L. (1999). Computing the discrete-time "analytic" signal via FFT. *IEEE Transactions on Signal Processing*, *47*(9), 2600-2603. https://doi.org/10.1109/78.782222

132. Martini, A., Troncossi, M., and Rivola, A. (2015). Automatic Leak Detection in Buried Plastic Pipes of Water Supply Networks by Means of Vibration Measurements. *Shock and Vibration*, *2015*, 165304. https://doi.org/10.1155/2015/165304

133. Mathai, A.M., and Provost, S.B. (1992). *Quadratic Forms in Random Variables*. Marcel Dekker: New York.

134. Matweb. (2023). *Overview of materials for Medium Density Polyethylene (MDPE), Extruded*. Retrieved 10 January 2023 from https://www.matweb.com/search/datasheet.aspx?matguid=6aee274e12d64436afb46fa35d8bb07e

135. Mishra, A., Al Gabani, S.H., and Jumaa Al Hosany, A. (2017). Pipeline Leakage Detection Using Fiber Optics Distributed Temperature Sensing DTS. *Proceedings of the Abu Dhabi International Petroleum Exhibition & Conference, Abu Dhabi, UAE*. https://doi.org/10.2118/188407-ms

136. Misiunas, D., Lambert, M., Simpson, A., and Olsson, G. (2005). Burst detection and location in water distribution networks. *Water Supply*, *5*(3-4), 71-80. https://doi.org/10.2166/ws.2005.0085

137. Miyoshi, M., and Kaneda, Y. (1988). Inverse filtering of room acoustics. *IEEE Transactions on Acoustics, Speech, and Signal Processing*, *36*(2), 145-152. https://doi.org/10.1109/29.1509

138. Moody, F.J., and Winterbone, D.E. (1991). Introduction to unsteady thermofluid mechanics. *International Journal of Heat and Fluid Flow*, *12*(4), 384-384. https://doi.org/10.1016/0142-727X(91)90028-T

139. Moore, S. (2016). A review of noise and vibration in fluid-filled pipe systems. *Proceedings of ACOUSTICS 2016*. https://www.acoustics.asn.au/conference_proceedings/AASNZ2016/papers/p112.pdf

140. Moulines, E., Duhamel, P., Cardoso, J.F., and Mayrargue, S. (1995). Subspace methods for the blind identification of multichannel FIR filters. *IEEE Transactions on Signal Processing*, *43*(2), 516-525. https://doi.org/10.1109/78.348133

141. Mpesha, W., Hanif Chaudhry, M., and Gassman, S.L. (2002). Leak detection in pipes by frequency response method using a step excitation. *Journal of Hydraulic Research*, *40*(1), 55-62. https://doi.org/10.1080/00221680209499873

142. Muggleton, J.M., Brennan, M.J., and Gao, Y. (2011). Determining the location of buried plastic water pipes from measurements of ground surface vibration. *Journal of Applied Geophysics*, *75*(1), 54-61. https://doi.org/10.1016/j.jappgeo.2011.06.030

143. Muggleton, J.M., Brennan, M.J., and Linford, P.W. (2004). Axisymmetric wave propagation in fluid-filled pipes: wavenumber measurements in in vacuo and buried pipes. *Journal of Sound and Vibration*, *270*(1-2), 171-190. https://doi.org/10.1016/s0022-460x(03)00489-9

144. Muggleton, J.M., Brennan, M.J., and Pinnington, R.J. (2002). Wavenumber prediction of waves in buried pipes for water leak detection. *Journal of Sound and Vibration*, *249*(5), 939-954. https://doi.org/10.1006/jsvi.2001.3881

145. Muggleton, J.M., and Yan, J. (2013). Wavenumber prediction and measurement of axisymmetric waves in buried fluid-filled pipes: Inclusion of shear coupling at a lubricated pipe/soil interface. *Journal of Sound and Vibration*, *332*(5), 1216-1230. https://doi.org/10.1016/j.jsv.2012.10.024

146. Murvay, P.-S., and Silea, I. (2012). A survey on gas leak detection and localization techniques. *Journal of Loss Prevention in the Process Industries*, *25*(6), 966-973. https://doi.org/10.1016/j.jlp.2012.05.010

147. Myakinin, O.O., Zakharov, V.P., Bratchenko, I.A., Kornilin, D.V., Artemyev, D.N., and Khramov, A.G. (2014). The Empirical Mode Decomposition algorithm via Fast Fourier Transform. *Proceedings of the SPIE Optical Engineering + Applications conference*, *9217 Applications of Digital Image Processing XXXVII, 921721*. https://doi.org/10.1117/12.2061808

148. NIST. (2012). *NIST/SEMATECH e-Handbook of Statistical Methods*. National Institute of Standards and Technology. https://doi.org/10.18434/M32189

149. Ofwat. (2022). *Leakage*. Retrieved 20 February 2023 from https://www.ofwat.gov.uk/leakage-in-the-water-industry/

150. Ofwat. (2023). *Leakage*. Retrieved 20 February 2023 from https://www.ofwat.gov.uk/households/supply-and-standards/leakage/

151. Oppenheim, A., V., Willsky, A., S., and Nawab, H., S. (1996). *Signals and systems* (2 ed.). Prentice-Hall: Upper Saddle River, New Jersey.

152. Oppenheim, A.V., and Schafer, R.W. (2010). *Discrete-time Signal Processing* (3rd ed.). Pearson: Upper Saddle River, New Jersey.

153. Oppenheim, A.V., Schafer, R.W., and Stockham, T.G. (1968). Nonlinear filtering of multiplied and convolved signals. *Proceedings of the IEEE*, *56*(8), 1264-1291. https://doi.org/10.1109/proc.1968.6570

154. Pal, M., Dixon, N., and Flint, J.A. (2010). Detecting and Locating Leaks in Water Distribution Polyethylene Pipes. *Proceedings of the 2010 World Congress on Engineering*, *II*.

155. Paolella, M.S. (2019). *Linear models and time-series analysis: regression, ANOVA, ARMA and GARCH*. Wiley: Newark.

156. Papastefanou, A. (2011). *An experimental investigation of leak noise from water filled plastic pipes* [PhD, University of Southampton]. Southampton, UK. https://eprints.soton.ac.uk/190853/

157. Papoulis, A., and Pillai, S.U. (2014). *Probability, random variables, and stochastic processes* (4 ed.). McGraw-Hill: New York.

158. Peeters, G. (2004). *A large set of audio features for sound description (similarity and classification) in the CUIDADO project*. IRCAM: Paris, France.

159. Percival, D.B., and Walden, A.T. (2000). *Wavelet Methods for Time Series Analysis*. Cambridge University Press: Cambridge, UK.

160. Peters, R.J. (2013). *Acoustics and Noise Control*. CRC Press: London, UK.

161. Petersen, K.B., and Pedersen, M.S. (2012). *The Matrix Cookbook*. Technical University of Denmark: Kongens Lyngby, Denmark. https://www2.imm.dtu.dk/pubdb/edoc/imm3274.pdf

162. Pinnington, R.J., and Briscoe, A.R. (1994). Externally Applied Sensor for Axisymmetric Waves in a Fluid Filled Pipe. *Journal of Sound and Vibration*, *173*(4), 503-516. https://doi.org/10.1006/jsvi.1994.1243

163. Pishro-Nik, H. (2014). *Introduction to Probability, Statistics, and Random Processes*. Kappa Research: USA.

164. Puust, R., Kapelan, Z., Savic, D.A., and Koppel, T. (2010). A review of methods for leakage management in pipe networks. *Urban Water Journal*, *7*(1), 25-45. https://doi.org/10.1080/15730621003610878

165. Quazi, A. (1981). An overview on the time delay estimate in active and passive systems for target localization. *IEEE Transactions on Acoustics, Speech, and Signal Processing*, *29*(3), 527-533. https://doi.org/10.1109/tassp.1981.1163618

166. Rabiner, L., and Gold, B. (1975). *Theory and Application of Digital Signal Processing*. Prentice Hall: Englewood Cliffs, New Jersey. https://doi.org/10.1002/piuz.19760070413

167. Rathnayaka, S., Shannon, B., Rajeev, P., and Kodikara, J. (2015). Monitoring of Pressure Transients in Water Supply Networks. *Water Resources Management*, *30*(2), 471-485. https://doi.org/10.1007/s11269-015-1172-y

168. Roe, G., and White, G. (1961). Probability density functions for correlators with noisy reference signals. *IRE Transactions on Information Theory*, *7*(1), 13-18. https://doi.org/10.1109/TIT.1961.1057613

169. Rogers, D. (2014). Leaking Water Networks: An Economic and Environmental Disaster. *Procedia Engineering*, *70*, 1421-1429. https://doi.org/10.1016/j.proeng.2014.02.157

170. Romano, M. (2012). *Near Real-Time Detection and Approximate Location of Pipe Bursts and Other Events in Water Distribution Systems* [PhD, University of Exeter]. Exeter, UK.

171. Romano, M., Kapelan, Z., and Savić, D.A. (2014). Automated Detection of Pipe Bursts and Other Events in Water Distribution Systems. *Journal of Water Resources Planning and Management*, *140*(4), 457-467. https://doi.org/10.1061/(asce)wr.1943-5452.0000339

172. Rosso, O.A., Blanco, S., Yordanova, J., Kolev, V., Figliola, A., Schürmann, M., and Başar, E. (2001). Wavelet entropy: a new tool for analysis of short duration brain electrical signals. *Journal of Neuroscience Methods*, *105*(1), 65-75. https://doi.org/10.1016/s0165-0270(00)00356-3

173. Saaty, R.W. (1987). The analytic hierarchy process—what it is and how it is used. *Mathematical Modelling*, *9*(3), 161-176. https://doi.org/https://doi.org/10.1016/0270-0255(87)90473-8

174. Schwarz, G. (1978). Estimating the Dimension of a Model. *The Annals of Statistics*, *6*(2), 461-464, 464. https://doi.org/10.1214/aos/1176344136

175. Scussel, O., Brennan, M.J., Muggleton, J.M., de Almeida, F.C.L., and Paschoalini, A.T. (2018). On the Dynamic Loading Effects of Soil on Plastic Water Distribution Pipes and its Significance for Leak Detection Using Acoustics. *Proceedings of the ASME 2018 International Mechanical Engineering Congress and Exposition, Pittsburgh, Pennsylvania, USA*, *11: Acoustics, Vibration, and Phononics*, V011T001A022. https://doi.org/10.1115/IMECE2018-87420

176. Seed, H.B., Wong, R.T., Idriss, I.M., and Tokimatsu, K. (1986). Moduli and Damping Factors for Dynamic Analyses of Cohesionless Soils. *Journal of Geotechnical Engineering*, *112*(11), 1016-1032. https://doi.org/doi:10.1061/(ASCE)0733-9410(1986)112:11(1016)

177. Sewerin. (2023). *Electroacoustic Water Leak Detection - Ground AND Valve Listening Stick Microphone AquaTest T10*. Retrieved 23 February 2023 from https://www.sewerin.co.uk/products/water-leak-location/aquatest-t10/

178. Shi, P., Yang, W., Sheng, M., and Wang, M. (2017). An Enhanced Empirical Wavelet Transform for Features Extraction from Wind Turbine Condition Monitoring Signals. *Energies*, *10*(7), 972. https://www.mdpi.com/1996-1073/10/7/972

179. Snedecor, G.W., and Cochran, W.G. (1989). *Statistical methods* (8th ed.). Iowa State University Press: Ames, Iowa.

180. Spiesberger, J.L. (1996). Identifying cross-correlation peaks due to multipaths with application to optimal passive localization of transient signals and tomographic mapping of the environment. *The Journal of the Acoustical Society of America*, *100*(2), 910-917. https://doi.org/10.1121/1.416250

181. Spiesberger, J.L. (1998). Linking auto- and cross-correlation functions with correlation equations: Application to estimating the relative travel times and amplitudes of multipath. *The Journal of the Acoustical Society of America*, *104*(1), 300-312. https://doi.org/10.1121/1.423257

182. Stein, S. (1981). Algorithms for ambiguity function processing. *IEEE Transactions on Acoustics, Speech, and Signal Processing*, *29*(3), 588-599. https://doi.org/10.1109/tassp.1981.1163621

183. Tijsseling, A.S. (1996). Fluid-structure interaction in liquid-filled pipe systems: a review. *Journal of Fluids and Structures*, *10*(2), 109-146. https://doi.org/10.1006/jfls.1996.0009

184. Tong, L., Xu, G., and Kailath, T. (1994). Blind identification and equalization based on second-order statistics: a time domain approach. *IEEE Transactions on Information Theory*, *40*(2), 340-349. https://doi.org/10.1109/18.312157

185. Tribolet, J.M. (1978). Applications of short-time homomorphic signal analysis to seismic wavelet estimation. *Geoexploration*, *16*(1), 75-96. https://doi.org/https://doi.org/10.1016/0016-7142(78)90008-X

186. Turkowski, M., Bratek, A., and Słowikowski, M. (2007). Methods and systems of leak detection in long range pipelines. *Journal of Automation, Mobile Robotics and Intelligent Systems*, 39-46.

187. Uchendu, N., Muggleton, J., Rustighi, E., and White, P. (2020). Comparative study of time delay estimators for steady-state and transient acoustic leak signals. *Proceedings of the 29th International Conference on Noise and Vibration Engineering (ISMA2020) and the 8th International Conference on Uncertainty in Structural Dynamics (USD2020)*, 2801-2815. https://past.isma-isaac.be/downloads/isma2020/proceedings/Proceedings_ISMA-USD2020.pdf

188. UNESCO. (2023). *The United Nations World Water Development Report 2023: partnerships and cooperation for water*. UNESCO World Water Assessment Programme: https://unesdoc.unesco.org/notice?id=p::usmarcdef_0000384655

189. Van Der Kleij, F.C., and Stephenson, M.J. (2002). Acoustic logging–the Bristol Water experience. *Proceedings of the IWA Specialised Conference: Leakage Management–A Practical Approach*.

190. Van Trees, H.L., Bell, K.L., and Tian, Z. (2013). *Detection estimation and modulation theory* (Second edition ed.). John Wiley & Sons: Hoboken, New Jersey.

191. Vaseghi, S.V. (1996). Spectral Subtraction. In *Advanced Signal Processing and Digital Noise Reduction* (pp. 242-260): Vieweg+Teubner Verlag.

192. Vrieze, S.I. (2012). Model selection and psychological theory: A discussion of the differences between the Akaike information criterion (AIC) and the Bayesian information criterion (BIC). *Psychological Methods*, *17*(2), 228-243. https://doi.org/10.1037/a0027127

193. Wagenmakers, E.-J., Lodewyckx, T., Kuriyal, H., and Grasman, R. (2010). Bayesian hypothesis testing for psychologists: A tutorial on the Savage–Dickey method. *Cognitive Psychology*, *60*(3), 158-189. https://doi.org/https://doi.org/10.1016/j.cogpsych.2009.12.001

194. Wang, X.-J., Lambert, M.F., Simpson, A.R., Liggett, J.A., and Vtkovský, J.P. (2002). Leak Detection in Pipelines using the Damping of Fluid Transients. *Journal of Hydraulic Engineering*, *128*(7), 697-711. https://doi.org/10.1061/(asce)0733-9429(2002)128:7(697)

195. Weinstein, E., and Weiss, A. (1984). Fundamental limitations in passive time-delay estimation--Part II: Wide-band systems. *IEEE Transactions on Acoustics, Speech, and Signal Processing*, *32*(5), 1064-1078. https://doi.org/10.1109/TASSP.1984.1164429

196. White, P.R. (1996). Detection Algorithms for Underwater Acoustic Transients. In *Control and Dynamic Systems* (pp. 193-224): Elsevier.

197. Wit, E., Heuvel, E.v.d., and Romeijn, J.-W. (2012). 'All models are wrong...': an introduction to model uncertainty. *Statistica Neerlandica*, *66*(3), 217-236. https://doi.org/https://doi.org/10.1111/j.1467-9574.2012.00530.x

198. Wu, S., Feng, F., Zhu, J., Wu, C., and Zhang, G. (2020). A Method for Determining Intrinsic Mode Function Number in Variational Mode Decomposition and Its Application to Bearing

Vibration Signal Processing. *Shock and Vibration*, *2020*, 8304903. https://doi.org/10.1155/2020/8304903

199. Wu, Y., and Liu, S. (2017). A review of data-driven approaches for burst detection in water distribution systems. *Urban Water Journal*, *14*(9), 972-983. https://doi.org/10.1080/1573062x.2017.1279191

200. Wu, Z., and Huang, N.E. (2004). A study of the characteristics of white noise using the empirical mode decomposition method. *Proceedings of the Royal Society of London. Series A: Mathematical, Physical and Engineering Sciences*, *460*(2046), 1597-1611. https://doi.org/10.1098/rspa.2003.1221

201. Xu, G., Liu, H., Tong, L., and Kailath, T. (1995a). A least-squares approach to blind channel identification. *IEEE Transactions on Signal Processing*, *43*(12), 2982-2993. https://doi.org/10.1109/78.476442

202. Xu, X.-L., Tewfik, A.H., and Greenleaf, J.F. (1995b). Time delay estimation using wavelet transform for pulsed-wave ultrasound. *Annals of Biomedical Engineering*, *23*(5), 612-621. https://doi.org/10.1007/bf02584460

203. Xu, Y.Z. (2013). *A general non-stationarity measure : Application to biomedical image and signal processing* [PhD, Institut National des Sciences Appliquées (INSA)]. Lyon, France.

204. Yang, J., Wen, Y., and Li, P. (2008). Leak location using blind system identification in water distribution pipelines. *Journal of Sound and Vibration*, *310*(1-2), 134-148. https://doi.org/10.1016/j.jsv.2007.07.067

205. Yazdekhasti, S., Piratla, K.R., Matthews, J.C., Khan, A., and Atamturktur, S. (2018). Optimal selection of acoustic leak detection techniques for water pipelines using multi-criteria decision analysis. *Management of Environmental Quality: An International Journal*, *29*(2), 255-277. https://doi.org/10.1108/MEQ-05-2017-0043

206. Zhang, J., and Di Mauro, E. (1998). *Implementing a reliable leak detection system on a crude oil pipeline* Advances in Pipeline Technology, Dubai, UAE.

207. Zhang, J., Feng, F., Marti-Puig, P., Caiafa, C.F., Sun, Z., Duan, F., and Solé-Casals, J. (2021). Serial-EMD: Fast empirical mode decomposition method for multi-dimensional signals based on serialization. *Information Sciences*, *581*, 215-232. https://doi.org/10.1016/j.ins.2021.09.033